

Efficient streamer plasma generation

Citation for published version (APA):

Winands, G. J. J. (2007). *Efficient streamer plasma generation*. [Phd Thesis 1 (Research TU/e / Graduation TU/e), Electrical Engineering]. Technische Universiteit Eindhoven. <https://doi.org/10.6100/IR627346>

DOI:

[10.6100/IR627346](https://doi.org/10.6100/IR627346)

Document status and date:

Published: 01/01/2007

Document Version:

Publisher's PDF, also known as Version of Record (includes final page, issue and volume numbers)

Please check the document version of this publication:

- A submitted manuscript is the version of the article upon submission and before peer-review. There can be important differences between the submitted version and the official published version of record. People interested in the research are advised to contact the author for the final version of the publication, or visit the DOI to the publisher's website.
- The final author version and the galley proof are versions of the publication after peer review.
- The final published version features the final layout of the paper including the volume, issue and page numbers.

[Link to publication](#)

General rights

Copyright and moral rights for the publications made accessible in the public portal are retained by the authors and/or other copyright owners and it is a condition of accessing publications that users recognise and abide by the legal requirements associated with these rights.

- Users may download and print one copy of any publication from the public portal for the purpose of private study or research.
- You may not further distribute the material or use it for any profit-making activity or commercial gain
- You may freely distribute the URL identifying the publication in the public portal.

If the publication is distributed under the terms of Article 25fa of the Dutch Copyright Act, indicated by the "Taverne" license above, please follow below link for the End User Agreement:

www.tue.nl/taverne

Take down policy

If you believe that this document breaches copyright please contact us at:

openaccess@tue.nl

providing details and we will investigate your claim.

Efficient Streamer Plasma Generation

PROEFSCHRIFT

ter verkrijging van de graad van doctor aan de
Technische Universiteit Eindhoven, op gezag van de
Rector Magnificus, prof.dr.ir. C.J. van Duijn, voor een
commissie aangewezen door het College voor
Promoties in het openbaar te verdedigen
op dinsdag 19 juni 2007 om 16.00 uur

door

Gerardus Johan Jozef Winands

geboren te Kerkrade

Dit proefschrift is goedgekeurd door de promotoren:

prof.dr.ir J.H. Blom
en
prof.dr.ir. G.M.W. Kroesen

Copromotor:
dr.ir. E.J.M. van Heesch

The work described in this thesis is part of the Dutch IOP-EMVT program (Innovatiegerichte Onderzoeksprogramma's – Elektromagnetisch Vermogens Techniek).

Printed and bound by universiteitsdrukkerij Technische Universiteit Eindhoven
Cover design by Jorrit van Rijt, Oranje Vormgevers

CIP-DATA LIBRARY TECHNISCHE UNIVERSITEIT EINDHOVEN

Winands, Gerardus Johan Jozef

Efficient streamer plasma generation / by Gerardus Johan Jozef Winands. – Eindhoven :
Technische Universiteit Eindhoven, 2007. - Proefschrift.

ISBN-978-90-386-1040-5

NUR 961

Trefw.: gasontladingen / hoogspanningstechniek / pulstechniek / pulsgeneratoren /
elektromagnetische interferentie / reactiekinetiek / plasmachemie / vrije radicalen /
productieoptimalisering / ozon

Subject headings: electric discharges / high-voltage techniques / pulsed power technology /
pulsed power supplies / electromagnetic compatibility / high-speed optical techniques /
reaction kinetics / plasma chemistry / free radicals / optimized production technology / ozone
/ impedance matching

Summary

The focus of this thesis is pulsed power induced atmospheric streamer plasmas with applications in chemical processing, in particular the removal of pollutants (e.g., VOCs, odor, tar and bacteria) from gases. Although several possibilities exist for generating streamers, this study concentrates on streamer plasmas generated by repetitively applied nanosecond time scale, multi-kilovolt pulses. The main reason for this choice is the high performance that can be obtained with this technology. Due to the complexity of the involved mechanisms, the relevant knowledge is very incomplete. To obtain additional knowledge, the interactions between the power source, the generated streamer plasma and the resulting chemical processes are investigated systematically. The individual interactions are studied by examining the energy transfer.

Basically the interactions comprise two steps: I) interaction between the pulse waveform and streamer plasma; II) interaction between the streamer plasma and the chemical processes. Initially the steps are studied separately. Thereafter, the obtained knowledge is combined to determine the energy transfer efficiency of the complete pulsed streamer plasma system.

The performed study is experimental in nature, while models and available theoretical knowledge are used to explain the results of the experiments. The developed power source is a sophisticated power modulator that can produce fast rising, high amplitude, short pulses at high repetition rates. Furthermore, the source allows for variation of these parameters in wide ranges (rise rates $0.5\text{-}3\text{ kV}\cdot\text{ns}^{-1}$, amplitudes $40\text{-}90\text{ kV}$, duration $35\text{-}250\text{ ns}$, positive and negative polarity, pulse repetition rate $10\text{-}1000$ pulses per second). Fast (80 MHz) differentiating-integrating measuring systems, designed and optimized for this study, monitor the electrical pulse waveforms. The power source is connected to the plasma reactor, a wire-plate system of electrodes. Streamer generation and propagation in this reactor are visualized by means of spatial ($100\text{ }\mu\text{m}$) and time resolved (nanosecond) ICCD photography. Ozone generation is chosen as a monitor for the oxygen radical yield. A chemical model is used to determine the actual oxygen radical yield through measurement of the produced ozone, the streamer plasma volume, the relative humidity and the gas temperature. A UV absorption spectroscopy tool measures the ozone production.

For the study of the first step: “*interaction between the pulse waveform and streamer plasma*”, an equivalent circuit-model was developed. The validity of the models was verified through a series of experiments. Three criteria were derived that should be obeyed to achieve high energy transfer efficiencies (i.e., well-matched systems): 1) The plasma should ignite before the energy transfer to the reactor capacitance reaches its maximum value; 2) The generated plasma should have a resistance equal to the output impedance of the power modulator, corrected for the DC bias voltage; 3) The DC coupling capacitor should be matched to the output capacitor of the power modulator.

Criterion 3 can be fulfilled by making proper parameter choices. The following strategy is to be employed to fulfill criteria 1 and 2: a) the applied electric field in the plasma reactor should be at a tolerable maximum above $10\text{-}15\text{ kV}\cdot\text{cm}^{-1}$ for positive polarity pulses and above $20\text{ kV}\cdot\text{cm}^{-1}$ for negative polarity pulses (because for high electric fields, the plasma resistance decreases to the output impedance of the source and the ignition delay becomes sufficiently low); b) Short pulses and/or long wire-plate distances should be avoided (the favorable load resistance values are obtained during the secondary streamer phase, not during the primary streamer phase (it is not possible to match the load to the source if only primary streamers are generated)); c) The energy density per meter of wire should be limited ($< 1\text{-}4\text{ J}\cdot\text{m}^{-1}$), at least for the pulse widths (30-250 ns) used during the measurements; d) The electric field on the wire surface should exceed $10^7\text{ V}\cdot\text{m}^{-1}$ otherwise almost no streamers are generated. The experiments show that a well-matched negative polarity system requires pulses with an amplitude approximately 50% higher than the amplitude required for well-matched positive polarity systems. For the same voltage amplitude, the plasma resistance is higher for the negative polarity. For sufficiently high voltages, the difference in matching between the polarities diminishes.

For the study of the second step: “*interaction between the streamer plasma and the chemical process*”, a key chemical process is monitored. As many pollutant removal processes are initiated by oxygen radicals, ozone production from ambient air, which also depends on these oxygen radicals, is selected as an appropriate process.

Streamer generation and oxygen radical yield (amount of radicals per unit of energy) were monitored in a set of experiments where pulse parameters and reactor dimensions were varied systematically. Both positive polarity streamers (CDS) and negative polarity streamers (ADS) were investigated. A data analysis procedure was used to obtain the radical yield of primary and secondary streamers separately. For CDS and ADS, typical oxygen radical yields were found to be in the range of $3\text{-}8\text{ mole}\cdot\text{kWh}^{-1}$. Typical differences between CDS, ADS, primary and secondary streamers can be listed as:

- For CDS, the oxygen radical yield of primary streamers exceeds that of secondary streamers (by up to a factor of two). The observed difference is contributed to the large electric field in the primary streamer head compared to the field in the secondary streamer. For primary streamer velocities up to $2.0\cdot 10^6\text{ m}\cdot\text{s}^{-1}$ it was observed that the yield of primary streamers is a rising function of the velocity. Above $2.0\cdot 10^6\text{ m}\cdot\text{s}^{-1}$, the yield starts to decrease. The secondary streamer yield was found to be constant. A well-founded explanation for the relation between primary streamer radical yield and its velocity could not be provided. Both the number of free electrons and the electron energy distribution function have to be known to explain the radical yield quantitatively. Neither of these parameters were determined during the experiments.
- The observations for the ADS are similar to the ones for the CDS: primary streamers outperform the secondary streamers (by up to a factor of 1.5), at least for streamer velocities exceeding $1.2\cdot 10^6\text{ m}\cdot\text{s}^{-1}$. Also, the primary streamer oxygen radical yield increases with streamer velocity. In contrast to the characteristics of the radical yield of

CDS secondary streamers, the yield of ADS secondary streamers increases as a function of the primary streamer velocity.

- The oxygen radical yield of ADS secondary streamers is considerably higher than the yield of CDS secondary streamers. An explanation could not be provided. However, it was determined that the electric field in secondary streamers is $22 \text{ kV}\cdot\text{cm}^{-1}$, for both CDS and ADS. As a result, the differences in the yield cannot be explained by differences in the average electron energy. Also, it is unlikely that the number of free electrons in ADS is higher than in CDS, since the plasma current of ADS is lower (for identical, but opposite polarity pulses). A lower current indicates a lower number of free electrons per unit-length of streamer.
- The oxygen radical yield of ADS secondary streamers was found to be almost equal to that of the CDS primary streamers. This finding clearly demonstrates that the average electron energy is not the only parameter of interest. A considerable amount of radicals can be produced, even when the average electron energy is low.
- The ADS primary streamer has a significantly higher oxygen radical yield than the CDS primary streamer. The different average applied electric fields during ADS and CDS measurements ($15\text{-}20 \text{ kV}\cdot\text{cm}^{-1}$ vs. $8\text{-}15 \text{ kV}\cdot\text{cm}^{-1}$) was mentioned as a possible explanation for the observed differences. However, since both the local electric field and the free electron density are unknown, no well-founded explanation for the difference could be provided.

High total system yield can be obtained when both the matching (step I) and the radical yield (step II) are optimized. For ADS, both the matching and the radical yield can be enhanced by increasing the applied voltage. Total system efficiencies of $4.6 \text{ mole}\cdot\text{kWh}^{-1}$ have been obtained. For CDS the situation is more complicated. The matching can be improved by increasing the applied voltage, increasing the pulse width or decreasing the wire-plate distance. All these changes, however, result in decreased radical yields. The changes in matching and in radical yield, as a result of changed system settings, cancel almost completely, resulting in the same total system efficiency η_{system} being obtained for almost all combinations of system settings. A difference is only attainable for low primary streamer velocities (below $2.0\cdot 10^6 \text{ m}\cdot\text{s}^{-1}$). The highest efficiencies obtained are $3.0 \text{ mole}\cdot\text{kWh}^{-1}$.

Based upon the results, a set of design criteria is presented that can be used to develop energy efficient pulsed plasma systems. It was demonstrated that, when these criteria are employed, a large scale (17 kW obtained average power), and energy efficient (more than 90% of power grid energy dissipated by the plasma) system can be constructed. To validate the pollutant removal capabilities of this large-scale system, a feasibility study was performed. Odor removal from air was chosen as the process. Measurements were performed on a (polluted) gas flow of $1,000 \text{ m}^3\cdot\text{h}^{-1}$. The best results show that the (VOC) pollutant concentration decreased by 87% (from $8.987 \text{ mg}\cdot\text{m}^{-3} \rightarrow 1.185 \text{ mg}\cdot\text{m}^{-3}$) and simultaneously the H_2S concentration decreased by 95% (from $15.3 \text{ }\mu\text{g}\cdot\text{m}^{-3} \rightarrow < 0.8 \text{ }\mu\text{g}\cdot\text{m}^{-3}$, energy density

7.2 J·L⁻¹, 250 pps, 8 J·pulse⁻¹). These results indicate that the presented technique is a suitable option for large scale, industrial odor abatement.

In addition to the gathered knowledge concerning the energy conversion efficiency of the streamer plasma system, the experiments also yielded a large amount of valuable data (velocity, diameter, density) concerning streamer development under different pulse conditions and reactor configurations. This data is presented in a systematic manner so it can be of value for future discharge related research.

Contents

Summary	iii
1 Introduction	1
1.1 Objective	1
1.2 Electrical discharges	2
1.2.1 Industrial applications	3
1.3 Pulsed power	5
1.4 Energy transfer efficiency	7
1.5 Aim of the work	8
1.6 Scientific approach	8
1.7 Chapter overview	9
2 From streamer discharge to chemical processing	11
2.1 Streamer mechanism	11
2.2 The local electric field in front of the streamer head	16
2.3 Electron Energy Distribution Function (EEDF)	19
2.4 Radical production	20
2.5 Chemical processing efficiency	21
2.5.1 Discharge phase	21
2.5.2 Reaction phase	24
2.5.2.1 Ozone production	24
2.5.2.2 O* radical production	24
2.5.2.3 O* radical termination	25
2.5.2.4 Ozone destruction	25
2.5.2.5 Production of H _x N _y O _z species	26
2.5.2.6 The kinetic model	26
2.5.3 Mixing phase	27
2.5.4 Determining the O* radical concentration using ozone as monitor	28
2.5.4.1 Effects of streamer volume on the evaluations	29
2.5.4.2 Effect of humidity on the evaluations	31
3 Experimental set-up and procedure	35
3.1 Power modulator	35
3.1.1 Low-voltage part	36
3.1.2 Pulse transformer	36
3.1.3 High-voltage part	38
3.1.4 Spark-gap switch and LCR trigger circuit	39
3.1.5 Transmission line transformer	40
3.1.6 DC bias voltage	42
3.2 Reactor configurations and R _{add}	43
3.3 Pulse parameter variation	45

3.4 Diagnostic tools and experimental procedure	45
3.4.1 Electrical measurements	45
3.4.1.1 Electrical measurements procedure	48
3.4.1.2 Electrical characterization of the experimental set-up	49
3.4.2 Chemical measurements and procedure	55
3.4.2.1 Chemical characterization of the set-up	57
3.4.3 Optical measurements	58
3.4.3.1 Optical measurements procedure	59
3.4.3.2 Optical characterization of the streamers	61
4 Matching a pulsed power modulator and a plasma reactor	67
4.1 Model	67
4.1.1 Load impedance before streamer generation	67
4.1.2 Load impedance during streamer generation	68
4.1.3 Load impedance after streamer generation	68
4.2 Energy transfer efficiency according to the model	69
4.2.1 Situation before streamer generation	69
4.2.2 Situation during streamer generation	72
4.2.3 Combining reactor charging and streamer generation	74
4.3 Energy transfer efficiency in the experimental situation, comparison with model	75
4.3.1 Before streamer generation	75
4.3.2 During streamer generation	77
4.3.2.1 Plasma impedance	77
4.3.2.2 Energy transfer efficiency	83
4.4 Energy transfer efficiency and reactor dimensions	83
4.5 Energy transfer efficiency for negative polarity pulses	87
4.6 Conclusions	87
5 Matching the pulsed power system and the radical production process	89
5.1 Parameters that do not affect the O^* radical yield	89
5.2 Radical yield of cathode directed streamers (CDS)	91
5.2.1 Effect of T_{pulse} on the O^* radical yield	92
5.2.2 Effect of T_{primary} on O^* radical yield	92
5.2.3 Coherent system of parameters that determine the O^* radical yield for CDS	96
5.3 O^* radical yield of anode directed streamers (ADS) and the comparison to the cathode directed streamers (CDS)	100
5.3.1 The effect of T_{pulse} on the O^* radical yield	100
5.3.2 Effect of T_{primary} on the O^* radical yield	101
5.3.3 Coherent system of parameters that determine the O^* radical yield for ADS	104

5.4 O* radical production by secondary streamers	106
5.4.1 Electric field in secondary streamers	106
5.5 O* radical production versus ozone production	108
5.6 Conclusions	108
6 Optimizing the total energy transfer efficiency of the pulsed plasma system	111
6.1 Combining matching results with radical yield	111
6.1.1 Cathode directed streamers	111
6.1.2 Anode directed streamers	115
6.2 Optimizing pulsed power system design: conclusions	116
7 Large scale, energy efficient plasma system	119
7.1 HPPS system	120
7.2 Electrical characterization	121
7.3 Industrial demonstration on odor emission abatement using the HPPS	128
7.3.1 Process layout	128
7.3.2 Gas analysis	129
7.3.3 Results	130
7.4 Conclusions	133
8 Conclusions and recommendations	135
8.1 Ozone production as monitor for O* radical yield	135
8.2 Optimizing the matching between the pulse modulator and the reactor	135
8.3 Increasing the O* radical yield of CDS and ADS	136
8.4 The total system efficiency of pulsed power modulators	138
8.5 Large-scale streamer plasma generation	139
8.6 Macroscopic streamer properties	140
Appendix A.I Ozone	143
Appendix A.II Reactions used in kinetic model	145
Appendix B.I Experimental set-up component values	151
Appendix B.II HPPS component values	152
Appendix C.I Details of the coaxial spark-gap switch	153
Appendix C.II Performance validation	153
Appendix D. Streamer observations and discussion	161
D.1 Side-view photography	161
D.1.1 Effect of pulse repetition rate and of preceding pulses on streamer appearance	161
D.1.2 Effect of DC bias voltage on streamer appearance	162
D.1.3 Streamer velocity	164

D.1.4 Streamer diameter	165
D.1.5 Streamer density	167
D.1.6 Secondary streamer length	169
D.2 Top-view photography	170
D.2.1 Effect of applied voltage, rise time, energy per pulse and pulse width	171
D.2.2 Effect of voltage polarity	171
D.2.3 Effect of reactor configuration	171
D.3 Peculiar observations	174
Bibliography	177
List of Abbreviations	187
Nomenclature	189
Acknowledgement	191
Curriculum Vitae	193

1 Introduction

The focus of this thesis is atmospheric streamer plasmas. A promising application for these non-thermal plasmas can be found in the field of pollution emission control. Although several possibilities exist to generate streamers, here the focus will be on pulsed power induced plasmas. By repetitively applying nanosecond time scale, multi-kilovolt pulses to an electrode configuration, streamers can be produced. In the past it has already been observed that the pollutant removal capability of pulsed streamer plasmas exceeds that of non-pulsed (AC, RF, microwave, etc.) plasmas, hence the interest in pulsed power.

After a description of the objectives, a short introduction regarding electrical discharges and pulsed power technology will be presented. Afterwards, consideration will be given to the specific challenges that still have to be overcome to deepen the understanding of the technique. The specific objective of the work is presented on the basis of these challenges.

1.1 Objective

Streamer plasmas used for the removal of pollutants from gases is a fairly new scientific discipline (first patent filed in 1985 [Miz(1987)]). The history of streamer plasmas induced by short voltage pulses is comparably short, since the required components for reliable pulsed power modulators have only become available in the last decade. The relevant knowledge in the field of “pulsed power induced streamer plasmas for pollutant removal from gases” is still incomplete. An important reason is the complexity of the problem. The factors listed below contribute to the difficulty and complexity of both theoretical and experimental investigation.

Regarding the *pulsed power modulator*:

- Applying fast, short, high-amplitude pulses to a plasma reactor is not simple because the pulse shape is determined by the impedance of the load (i.e. the plasma reactor), a non-constant parameter that cannot easily be controlled. The required technology is not yet available and will have to be developed. Advancement in the development of reliable, durable, low-cost systems requires a thorough understanding of pulsed power technology and of the interaction between the pulse modulator and the load.

Regarding *streamer plasmas*:

- The dynamic range of the relevant time scales is wide. The fastest processes (collisions, photo-ionization, etc.) occur on the picosecond time scale, whereas times for changes in typical macroscopic properties (average temperature, gas composition, etc.) are in the order of seconds. Streamer transit times are tens of nanoseconds and ion travel is measured on a millisecond time scale.

- The dynamic range of the typical length scales differs considerably as well. The reactor configuration can have dimensions in the order of several meters, whereas the characteristic length scale of the streamer-head is only a few micrometers.
- Streamer formation and propagation has a 3D geometry.
- The involved processes/mechanisms are strongly non-linear.
- Typical streamer properties depend on the interaction with the power source and on the reactor configuration.

Regarding the *induced chemistry*:

- Many species are produced in the streamers. The induced chemistry is complex.
- Chemical species are produced intermittently and locally. As a result, mixing of the species with the background gas, both in time and in space, has to be taken into account.
- The range of time scales for the various chemical processes is wide.

To increase the relevant knowledge, it is preferable to include all three subjects in the study, since they are always inter-related. The interactions determine the actual performance of a pulsed streamer plasma system.

In this thesis, the individual subjects and their interactions are studied by looking at the energy transfer. In other words, which parameters and mechanisms determine the amount of energy (taken from the power grid) that is utilized by the plasma for the desired process (pollutant removal). It is recognized that the system's energy transfer efficiency is determined by several distinct processes that all have to be studied systematically (see Section 1.4). Up until now such a systematic study, dealing with the complete chain of processes (from power grid, via pulse modulation and plasma generation, into chemical processing) is not available. By studying the complete chain, many of the topics mentioned above must be dealt with.

Before the aim of the work and the adopted research approach is described in more detail, a short introduction regarding electrical discharges and pulse power generation will be presented.

1.2 Electrical discharges

An electrical discharge can be defined as the passage of electrical current through a medium which normally does not conduct electricity. The charge transport is often accompanied by light emission. Typical examples of electrical discharges are: lightning flashes, St Elmo's fire, coronas, and discharge lamps.

Electrical discharges have been studied extensively since the middle of the 19th century, when vacuum pumps and sources of electricity became available. Substantial scientific progress was made by Townsend [e.g. Tow(1947)] in the early 1900s, when he described the breakdown mechanism. His formulations were based upon the knowledge that electrons have

to be produced in the discharge to create a conducting path. Based upon this knowledge, it was possible to determine the theoretical criterion for the spark breakdown voltage of an insulating gas as a function of the gas pressure multiplied by the electrode separation. The result, the so-called Paschen Law, enabled researchers to predict the occurrence of spark discharges in laboratory conditions.

Although Townsend's theory was useful for understanding spark breakdowns at low voltages and pressures, not all electrical discharge behavior could be explained by adopting this theory. For example, the streamer discharges studied in this thesis transit with a velocity that is too large to be explained by Townsend's breakdown theory. Also, streamer discharges can transit into regions where, according to Townsend, the applied electric field is too low for propagation. To ionize insulating gases a minimum electric field is required. Since electrons have to be created to maintain the conducting path, discharge propagation into low electric fields requires another mechanism, not known at that time.

In the 1940s, the mechanisms of streamer discharges were described by *Loeb(1940a, 1940b)*, *Meek(1940)* and *Raether(1939)*. They correctly pointed out that the differences with the ordinary Townsend breakdown are caused by the effects of the self-induced electric field of the discharges. For the normal Townsend breakdown, the amount of space charge is limited and the resulting self-induced electric field is negligible compared to the applied electric field. If, however, the amount of space charge increases, the induced electric field can become comparable to the external field and, as a consequence, can no longer be disregarded.

Although much has been learned about streamer discharges since the work of Loeb, Meek and Raether, we still do not understand all the mechanisms. An extensive amount of research is being performed (and is required!) to deepen our understanding.

1.2.1 Industrial applications

Besides being interesting phenomena to observe and to study, electrical discharges also contain qualities that make them suitable for various industrial processes. Possible applications seem limitless and can be found everywhere. When talking about plasmas for industrial applications, it is useful to make a distinction as shown in Figure 1.1.

The distinction between *atmospheric* and *low-pressure* can be made when considering the pressure at which the plasma is generated. Although plasmas generated at low pressure exhibit interesting properties, from the perspective of industrial applications working at atmospheric pressure has great advantages, since processing can be continuous and vacuum vessels, pumps, and batch processing are unnecessary. A good overview of the applications for atmospheric pressure plasmas can be found in *Kog(2004)*.

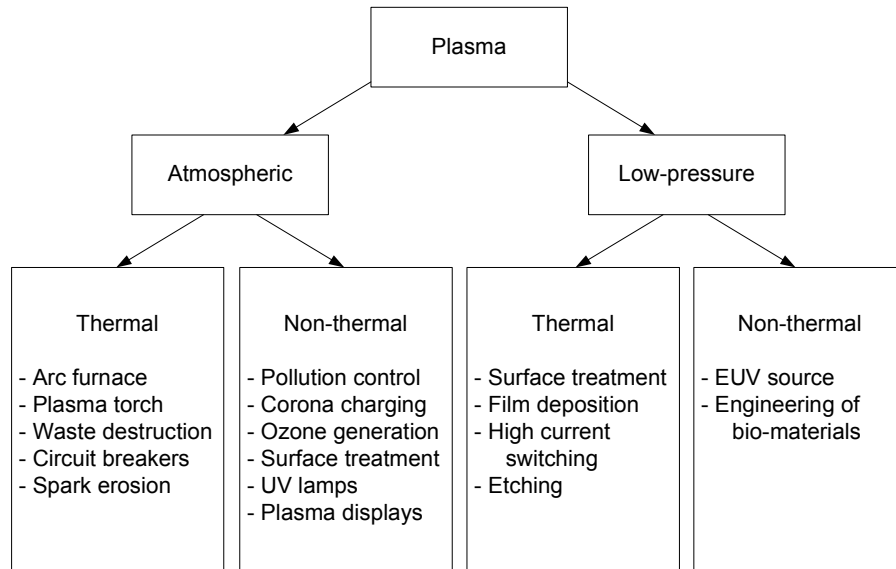


Figure 1.1. Overview of plasma applications. The examples only give an indication of the possibilities.

Both categories can be further divided when the gas temperature is taken into consideration. In a plasma, the electrons obtain high energies. If the electrons and other species (molecules, ions, etc.) obtain a thermal energy distribution at the same high temperature, the plasma is called *thermal*, indicating that the plasma is in thermal equilibrium. If the electrons and the other species are not in thermal equilibrium (i.e. if only the electrons have high energies), the plasma is called *non-thermal*.

The streamer plasma described in this thesis is a non-thermal atmospheric plasma, energized by a high-voltage pulse source. The main advantages, thus, are that the processing can be performed at normal, atmospheric pressure and that no energy is lost as a result of gas heating. The main application of the plasma studied in this thesis is pollution control [Hac(2000), Kim(2004), Miz(1987), Vel(1999), Yan(1998)]. With regard to this field of interest, historically the two most popular techniques are electrostatic precipitation (ESP) of dust (charging of dust particles and subsequent removal by a DC electric field) and ozone production (conversion of O_2 into O_3).

The basic mechanism for pollution control (shown schematically in Figure 1.2) can be described as follows. Voltage (A) is applied to a reactor configuration. Free electrons in the reactor gain energy during their acceleration in this applied electric field (B), creating a plasma (C). If they gain sufficient energy, they can dissociate gas molecules upon collision (D). As a result of these dissociation collisions, radicals are produced that are highly reactive. Radicals are characterized by an unpaired electron in the outer shell. Since they are neutral, their reactivity is different from that of similar ions. In gas mixtures, the radicals readily react with the present species (E). Along these lines pollutants can be converted in easier to handle compounds.

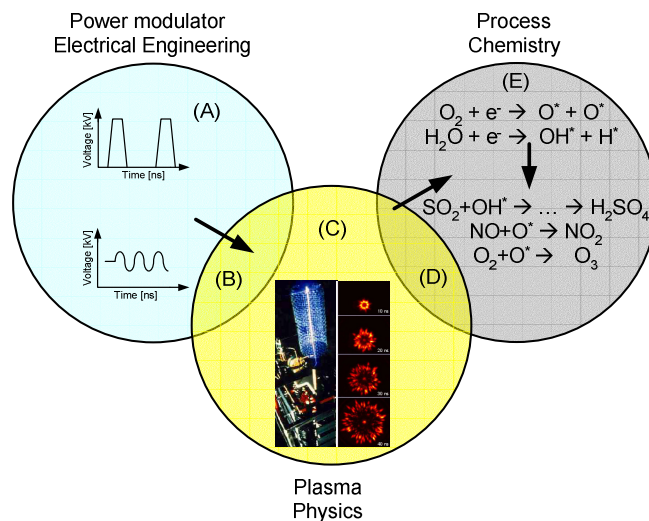


Figure 1.2. Schematic drawing of the field of research. The chemical reactions shown in the circle at the right only serve as an example. The actual kinetics are more complex.

The applicability of this technique has been proven on numerous occasions [Eli(1991), Hac(2000), Kim(2004), and many others]. Pollutants that can be removed include VOCs [Yam(1998)], NO_x [Cle(1989), Din(1990), Hac(2001), Mas(1990), Yan(1999)], odor [Wan(2001), Win(2006d)], and tar [Nai(2004)]. The first large-scale industrial streamer plasma system was reported by ENEL for simultaneous removal of dusts, SO_2 , NO_x , and heavy metals from exhaust gases [Din(1990)]. Unfortunately, the lack of efficient streamer plasma generation and processing techniques discouraged industrial use.

1.3 Pulsed power

Pulsed power is generated by instantaneously delivering the energy stored in an energy storage component, which has been accumulated there gradually, to a load. By releasing the stored energy over a very short time interval, a huge amount of peak power can be delivered.

The first, large-scale research effort related to pulsed power took place during WWII (radar applications). From that time on, there has been an ever increasing interest in this field of research. This is mainly the result of:

- The enormous number of applications:
 - Scientific (e.g. particle accelerators)
 - Medicine (e.g. X-ray equipment)
 - Consumer products (e.g. sterilization of food and drinks)
 - Military (e.g. launching systems, radar)
 - Environment (e.g. waste cleaning, pollution control)
 - Etc.

- Advancement in pulsed power technology: New switching concepts, innovative circuit topologies, developments in the semi-conductor and materials fabrication industry. The major advantages of these developments are the increased reliability and lifetime, and the reduced costs and dimensions of the systems. Also, a larger range and controllability of the power density and less EM interference can now be attained.

Based on the energy storage components used for the pulse modulator, the following four pulse-modulator categories can be distinguished:

- Capacitors (electric-field)
- Inductors (magnetic-field)
- Flywheels (mechanical energy)
- Batteries/explosives (chemical)

The last two options are especially useful for applications that require extremely high pulse energies, but only for a single pulse or very low repetition rates. The first two options are most suitable for repetitive pulsing at repetition rates up to thousands of pulses per second, with a moderate amount of energy per pulse. In this thesis, a capacitor-based pulsed power modulator is used: a capacitor bank is charged to high voltage and subsequently discharged “instantaneously” using a heavy-duty switch. In the past, the switch was usually the critical/weak component of pulsed power modulators. In this thesis, a new, coaxial type spark-gap switch will be described that was specifically designed to overcome the problems commonly associated with pulsed power generation (see Chapter 3 and Appendix C).

The history of plasmas generated by high-voltage pulses goes back to the 1930s, when Siemens filed his patent for “pulsed” ozone generation. In the following years, research continued, but, as stated in Section 1.1, the first patent concerning the use of streamer plasmas (energized by pulses) for pollutant removal from gases was not filed until 1985. From that time on, however, the interest for this particular field of research has grown enormously.

Besides the recent progress in pulsed power modulator design, this interest can be explained by the increased system performance when using pulsed power as opposed to other energizing methods (AC, DC, RF, etc.), especially for large volume gas-cleaning applications. The most important reasons for this enhanced performance are discussed in this thesis. Although pulsed power based streamer plasmas systems are considerably more complex than, for example, DC based systems, the increased overall performance is of great interest from the perspective of industrial applications.

1.4 Energy transfer efficiency

In this thesis, pulsed streamer plasmas are studied from the perspective of energy transfer. For purposes of discussion it is proposed that the energy transfer of the complete system be divided into four steps, as shown in Figure 1.3.

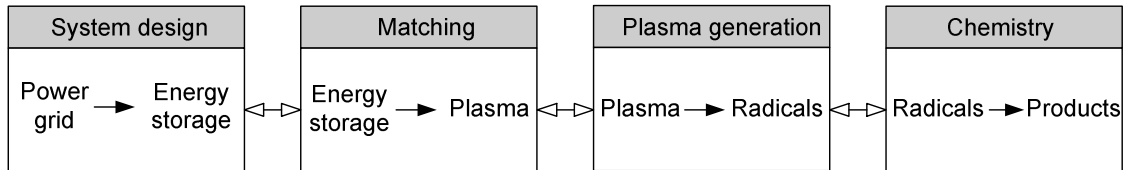


Figure 1.3. Steps in the total energy transfer of the plasma system.

The first step is related to power modulator design. To generate pulses, energy has to be accumulated and stored in the source. A proper source design ensures that most of the energy taken from the power grid goes into the energy storage components.

The second step concerns the matching between the modulator and the reactor. The energy stored in the source has to be inserted into the load, which is the plasma in the reactor. If the output impedance of the source does not equal the load impedance, part of the pulse energy reflects back from the load and is hence lost for plasma generation. The difficulty with matching is the varying impedance of the load before, during and after corona plasma generation. To optimize the matching, the entire energization process should be considered. In this thesis, this step is referred to as “*matching*”.

The third step is related to radical generation. Inserting a considerable amount of energy into the reactor does not necessarily imply a high chemical processing yield of the system. The energy distribution function of the generated plasma determines which processes are dominant in the reactor volume. The energy distribution function has to be matched to the activation energy of the desired reactions. In this thesis, the radical yield (i.e. the amount of plasma energy used for radical production) is referred to as “*chemical efficiency*”.

The fourth step is based on chemistry. By changing process parameters like temperature, flow and humidity, by inserting additives and catalysts, or by applying processing steps in series or in parallel, the required conversion reactions can be enhanced. An excellent example of research related to this step can be found in *Nai(2004)*.

In this thesis, the second and third steps are investigated. Optimization (>95% efficiency) of the first step was already performed in *Yan(2001)*. The modulator used for the experiments is almost identical to the one described in that thesis. The fourth step is not discussed. Understanding the complete chemistry initiated by the discharges is beyond the scope of this thesis.

The energy conversion efficiency of the individual steps is determined by the pulse parameters and the reactor configuration. The actual combination of these parameters determines the properties of the streamers and, consequently, of the initiated chemistry. Some work can be found in the literature that discusses the role of the pulse parameters and reactor configuration on the matching and the chemical processing efficiency.

The effect of pulse parameters on the chemical processing efficiency has been investigated by several researchers [Cre(1994), Fuj(2006), Nam(2000), Rou(1996), Yao(2001)] by studying the effects of varying pulse parameters on pollutant removal (like NO_x or Toluene) from small gas flows. The main observations can be summarized as follows: 1) The chemical processing efficiency increases if the pulse duration is decreased; 2) Increasing the voltage amplitude results in a small reduction of the chemical processing efficiency; and 3) The effect of the voltage rise-time on the processing efficiency is limited. Unfortunately, the studies found in the literature are seldom systematic. Usually, only one or two parameters have been varied and little is reported about the variation of other parameters such as the energy density.

Work regarding the effect of pulse parameters and reactor configuration on the matching (i.e., energy transfer efficiency from energy storage capacitor into the plasma) can also be found in the literature [Mok(1999), Rea(1995), Yan(2001)]. Guidelines are presented that should be followed for system design with high matching. In particular, the work of Yan(2001) must be mentioned as it deals with many aspects of the matching process. Yan's work will be extended and detailed in the present study.

1.5 Aim of the work

Systematic studies, dealing with all the relevant interactions, are presently unavailable. The goal of this thesis is to obtain knowledge required to analyze the complete chain of the process, starting from the power grid and ending with the chemical processing. The performed work can be summarized as follows:

The interactions between the power modulator, the generated streamer plasma and the resulting chemical processes are studied systematically. An analysis of streamer plasma processing is presented, supported by models and measurements from which guidelines are derived that can be used to design large scale, energy efficient, pulsed plasma systems for pollution emission control.

1.6 Scientific approach

The matching and chemical efficiency steps were first studied separately. Afterwards, the obtained knowledge for the different steps was combined to determine the energy transfer efficiency of the complete pulsed streamer plasma system. Based upon this discussion, guidelines for the design of energy efficient systems were derived.

For the matching step, an equivalent circuit was developed that could be used for the analysis. The modulator-source interaction was studied by looking at three different regimes: before, during and after plasma generation. The results of the analysis were verified by means of a set of experiments in which the effects of modulator settings and reactor configuration on the energy transfer efficiency were determined. The results obtained from ICCD pictures were used to explain the characteristic behavior of the plasma as a function of the system parameters.

For the chemical processing step, it was necessary to study a chemical process initiated by the streamer discharges. It was chosen to study ozone production in ambient air. This choice was made because:

- The O^* radical yield can be calculated from the ozone yield, as will be demonstrated in Chapter 2. Ozone production is shown to be a suitable monitor for the O^* radical production efficiency of the plasma.
- When studying the removal mechanisms of various pollutants, it can be observed that most of these are initiated by O^* radicals. It is believed that if O^* radical production can be optimized for a specific process, the same procedure can be used to optimize the chemical efficiency for processes that require O^* radicals as the initiator. Processes that are initiated by other radicals like OH^* [Su(2002)] might require different conditions (pulse parameters, reactor configuration, etc.) for improved efficiency.
- The amount of information available on ozone production is extensive. Most reaction mechanisms and their typical reaction constants are known and can be found in the literature. Even more, ozone production in air is a relatively simple process when compared to other pollutant removal processes (like NO_x or tar removal). As a result, it is possible to obtain a meaningful interpretation of the results of ozone measurements. Also, the obtained results can be used to compare the attained chemical processing efficiency with that of other ozone generators.

A kinetic model was developed that can be used to determine the O^* radical yield using the produced ozone as input parameter. An extensive set of experiments was performed to determine those parameters that affect the radical yield of the system. Parameters (pulse and reactor) were varied systematically over wide ranges. The results from ICCD pictures were used to determine those changes in streamer appearance responsible for the changes in the radical yield. By critically analyzing the obtained data, and by using knowledge obtained from the literature, dominant mechanisms could be identified.

1.7 Chapter overview

A fundamental description of streamer discharges is presented in Chapter 2. Several difficulties encountered when studying streamers are highlighted. A kinetic model is also presented in this chapter that can be used to determine the initial O^* radical production of the discharge using the ozone concentration in the exhaust of the reactor, the streamer volume,

and the relative humidity as input parameters. The correctness of this method is discussed in detail.

In Chapter 3, the experimental set-up and the experimental procedure are presented. The employed diagnostic tools are discussed and the general characteristics of the power modulator, the ozone production, and the streamers are shown.

In Chapter 4 the “*matching*” step is discussed. A model is used to deepen the understanding of the modulator-plasma interaction. The model is validated by means of a series of experiments. Criteria are derived that can be used to optimize the energy transfer efficiency between the modulator and the reactor.

Chapter 5 presents the measurements performed to study the “*chemical efficiency*” step. Based upon the obtained results, criteria are derived for plasmas with optimized chemical process efficiency. Both positive and negative polarity streamers are discussed.

The criteria in Chapters 4 and 5 do not always reinforce each other. Therefore, in Chapter 6, a discussion is presented based upon the combination of all the criteria obtained so far. This chapter provides the knowledge on how to build an energy efficient pulsed streamer plasma processing system.

In Chapter 7 it is shown that, by taking into account the matching criteria, it is not only possible to build efficient systems, but also on a large scale. A demonstration experiment is described that shows that such systems are a suitable option for industrial scale gas cleaning processes.

In Chapter 8 the most important conclusions are summarized and recommendations for future research presented.

This thesis also contains four appendices. In Appendix A, general information regarding ozone (production) is presented, along with the chemical reactions used for the kinetic model. Appendix B lists typical values for the components used in the modulators. In Appendix C, a detailed discussion regarding the high-voltage spark-gap switch is presented. Finally, in Appendix D the ICCD pictures are presented and resulting information is summarized. Information obtained from these pictures, such as the streamer velocity, diameter, and the number of streamers per meter, are presented systematically as a function of pulse-parameters and reactor configuration so it can be used for future discharge related research.

2 From streamer discharge to chemical processing

In this chapter the mechanisms of streamer discharges and the initiation of chemical processes will be described. Physical properties of streamer generation and propagation, and radical production are discussed. The local electric field in front of the streamer head determines the streamer properties and is hence considered a crucial parameter. Determining this local electric field is not straightforward, as will be shown by a literature review. During their acceleration in the electric field, the electrons gain energy that enables them to dissociate gas molecules. As a result of dissociation, radicals are produced that initiate chemical reactions. These chemical reactions are the desired process, as was explained in Chapter 1. Since the number of electrons capable of dissociation depends on the energy they can gain from the field, the chemical processing efficiency of a plasma system is determined by the local electric field. To investigate if, and how, the radical production efficiency of the streamers can be controlled by external means (pulse shape, reactor configuration), the radical production in the streamer head as function of these parameters must be determined. As a chemical monitor, ozone production in ambient air was chosen. A kinetic model will be presented that can be used to calculate the actual oxygen radical concentration, using the measured ozone concentration and relative humidity as input parameters.

2.1 Streamer mechanism

The non-thermal plasma studied is characterized by its channel-like appearance. The channels, usually referred to as streamers, originate near the active electrode and propagate towards the collecting electrode. As was discussed in *Bri(2006)*, *Gax(1999)* and *Ken(1995)*, to understand the streamer structure it is necessary to distinguish different stages of the dynamics: i) the inception and nucleation of the avalanche, ii) the streamer propagation, iii) the late stages of evolution, after the streamers have crossed the gap.

The electron avalanche phase

For a streamer to start, at least one free electron is required. Approximately 10^1 - 10^3 free electrons·cm⁻³ are always present in our environment as a result of cosmic radiation, radioactivity and/or electron liberation from electronegative gasses. In an electric field, a free electron will accelerate, and hence it gains energy. Upon collision with a molecule, it can liberate an electron, provided it has gained sufficient energy during its acceleration. This is referred to as electron impact ionization. As a result of the ionization, two free electrons are now present in the electric field. Both electrons subsequently accelerate in the electric field.

During the transit through the electric field, the electron may undergo multiple ionization collisions. In discharge physics, this is usually quantified using the first Townsend coefficient α . The value for α represents the number of ionization reactions a single electron undergoes upon transiting a centimeter of path in the direction of the field.

As a result of attachment, a portion of the created electrons is lost again. This can be expressed using the attachment coefficient η , which gives the number of attachments per centimeter of path along the electric field. Both α and η depend on the electric field and the gas density. The difference $\alpha - \eta$ is known as the net-ionization coefficient $\underline{\alpha}$. If $\underline{\alpha} > 0$, the number of electrons increases exponentially, resulting in an electron avalanche. If $\underline{\alpha} < 0$, the discharge is quenched, since the number of free electrons decreases. In air at normal temperature and pressure (NTP: 293 K, 1 bar) the electric field has to exceed $30 \text{ kV}\cdot\text{cm}^{-1}$ to obtain $\underline{\alpha} > 0$.

An electron avalanche will develop a self-induced electric field because the electrons and positive ions move in opposite directions (space charge creation). In the past, analytic studies [e.g., Mee(1978), Rae(1964)] have shown, for NTP, that if the number of space charge species is $\sim 10^8$ - 10^9 , the amplitude of the self-induced electric field becomes of the same order of magnitude as the applied electric field E_{applied} . At that moment the avalanche transits into a streamer. More recent studies [Mon(2005), Mon(2006a)] have shown that besides geometrical considerations, diffusion should also be taken into account to determine the condition for the transition into a streamer. Depending on the value of the diffusion constant, the critical number of space charge species can be substantially different from 10^8 - 10^9 .

The streamer phase

The streamer phase is characterized by the large field enhancement in front of its head, which dominates the streamer propagation. The field enhancement is high enough to ensure a positive net ionization coefficient $\underline{\alpha}$. Consequently, many new electrons are created directly in front of the streamer head. The streamer will propagate mainly in the direction of the field enhancement, resulting in the channel-like appearance of the streamer. Numerical simulations [Dha(1987), Ebe(2006), Mon(2006b)] have shown that the streamer head is a thin sheath surrounding the tip of the streamer channel (see Figure 2.1). In this sheath the gradient of the net charge density is large. The local electric field (self-induced electric field plus the applied electric field) can become as high as $250 \text{ kV}\cdot\text{cm}^{-1}$, as will be discussed in Section 2.2.

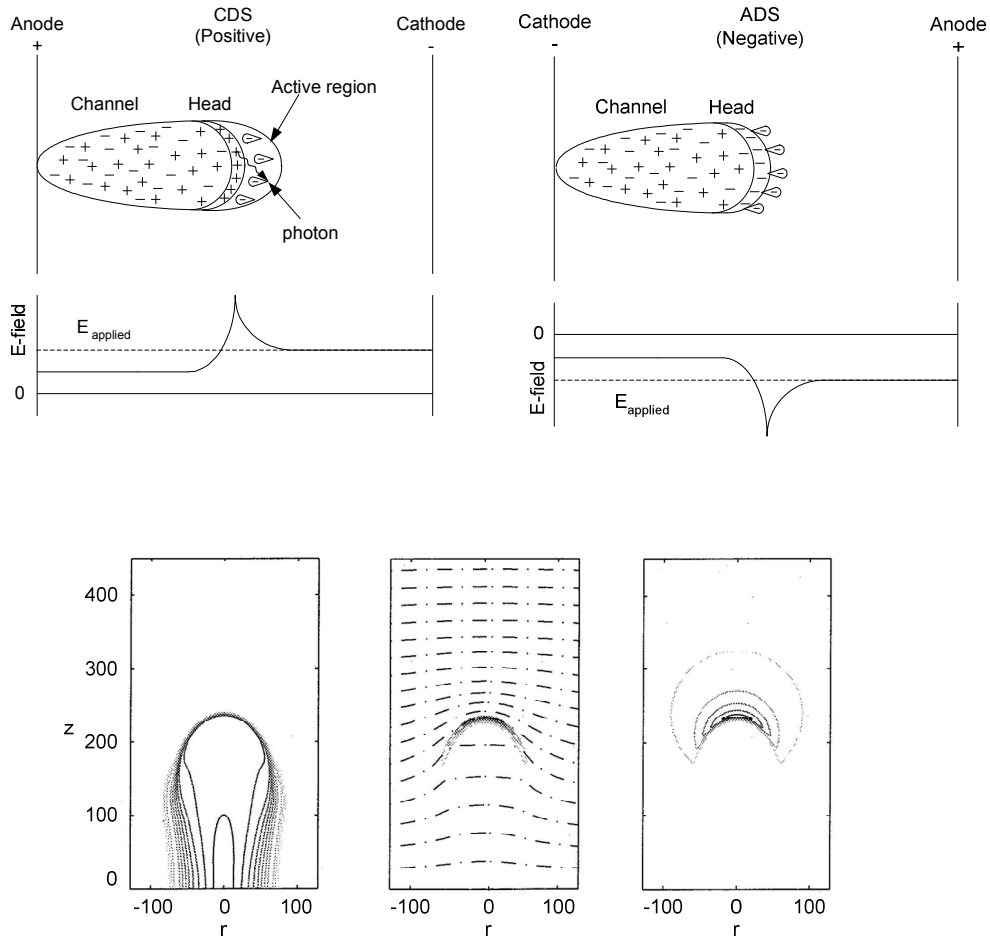


Figure 2.1. Top: Cathode directed streamer (left) and anode directed streamer (right). Below these simplified representations of the streamer the total electric field (schematically, not to scale) is plotted. For simplicity, the applied electric field E_{applied} is constant. In the channel, there is a quasi-neutral plasma, and as a result the electric field is lower than E_{applied} . Directly in front of the streamer head, the field is enhanced due to the space-charge layer. At even larger distances, the field is equal to E_{applied} . For clarity, the sizes of the head and active region have been greatly enhanced relative to the streamer channel. Also, the active region and the streamer head are not clearly separated in space; there is a gradual transition from one region into the other. Bottom: Results of numerical simulations as performed by *Montijn* [Mon(2005)]. The simulations have been performed for negative polarity streamers in pure nitrogen in a uniform (parallel plates) electrode configuration. Dimensionless units have been plotted. Left: the logarithm of the (dimensionless) electron density. Middle: the net charge density. Right: the electric field strength. This figure clearly shows the small scale of the space charge layer, the characteristic shape of this layer and the strong field enhancement near the streamer head.

The minimum electric field strength (inception field) required to create a streamer in air-like mixtures is in the order of 10^2 - 10^3 kV·cm⁻¹. Such high fields can be generated when use is made of strongly non-uniform electrode geometries (like wire-plate, wire-cylinder, point-plate) onto which high voltage is applied. To prevent complete breakdown of the gap, precautions have to be taken, such as the use of short high-voltage pulses. If the electric field in the vicinity of the electrode with the highest curvature is above the inception field strength, streamers are generated. The self-induced electric field of the streamer head allows the streamer to continue propagating, even into regions where the applied electric field is insufficient to ensure a positive net ionization.

For streamers to continue propagating, it is important that new free electrons become available, which can develop into an avalanche. At this point it becomes necessary to distinguish between cathode directed (or positive) streamers CDS and anode directed (or negative) streamers ADS (see Figure 2.1). The difference is the result of the applied voltage polarity on the electrode with the highest curvature (active electrode). There is a major difference between the CDS and ADS when looking at the streamer propagation direction relative to the applied electric field. For the CDS these directions are parallel, for the ADS antiparallel. For the ADS this implies that the electrons travel in the same direction as the streamer. The required secondary electrons are generated in the streamer head and then accelerate in the direction of streamer propagation.

For the CDS the situation is more complicated, because the electrons travel in the direction opposite to the streamer. For CDS to continue propagating, a mechanism is required that generates free electrons in the sheath surrounding the streamer head, which then accelerate towards this head (creating an avalanche). If the electrons are generated too far from the streamer head, the electric field is too low to obtain a positive net ionization coefficient. The region suitable for new avalanche creation is indicated in Figure 2.1 as the “active region”, in accordance with *Bad(1972)* and *Gal(1972)*.

Several possibilities exist for the creation of the free electrons in the active region. For single-shot streamer generation in air-like mixtures, it is generally accepted that photo-ionization is the dominant process (situation can be different if other gasses are used). Photons created in the streamer head can ionize molecules at a small distance. When streamers are generated repetitively, in addition to photo-ionization, it is also possible that background ionization processes (e.g., electron-detachment from electronegative gasses) are responsible for the creation of the secondary electrons. As a result of the plasma residue (ions, meta-stables like the oxygen $a^1\Delta_g$ [Low(1992)] or N₂ vibrational meta-stables [Har(1975)]) from the preceding discharges, new free electrons can be created more easily. Models have shown that both mechanisms can be used to explain streamer propagation [Kul(2000), Pan(2001), Pan(2005)]. For the typical problem conditions used in *Pan(2001)*, when photo-ionization is completely neglected, pre-ionization concentrations in the order of 10^7 cm⁻³ are required to enable streamer propagation. According to *Pan(2001)* such high concentrations can be obtained if the pulse repetition rate is above a few pulses per second.

The streamer will continue propagating in the gap as long as: 1) the local electric field in the streamer head is high enough to ensure a positive net ionization coefficient; 2) the applied voltage is large enough to sustain the quasi-neutral streamer channel left behind by the streamer head. Values for this so-called stability field found in literature are $\sim 5\text{-}8.5\text{ kV}\cdot\text{cm}^{-1}$ for the CDS in air [Ale(1996), All(1991), Gal(1972), Mor(1997), Rai(1991)]. For the ADS, the stability field was estimated to be higher: $\sim 12\text{ kV}\cdot\text{cm}^{-1}$ [Bab(1997)]. In general, to create an ADS, a higher field should be applied to the reactor [Rai(1991)]. However, for high enough applied fields (depending on reactor configuration and gas composition), the differences between ADS and CDS seem to disappear [Bab(1997), Blo(1997)].

The secondary streamer phase

If the streamer reaches the collecting electrode and the applied voltage on the reactor is not removed, current can continue flowing through the streamer channel. According to *Sigmond* [Sig(1984)], at the moment the primary streamers reach the electrode, the electric field is redistributed along the original streamer channel with a velocity in the order of the speed of light. After this field redistribution, as a result of attachment instability, two stable conducting paths will form (in series) in the residue of the primary streamer channel. Near the active electrode a 'high' electric field ($\sim 28\text{ kV}\cdot\text{cm}^{-1}$) region develops, protruding a certain distance (depending on the applied electric field) into the gap. In the remainder of the gap, a 'low' electric field ($\sim 6\text{ kV}\cdot\text{cm}^{-1}$) region is present. In the high electric field region molecules are still excited frequently by electron impact. Light is emitted as a result of radiative quenching, which can be observed visually. In the low electric field region, a negligible amount of light is produced. On photographs, the secondary streamers can thus be seen as a re-illumination of the original primary streamer channel, starting from the active electrode, protruding a certain distance into the gap.

In the secondary streamer, the net ionization coefficient is below zero. As a result, the number of free electrons decreases with time, i.e., the conductivity decreases. However, as the secondary streamer continues to dissipate energy, the channel will heat up. As a result, the total species density in the channel decreases. As was explained by *Sigmond*, this latter effect causes the high electric field region to expand across the electrode gap. Depending on which of these two processes is dominant, the discharge is either quenched or the secondary streamer crosses the electrode gap completely. In the latter case the streamer will transit into a complete breakdown. Besides the fact that these breakdowns can damage the corona plasma system, they are also extremely ineffective from a chemical processing point of view. As mentioned previously, breakdown can be prevented by using short, high-voltage pulses. The difficulty for systems using high-voltage pulses arises from the fact that the streamer-to-breakdown time is short, in the order of a few microseconds. Another possibility is to use a dielectric material on at least one of the electrodes (dielectric barrier discharge reactor, DBD). Charge is accumulated on this dielectric, reducing the electric field strength in the reactor configuration. As a result of this process, the streamer is quenched.

2.2 The local electric field in front of the streamer head

The local electric field E in front of the streamer head is the driving force for streamer propagation. All streamer processes depend on the amplitude and direction of this field. The electrons are accelerated by the field, and the resulting collisions depend on the gained energy. In discharge physics, the reduced electric field E/N is usually used, with N representing the particle density. This parameter is expressed in Td^* , where $1 \text{ Td} = 10^{-17} \text{ V}\cdot\text{cm}^2$. Townsend already found that the electron transport coefficients (ionization, attachment, electron drift, etc.) are solely functions of the reduced field strength, thus independent of the quantities E and N separately. The significance of these so-called *similarity laws* is that experimental findings can be scaled to other dimensions. This is extremely useful, for example, for atmospheric discharge studies, since use of the similarity laws allows the large-scale discharges occurring in the Earth's atmosphere to be compared to the smaller scale discharges studied in laboratories [e.g., Pas(2002)]. Theory [Liu(2006), Luq(2007)] suggests corrections to the scaling-laws for pressures above 80 mbar in order to correct for the non-trivial pressure dependence introduced by the photo-ionization. Some experimental results [Man(2004), Mol(1988)] do indeed show deviations from the similarity law for pressures exceeding 80 mbar. However, those deviations were not observed in Bri(2005a) for pressures up to 1 bar. An explanation for this discrepancy is not available.

Calculation of the local electric field in front of the streamer head is not simple. Either an analytical model must be used, or the problem has to be solved numerically. At this time, the available models can be used to predict streamer properties under the conditions that: 1) only one streamer is generated; 2) the streamer development is symmetric around the axis of propagation. Neither of these conditions are fulfilled for the measurements presented in this thesis. Therefore these models cannot be used to obtain quantitative information regarding the local electric fields in the streamers discussed in this work. Measurements to determine the local electric field are not clear-cut either. A technique like Stark spectroscopy [Jia(2006), Wag(2006)], for example, appears to be a promising candidate. However, for atmospheric discharges, as studied in this thesis, Stark spectroscopy is not readily applicable since, as a result of the present status of this technique, a stable or periodically reproducible plasma generated under low pressure conditions is required to obtain useful data.

The goal of this thesis is not to determine the local electric field quantitatively; however, some knowledge about this field is desired to analyze the radical production efficiency (Sections 2.3 and 2.4). Information available in the literature does not give a consistent picture of the local electric field in the streamer head, although some agreement can be found. Obtained results depend on the employed problem conditions (applied field distribution, electrode distance, applied voltage, gas composition, etc.). The differences in streamer appearance (diameter, velocity, number of branches) have also been observed during experimental studies [e.g., this work, Bri(2006), Win(2006a)].

* In this thesis, all experiments are performed at: 1 bar, 293 K. As a result, N is constant. A reduced electric field of 1 Td therefore corresponds to $\sim 0.25 \text{ kV}\cdot\text{cm}^{-1}$.

Studies [Bab(1997), Kul(1998), Mor(1997), Pan(2001), Pan(2003)] that adopt conditions (see Table 2.1) comparable to those used during the performed experiments show that the typical maximum electric fields in the streamer head are 100-200 $\text{kV}\cdot\text{cm}^{-1}$. These electric fields are well above the critical value for net-ionization ($\sim 30 \text{ kV}\cdot\text{cm}^{-1}$). Although the reported local electric field values differ, the relation between the field and parameters like the applied voltage, streamer diameter, and streamer length, show reasonable agreement (see summary in Table 2.2).

Table 2.1. Summary of the literature review: employed conditions.

Reference	Electrode distance [cm]	Electrode configuration	V_{applied} [kV]	Model	Medium
Bab(1997)	1	Plate-plate	5-35	Numerical	Air
Kul(1998)	1	Point-plate	13	Numerical	Air
Kul(1998)	5	Point-plate	20-40	Analytical	Air
Pan(2001)	1	Point-plate	13	Numerical & Analytical	99% N_2 , 1% O_2
This study	3.7-7.7	Wire-plate	40-90	Experiments	Air

In the streamer models of *Bab(1997)*, *Kul(1998)* and *Pan(2001)*, where average applied fields of $\sim 10\text{-}30 \text{ kV}\cdot\text{cm}^{-1}$ have been used, it was found that the local electric field in the streamer head is constant throughout propagation. Only near the plate electrode is the field enhanced again, due to the proximity effect. It was also observed in these studies that the streamer velocity is constant in the gap, as long as: 1) the applied voltage is constant; 2) the applied average electric field remains below $20 \text{ kV}\cdot\text{cm}^{-1}$. For higher fields, the streamer velocity increases during propagation. In studies like *Mor(1997)*, where average applied electric fields less than $5 \text{ kV}\cdot\text{cm}^{-1}$ have been used, i.e., below the stability field, the findings differ in that the local electric field and the streamer velocity decrease during streamer propagation. The applied field is too low to maintain the streamer channel, and consequently the discharge decays. Clearly, the determined local electric field depends on the problem conditions; however, when comparable conditions are used, similar results are obtained.

The analytical models used in *Kul(1998)* and *Pan(2001)* show that the local electric field decreases as the applied voltage increases. This is a result of the growth of the head diameter for higher voltages. However, in these models, the shape of the space charge region was defined as a uniformly charged sphere. As was mentioned in Section 2.1, this is not an accurate representation of the actual shape. *Babaeva* [Bab(1997)] found the opposite relation, using a numerical model. Here the local electric field and the streamer velocity increase as the applied voltage is increased. The increased velocity as function of the applied voltage has also been observed during the experiments performed for this thesis.

Although some agreement can be found, this literature review demonstrates that the obtained knowledge regarding the electric field strongly depends on the employed problem conditions. Also, besides these differences, all models deal with single streamer propagation only. In other words, the interaction between adjacent streamers is ignored. In *Nai(1996)* it was shown that the inclusion of other streamers in the model has significant effects on the results of the calculations. Local electric fields increased considerably, and the agreement between model and experiment could be improved. As none of the available literature references describe models that have exactly the same problem conditions employed during the present study, the following indirect method is applied to obtain (qualitative) information regarding the electric field in the streamers. In this thesis, based on agreement with the work of *Babaeva*, it is assumed that an increased primary streamer velocity indicates that the local electric field in the streamer head has increased as well. To determine the electric field in the secondary streamers, the *Sigmond* paper is used (see Chapter 5).

Table 2.2. Summary of the literature review. Typical quantitative information is given. E_{local} is the local electric field in the streamer head, V_{applied} is the applied voltage and E_{average} is the average applied electric field.

E_{local} during transit	Velocity during transit	Diameter during transit	E_{local} for increasing V_{applied}	Velocity for increasing V_{applied}	Average diameter for increasing V_{applied}	Reference
[$\text{kV}\cdot\text{cm}^{-1}$]	[$10^6 \text{ m}\cdot\text{s}^{-1}$]	[mm]	[$\text{kV}\cdot\text{cm}^{-1}$]	[$10^6 \text{ m}\cdot\text{s}^{-1}$]	[mm]	
Constant 160	Constant ~ 1.5	Increase $0.3 \rightarrow 1$	$160 \rightarrow 190$ If V_{applied} $15 \rightarrow 35 \text{ kV}$	$0.5 \rightarrow 2.0$ If V_{applied} $5 \rightarrow 15 \text{ kV}$	---	Bab(1997)
Constant 100	Constant 0.4	Constant 2	---	---	---	Kul(1998) Numerical
Decrease $150 \rightarrow 90$	---	Increase $1 \rightarrow 3$	$250 \rightarrow 100$ If V_{applied} $20 \rightarrow 40 \text{ kV}$	---	$0.5 \rightarrow 7.0$ If V_{applied} $20 \rightarrow 40 \text{ kV}$	Kul(1998) Analytical
Constant 150	Constant 0.5	Constant 0.5	$250 \rightarrow 100$ If V_{applied} $10 \rightarrow 50 \text{ kV}$	---	$0.3 \rightarrow 2.5$ If V_{applied} $10 \rightarrow 50 \text{ kV}$	Pan(2001)
---	Constant ~ 1.5	Increase $0.7 \rightarrow 3$	---	$0.5 \rightarrow 2.5$ If V_{applied} $40 \rightarrow 90 \text{ kV}$	$0.9 \rightarrow 2.0$ If V_{applied} $40 \rightarrow 90 \text{ kV}$	This study

The streamer diameter, and its relation to the applied voltage, is also discussed in the literature. According to *Bab(1997)* and *Kul(1998)* the diameter of the streamer increases as function of streamer length. Furthermore, in *Kul(1998)* it was shown that if the applied field is below $10 \text{ kV}\cdot\text{cm}^{-1}$, the increase is linear. For the experiments presented in this thesis it was

found that the diameter increase is always linear, even if the average applied field is as high as $15 \text{ kV}\cdot\text{cm}^{-1}$.

For the employed experimental settings, based upon the (experimental and literature) findings it is assumed that:

- The local electric field is constant during propagation, as is the streamer velocity, in agreement with *Bab(1997)*, *Kul(1998)* and *Pan(2001)*.
- The velocity and the local electric field increase for increasing applied voltages, in agreement with *Bab(1997)*. Based on this, it is assumed that a higher streamer velocity indicates that the local electric field is higher as well.
- The diameter of the streamer increases (linearly) during propagation with a velocity that is a function of the applied voltage, in agreement with *Bab(1997)* and *Kul(1998)*.

2.3 Electron Energy Distribution Function (EEDF)

Because of the acceleration in the electric field, the electrons gain energy, which they subsequently lose due to collisions with gas molecules. Since not all electrons gain the same amount of energy, an electron energy distribution function[†] will be formed. To determine this distribution function, the Boltzmann equation for the electrons has to be solved. This equation is a continuity equation that relates the equilibrium between the energy gains and losses in the electric field. The solution of the Boltzmann equation is the electron distribution function. This function describes the location and velocity of the electrons in time and space. From the velocity distribution, the electron energy distribution function (EEDF) can be calculated.

In the literature, several numerical studies can be found in which the calculations have been performed under ideal plasma conditions (like uniform field distribution, uniform plasma distribution, 2D approximation), i.e., far from streamer conditions. Nevertheless, the results of these studies can be of use as an indication of the conditions in a streamer. The results of these studies can be summarized as: 1) The distribution converges to a stable situation within $\sim 5\text{-}10 \text{ ps}$ [*Bra(1991)*, *Li(2007)*]; 2) As a first order approximation, the shape of the distribution function can be described as a Maxwell-Boltzmann or a Druyvesteyn distribution. The population of the lower energy levels is significantly higher than that of the higher energy levels. Nevertheless, there is a tail of highly energetic electrons. 3) If the electric field is increased, the average electron energy increases as well. In *Bra(1991)* and *Li(2007)* it was shown that the average electron energy increased from $\sim 2 \text{ eV}$ when the electric field is $25 \text{ kV}\cdot\text{cm}^{-1}$ to values above 12 eV if the field is increased above $200 \text{ kV}\cdot\text{cm}^{-1}$.

[†] To be able to use a statistical energy distribution to describe a plasma, it is required that the number of electrons in the Debye sphere is large ($\gg 1$) and that the mean free path length between collisions is short (compared to the macroscopic scale of the plasma). Both these requirements are fulfilled for the discharges described in this thesis.

2.4 Radical production

The energy of the electrons determines which types of collisions with gas molecules occur. All these collisions together determine the plasma properties. A distinction can be made to form the following categories:

1. *Elastic collisions.* These collisions occur most often. However, the energy exchange is small because of the large difference in electron and molecule mass.
2. *Rotational and vibrational excitation.* These processes particularly absorb energies in the order of 1 eV per collision. The absorbed energy is usually transformed into heat and can thus be considered lost for radical production.
3. *Excitation.* The energy absorbed during these processes can be large: 1-10 eV. This energy is not completely lost; it can still contribute to radical production since the energy released during de-excitation can be sufficient to dissociate a molecule.
4. *Dissociation.* Typical energies required are > 5 eV, depending on the gas molecules. As a result of dissociation, radicals are produced.
5. *Ionization.* The processes require energies > 10 eV. Although this energy is lost for radical production, ionization is necessary to create the plasma.

According to the literature survey in Section 2.2, the reduced electric field in the streamer head is in the range $100\text{-}200 \text{ kV}\cdot\text{cm}^{-1}$. This means that a significant portion of the electrons can become sufficiently energetic to dissociate and ionize gas molecules [Kul(1997)]. The streamer head can thus be considered as an effective radical producer. In secondary streamers, the electric field cannot reach high values, as was discussed in Section 2.1. Based upon the large differences in electric field, and consequently in the average electron energy, it appears that radicals will be produced most efficiently in the primary streamer head. However, the amount of radicals produced depends on the product of the probability that an electron will dissociate a molecule and the number of free electrons in the electric field. Consequently, since the high electric field region of the streamer head is small compared to that of a secondary streamer, it is still possible that a large amount of radicals will be produced in the secondary streamers, since more free electrons participate in the collision reactions.

This thesis investigates whether there is a difference between the radical production efficiency of primary and secondary streamers. Also, since the radical production efficiency is determined by the local electric field (via the electron energy), it will be investigated whether this production efficiency can be changed if the field is varied.

2.5 Chemical processing efficiency

Many plasma-driven pollutant removal processes are initiated by plasma-produced O^* radicals. In this thesis the production of O^* radicals by the streamer plasma is studied to analyze the plasma processing efficiency. Ozone[‡] formation by streamer plasmas in air was chosen to monitor the radical production. A kinetic model was applied to link the ozone measurements to the O^* radical production.

Figure 2.2 shows an overview of the different steps in the ozone production process. During the discharge phase, radicals and excited species are produced by the energetic electrons in the discharge. The duration of this phase is determined by the pulse-width, which is in the order of 100 ns. After the streamers have quenched, the reaction phase starts, in which the chemical reactions between radicals and molecules occur. The duration of this phase is in the order of 100 μ s. Strictly speaking, chemical reactions between the various species start at the moment the first radicals are produced. However, due to the large differences in time scale it is acceptable to treat the two phases separately (see also Figure 2.3). Finally, after the reaction phase, the species created in the streamer volume mix with the gas in the reactor. The duration of the mixing phase depends on the characteristic time scales of the processes involved (diffusion, gas-flow rate, air-flow pattern, electric wind, etc.). The required time for complete mixing of the gas can exceed the inter-pulse duration.

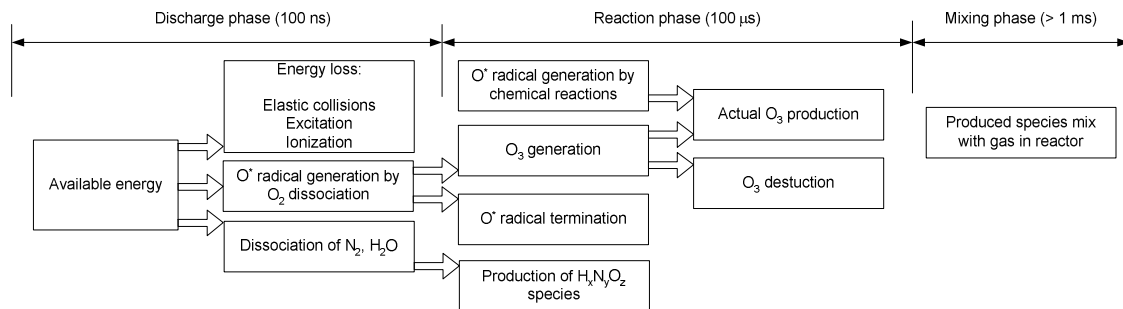


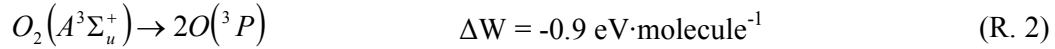
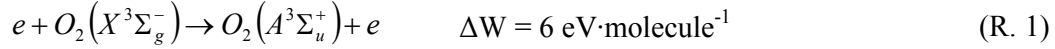
Figure 2.2. Overview of the ozone production mechanism.

2.5.1 Discharge phase

During the discharge phase, energetic electrons collide with the gas molecules. The available energy is partly used for O^* radical production. The remainder of the energy is converted as a result of elastic collisions, excitation, ionization and dissociation of N_2 and H_2O molecules. For an efficient plasma, the fraction of energy used for O^* radical production should be maximized. The O^* radicals can be produced according to the following mechanisms [Bra(1991)]:

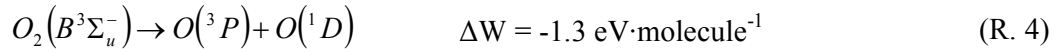
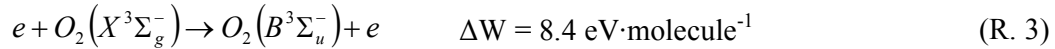
[‡] General information about ozone (generation) can be found in Appendix A.I.

- *Electron impact dissociation:* Free electrons with sufficient kinetic energy can dissociate O_2 atoms upon collision:

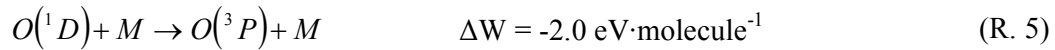


The first reaction excites a ground-state oxygen molecule into the Herzberg band. The term ΔW is the energy required for the reaction to take place. The energy released during R. 2 is insufficient for dissociation and can thus be considered as a loss. Since the reactions R. 1 and R. 2 produce two O^* radicals, the energy cost to produce a single O^* radical is 3 eV.

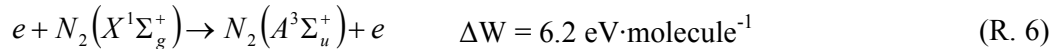
Free electrons can also excite a ground state O_2 into the Schumann-Runge band:



The energy released during R. 4 is lost for radical production. Via this mechanism, the energy cost to produce an O^* radical is 4.2 eV. Basically there is no difference in oxygen states $O(^1D)$ and $O(^3P)$ when considering ozone production. The excited $O(^1D)$ state rapidly loses its excessive energy due to relaxation collisions with gas molecules:



- *Dissociation by excited N_2 molecules:* In an air-like mixture, free electrons not only dissociate O_2 molecules, but also excite N_2 molecules (among others):

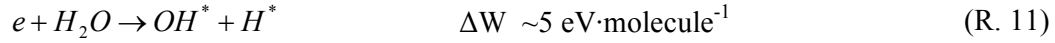
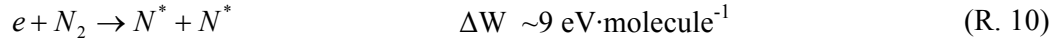


Upon collision with an O_2 molecule, several reactions can occur:



The exact probability distribution of these three reactions is not known. Several values can be found in the literature. The probability ratio 3:17:80 was used in *Bra(1991)*. Consequently, it can be seen that a considerable amount of O^* radicals is produced as a result of reactions with excited nitrogen molecules.

N^* , OH^* and H^* radicals are produced according to the following collisional reactions:



Possibly, besides dissociation by direct electron impact, other pathways for N^* , OH^* and H^* radical creation contribute to the production of these species as well (e.g., dissociation by collision with an excited nitrogen molecule). These reactions, and the reaction cross-sections, are unknown however.

The produced N^* , OH^* and H^* radicals participate in the reaction kinetics. For the kinetic model, the amount of all radicals produced by the discharge must be known. The exact ratio of $O^* : N^* : OH^* : H^*$ is determined by the gas composition and the EEDF. Since the EEDF was not determined during this study, an assumption for the ratio must be made. For the kinetic model, the same ratio as used by *Peyrous* [Pey(1990)] is adopted:

$$O^* : N^* : OH^* : H^* = 1 : 0.06 : 0.6 \cdot 10^{-3} RH : 0.6 \cdot 10^{-3} RH \quad (\text{eq. 2.1})$$

RH represents the relative humidity in percent. This ratio was derived by *Peyrou* under the assumption that radicals are only produced by direct electron impact dissociation, i.e., R. 1 - 4, for O^* radical production, R. 10 for N^* production and R. 11 for OH^* and H^* production. O^* radical production by excited N_2 species has been ignored.

Calculations using the kinetic model described in Section 2.5.2 have been used to determine the effect of the assumed ratio on the ozone production evaluation. It was found that the sensitivity is limited: the amounts of N^* , OH^* and H^* radicals must be increased by an order of magnitude (relative to the amount of O^* radicals) to change the ozone production by 10%. This result also indicates that adopting a fixed ratio between the amounts of radicals produced by the discharge is allowed. Basically, if the EEDF is changed, so will the ratio between the produced radicals. The calculations indicated, however, that the evaluation of the ozone production is not very sensitive with respect to the ratio.

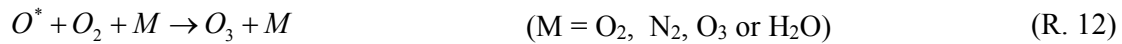
A conclusion that can be drawn from Equation 2.1 is that the amount of energy lost for O^* radical production depends on the relative humidity of the gas. Since the measurements have been performed under slightly varying humidity (13-18%), it appears that the results cannot be compared directly. However, the variation in humidity is limited and the energy loss as a result of H_2O dissociation is small since the amount of H_2O molecules present in the gas is small compared to the amount of O_2 . As a result, the effect of humidity on the O^* radical production during the discharge phase ($t < 100 \text{ ns}$) can be ignored.

2.5.2 Reaction phase

During the reaction phase, the created species will react with the gas molecules that are present and each other. The chemistry is complex, as various species participate and the number of possible reactions is large. In this thesis, a total of 65 different chemical reactions, involving 17 different species have been used to describe the gas phase chemistry. The reactions and their rate constants can be found in Appendix A.II[§]. From the perspective of ozone production, the chemistry can be divided into different regimes, as was previously indicated in Figure 2.2: ozone production, O* radical production, O* radical termination, and ozone destruction. Besides ozone, other species are produced as well as a result of the N*, OH* and H* that are present.

2.5.2.1 Ozone production

A portion of the O* radicals will react with O₂ molecules to form ozone:

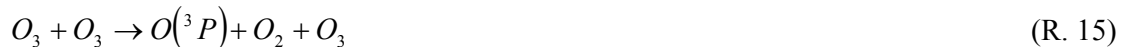


This reaction gives the main contribution to ozone production. However, another reaction (R. 13) has also been used in the model. The contribution to ozone production as a result of this reaction is small: < 1%.



2.5.2.2 O* radical production

Ozone and nitric oxides produced during the electrical discharge can be destroyed again upon collision with third-body particles or due to thermal decomposition. Several of these destruction reactions result in the production of an O* radical. Eleven reactions that produce an O* radical are included in the kinetic model, e.g.:



[§] The kinetic scheme used is identical to the one presented in *Pey(1990)*.

Under normal circumstances**, the contribution to O^* radical production by means of chemical reactions is small (~1%) compared to production during the discharge phase.

2.5.2.3 O^* radical termination

Not all O^* radicals will react with oxygen into ozone. A part will be lost due to reactions with other species/molecules. The majority of the O^* radical termination can be contributed to the reaction with water vapor [Ono(2003a)]:



For humid air, up to 90% of the available O^* radicals can be lost for ozone production as a result of R. 18 (see also Figure 2.5). Other O^* radical termination reactions such as R. 19 and R. 20 also result in decreased (~1%) ozone production. However, compared to the loss as a result of R. 18, this contribution is small.



A total of seventeen O^* radical termination reactions has been taken into account, among which R. 18-R 20 have the largest contribution.

2.5.2.4 Ozone destruction

Ozone destruction can be contributed to one of the following mechanisms:

- *Ozone destruction by chemical reactions*: Produced ozone reacts readily with almost all species present in the reactor, e.g.:



Nine O_3 “chemical” destruction reactions have been used in the kinetic model.

- *Thermal decomposition*
The thermal ozone destruction process:



** Under normal circumstances the concentration of species created by the discharge is much smaller than the concentration of N_2 and O_2 molecules. For the measurements described in this thesis, this is always the case.

is greatly enhanced for increasing temperatures. To determine the maximum increase in gas temperature in a streamer channel as a result of the dissipated energy, some of the results presented later in this thesis have to be used. The maximum energy per streamer obtained was ~ 3 mJ. The streamer volume can be calculated by using its length of 57 mm and average diameter of 2 mm. This results in an energy dissipation of ~ 17 kJ·m⁻³. The maximum temperature increase in the streamer channel can then be calculated to be 13 K. Assuming the gas is well mixed in between the pulses, and taking into account the large difference in streamer volume relative to the total gas volume ($\sim 1:300$), it can be determined that the increase in average gas temperature caused by a single pulse is limited. During the residence in the reactor, the gas is energized multiple times (N_{pulses}). As long as N_{pulses} remains below a few hundred, the increase in average gas temperature as a result of repetitive pulsing can be ignored.

- *Destruction by electron impact*

Ozone molecules can be destroyed by direct electron impact, when the electron has an energy of 1.084 eV.



Because this energy is so low, most of the electrons created during the discharge are capable of destroying an ozone molecule. However, ozone is mainly formed during the reaction phase, whereas energetic electrons are only present during the discharge phase. Due to the differences in time scale, ozone destruction as a result of electron impact is negligible.

2.5.2.5 Production of $H_xN_yO_z$ species

The presence of N^* , OH^* and H^* radicals induces complex chemical kinetics that result in the production of species other than ozone. The production of 9 different species (H_2O_2 , NO , NO_2 , NO_3 , N_2O , N_2O_5 , HO_2 , HNO_2 , HNO_3) has been taken into account, using a total of 50 chemical reactions.

2.5.2.6 The kinetic model

The kinetic model is based on the chemical reactions mentioned in Appendix C.II. To perform the calculations, the species concentrations are required. These concentrations can be determined by dividing the number of particles N_X per species X by the total streamer volume V_{streamer} . Equation 2.2 is used to obtain an estimate of V_{streamer} . In this equation: d_{reactor} [cm] is the wire-plate distance, r_{begin} [cm] is the streamer radius at the wire, r_{end} is the streamer radius near the plate, S_{leaving} is the number of streamers leaving the corona wire, and S_{arriving} is the number of streamers arriving at the plate electrode. These values are obtained from the ICCD pictures.

$$V_{streamer} = \left(\frac{S_{leaving} + S_{arriving}}{2} \right) \cdot \pi \cdot \left(\frac{r_{begin} + r_{end}}{2} \right)^2 \cdot d_{reactor} \quad (\text{eq. 2.2})$$

This equation gives an estimate of the actual volume. The error introduced as a result of the proposed relation is discussed in Section 2.5.4.

Based on the chemical reactions, differential equations can be constructed that describe the various species concentrations as function of time. The corresponding reaction rates often depend on the local temperature. For the calculations, a temperature of 300 K has been assumed. This temperature is slightly above the ambient temperature, as a result of the dissipated energy. Typically, the increase in gas temperature in the streamer channel is less than 13 K.

The set of differential equations (17, one for each species) can be solved analytically. The procedure is cumbersome, however. Instead, it was chosen to solve the equations numerically, using the *PolyMath* [Pol 5.1] software package. The differential equations are solved using a stiff equation solving scheme. The model only describes the reaction phase. The radical production, according to the ratio shown in Equation 2.1, is assumed to be infinitely fast at $t = 0$.

Figure 2.3 shows a typical example of the species concentrations as function of time. For clarity, only those species with a significant concentration have been shown. The figure shows that during the discharge phase, only a small portion of ozone is produced. The majority of the reactions take place during the reaction phase. The assumption that both phases can be treated independently is therefore justified.

Besides ozone, a significant amount of H_2O_2 and HNO_2 is also produced. These species are produced due to the presence of water vapor. In dry air, besides ozone, mostly NO_x is created. However, the concentration of NO_x is typically two orders of magnitude smaller than that of ozone. In Figure 2.3, it can be seen that only a portion of the O^* radicals is used to produce ozone. The radical loss is mainly due to the presence of H_2O .

2.5.3 Mixing phase

After the reaction phase, the species produced in the streamer volume mix with the gas in the reactor. The mixing is a result of the gas flow, diffusion and plasma-induced flow [Fra(2000)]. It is assumed that in between two pulses, the gas is well mixed. Although the species concentration in the streamer channels can become high as a result of mixing and the large difference in streamer volume relative to the total gas volume ($\sim 1:300$), the concentration of the species in the total gas volume is relatively low. Consequently, when the next discharge phase occurs, the gas composition is almost completely restored to neutral conditions. Only for high pulse repetition rates is this assumption not true. In Chapter 3 it

will be demonstrated that for the experimental conditions, the pulse repetition rate (prf) does not affect the O_3 production, i.e., the relation between the pulse repetition rate and the O_3 production is linear. This implies that the gas is well mixed in between the pulses and, as a result, the background species concentrations from previous pulses at the beginning of the new pulse are too low to significantly affect the chemical kinetics.

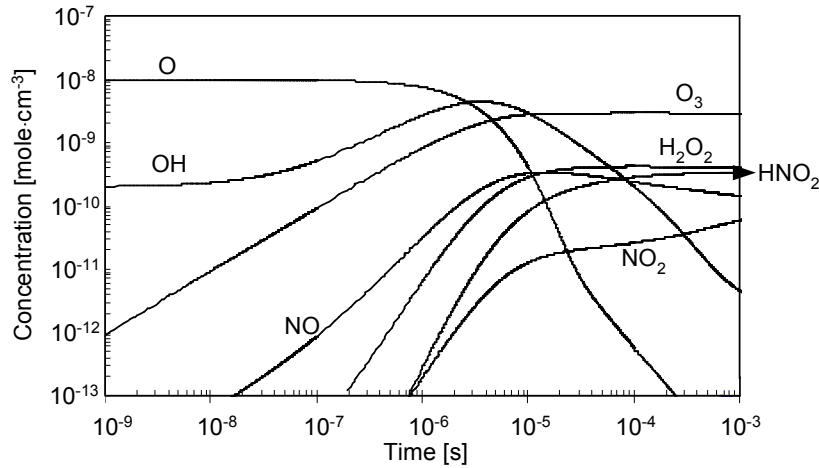


Figure 2.3. Concentration of various species as function of time. For this example, the relative humidity was 15%. The initial O^* radical concentration was set at 10^{-8} mole·cm $^{-3}$. The initial concentrations of the other radicals were determined using Equation 2.1.

The ozone concentration in the exhaust channel of the reactor $[O_{3, \text{exhaust}}]$ in [mole·cm $^{-3}$] is related to the ozone concentration produced per pulse in the streamer volume $[O_{3, \text{streamer}}]$ in [mole·cm $^{-3}$] accordance with the following relation:

$$[O_{3, \text{exhaust}}] = \frac{[O_{3, \text{streamer}}] \cdot V_{\text{streamer}} \cdot f}{F} \quad (\text{eq. 2.3})$$

where f in pps, V_{streamer} in m 3 and F in m 3 ·s $^{-1}$ are the pulse repetition rate, the total plasma volume and the gas flow rate respectively. The use of this equation is only allowed if the gas is well mixed in between the pulses and the ozone concentration is a linear function of the pulse repetition rate.

2.5.4 Determining the O^* radical concentration using ozone as monitor

From the foregoing sections it can be concluded that the amount of ozone produced, and the related production costs, can be calculated when the species (radicals, H_2O) concentrations at the end of the discharge phase, the gas temperature, and the energy input are known. Figure 2.4a shows an overview of this procedure. In this thesis, the procedure is used in reverse order, as shown in Figure 2.4b. Since the humidity, temperature, ozone

concentration in the exhaust of the reactor and the streamer volume are known from measurements, the initial O^* radical concentrations can be determined. Using the streamer volume, the actual amount of O^* radicals can be calculated. If this amount is divided by the pulse energy, the O^* radical production costs can be determined. For ozone generation to be a suitable monitor for O^* radical production, it is important to assess the accuracy with which the calculations can be performed. Two parameters have a significant effect on the evaluations: the streamer volume and relative humidity.

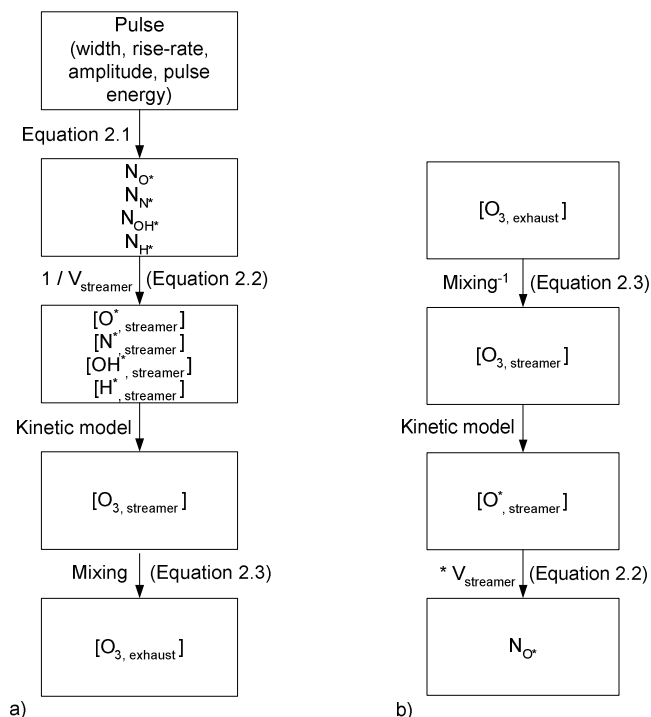


Figure 2.4. The brackets denote the species concentration; N_X is the amount of species X. a) Procedure to determine the O_3 concentration in the exhaust of the reactor starting from the radical production during the discharge phase. b) Procedure to determine the O^* radical production using the measured O_3 concentration in the exhaust of the reactor.

2.5.4.1 Effects of streamer volume on the evaluations

Equation 2.2 is used to determine the streamer volume $V_{streamer}$. This equation only gives an estimate of the actual streamer volume, since obtaining the required input parameters is not straightforward. As can be concluded from Figure 3.16, 3.17 and 3.19, determining the streamer radius and the number of streamers accurately is difficult. Also, the length of the streamers is not constant, as not every streamer follows the shortest path from wire to plate electrode (see Figure 3.20). Based on the accuracy of the parameters in the formula, it is estimated that the maximum uncertainty in $V_{streamer}$ is a factor four, i.e., the actual streamer volume can be twice as high or twice as low as the calculated $V_{streamer}$.

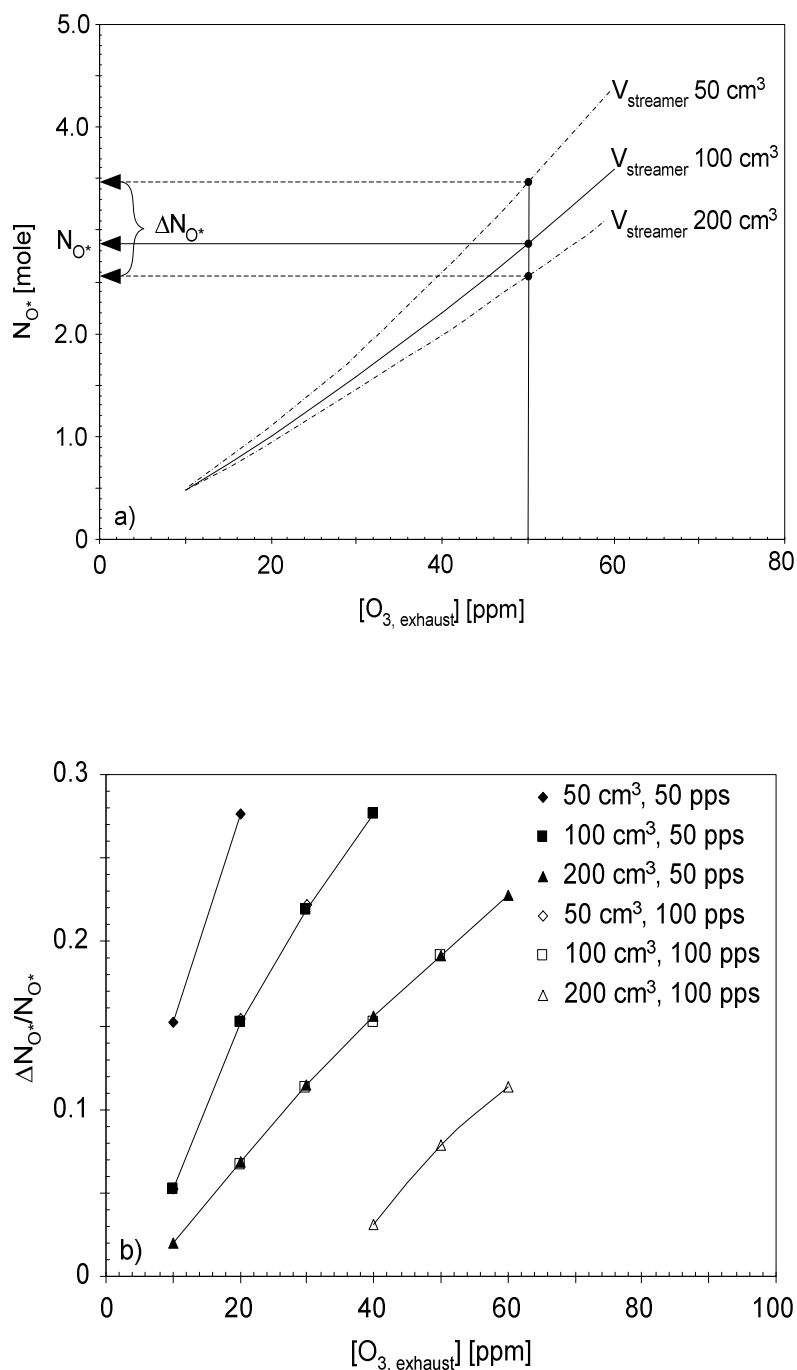


Figure 2.5. a) Moles of O^* radicals produced by the discharge as function of the ozone concentration in the reactor exhaust. For the calculations, a pulse repetition rate of 50 pps and a humidity of 15% were used. b) Error in N_{O^*} , as caused by the inaccuracy in $V_{streamer}$, as function of the ozone concentration in the reactor exhaust. The pulse repetition rate and $V_{streamer}$ are as indicated in the legend. The humidity was 15%.

The streamer volume has a significant effect on the chemical kinetics, as the chemistry is determined by the species concentrations (N_x divided by V_{streamer}). The relation between species concentration and ozone production is non-linear. As a result of the uncertainty in determining V_{streamer} , an error is introduced in the calculated amount of O^* radicals produced by the discharge. This is demonstrated in Figure 2.5a, where the calculated amount of O^* radicals (N_{O^*}) is plotted as function of the ozone concentration in the reactor exhaust. For the calculations, it was assumed that the pulse repetition rate was 50 pps and the relative humidity 15%. The calculations have been performed using $V_{\text{streamer}} = 100 \text{ cm}^3$ (solid line). If in reality the streamer volume is twice as high, or twice as low, different results are obtained, as indicated by the dotted lines. Using the data presented in Figure 2.5a, it is possible to determine the error in N_{O^*} ($\Delta N_{O^*}/N_{O^*}$) as function of the measured ozone concentration in the reactor exhaust, the humidity and the pulse repetition rate. For different V_{streamer} , pulse repetition rate and humidity, plots similar to the one shown can be created. The error in N_{O^*} for different combinations of these parameters can then be determined. The results of these calculations are shown in Figure 2.5b. All experiments have been performed in the range ($[O_3, \text{exhaust}]$: 10-65 ppm, V_{streamer} : 50-200 cm^3 , prr: 50-100 pps) as indicated in this figure. It can be concluded that the error in N_{O^*} varies from $\pm 1\%$ - $\pm 14\%$. This error is small, even though the assumed variation in V_{streamer} is considerable.

2.5.4.2 Effect of humidity on the evaluations

Comparable to the situation for the streamer volume, the error in the humidity determination also has an effect on the accuracy with which N_{O^*} is determined. As humidity increases, the amount of ozone produced decreases, as shown in Figure 2.6. The initial O^* radical concentration was $10^{-8} \text{ mole}\cdot\text{cm}^{-3}$, a typical value obtained during the measurements.

The decreased ozone production for increased humidity is caused by the increased O^* radical termination as a result of R. 18. Especially for low humidity, the decrease $\Delta O_3/O_3$ with increasing humidity is large. This observation is also reported in the literature [Che(2005), Ono(2003b), Pey(1989)]. For RH above 30-40%, the relative decrease in ozone production becomes smaller, as was also observed in experimental studies such as *Pey(1982)* and *Vin(1992)*.

Under the experimental conditions, the RH (in the reactor) varied in the range of 13-18%. The accuracy with which the humidity is determined is $\pm 1\%$ (in RH). If the actual humidity is 1% higher than the humidity used for the calculations, more O^* radicals are required to obtain the same ozone production, i.e., the calculated N_{O^*} is underestimated. Moreover, when N_{O^*} has to be increased, more O^* radical termination reactions occur. Consequently, the value of N_{O^*} must be increased even further to obtain the measured ozone concentration in the reactor exhaust. Obviously, if the actual humidity is 1% lower than the measured humidity, the opposite is true.

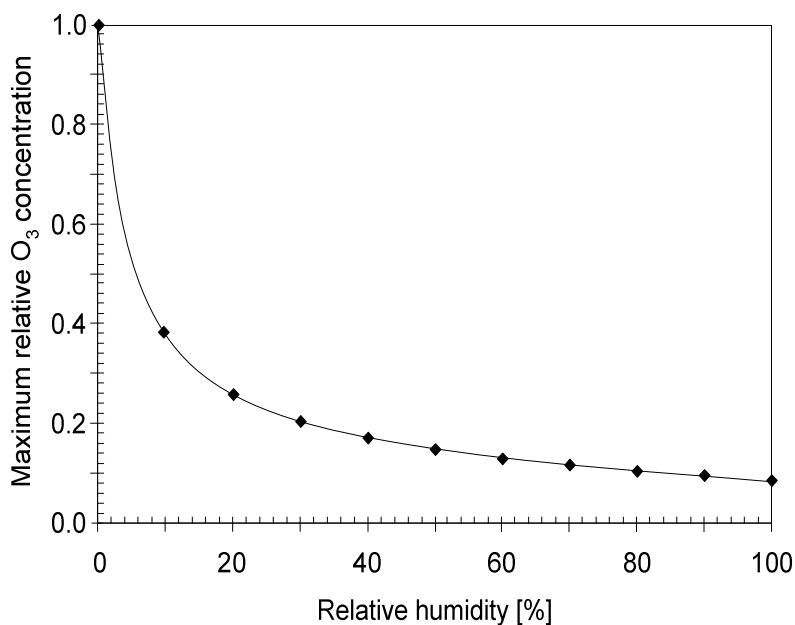


Figure 2.6. Relative ozone concentration as function of the relative humidity. The initial O^* radical concentration was 10^{-8} mole \cdot cm $^{-3}$. For the example presented, a relative O^* concentration of 1 is equal to $9.8 \cdot 10^{-9}$ mole \cdot cm $^{-3}$. It can be seen that if the RH is zero, almost all O^* radicals react (with O_2) into O_3 .

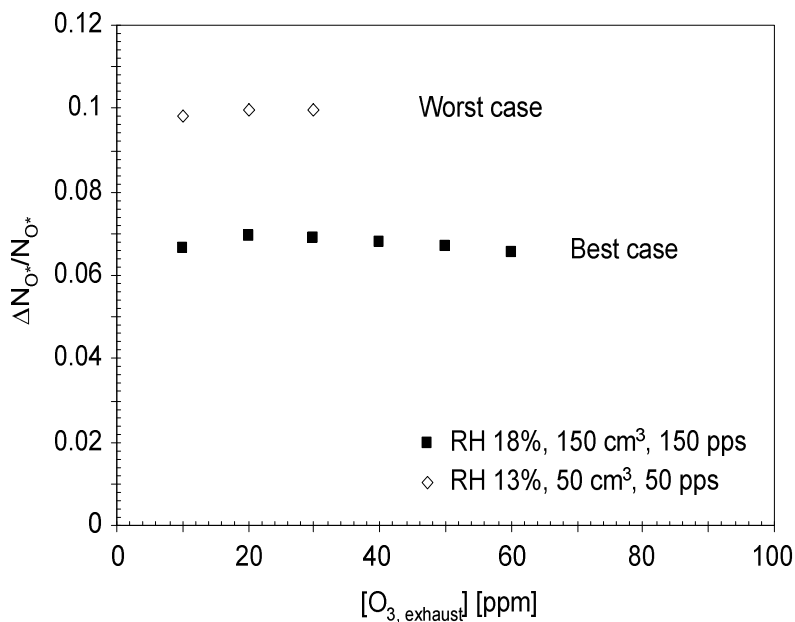


Figure 2.7. Error in N_{O^*} , as caused by the inaccuracy in the RH, as function of the ozone concentration in the reactor exhaust. The pulse repetition rate and V_{streamer} are as shown in the legend. It can be seen that the error only depends on RH, not on the initial O^* radical concentration.

The error in N_{O^*} as a result of inaccurate measurement of the relative humidity can be determined in a similar fashion as discussed in Section 2.5.4.1. The results are summarized in Figure 2.7. This figure shows the worst case (low RH, low V_{streamer} , low prr) and the best case (high RH, high V_{streamer} , high prr). It can be seen that the error in N_{O^*} caused by the inaccuracy in the RH varies from $\pm 3.5\%$ - $\pm 5\%$.

Combined with the error as a result of the uncertainty in V_{streamer} , it can be concluded that the error in the determined N_{O^*} as a result of the evaluations varies from $\pm 5\%$ - $\pm 20\%$. The actual value depends on $[O_{3, \text{exhaust}}]$, the relative humidity, the pulse repetition rate and the streamer volume.

3 Experimental set-up and procedure*

This chapter describes the experimental set-up, the diagnostic tools and the experimental procedure. A schematic overview of the set-up is shown in Figure 3.1. A pulsed power modulator is used to energize a wire-plate reactor. Voltage and current waveforms are monitored using differentiating-integrating sensors. Streamer generation is studied using an intensified charge coupled device camera (ICCD). O^ radical production efficiency of the plasma is determined by measuring the ozone production using the UV absorption technique. A key feature of the power modulator is the ability to vary pulse parameters (Section 3.3). The pulsed power modulator and the reactor configuration are discussed in Sections 3.1 and 3.2. The different diagnostic tools and the experimental procedure are discussed in Section 3.4.*

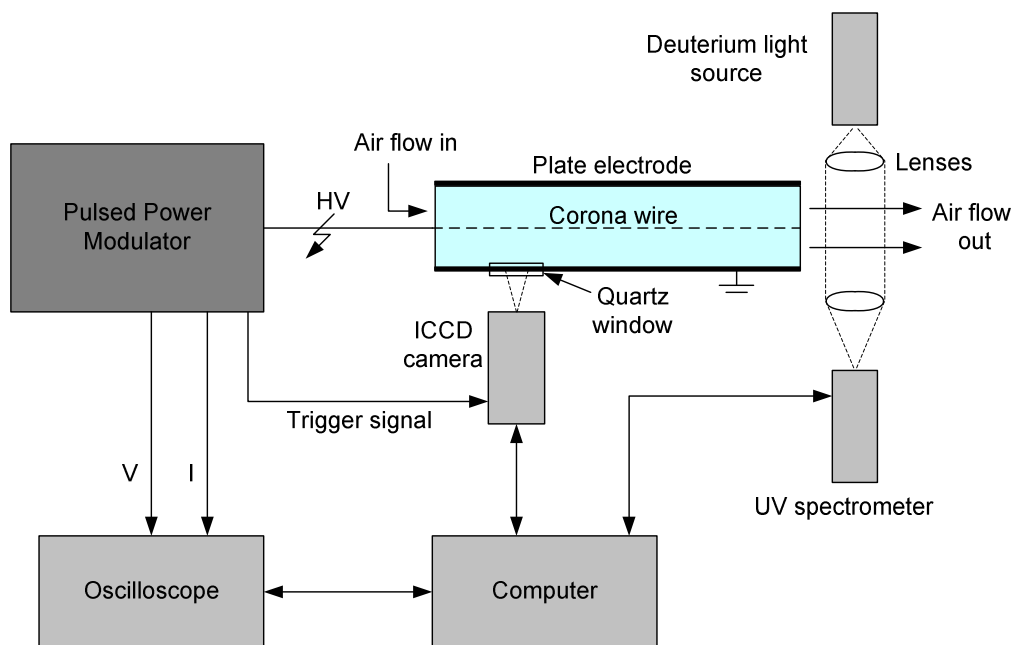


Figure 3.1. Schematic overview of the experimental set-up.

3.1 Power modulator

To generate nanosecond pulses, various circuit topologies can be adopted. A main distinction can be made when considering the energy storage mechanism used in the intermediate stages of the power modulator: inductive or capacitive. The main problem

* Parts of this chapter have already been published in *Win(2004a)* and *Win(2005a, b, c, d)*.

encountered in inductive energy storage-based systems is the opening switch [Pok(2002)]. These switches are not readily available and are difficult to develop. A promising technique is the use of fast-recovery diodes [Gre(2000), Pem(2003)] that have the ability to go from a conductive to a blocking state in a (fraction of a) nanosecond. A capacitive energy storage source requires a heavy-duty closing switch. Construction of such a switch is also not straightforward. Section 3.1.4 describes the design of the durable spark gap switch used for this study.

A circuit diagram of the power modulator is presented in Figure 3.2 [Win(2004a, Win(2005a), Yan(2004)]. Typical component values can be found in Appendix B.I. The modulator is similar to the one described in Yan(2001), however, several modifications have been introduced to enable pulse-parameter variation (Section 3.3). The principle of the circuit is to charge a pulse forming line (PFL) to high-voltage (V_{sg}) and subsequently to discharge it into the reactor. The pulses can be superimposed on a DC voltage (Section 3.1.6).

3.1.1 Low-voltage part

All components on the left side of the pulse transformer form the low-voltage part of the system. Basically, the low voltage part is a resonant charging unit for the high-voltage part. The PFL (with capacitance C_h) is resonantly charged by consecutive switching of the thyristors Th_1 and Th_2 . Th_3 is switched after the PFL is discharged, to remove possible negative charge on C_L . In Yan(2001) it was shown that this results in stable pulse-to-pulse energy transfer from the low-voltage to the high-voltage part. For optimal energy transfer between the low-voltage and high-voltage parts, the following relation should be obeyed: $C_L = n^2 \cdot C_h$, where n is the winding ratio of the pulse transformer. The RC snubbers and the suppressor S are added for correct operation and protection of the thyristors. Output characteristics of the low-voltage part (maximum values): voltage, current, pulse energy, and pulse repetition rate: 1kV, 1kA, 10 J and 1000 pps (pulses per second) respectively.

3.1.2 Pulse transformer

The output of the low-voltage part is fed into the primary of the step-up pulse-transformer. A 1:60 pulse transformer was developed for the experiment. The core, shown in Figure 3.3a, was constructed by gluing I-core Ferroxcubes (3C94, $\mu_r \sim 2300$, $B_{sat} = 340-430$ mT) together. The glued interfaces introduce an air gap in the core. As a result of this gap, core-saturation was prevented. The disadvantage of the air gap is that the effective permeability μ_r^* decreases. By using the measured inductance and the dimensions of the secondary windings, the value for μ_r^* was determined to be ~ 1200 . Using this result, the total air gap in the core can be determined to be 0.4 mm.

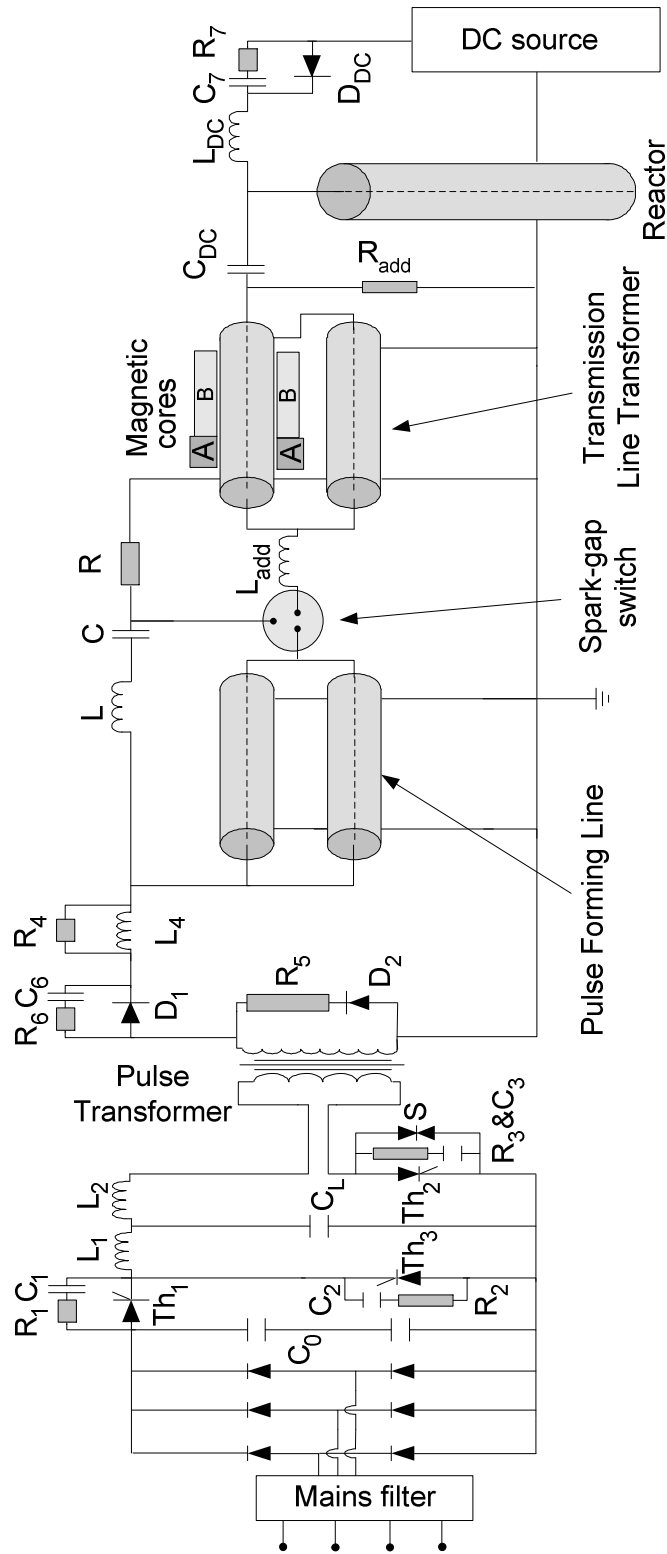


Figure 3.2. Schematic overview of the power modulator.

The windings (wound around glass-fiber-reinforced epoxy tubes) were positioned as shown in Figure 3.3b. A grounding shield was positioned in between the primary and secondary windings to reduce the capacitive coupling and as protection for possible secondary to primary breakdowns. Special care was taken with regard to control of the high electric fields. Field enhancement near conductors was minimized by choosing proper conductor shapes. The transformer was immersed in transformer oil to increase the dielectric strength and consequently to be able to reduce the distances required. The measured primary and secondary inductances were 1.96 mH and 7.09 H respectively, resulting in an effective winding ratio (n) of 60. The coupling factor was determined to be 0.996. The magnetization current I_M was calculated to be < 5 A for 5.5 J and 1 kA (primary current I_{primary}) pulses, i.e., the worst possible experimental settings, so the condition $I_M \ll I_{\text{primary}}$ is met.

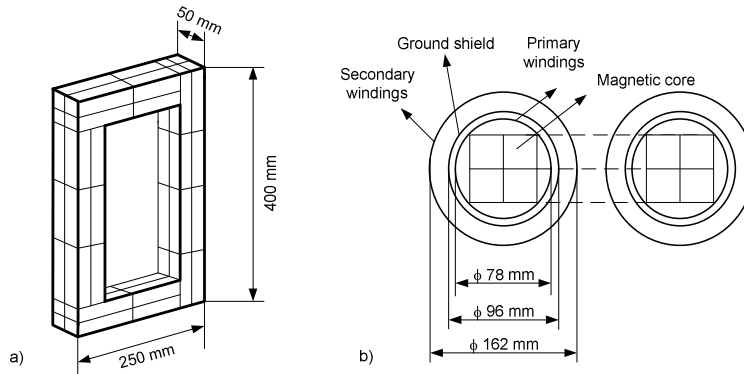


Figure 3.3. Schematic drawings of: a) transformer core and b) primary and secondary positioning.

3.1.3 High-voltage part

The high-voltage diode D_1 is required for the resonant charging of the PFL from C_L . The resistor R_4 is added to dissipate the reflected energy in case of improper matching between pulse modulator and reactor. To minimize resistive losses during charging of the PFL, inductance L_4 was added. The components R_4 and L_4 have been dimensioned in such a way that during charging the impedance of L_4 is much less than R_4 . During and after switching, the impedance of the inductor should be much larger than R_4 .

The PFL was constructed from two 50 Ω coaxial high-voltage cables, connected in parallel. Instead of a PFL, it is also possible to use capacitors for energy storage. The advantage of using a PFL is that when the cables are discharged rectangular pulses are generated with a pulse width of twice the cable transit time (5 ns·m⁻¹). A possible disadvantage of discharging a PFL is that the generated pulse has an amplitude of only half the charging voltage. Two coaxial cables in parallel were used to match the PFL impedance to the input impedance of the TLT (25 Ω , Section 3.1.5). The line impedance of the switch (Section 3.1.4.) was also designed to be 25 Ω . As a result, the PFL can be discharged into a matched load, i.e., there will be no reflections.

Diode D_2 and resistor R_5 are added to dissipate the energy remaining in the transformer core as a result of the magnetization current I_M , and the energy stored in the secondary coil capacitance. Also, after pulse generation, the PFL can remain charged negatively. The remaining energy is then dissipated by R_5 . As a result, the remaining energy is not dissipated in the spark-gap switch, were it would cause increased electrode erosion.

3.1.4 Spark-gap switch and LCR trigger circuit

For pulsed power applications, the heavy-duty closing switch is usually the most critical component. Several types of switches are available such as [Bur(1979)]: IGBT, transistors, thyristors, thyratrons and spark-gap switches (gas, liquid). For large-scale pulsed power applications using short nanosecond-pulses, spark-gap switches are often used. Solid state switches followed by magnetic pulse compression stages are also sometimes adopted. The main disadvantage of magnetic pulse compression is the low energy efficiency for ultra-short pulses ($\sim 20\text{-}50$ ns). For spark-gap switches, the durability was the major limiting factor. Other disadvantages with spark gaps are related to: limited pulse repetition rate, electrode erosion, insulator degradation, arc-inductance, triggering and flushing requirements.

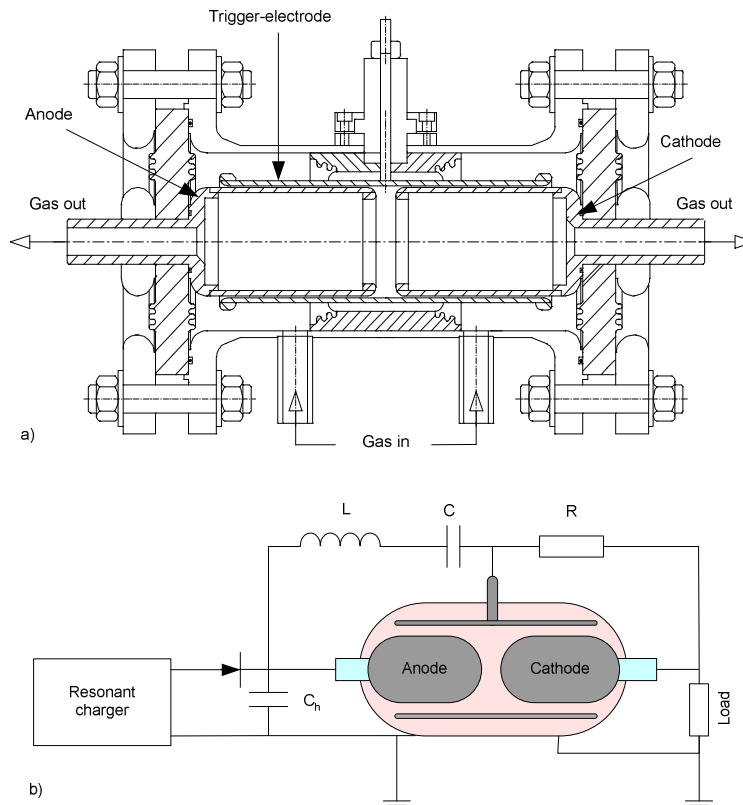


Figure 3.4. a) Construction drawing of coaxial spark gap. The white arrows indicate the air flow direction. b) Schematic depiction of the spark gap, together with the LCR trigger circuit.

For the presented set-up, a newly developed coaxial spark-gap switch [Win(2005b, Win2005c)] with large surface electrodes is used (see Figure 3.4). Details are presented in Appendix C.I. The design of the electrodes ensures a long switch lifetime (more than 10^{10} shots, see Appendix C.I.). The coaxial structure and the short inter-electrode distances ensure a low inductance [Per(1992)], correct EMC behavior, and a line-impedance of 25Ω . The spark gap is pressurized (< 7 bar) and continuously flushed with dry air ($< 35 \text{ Nm}^3 \cdot \text{h}^{-1}$) to increase the attainable pulse repetition rate, to remove spark residue from the gap [Tha(1988)] and to cool the electrodes. For the switch to close completely, both the gap between the anode and the trigger electrode, and the gap between the trigger electrode and the cathode must close. The switch is designed in such a way that the anode-trigger electrode gap closes first. As a result, the trigger electrode-cathode gap becomes strongly over-volted, and subsequently closes quickly. In *Liu2006a* it was demonstrated that such a "multiple spark gap switch" is a useful device to decrease the switching time, i.e., to increase the rise-rate of the generated pulses.

For reliable switching behavior, the switch is used with an LCR trigger circuit [Yan(2001)]. When designed correctly, the LCR circuit always causes the switch to close quickly ($10 \mu\text{s}$) after the PFL charging has been completed. Several experiments were performed to validate the switch performance. Details can be found in Appendix C.II.

3.1.5 Transmission line transformer

The transmission line transformer (TLT) is added to the circuit to obtain voltage multiplication and to improve the impedance matching between source and reactor. A TLT [Smi(2002)] can be described as a set of transmission lines (impedance Z_0) connected in series/parallel configuration at the input and output sides. An example of a 2-stage TLT is shown in Figure 3.5. As a result of the connections (in parallel at the input side and in series at the output side), this TLT acts as a voltage multiplier. As can be seen in Figure 3.5, the input impedance of the TLT is $Z_0/2$ and the output impedance is $2Z_0$. Besides voltage multiplication, the TLT thus acts as an impedance matching network as well.

When designing a TLT, two aspects have to be considered simultaneously. First, the voltage (or current) gain, which is determined by the number of lines n , must be determined. Theoretically the maximum gain would be n , but due to losses (see next paragraph) this maximum value will not be obtained. The second aspect is the energy conversion efficiency from the energy storage capacitor to the load. Both the voltage gain and the energy conversion efficiency not only depend on the matching between the modulator and the load, but also on the secondary mode impedance Z_s , which is defined as the characteristic impedance between the outer conductor of the upper cable and ground. The corresponding current is the secondary mode current. For optimal gain and energy transfer efficiency, this second mode current should be kept as low as possible, thus Z_s should be maximized. In practice this can be accomplished by covering the upper stage of the TLT with magnetic cores.

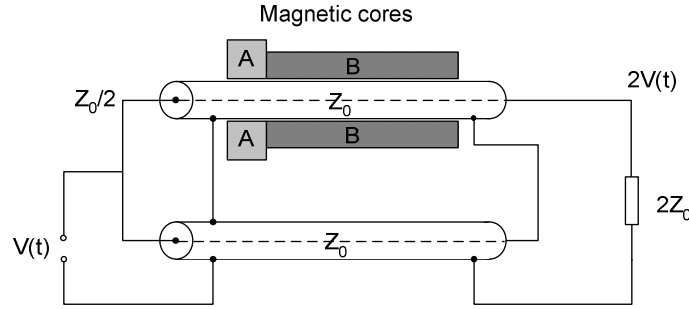


Figure 3.5. A two stage TLT. The impedance of the lines is Z_0 . The output impedance is $2Z_0$, the output voltage is $2V_0(t)$. Magnetic cores B are added to increase the secondary mode impedance and thus to improve the energy efficiency. Magnetic cores A are added to absorb energy reflections from the reactor after the plasma is quenched.

Since for long pulses the TLT is actually a short circuit, the length l of the TLT has to be matched to the width ΔT of the pulses generated by the modulator. The minimum length required can be calculated as [Yan(2001)]:

$$l \geq \frac{1}{2} \cdot \frac{c \cdot \Delta T}{\sqrt{\mu_r \epsilon_r}} \quad (\text{eq. 3.1})$$

where c , μ_r and ϵ_r are the speed of light in vacuum, the magnetic permeability and the dielectric constant of the magnetic core material respectively. This equation is derived on the assumption that the complete TLT is covered with magnetic cores. If this is not the case, a correction has to be made for the propagation delay along that part of the coaxial cable that is not covered with cores. The magnetic material used has $\mu_r = 245$ and $\epsilon_r = 1$. Since the longest pulses used are shorter than 300 ns, it can be calculated that l should be at least 2.9 m. For the described experimental set-up, the length of the TLT was chosen to be considerably longer (15 meters) than this minimum required length, since a 75 ns delay line for the high-voltage pulse was also required (to be able to trigger the ICCD camera on time, see Section 3.4.3). The TLT was only partly covered (3 meters) with magnetic material.

During measurements it was determined that the gain of the employed 2-stage TLT is ~ 1.98 , i.e., close to the maximum value. This implies that Z_s is large. This impedance can be determined using the following equation [Yan(2001)]:

$$\frac{V_{\text{reactor}}(\text{open})}{V_{\text{reactor}}(\text{matched})} = 2 - \frac{1}{2 \left(\frac{Z_s}{Z_0} + 1 \right)} \quad (\text{eq. 3.2})$$

where “open” and “matched” refer to an open connection at the end of the TLT or the use of a matched resistive load respectively. Since the gain of the TLT is close to 2, the determination of Z_s becomes extremely sensitive to the accuracy of the measurement. Averaging the results over 10 measurements yielded a secondary mode impedance of 1600Ω ($\pm 500 \Omega$). The error has been calculated by taking into account the measuring inaccuracy of the voltage measurement (5%) and the averaging procedure.

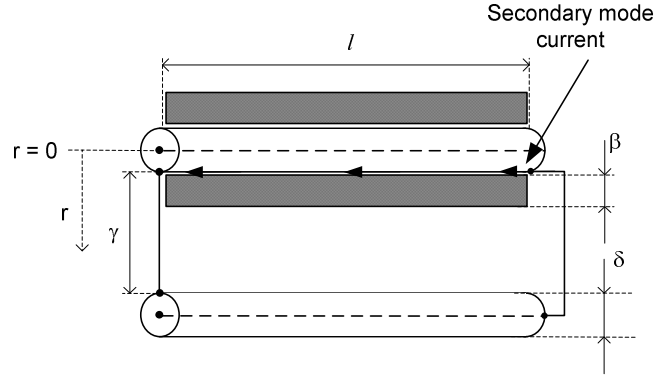


Figure 3.6. Schematic drawing of the 2-stage TLT.

The value of Z_s can also be calculated by considering the geometrical construction. For the calculations it is assumed that the secondary mode circuit can be modeled as a transmission line. The secondary mode impedance Z_s can be calculated as:

$$Z_s = \sqrt{\frac{L_s}{C_s}} = \sqrt{\frac{\mu_0}{2\pi^2 \varepsilon_0} \cdot \left[\mu_r \ln\left(\frac{\delta/2 + \beta}{\delta/2}\right) + \ln\left(\frac{\delta/2 + \gamma}{\delta/2 + \beta}\right) \right] / \ln\left[\left(\frac{\gamma + \delta}{\delta}\right) + \left(\frac{(\gamma + \delta)^2}{\delta^2} - 1\right)^{\frac{1}{2}}\right]}$$

(eq. 3.3)

where ε_0 and μ_0 are the dielectric constant in vacuum and the magnetic permeability in vacuum, respectively. The values of δ , β and γ were determined to be 0.022 m, 0.012 m and 0.09 m, respectively. Combining this with $\mu_r = 245$, the secondary mode impedance can be calculated to be 1740Ω . Even though some approximations have been used during the derivation of Equation 3.5, the agreement with the experiment is good.

3.1.6 DC bias voltage

The pulses can be superimposed on a DC bias voltage. In the past it was already observed that as a result of the DC voltage, the energy per pulse can be increased and the energy transfer efficiency from the PFL into the reactor can be improved ($> 95\%$, Chapters 4 and 7). Also, because of the DC voltage, the system acts as an electrostatic precipitator (ESP) in between the pulses. The pulse modulator and DC voltage supply are separated via the coupling capacitor C_{DC} . For high energy transfer efficiency, the value of the coupling capacitor should obey the inequality as derived in *Yan(2001)*:

$$C_{DC} \geq \frac{C_h \cdot V_{sg}}{2V_{DC}} \quad (\text{eq. 3.4})$$

where V_{sg} is the charging voltage on the PFL (with capacitance C_h). When the equality is true, the voltage across C_{DC} decreases to zero after the voltage pulse and all available energy is used for streamer generation. In Chapter 4, Equation 3.6 will be discussed in detail.

When using a DC bias voltage, two separate processes energize the reactor. Before a high voltage pulse is applied, the reactor and the coupling capacitor C_{DC} are resonantly charged to V_{DC} by the DC voltage source in about 100 μs , (via D_{DC} , L_{DC} , C_{DC} and the TLT). At the moment the spark gap is fired, the energy stored in C_{DC} and the PFL is transported to the reactor simultaneously. After streamer generation, the reactor and C_{DC} are charged again by the DC source.

Until now, it had not been determined whether the DC bias voltage had a separate effect on streamer generation and the chemical processing efficiency. In Chapter 5, results are presented that show that the DC bias voltage does not have a separate effect on the chemical processing efficiency. In Appendix D, it will be shown that the visual appearance of the streamers changes slightly (~10-20%) when DC voltages above the corona onset are used.

3.2 Reactor configurations and R_{add}

For the present study, a wire-plate reactor was considered the most suitable. The main reason is that this configuration permits optical access from the side and the top without disturbing the electric field. For wire-cylinder configuration, openings have to be made in the cylinder to obtain optical access from the side. Another advantage of the chosen reactor configuration is the ability to easily change reactor dimensions, such as the wire-plate distance.

Two reactors (Figure 3.7) were constructed to perform the measurements. Aluminum plates (connected to ground) were used as the reactor walls. The remaining four sides of the reactor were closed with Lexan plates (sealed to the aluminum plates using a PTFE sealant). For reactor A, quartz windows were installed at the top and the side of the reactor to allow the UV-VIS light emitted by the discharges to be photographed. The reactor wires were positioned vertically between the plates. At the top and bottom these wires were supported using brass rods, which were field-controlled to prevent plasma activity and sparking.

For industrial applications, several reactor configurations are suitable, including wire-cylinder or wire-plate reactors [e.g., Hac(2000), Lee(2003), Mok(2001)]. Multipoint-plate configurations, in which one or both of the electrodes are covered with sharp points protruding into the electrode gap, are also possible.

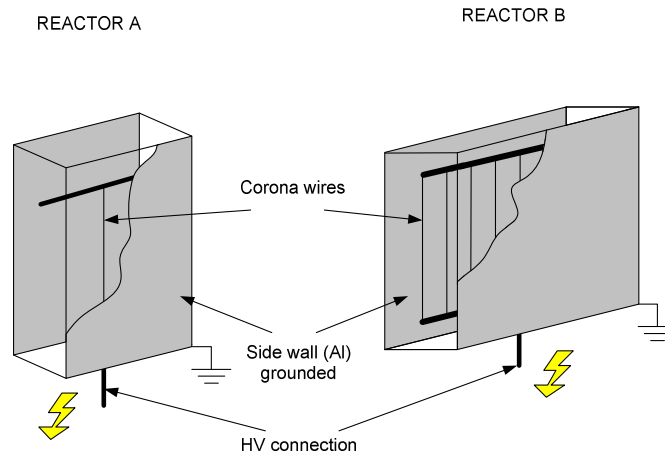


Figure 3.7. Layout of the employed reactor configurations. Lexan plates are used to close the four, non-metal sides of the reactor. For clarity, some aspects of the reactor are not shown: reactor A) the quartz windows fitted into the Lexan plates. The gas inlets: four $\frac{1}{2}$ " nozzles at the top corners of the plates. The exhaust connections: two 10 centimeter diameter pipes in the Lexan plates at the bottom of the reactor. Reactor B) gas input: top side is left open. Exhaust connections: two 10-centimeter-diameter pipes in the corners of the bottom Lexan plate. A compressor with built-in air dryer was used to supply the air flow in the reactor.

Table 3.1. Specifications of the employed reactor configurations.

Parameter	Reactor A	Reactor B
Plate height [m]	1.1	1.2
Plate width [cm]	22	90
Plate-plate distance [cm]	7.4-15.4	11-23
# wires	1	< 13
Wire diameter [mm]	0.2-15	2
Wire length [m]	< 0.9	1.0
Reactor capacitance [pF]	80	180
Max. flow used [$\text{m}^3 \cdot \text{h}^{-1}$]	30	450

The specifications of the reactors are listed in Table 3.1. Reactor B is more similar to an industrial reactor. However, this reactor has some disadvantages:

- Due to its large dimensions, the reactor capacitance is large. As a result, the maximum rise rate of the voltage pulses is reduced (Chapter 4).
- The air-flow pattern inside the reactor could not be controlled and was considered far from optimized.
- When photographing the streamer generation from the side, the plasma activity at all the wires is seen. Due to the large number of streamers generated and the limited depth of field of the camera system, individual streamers could not be distinguished.

Reactor A was developed to avoid these problems. The dimensions of this reactor were kept as small as possible to reduce the capacitance and to control the flow; only one wire was used in order to avoid problems with photographing several wires simultaneously.

As can be seen in Figure 3.2, a resistor R_{add} ($\sim 390 \Omega$, non-inductive resistor) could be connected in parallel to the reactor. This resistor was added to absorb energy reflections during measurements for which the system was not properly matched (Section 3.4.1.2).

3.3 Pulse parameter variation

The key feature of the experimental set-up is the ability to change pulse parameters. An overview of the parameters that can be varied is shown in Table 3.2. The pulse parameters can be varied as indicated in the third column. As can be concluded from this table, it is not a simple matter to vary only one parameter. Usually when one parameter is changed, other parameters change as well. This effect will have to be counterbalanced by simultaneously adjusting the other parameters (Section 3.4.1.2). Another (adopted) strategy is to collect data from broad ranges of combinations of settings and rigorously sort these data afterwards for desired combinations of parameters.

Table 3.2. Pulse parameter variation.

Parameter	Range	Change
Pulse width	30-250 ns	length of the PFL
Rise time (20-80%)	15-50 ns	value L_{add}
Rise rate	$0.5-3.5 \text{ kV}\cdot\text{ns}^{-1}$	value L_{add} , charging voltage PFL
Peak voltage	50-90 kV	DC voltage, charging voltage PFL
DC voltage	0-20 kV	DC bias voltage
Pulse repetition rate	10-1000 pps	Thyristor control
Energy per pulse	0-4.5 J	C_h and voltage
Voltage polarity	Positive-negative	Polarity of transformer, D_1 , D_2 . Use of negative DC supply.

3.4 Diagnostic tools and experimental procedure

The performed measurements can be divided into three categories: electrical, chemical and optical. A description is given below.

3.4.1 Electrical measurements

To be able to measure fast, high amplitude voltage and current waveforms in an environment with large EM fields, much attention has to be paid to the measuring systems from EMC point of view. Several systems can be used, like capacitive dividers, resistive

dividers and differentiating-integrating (D-I) circuits [Deu(1993), Deu(2006), Hee(1989), Hou(1990), Kel(1964), Smu(2001)].

From among all the possible techniques, the D-I measuring system (Figure 3.8) was chosen. In a D-I system, a differentiated signal is transported via a coaxial cable to the passive RC input section of an integrator at the wall of an EMC cabinet. As a result of the differentiation, the high frequency components of the signal are amplified with respect to the lower frequencies. The integrator restores the original waveform, but with a much smaller amplitude. Now the amplitude of the high frequencies is decreased with respect to the lower ones. A major advantage resulting from this mechanism is the high signal to noise ratio, since the high-frequency noise that couples in via the coaxial cable will also be suppressed by the integrator. Other reasons to opt for the D-I systems: the possibility to apply large amplitude signals to the sensors, a very wide dynamic range, the bandwidth of the sensors (can be as large as several hundred MHz), differentiating sensors do not load the system, the sensors can be constructed with excellent EMC properties, the components used for construction are commercially available and inexpensive, and only one high-voltage component is required.

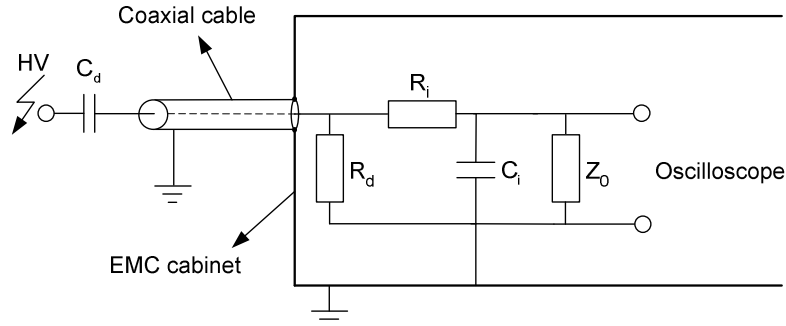


Figure 3.8. Basic principle of D-I measuring system.

For a voltage measurement, a capacitive sensor (with capacitance C_d) is used to determine the voltage waveform V_{HV} . The output of this sensor induces a voltage across the resistor R_d equal to: $R_d C_d \cdot dV_{HV}/dt$. This signal is integrated by the passive R_i - C_i network. The total transfer function of the D-I system as shown in Figure 3.8 can be approximated (ignoring parasitic effects) as:

$$V_{HV}(t) = \frac{1}{R_d C_d} \left(R_i C_i V_{scope}(t) + \left(1 + \frac{R_i}{Z_0} \right) \int V_{scope}(t) dt \right) \quad (\text{eq. 3.5})$$

where $V_{scope}(t)$ is the waveform acquired on the LeCroy Waverunner 2 oscilloscope (1 GHz, 4 GSamples \cdot s $^{-1}$). As the capacitive voltage sensor is usually a small electrode viewing a high-voltage conductor, calculating the value of C_d is not sufficiently accurate. Instead, the sensor has to be calibrated.

The value of $(R_d C_d)^{-1}$ can be considered as the calibration factor of the D-I system. It can be determined by comparing the output signal of the D-I system with that of a calibrated voltage probe. For this study, a Tektronix P6015 high-voltage probe was used to determine the calibration factor.

For a current measurement, the capacitive voltage sensor is replaced with a Rogowski coil. This differentiating sensor gives an output voltage equal to $M \cdot dI/dt$, where M is the mutual inductance between the coil and the conductor passing through it. The transfer function of a D-I system for current measurements now becomes:

$$I_{HV}(t) = \frac{R_i C_i}{M} V_{scope}(t) + \frac{1}{M} \left(1 + \frac{R_i}{Z_0} \right) \int V_{scope}(t) dt \quad (\text{eq. 3.6})$$

As was the case for the voltage sensor, the current sensor must also be calibrated since the value of M cannot be calculated with sufficient accuracy. For this study, the current sensor was calibrated by comparing the obtained signal with that of a Pearson 7885 current monitor.

The effects of the parasitic inductances and capacitances of the sensors have been ignored during the derivation of Equations 3.7 and 3.9. In general, these parasitic effects deteriorate the high-frequency response of the sensors. In the ideal case, the high frequency cut-off of the D-I systems can be approximated as $(Z_0 \cdot C_d)^{-1}$, where Z_0 is the impedance of the coaxial cable.

In the ideal case, the low frequency cut-off of the D-I systems can be approximated as $(Z_0 \cdot C_i)^{-1}$. The second term on the right-hand side of Equations 3.7 and 3.9 is a correction factor for these low frequency signals. After the waveforms have been acquired, these corrections have to be performed numerically. For correct signal determination, the correction factor should be a small function of the main (frequency independent) solution. Together with the required attenuation of the sensor, this imposes the design criteria.

By taking into account the temperature and frequency response of the employed components, the accuracy of the obtained waveforms was determined to be $\sim 5\%$. The bandwidth of the system was measured using a HP 4396A network/spectrum analyzer and was found to be 80 MHz.

A disadvantage of the D-I systems is the inability to measure DC signals, since capacitive sensors are used. The data of the applied DC bias voltage has to be added numerically to the measured signal to obtain the total reactor voltage.

3.4.1.1 Electrical measurement procedure

The positioning of the voltage and current sensors is shown schematically in Figure 3.9. As can be seen, the voltage V_{sg} on the PFL was measured with a separate D-I system.

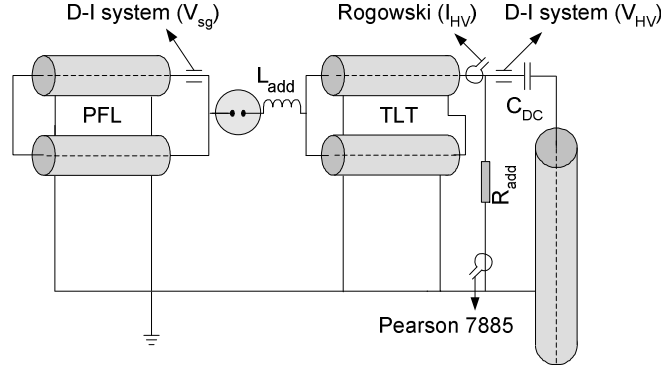


Figure 3.9. Positioning of the various voltage and current sensors.

During measurements with the resistor R_{add} , an additional current sensor (Pearson 7885) was mounted on the grounding wire of this resistor. The reactor current I can then be determined by subtracting this measured current $I_{R_{add}}$ from the Rogowski coil signal, i.e.:

$$I = I_{HV} - I_{R_{add}} \quad (\text{eq. 3.7})$$

Since the voltage sensor V_{HV} measures the voltage before the coupling capacitor, a correction has to be made for the voltage drop across this capacitor to determine the actual reactor voltage $V_{applied}$. This correction can be made because the current and the capacitance are known. The voltage on the reactor can thus be described as:

$$V_{applied} = V_{HV} + V_{DC} - \frac{1}{C_{DC}} \int Idt \quad (\text{eq. 3.8})$$

The current I contains both the capacitive reactor charging current I_{cap} and the plasma current I_{plasma} . The actual plasma current can be determined by subtracting I_{cap} from I . To determine I_{cap} , the reactor capacitance C_r has to be known. This value can be measured by applying a voltage pulse to the reactor with an amplitude lower than the corona inception voltage. In this case $I = I_{cap}$. Since the voltage waveform is known, C_r can be determined. For reactor configuration A, $C_r = 80$ pF was found. For reactor configuration B, the capacitance was larger: 180 pF.

The power waveform is determined by multiplying the reactor voltage and current waveforms. As a result, the power waveform includes both the plasma power and the capacitive power, if the correction for I_{cap} is not made. Because the energy per pulse W_{pulse} is

calculated by integrating the power waveform, it appears that the obtained result is not equal to the plasma energy W_{plasma} but also includes a contribution from the capacitive energy transport. However, using Equation 3.9 it can be seen that this is not the case if the initial and final values of the integral are chosen wisely:

$$\begin{aligned}
 W_{\text{pulse}} &= \int_{t_1}^{t_2} V_{\text{applied}} I dt = \int_{t_1}^{t_2} V_{\text{applied}} (I_{\text{plasma}} + I_{\text{cap}}) \cdot dt = \int_{t_1}^{t_2} V_{\text{applied}} I_{\text{plasma}} dt + \int_{t_1}^{t_2} V_{\text{applied}} I_{\text{cap}} dt = \quad (\text{eq. 3.9}) \\
 &= W_{\text{plasma}} + \int_{t_1}^{t_2} V_{\text{applied}} C_r \frac{dV_{\text{applied}}}{dt} dt = W_{\text{plasma}} + C_r \int_{V_1}^{V_2} V_{\text{applied}} dV_{\text{applied}} = W_{\text{plasma}} + \frac{1}{2} C_r V_{\text{applied}}^2 \Big|_{V_1}^{V_2}
 \end{aligned}$$

where I and V_{applied} are determined using Equations 3.7 and 3.8 respectively. To determine W_{plasma} , it is thus required to add the initial energy in C_r to the calculated W_{pulse} and to subtract the energy remaining in C_r . If, however, the boundaries t_1 and t_2 are chosen such that $V_{\text{applied}}(t_1) = V_{\text{applied}}(t_2)$, the second term on the right-hand side of the equation equals zero. Consequently, the calculated energy E_p is equal to the plasma energy E_{plasma} .

Unless stated otherwise, all results shown are an average of more than 100 pulses. This averaging was performed to decrease the small statistical noise on the signals (compare the averaged waveform in Figure 3.10 and single shot waveform in Figure 3.11c).

3.4.1.2 Electrical characterization of the experimental set-up

For reliable experiments, stable and reproducible voltage pulses are required. Pulse-to-pulse stability (rise rate, peak voltage, energy per pulse, pulse width, etc.) was found to be better than 99% during all the measurements.

Before the results of pulse parameter variation and the mutual parameter interactions are shown, the “standard” electrical waveforms are first discussed. A typical result of the voltage, current, power and energy waveforms is shown in Figure 3.10. The rise time (20-80%) of the voltage pulse is 15 ns. The fastest rise time obtained during the measurements was 13 ns. This value is close to the theoretical fastest rise time of 11 ns, as can be derived from Equation 4.3. According to this equation, the rise time is limited by the reactor capacitance ($C_r = 80$ pF) and the output impedance of the modulator ($Z_{\text{out}} = 100 \Omega$). The voltage pulse width (FWHM) is 100 ns, which is a direct result of the use of a ten-meter-long PFL.

The first peak in the current waveform is due to capacitive charging of the reactor. The moment the current starts to rise again after this peak corresponds to the moment the voltage on the reactor drops from its peak value. This is a result of the ignition of the plasma. The increase in current indicates that current flows into the plasma. As the voltage drops back to zero, a negative overshoot of the current can be seen. This is a result of the discharging of C_r .

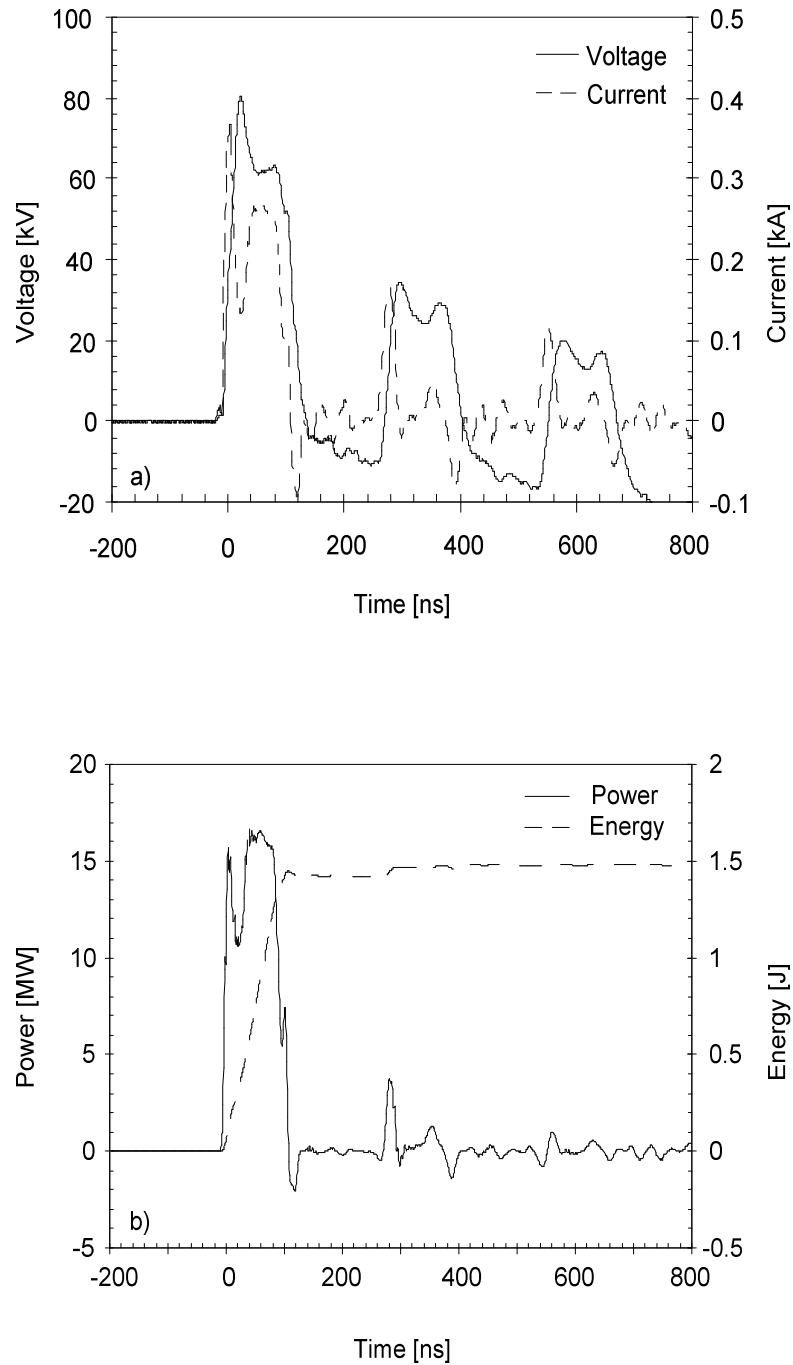


Figure 3.10. Typical waveforms generated on reactor A. Two ten-meter-long coaxial cables were used to construct the PFL. No DC bias voltage, L_{add} or R_{add} were used.

Approximately 250 ns after the voltage pulse arrived at the reactor, the first reflection can be seen. Although the amplitude of the voltage reflections is large, there is no significant plasma current (only capacitive current). This is also shown in the energy waveform. Energy is mainly dissipated during the first pulse, not during the reflections. The reflection time of 250 ns can be explained by taking into account the length of the TLT (15 m) and the PFL (10 m) and the propagation time of the cable ($5 \text{ ns}\cdot\text{m}^{-1}$): $250 \text{ ns} = 2\cdot(15 \text{ m} + 10 \text{ m})\cdot 5 \text{ ns}\cdot\text{m}^{-1}$. This result indicates that the spark-gap switch is still conducting at the moment the voltage reflection arrives at the switch. If the spark-gap switch had stopped conducting after discharging of the PFL, the reflection of the pulse would have been registered 150 ns after the first pulse.

The capacitive charging and discharging of the reactor can also be seen in the power waveform but, as explained above, the energy per pulse can still be determined correctly.

Figure 3.11 summarizes the results obtained when power modulator settings are changed. The results presented here only show positive polarity pulses, since negative polarity pulses are in no way different (apart from the polarity). Pulse parameters were varied according to the methods shown in Table 3.2. Variation in pulse repetition rate is not shown.

When looking at the effect of the charging voltage V_{sg} (voltage on the PFL) on the resulting voltage waveform in the reactor, several observations can be made. Firstly, for higher charging voltages, a small voltage drop occurs shortly after the reactor voltage reaches its maximum value. As was mentioned above, this small voltage drop is a result of the plasma generation. The source has to deliver more current to the discharge than it can supply. For lower charging voltages this seems not to be the case. The explanation can be found when considering some of the results as presented in Chapter 4 (Figure 4.7): For lower charging voltages the plasma impedance is high, indicating that the current flow into the plasma is low. Below a certain voltage, the source will have to deliver less current than it can supply and, as a result, there will be no voltage drop on the reactor. As a second observation, the height of the voltage reflections relative to the initial pulse amplitude decreases for increasing voltages. This observation is a result of matching. For high voltages the matching is much better (Chapter 4) compared to low voltages. As a consequence, more of the available energy will be dissipated by the plasma when high amplitude pulses are used, and less energy is left for the reflections.

The results from Figure 3.11b show that the peak voltage increases when increasing the DC level, but not linearly. In other words, for increasing DC bias voltage, the pulse voltage decreases. Again, the explanation can be found when considering the impedance of the plasma. With reference to Figure 4.1, the voltage on the reactor is determined by the output impedance of the source and the reactor impedance. When ignoring C_r and C_{DC} , the two impedances act as a voltage divider. The reactor voltage is thus affected by the plasma impedance. For higher voltages this impedance decreases and hence the voltage on the reactor also decreases (relatively).

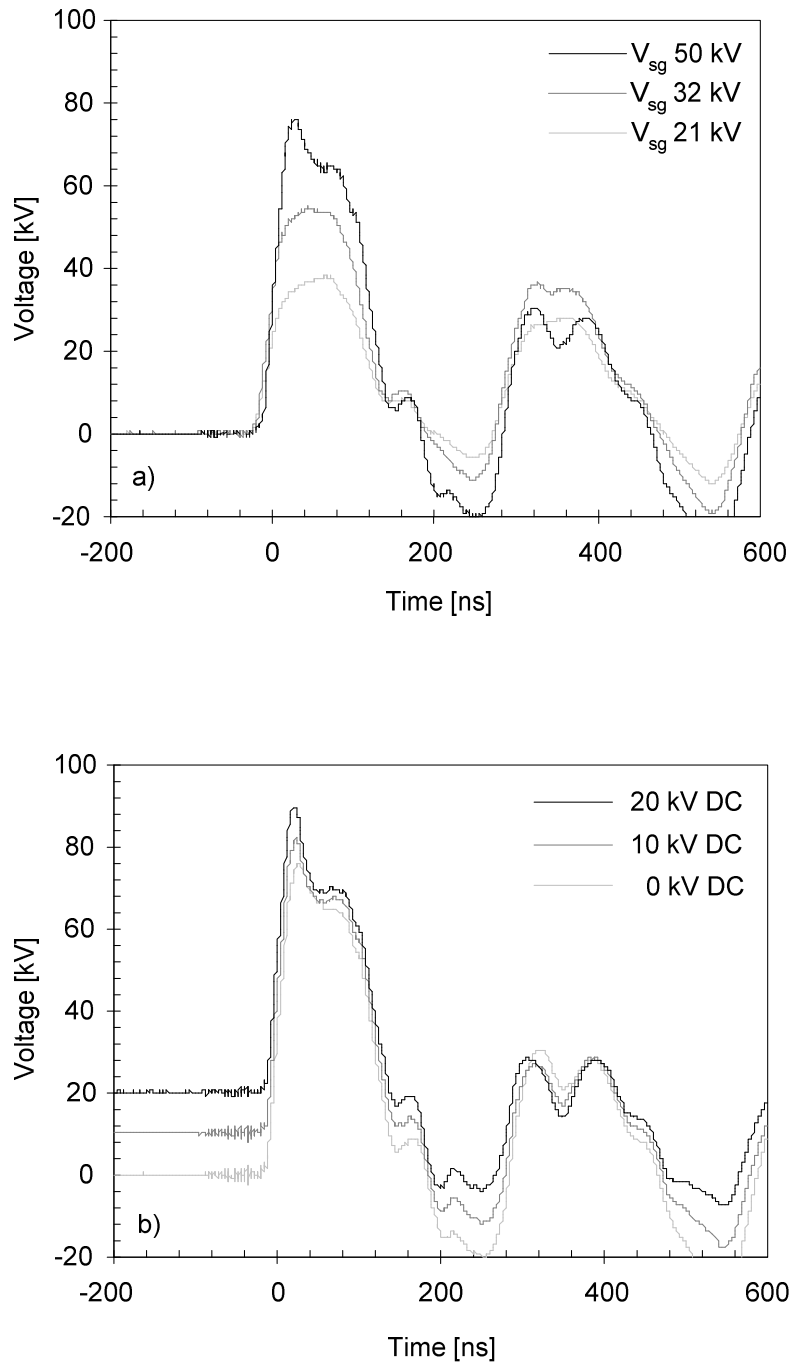


Figure 3.11. Single shot measurements of the voltage waveform on reactor configuration A are shown. a) Effect of the high voltage capacitor charging voltage V_{sg} . b) Effect of the DC bias voltage. For every plot, only one adjustment to the power modulator was made; other settings were kept constant.

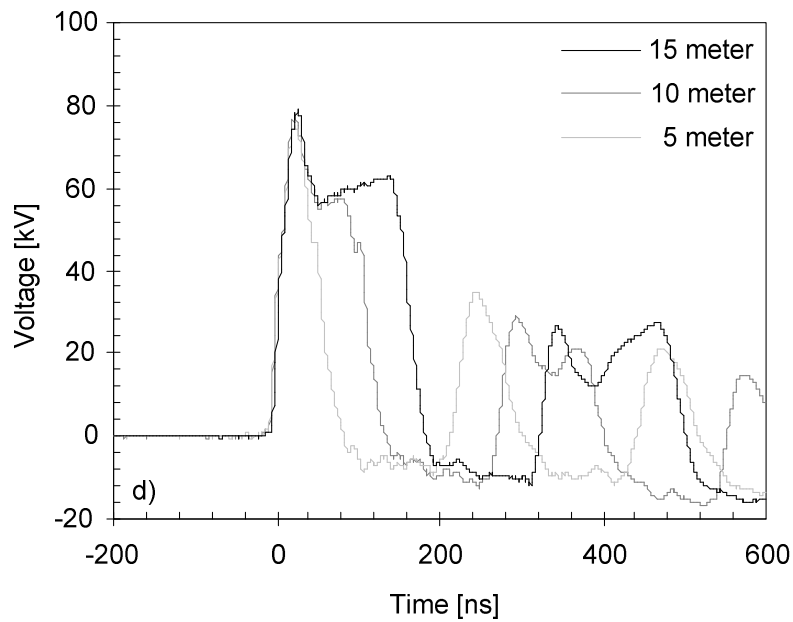
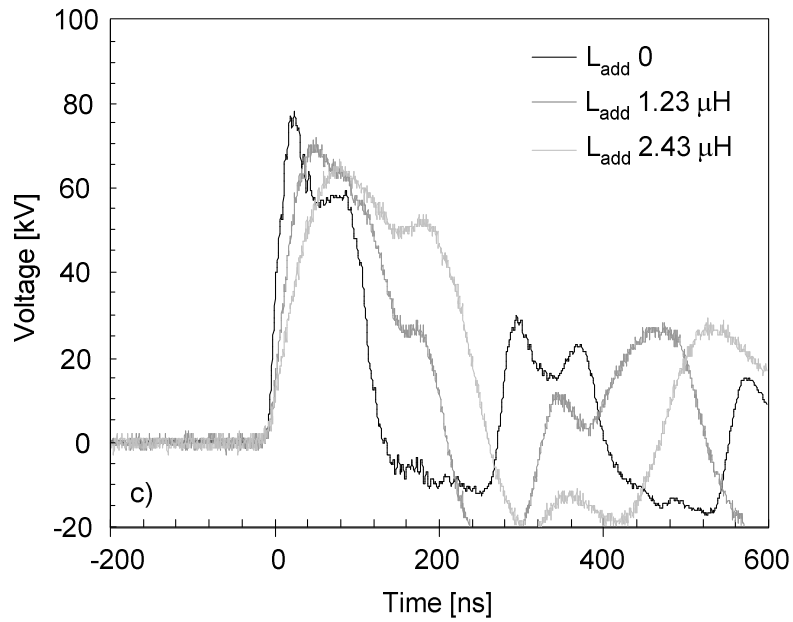


Figure 3.11 (continued). c) Effect of the additional inductor L_{add} . d) Effect of PFL length.

Figure 3.11c shows that the rise time of the voltage pulse can be increased by increasing the inductance of L_{add} . It can also be seen that, through addition of the inductor L_{add} , not only the rise time, but also the peak voltage, pulse width and energy per pulse changes (Figure 3.12). In other words, by changing a single modulator setting, several pulse parameters vary. This behavior can be observed for other modulator settings (DC bias voltage, pulse-width, etc.) as well. Fortunately, by changing more than one modulator setting, it is possible to achieve a change to a single pulse parameter (see Section 3.3). This is desirable from a research perspective, as this makes it possible to investigate the effect of each pulse parameter separately.

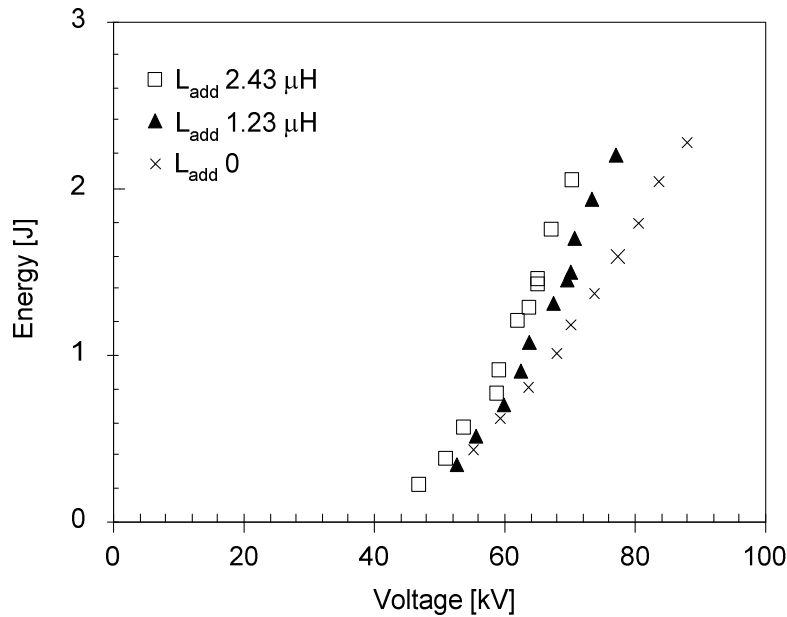


Figure 3.12. Pulse energy as function of peak voltage for different voltage rise times. The length of the PFL was fixed at 10 meters. Different DC levels were used, but no separate effect on pulse energy could be observed; only the total peak voltage is important, as well as the rise time.

Although the guidelines for well matched pulsed streamer systems were incorporated in the experimental set-up, the majority of the measurements had to be performed under non-matched conditions. Since one of the objectives of this study is to change pulse parameters over a wide range, several non-matched conditions automatically occur. The problem associated with the non-matched conditions is that the energy that remains after the pulse starts to oscillate in the system. It was observed that in some situations this oscillation re-ignited the plasma (see Appendix D). As a result, energy is deposited in the reactor a couple of times for every voltage pulse. Although this might lead to enhanced radical production efficiencies, for this study it was considered undesirable since interpretation of the radical yields is severely disturbed. It was also observed that in some cases (those with a high reactor voltage) the oscillations could lead to complete breakdown of the reactor gap.

To solve the problems for the non-matched situations, only measurements with an energy reflection of less than 10% were used during this study. The reflection was defined as the ratio of energy deposited in the reactor long after the pulse to the energy deposited directly after the pulse (see Figure 3.13). For those measurements with reflections of less than 10%, the energy deposited long after the reflections was used for the calculations. To enlarge the range with measurements fulfilling this criterion, an additional resistance R_{add} (390 Ω) could be added in parallel to the reactor. The resistance was connected as close as possible to the reactor, to minimize inductance.

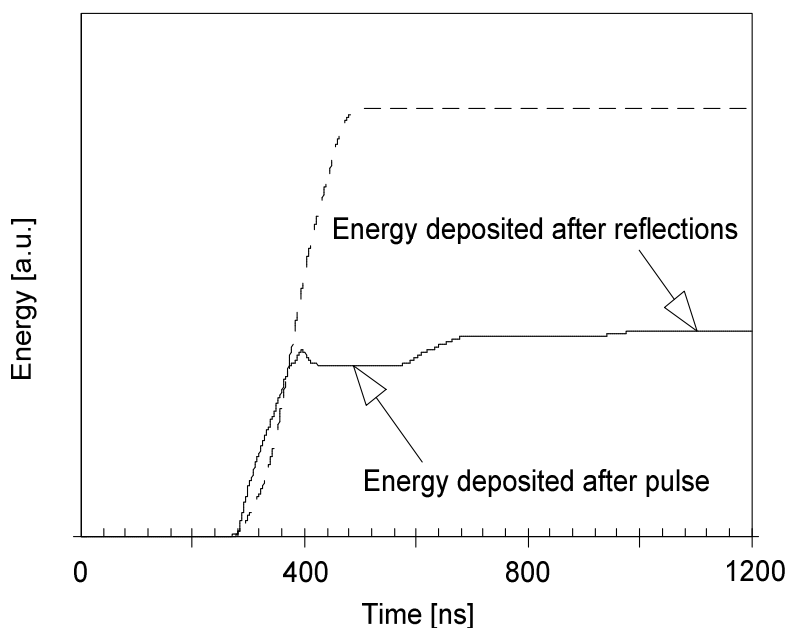


Figure 3.13. The dotted line is an example of a measurement with negligible reflections. The solid line indicates a measurement that cannot be used for analysis due to the large ($> 10\%$) reflections.

3.4.2 Chemical measurements and procedure

The ozone concentration was determined using the UV absorption technique (Figure 3.14) in the Hartley-band (230-290 nm), where the absorption of ozone is largest. As UV source, an Ocean Optics Deuterium light source was used. An HR2000 (Ocean Optics) spectrometer was used to acquire the spectra (wavelength 200-400 nm, resolution 0.1 nm). Laboratory-grade solarization-resistant optical fibers (400 μm diameter) were used for the optical connection between the UV source, the measuring cell, and the spectrometer. Two collimating quartz lenses were used to focus the light in the measuring cell. The measuring cell was homemade and constructed from brass. The optical path length (d) in the cell is 0.149 m. The measuring cell was located in the exhaust pipe of the system at a distance of approximately 1.5 meters from the reactor.

The ozone concentration in the exhaust gas flow can be determined using Lambert-Beer's law:

$$\ln\left(\frac{I(\lambda)}{I_0(\lambda)}\right) = c_{O_3} \cdot \varepsilon(\lambda) \cdot d \quad (\text{eq. 3.10})$$

in which c_{O_3} is the ozone concentration ($\text{molecules}\cdot\text{m}^{-3}$), $I(\lambda)$ is the absorption spectrum, $I_0(\lambda)$ is the background spectrum (gas flow without ozone) and $\varepsilon(\lambda)$ is the absorption cross-section ($\text{m}^2\cdot\text{molecule}^{-1}$) of ozone as function of wavelength. The values for $\varepsilon(\lambda)$ can be found in the literature [e.g., Sei(1986)].

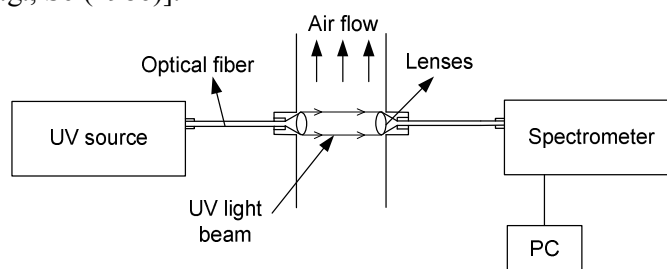


Figure 3.14. Schematic overview of UV absorption technique set-up.

The spectrometer is controlled via a personal computer. Before switching on the plasma, a background spectrum $I_0(\lambda)$ is recorded (making sure no ozone is present in the reactor). Once the set-up is started, the absorption spectrum is monitored. After 5-10 seconds the absorption level reaches a stable value ($< 1\%$ variation for at least half an hour), indicating a constant ozone production. At this moment the absorption spectrum $I(\lambda)$ can be determined. After determining $I(\lambda)$, the set-up is switched off, while maintaining the air flush in the reactor. After about one minute, all produced ozone is removed from the reactor and a new measurement can be performed (including recording a new background spectrum).

Using the obtained spectra $I_0(\lambda)$ and $I(\lambda)$, in combination with Equation 3.10, the actual ozone concentration was determined. To reduce the measuring error, calculations were performed at (and subsequently averaged over) 20 different wavelengths from 250-270 nm. The resulting measuring error is estimated to be less than 5%. The reproducibility of the chemical measurements was verified by repeating some of the measurements. The results showed agreement within the measuring error.

During the chemical measurements the properties of the ambient air flow were also determined:

- The temperature was measured directly before and directly after a measuring sequence (approximately 15 minutes) in the exhaust of the reactor using an Omega HH-25KC thermocouple. Temperature was found to be 20-24 °C during all the measurements. No noticeable increase in temperature as a result of plasma generation was observed.

- The relative humidity was monitored using a standard relative humidity meter (ST-321) in the exhaust of the reactor.
- The air flow rate was monitored in the exhaust of the reactor using a Testo 435 vane anemometer. It was determined that the changes in the flow rate have a standard deviation of less than 1% compared to the mean value, measured over a time period of 2 hours.

The air flow rate and the relative humidity in the reactor were derived from the values measured in the exhaust channel, taking into account the dilution of the air as a result of air influx in the piping connecting the reactor to the exhaust channel.

3.4.2.1 Chemical characterization of the set-up

Figure 3.15 shows that the ozone concentration can be increased by increasing the energy density (by changing the pulse repetition rate). It can be seen that for these low ozone concentrations, the increase is linear with the energy density. Obviously, in between the pulses the gas is mixed well again and ozone destruction as a result of repetitive pulsing is not significant in this regime. This finding is in agreement with *Bra(1990)* and *Šim(2002)* who found that energy densities of $> 100 \text{ J}\cdot\text{L}^{-1}$ were required to change the linear dependency of ozone concentration on energy density.

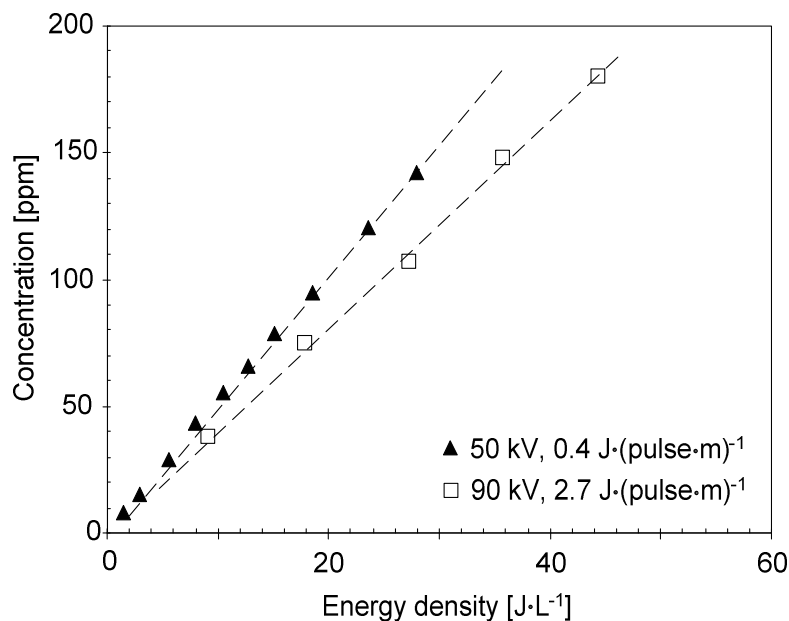


Figure 3.15. Ozone concentration (in parts per million, ppm) as function of energy per pulse per meter of corona wire. Results for two different pulse shapes are shown. Reactor configuration A was used.

The maximum ozone yield obtained was $105 \text{ g}\cdot\text{kWh}^{-1}$, which is high when considering that air with a relative humidity of 13-18% was used. This result shows that streamer plasmas are efficient radical producers.

3.4.3 Optical measurements

To study the spatial and temporal development of the streamer plasma generation, an intensified charged coupled device (ICCD) was used. A Princeton Instruments 576G/RB intensified CCD camera was used (180-800 nm, 576x384 pixels). The image intensifier is coupled to the CCD element by a glass fiber connection (minimal loss of light) and has a maximum gain of 80 counts per photon. No effort was made to relate the measured intensity to the number of photons emitted by the discharge. An external pulser (Princeton Instruments type FG-100, 5 ns minimal pulse width) was used to control the fast gate function of the camera. A Sigma 180 lens was used to focus the camera on the discharge activity.

Figure 3.16 shows an overview of the circuit required for time-resolved ICCD photography. The CSMA software package running on the personal computer is used to initialize the programmable delay (0-625 ns, step size 5 ns). It also initializes the controller (Princeton Instruments, ST130) and the ICCD camera. After the initialization, the plasma system can be started. At the moment a picture is required, switch S is closed manually and the trigger signals are allowed to enter the camera's control circuits. The trigger signal is generated by a capacitive sensor connected to the trigger electrode of the spark-gap switch. This sensor detects the moment the switch closes.

The generated pulse triggers the programmable delay, which sends a delayed pulse to the pulse generator. The generator in turn produces the actual pulse to gate the camera. After the generator has produced the pulse, the programmable delay becomes inactive, preventing consecutive pulses from triggering the camera again. After the picture is taken, the data is sent to the computer where it can be processed using a homemade Matlab routine. As soon as the data transfer is completed and stored to hard disk (~30 seconds) a new picture can be taken.

The gate pulse to the ICCD camera is detected using a small capacitive sensor. The resulting signal is recorded on the oscilloscope simultaneously with the reactor voltage-waveform. By comparing the signals, the time delay between the start of the voltage pulse ($t = 0$) and the gating of the camera can be determined (accuracy and repeatability: $< 1 \text{ ns}$). Before the measurements started, the exact time-delay was calibrated. This was done by comparing the output signal of a fast Hamamatsu H5773-01 PMT (focused on the corona wire) with the signal of the small capacitive sensor. Since the time delay of the PMT (and the connecting coaxial cables) were known, the exact moment the camera opened could be determined.

Because of the internal time delays of the camera, the control circuits, and the coaxial cables (total of all delays: 70 ns), and the fact that the camera is triggered at the moment the spark-gap switch closes completely, the actual high-voltage pulse between the spark-gap switch and the reactor must be delayed if the first stages of the plasma generation are to be photographed. The high-voltage pulse was delayed by the use of a 15-meter-long TLT (75 ns delay).

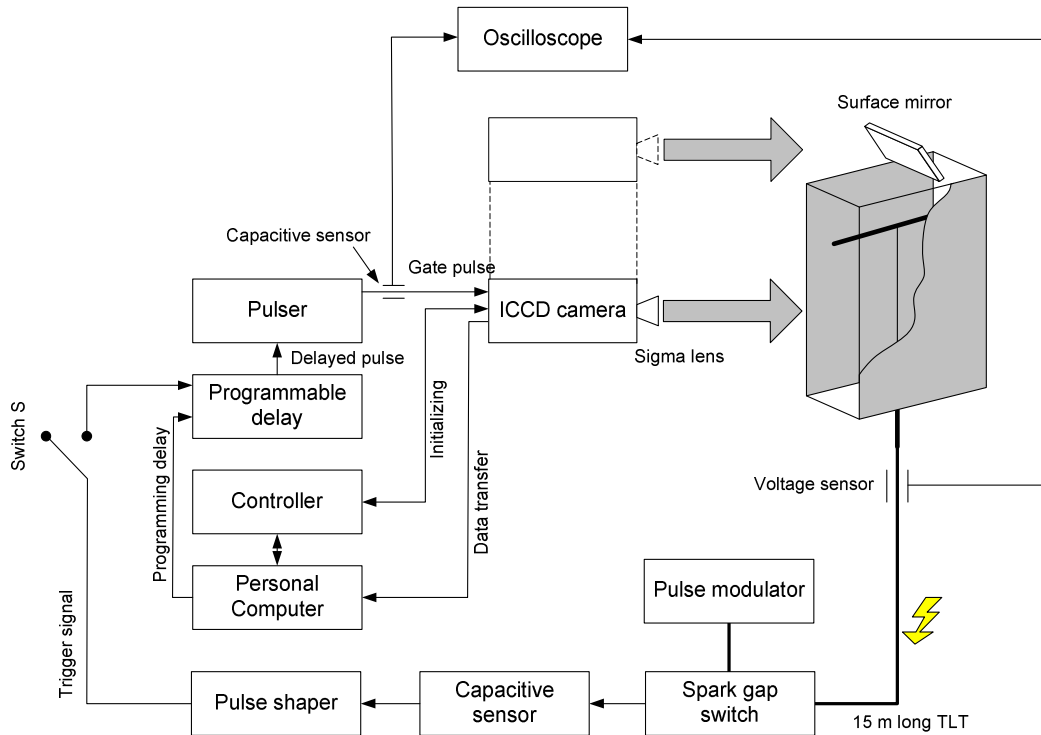


Figure 3.16. Schematic overview of the ICCD system. Adequate EMC precautions have been taken to obtain reliable operation.

3.4.3.1 Optical measurement procedure

The measurements can be divided into top-view and side-view pictures. For the side-view pictures two gate times of the camera were used: the shortest (5 ns) to study the temporal development of the streamers; and a longer gate-time (400 ns) to study the complete plasma generated by a single pulse. For the top-view pictures only the long gate time of 400 ns was used. The reasons that the temporal resolved measurements were not performed for the top view are twofold. Firstly, the depth resolution of the camera system is insufficient to allow focusing over the complete reactor wire. Secondly, since a large number of streamers per meter is generated, it is impossible to distinguish individual streamers. As a result little information about streamer properties can be obtained from top-view pictures.

Side-view pictures were taken at a distance of 1 m from the reactor wire, resulting in a pixel size of $\sim 100 \times 100 \mu\text{m}$. For the top-view pictures, the camera was positioned at a distance of 3.5 m from the reactor, resulting in a pixel size of $\sim 350 \times 350 \mu\text{m}$. A flat mirror, positioned at an angle of 45 degrees, was used to obtain the top-view pictures. The accuracy of the performed measurements is roughly 2 pixels, i.e., $200 \mu\text{m}$ and $700 \mu\text{m}$ for the side-view and top-view pictures respectively. This value was found by performing measurements on an ICCD picture of a well defined shape.

During the 5 ns gate time measurements, the gain of the intensifier was set to its maximum value. For the time-integrated side-view pictures the gain was set to 85%. For the time-integrated top-view pictures the gain was set to 75%. These values were chosen to obtain sufficient intensity for the low-energy discharges, but to prevent overexposure of the CCD element during the high-energy discharges.

During experiments with various pulse repetition rates up to 400 pps, it was found that no differences in plasma generation could be observed. All investigated parameters (velocity, diameter, etc.) remained unchanged as function of the pulse repetition rate. As a result, all the measurements were performed using the lowest pulse repetition rate of 10 pps.

Interpreting the pictures is not straightforward, since the generated plasma is 3D in nature. Not all streamers transit in the focal plane of the camera. For the side-view pictures only those streamers protruding farthest into the gap are used for analysis, since they are closest to the focal plane of the camera.

The pictures shown in this thesis are colored artificially, since the ICCD camera produces 14-bit grey-scale images. The adopted color scheme in this thesis was chosen for its close resemblance to the actual light emitted by the discharges. No adjustments to the intensity have been made for any of the pictures that are shown.

During the 5 ns time-resolved side-view measurements, ten pictures, individually delayed in time, were taken of every combination of power modulator settings. This way the temporal evolution of the streamers could be monitored. Since the camera can take only one picture in ~ 30 seconds, the pictures shown in this thesis are not from a single pulse, but from different pulses. The reproducibility of the voltage pulses (peak voltage, pulse width and rise time) was tested and found to be $> 99\%$, which justifies comparing pictures taken from different shots. The reproducibility of the ICCD pictures was also tested. For identical voltage waveforms, the differences observed in streamer dimensions, intensity, number, and velocity were found to be smaller than the measuring accuracy of the ICCD system. This also demonstrates that the jitter in the streamer inception time delay [Vel(2003)] is negligible. This is a result of the fast-rising, high-voltage pulses that were used. Furthermore, for the side-view pictures it was found that the location on the wire at which the pictures are taken is non-significant, indicating a uniformly distributed discharge along the wire. The only exception found was at the ends of the wire, where due to field control

less discharge activity was observed. Since the region of field distortion is small (1-2 cm) compared to the total wire length, these effects have been neglected in the calculations.

3.4.3.2 Optical characterization of the streamers

Figure 3.17 shows a typical example of the time-resolved development of the streamers as a result of a positive-polarity voltage pulse. The time at which the photo was taken, relative to the voltage pulse, is shown in 3.17i. In Figures 3.17a-3.17h, typical primary and secondary streamer generation is shown. Starting soon after the voltage increases (a), primary streamers are formed which transit the complete gap (a-f). During their transit, the streamer diameter (determined at 20% of the maximum intensity value) increases from roughly 0.7 to 3 mm (see below). At the moment the primary streamers reach the cathode (f), secondary streamers are formed [Mar(1981), Sig(1984), Tar(2002)]. The secondary streamers are always in the same channel as that in which the primary streamers were generated (Figure 3.20). They travel only partly (1-2 cm, depending on the applied electric field) into the inter-electrode gap (f-h) and always remain attached to the anode. Their diameters are ~ 1 mm, comparable to the primary streamers at these positions.

Figure 3.18 shows the situation when the applied voltage has a negative polarity. Basically, the situation is identical to that of the positive polarity. A striking difference is that the secondary streamers protrude further into the reactor gap.

Pictures similar to those shown in Figures 3.17 and 3.18 are useful to determine the streamer head position (relative to the wire), the streamer diameter, and the average light intensity as function of time. For the position and diameter measurements, only those streamers protruding farthest into the gap are used, since these streamers are closest to the focal plane of the camera. By plotting the streamer head position and the streamer diameter as function of time, the typical growth velocities can be determined. This is shown in Figure 3.19 for different (positive) voltages.

From Figure 3.19a it can be concluded that the streamer velocity is almost constant throughout the first part of the reactor gap (in the order of 10^6 m·s⁻¹). The streamer head only accelerates near the plate electrode. This acceleration occurs particularly at the higher voltages. This behavior can be explained by considering that the streamer is a conductive channel. Part of the externally applied voltage will drop across the streamer channel, but the remaining part will be between the streamer head and the plate electrode. For high voltages and short distances this will result in enhanced electric fields just before the streamer head, and as a result higher streamer velocities. The measured velocities are comparable to values found in literature: 10^5 - 10^6 m·s⁻¹ [e.g., Blo(1997), Cre(1994), Ono(2003a), Tar(2002), Vel(2002), Won(2002), Yi(2002)], the exact values found depending on the applied voltage, and the geometry of the discharge gap. Similar results have been obtained from modeling studies [e.g., Kul(2000), Pan(2001)].

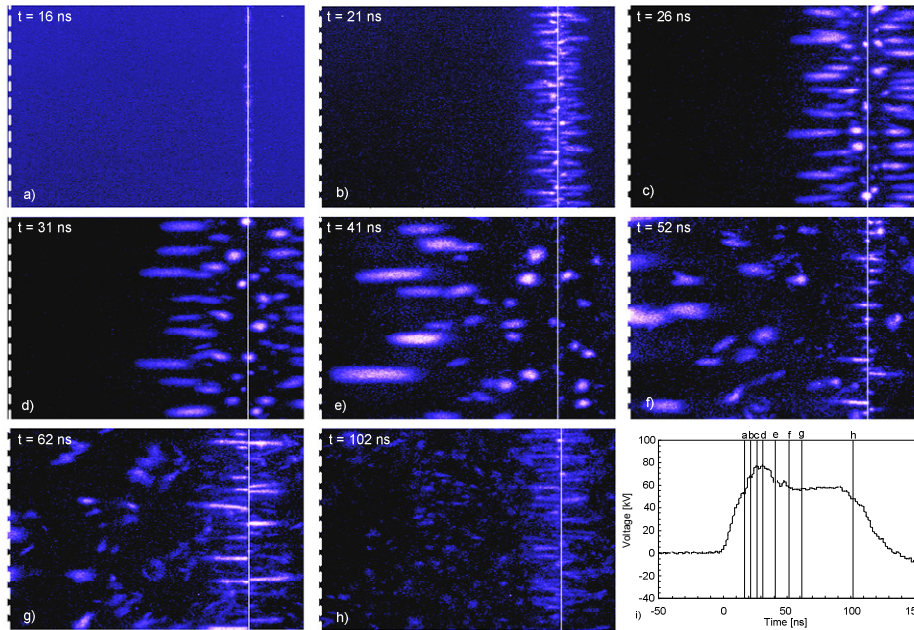


Figure 3.17. Time-resolved side-view ICCD pictures for the pulse shown in i). Pulse parameters: pulse width 110 ns, pulse voltage 74 kV, rise rate $2.7 \text{ kV}\cdot\text{ns}^{-1}$. Picture size is $\sim 7 \times 5 \text{ cm}$. White line: reactor wire. Dotted line: reactor wall. The time the picture is taken, relative to the moment the voltage on the reactor begins to increase, is shown in the top-left corner and is also shown in i).

Figure 3.19b shows the streamer diameter as function of time. The observed behavior is similar to that of the streamer head position. The growth of the diameter is constant throughout the gap and increases with voltage. The acceleration near the plate electrode is less pronounced. Typical streamer diameters found are in the range of 0.7-3.0 mm. Streamers with a comparable diameter have been observed and modeled in various studies [e.g., Blo(1997), Bri(2005a), Kul(1998), Pan(2003), Won(2002)]. These thick streamers are always observed when the applied reactor voltage is high, i.e., well above the breakdown voltage of the gap, as is the case for this study. The voltage pulses have to be short for such high voltages, otherwise the streamers will transit into spark discharges. Also, the modulator should be able to deliver sufficient current. In most literature, thin streamers are observed/modeled: 100-200 μm [e.g., Ono(2003a), Vel(2002)]. During these studies, however, relatively low voltages have been used to generate the streamers.

For the experiments as discussed in this thesis, the smallest diameters are always found close to the wire, for low-voltage and long rise time pulses, i.e., when the applied electric field is low and the charge influx is limited by the inductor L_{add} . It can also be seen that during the transit through the gap, the diameters almost double. Typical growth velocity is $10^5 \text{ m}\cdot\text{s}^{-1}$; i.e., an order of magnitude less than the primary streamer transit velocity.

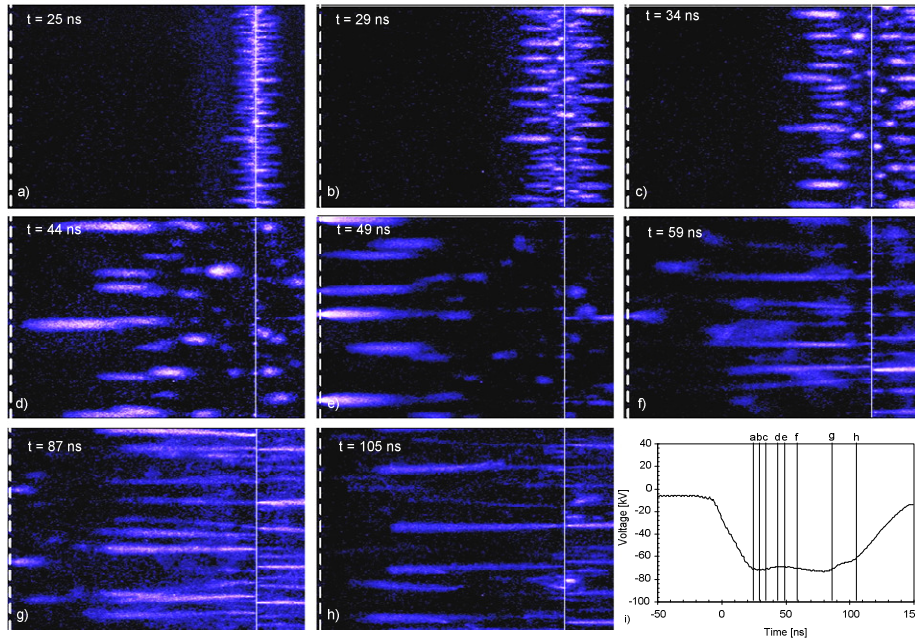


Figure 3.18. Time-resolved side-view ICCD pictures for the pulse shown in i). Pulse parameters: pulse-width 110 ns, pulse voltage -72 kV, rise rate 2.7 kV \cdot ns $^{-1}$. Picture size is $\sim 5.5 \times 4$ cm. White line: reactor wire. Dotted line: reactor wall. The time the picture is taken, relative to the moment the voltage on the reactor begins to increase, is shown in the top-left corner and is also shown in i).

Figure 3.19c shows the average light intensity (total number of counts divided by the number of CCD pixels) as function of time. During the primary streamer transit, the light intensity increases until a maximum value is obtained, shortly after the primary streamers have bridged the gap. Then the light intensity steadily decreases until the plasma is completely quenched. For higher voltages, two observations can be made. Firstly, the average light intensity increases. This is a result of the increased energy dissipation. Secondly, the peak in light intensity shifts to the left for higher voltages. This can be explained using the data provided in Figure 3.19a. Higher voltages result in higher streamer velocities. As a result, the primary streamers cross the gap in a shorter duration.

To determine the number of streamers, their spatial distribution, branching, etc., the pictures shown above are not optimal. For these measurements it is preferable to use the longer (400 ns) gate-time pictures shown in Figure 3.20. With these, the complete paths of the streamers can be observed. Numerous streamers do not reach the plate electrode but only cross the gap partly. At the position where those primary streamers that do cross the complete gap connect to the plate electrode, a small bright spot can be observed. The secondary streamers are visible as bright re-illumination of the primary streamer filaments near the reactor wire. Besides the individual streamers, the interaction between adjacent streamers also becomes visible. Branching can be observed and sometimes interconnecting streamers (two streamers merging into a single channel) are visible (Appendix D).

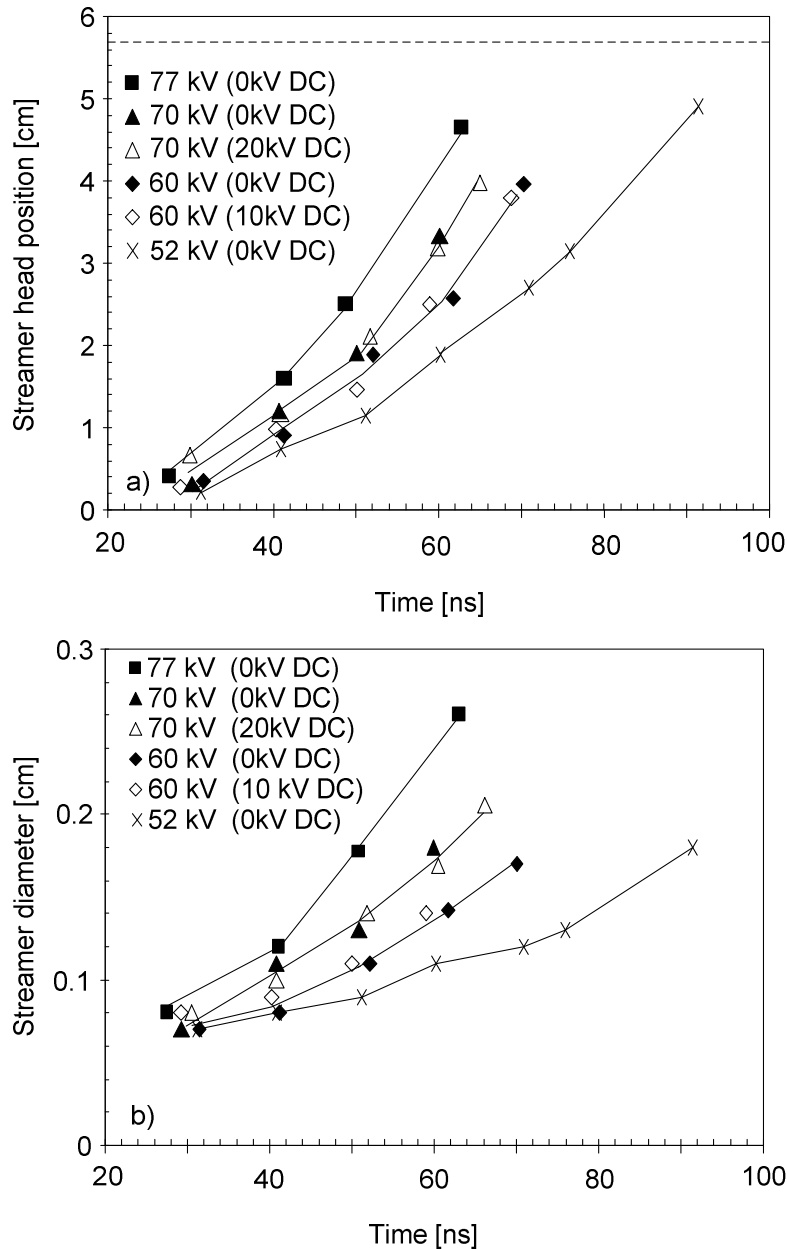


Figure 3.19. The voltage indicated in the legend is the total peak voltage. The applied DC bias voltage is shown between the brackets. The dashed line in a) gives the position of the plate electrode (cathode). The wire (anode) is at position 0 cm. In a), b), and c) the rise-time is 25 ns and the pulse-width is 100 ns. The closed markers indicate situations where only pulses are applied, open markers indicate measurements for which DC bias voltage was also used. The corresponding markers in the three different plots are from the same ICCD picture. a) Distance of streamer head from wire as function of time for different reactor voltages. b) Streamer diameter as function of time and applied voltage.

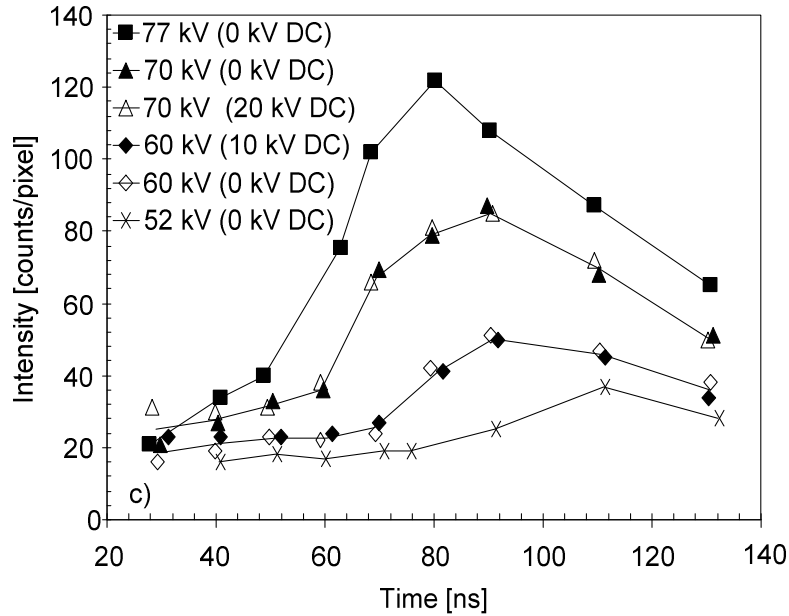


Figure 3.19 (continued). c) Average light intensity as function of time for different voltages.

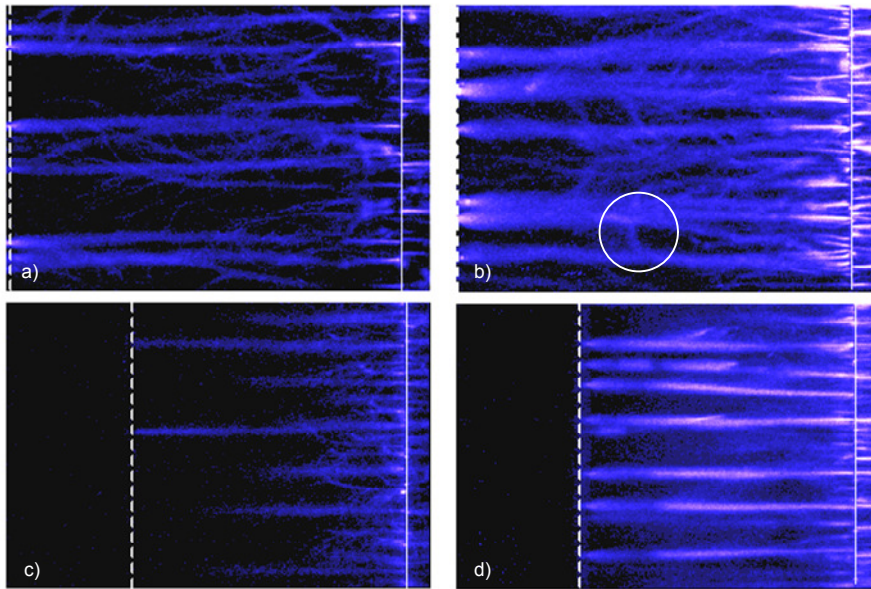


Figure 3.20. Examples of 400 ns side-view ICCD pictures. Solid line: reactor wire, dashed line: reactor wall, picture size: 6x4.5 cm, pulse width 100 ns, voltage rise rate $2.8 \text{ kV}\cdot\text{ns}^{-1}$. a) +53 kV, $0.4 \text{ J}\cdot\text{pulse}^{-1}$, wire-plate distance 57 mm. b) +82 kV, $1.9 \text{ J}\cdot\text{pulse}^{-1}$, wire-plate distance 57 mm. c) -61 kV, $0.1 \text{ J}\cdot\text{pulse}^{-1}$, wire-plate distance 37 mm. d) -75 kV, $1.3 \text{ J}\cdot\text{pulse}^{-1}$, wire-plate distance 37 mm. In the white circle in b) an interconnection between two adjacent streamers can be observed.

Quantitative data that can be obtained from the pictures is limited to: the average light intensity, the number of streamers leaving the wire and the number of streamers arriving at the plate. Streamer densities are determined by counting the streamers visible on the picture and extrapolating the obtained result for the complete reactor wire. To do this, the plasma development along the entire wire has to be uniform. As was discussed in Section 3.4.3.1 this is the case for the experimental conditions used. Due to the large number of streamers in a single photo and the irregularity of the streamer paths, the accuracy with which the streamer densities can be determined is low. Typical inaccuracies can be as large as 20%. Branching, streamer interconnection and other properties of the generated plasma were not quantified. Only general trends were observed.

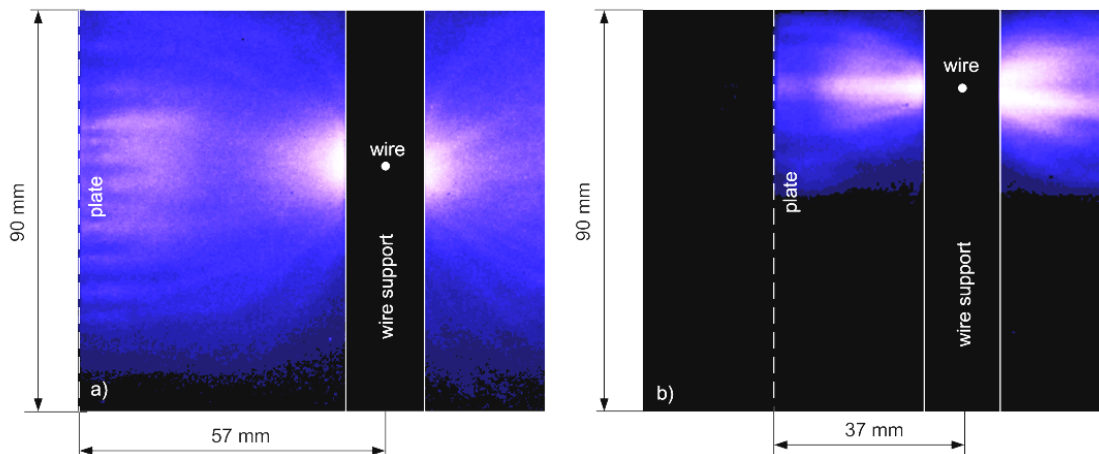


Figure 3.21. 400 ns gate time, top-view picture of streamer discharge, in reactor A. a) Voltage pulse parameters: peak voltage 75 kV, voltage rise rate $3.0 \text{ kV}\cdot\text{ns}^{-1}$, $1.6 \text{ J}\cdot\text{pulse}^{-1}$, pulse width 100 ns, wire-plate distance 57 mm. b) Voltage pulse parameter: peak voltage -81 kV , $2.6 \text{ kV}\cdot\text{ns}^{-1}$ rise rate, $1.5 \text{ J}\cdot\text{pulse}^{-1}$, pulse width 100 ns, wire-plate distance 37 mm.

Typical examples of top-view pictures can be found in Figure 3.21. The voltage pulse characteristics can be found in the figure caption. Clearly, the streamers cannot be distinguished individually. The region near the wire is blocked by the metal rod that supports the wire electrode. This thick ($\text{Ø } 15 \text{ mm}$) piece of brass was required for field control at the end of the corona wire. Without it, unwanted discharge behavior at the end of the wire was observed. Logically, the light intensity is the strongest at the wire and decreases nearer to the plate due to the high streamer density and the presence of secondary streamers at the wire.

Information that can be obtained from these top-view pictures is the average light intensity and the plasma coverage on the plate electrode.

4 Matching a pulsed power modulator and a plasma reactor*

In this chapter, the matching between the power modulator and the plasma reactor is discussed. The matching is expressed as the energy transfer efficiency between the modulator and the reactor. For a completely matched system, all of the available energy in the power modulator is used to generate the streamer plasma. The criterion for optimal matching between a source and a load is that the output impedance of the source is equal to the load impedance. When trying to match a pulsed power modulator to a plasma reactor this criterion is difficult to obey since the load impedance changes rapidly before, during and after plasma generation. To simulate the response of the load as function of the voltage pulse, a simplified equivalent circuit is used. This circuit was used to analyze the matching between the modulator and the load. Measurements will be presented that support and extend the derived model. Based upon the findings, guidelines to optimize the matching between the modulator and reactor are derived.

4.1 Model

Figure 4.1 shows an equivalent circuit of the source in combination with the reactor load. The actual source in this circuit is the PFN-TLT combination, used between the modulator and the reactor. It can be modeled as a voltage source of $2v(t)$ and an internal resistance Z_{out} ($= 100 \Omega$, equal to the output impedance of the TLT). $v(t)$ is the voltage waveform at the input-side of the TLT. The load is the combination of the coupling capacitor C_{DC} , the inductance L_r (the connections and the plasma inductance), the reactor capacitance C_r and the streamer plasma resistance R_r . Instead of trying to obtain the transfer function of the complete circuit, a distinction was made between several time regimes, as was also done by Yan(2001): before, during and after streamer generation.

4.1.1 Load impedance before streamer generation

Before streamer generation, the load can be modeled as a capacitor C_r in series with the coupling capacitor C_{DC} . Using a *MicroCap* [Mic 8.0] computer model it was determined that the inductance L_r of the reactor connections, (estimated to be 50 nH) can be ignored compared to the effect of the $Z_{out} - C_{DC} - C_r$ combination. Before streamer generation, C_r has a constant value, in the order of 100 pF. The exact value depends on the reactor dimensions and its connections. C_{DC} is 1.5-3 nF, for the experimental conditions. Since the switch does not close during this regime, R_r can be ignored.

* Parts of this chapter have already been published in *Bel(2005)*, *Win(2005e)* and *Win(2006c)*.

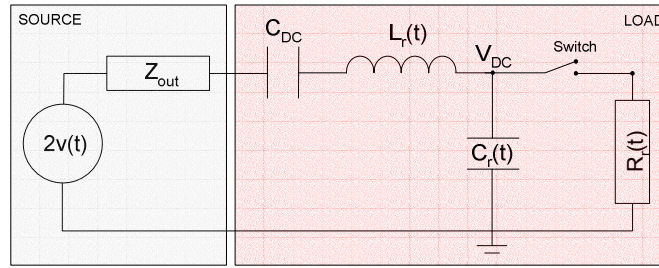


Figure 4.1. Equivalent circuit for the modulator-load interaction. The effects of the spark-gap resistance are ignored. The PFN-TLT combination is modeled as a voltage source of $2v(t)$ with an internal impedance of Z_{out} . The bias voltage V_{DC} is taken into account as an initial condition. C_r , L_r and R_r are the load capacitance, inductance and resistance respectively. C_{DC} is the coupling capacitor. The ignition of the streamer plasma is modeled by closing the switch.

4.1.2 Load impedance during streamer generation

During streamer generation, the effect of the inductance of the load will be negligible in comparison to the resistance. The inductance of the load is the result of the inductance of the connections to the reactor (~ 50 nH) and the inductance of the streamer plasma. This latter inductance is the result of the combination of many streamers in parallel, distributed over the entire length of the corona wire. Since each streamer has an inductance of less than 50 nH, the streamer plasma inductance, including the wire, is less than 1 nH. Using these estimates, it can be shown that characteristic L_r/R_r times are considerably shorter than the fastest voltage rise time of 15 ns, which means that the effect of L_r can be ignored.

Strictly speaking, the value of C_r changes during streamer propagation. Although the reactor capacitance is constant, the decreasing distance between the heads of the conducting streamer filaments and the reactor wall results in an increased capacitance C_r . In *Mok(2000)* it was determined that the capacitance can increase by a factor of three. For the present discussion, the variation of C_r as function of time has been ignored. In Section 4.3.2.1 it will be demonstrated that the plasma resistance R_r is constant during the secondary streamer phase. For the systems described in this thesis, $R_r \sim 100\text{-}2000 \Omega$.

4.1.3 Load impedance after streamer generation

After plasma generation, $R_r \rightarrow \infty$ while the voltage remains high. As a result the energy transfer stops. The load behaves as a capacitor again, and the remaining energy will oscillate between the load and the modulator. Attention must be paid to this oscillation since:

- The energy can re-ignite the plasma.
- The spark-gap switch cannot recover from its conducting state.
- Part of the energy will be dissipated in the modulator components.

To prevent these problems, the oscillations must be quenched. For the presented system this was accomplished using energy absorbing magnetic cores around the upper stage of the TLT.

4.2 Energy transfer efficiency according to the model

4.2.1 Situation before streamer generation

Some calculations for the situation before streamer generation have been performed by *Yan(2001)*, although the effects of the DC bias voltage and the coupling capacitor C_{DC} were not taken into account. The following pulse waveform was used to perform the calculations:

$$v(t) = \begin{cases} \frac{t}{\tau} V_0 & t \leq \tau \\ V_0 & t > \tau \end{cases} \quad \text{if} \quad \text{(eq. 4.1)}$$

where V_0 and τ are the peak voltage and rise time of the pulse at the input side of the TLT, respectively. The energy transfer efficiency η in *Yan(2001)* was calculated by dividing the amount of energy delivered to C_r by the amount of energy that would be dissipated in a matched resistive load under the same voltage pulse conditions. It was assumed that the streamers are generated at $t = \tau$. The calculations showed that an optimal energy transfer efficiency of ~ 0.97 is obtained when:

$$\tau = 2Z_{out} \cdot C_r \quad \text{(eq. 4.2)}$$

Here the calculations are extended to include the possibility that the plasma ignites at an arbitrary time θ and to incorporate the effect of C_{DC} . Assuming the same voltage pulse at the input of the TLT (Equation 4.1), the voltage waveform $V_{reactor}$ on C_r before the plasma is ignited (i.e., $t < \theta$) can be calculated as:

$$V_{reactor}(t) = \begin{cases} \frac{2V_0}{\lambda_1} \frac{C^*}{C_r} (\lambda_2(t) - 1 + \exp(-\lambda_2(t))) + V_{DC} & t \leq \tau \\ \frac{2V_0}{\lambda_1} \frac{C^*}{C_r} ((\lambda_1 + \exp(-\lambda_2(t)) - \exp(\lambda_1 - \lambda_2(t)))) + V_{DC} & t > \tau \end{cases} \quad \text{if} \quad \text{(eq. 4.3)}$$

For convenience, the following substitutions have been used: $C^* = C_{DC} \cdot C_r / (C_{DC} + C_r)$, $\lambda_1 = \tau / (Z_{out} C^*)$ and $\lambda_2(t) = t / (Z_{out} C^*)$. It can be observed that the voltage rise time on the reactor depends on Z_{out} and C^* and is not solely determined by τ .

The energy transfer efficiency from the modulator to C_r at the moment ($t = \theta$) the plasma ignites is given by:

$$\eta(\theta) = \begin{cases} \frac{\frac{1}{2} C_r V_{reactor}^2(\theta)}{\int_0^\theta \frac{V_0^2}{Z_{out}} \cdot \left(\frac{t'}{\tau}\right)^2 dt'} & \text{if } \theta \leq \tau \\ \frac{\frac{1}{2} C_r V_{reactor}^2(\theta)}{\frac{V_0^2}{Z_{out}} \cdot (\theta - \tau) + \int_0^\tau \frac{V_0^2}{Z_{out}} \cdot \left(\frac{t'}{\tau}\right)^2 dt'} & \text{if } \theta > \tau \end{cases} \quad (\text{eq. 4.4})$$

The denominator in this equation is the energy that is delivered by the voltage source into a matched (impedance Z_{out}) resistive load. In the ideal case, the coupling capacitor does not affect the energy transfer from the source into the load. Equation 4.4 can only be used if V_{DC} is zero. For the simplified model, however, the efficiency before streamer generation is not affected by the presence of V_{DC} . Inserting Equation 4.3 into Equation 4.4, the following result is obtained:

$$\eta(\theta) = \begin{cases} \frac{6}{\lambda_2(\theta)} \frac{C^{*2}}{C_r^2} (\lambda_2(\theta) - 1 + \exp(-\lambda_2(\theta)))^2 & \text{if } \theta \leq \tau \\ \frac{6}{\lambda_1^2} \frac{C^{*2}}{C_r^2} \frac{(\lambda_1 + \exp(-\lambda_2(\theta))) \cdot [1 - \exp(\lambda_1)]^2}{3\lambda_2(\theta) - 2\lambda_1} & \text{if } \theta > \tau \end{cases} \quad (\text{eq. 4.5})$$

In Figure 4.2a, $\eta(\theta)$ is plotted as function of the relative time λ_2 for various λ_1 . For the example shown, it has been assumed that $C_{DC} \gg C_r$. It can be seen that the maximum in this curve is constant for $\lambda_1 \geq 2$. For lower values of λ_1 (fast rise time, or large Z_{out} and large C_r), the maximum obtainable energy transfer efficiency is lower. As long as $C_{DC} \gg C_r$ and $\lambda_1 \geq 2$, an energy transfer efficiency of 97% before streamer generation can be obtained when the streamers are ignited at the moment the energy transfer efficiency reaches this maximum value. This effect is also shown in Figure 4.2b. In this graph the diamond shaped markers correspond to the maxima of the curves shown in Figure 4.2a. Clearly, as long as $\lambda_1 \geq 2$, the maximum energy transfer efficiency before streamer generation can always be obtained. Also shown in Figure 4.2b are the results when C_{DC} is not infinitely larger than C_r . The shown results have been obtained by determining the maximum values of plots similar to the ones shown in Figure 4.2a, only now for the corresponding capacitance ratio. For the experimental range usually $C_{DC} : C_r = 25 : 1$. According to Figure 4.2b this implies that the maximum energy transfer efficiency before streamer generation is ~88%.

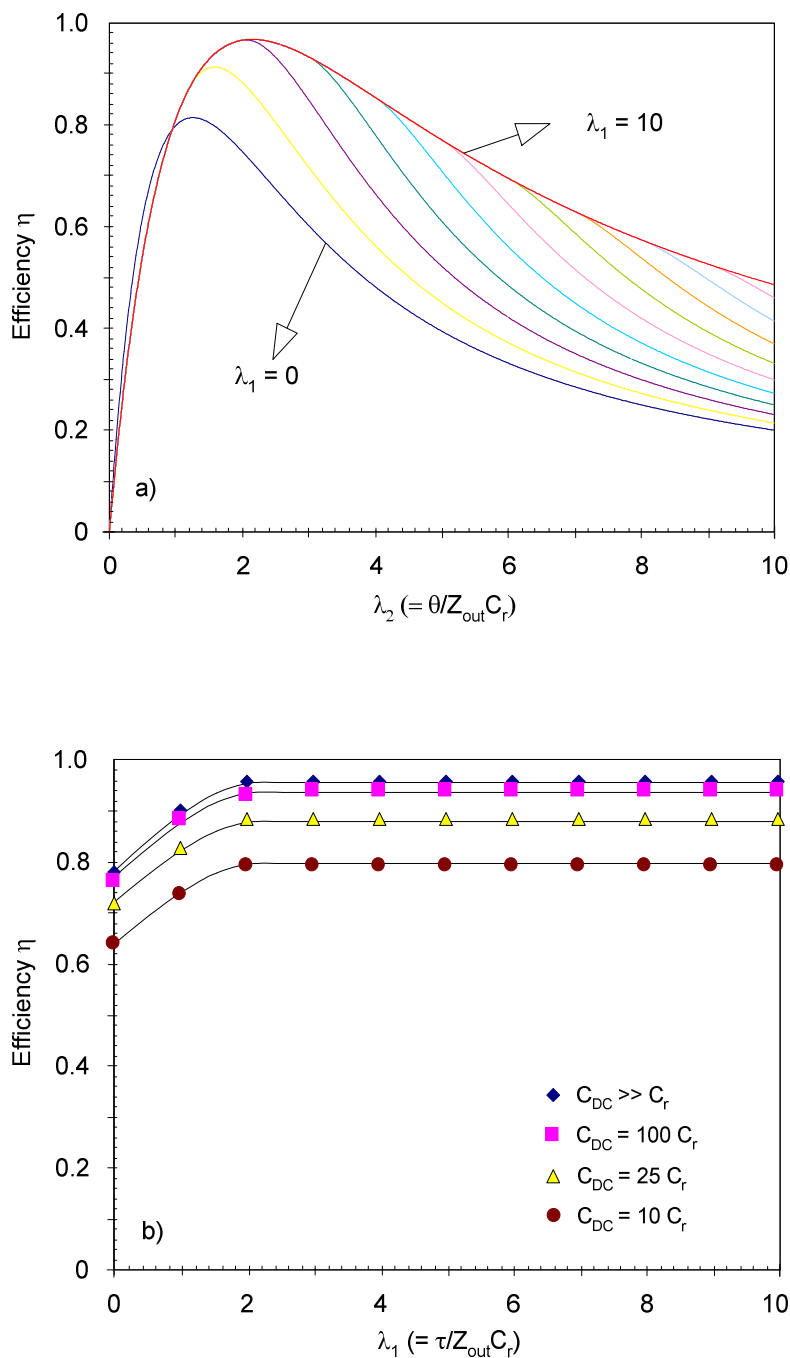


Figure 4.2. Energy transfer efficiency to C_r as function of λ_1 and λ_2 . a) Effect of λ_1 on energy transfer efficiency. Lines for integer values between 0 and 10 are plotted. $C_{DC} \gg C_r$, $V_{DC} = 0$. b) Maximum energy transfer efficiency as function of λ_1 and the ratio between C_{DC} and C_r .

4.2.2 Situation during streamer generation

During streamer generation, the streamer plasma is modeled as a resistor. In the ideal case, $C_{DC} = \infty$ and $C_r = 0$. The equivalent circuit then reduces to the load resistance R_r connected to the voltage source and the impedance Z_{out} . To obtain the optimal energy transfer efficiency in this case, the following equation should be obeyed:

$$Z_{out} = R_r \quad (\text{eq. 4.6})$$

For the experimental conditions, the effects of the capacitors cannot be ignored. Determining the criterion for optimal energy transfer efficiency in this case is difficult since the time response of the system is determined by the shape of $v(t)$. Although no effort is put into determining this time response, the following remarks can be made, the validity of which will be proven in Section 4.3:

- During the primary streamer phase, R_r is the result of the resistance of the primary streamer channels (that have not yet crossed the complete reactor gap) and the capacitance of the streamer heads with respect to the collecting electrode. This capacitance represents a high impedance in comparison with the resistance of the streamer channels. Since both impedances are in series, R_r will be high as well. Consequently, it is expected that during the primary streamer phase, the load cannot be matched to the source.
- At the moment the primary streamers have crossed the reactor gap, there is a conducting path in the reactor. Now C_r is in parallel with a relatively low resistance. Since for the experimental conditions $R_r \cdot C_r$ is much less than the pulse duration and $R_r \cdot C_{DC}$ exceeds the pulse duration, the situation resembles that of the ideal case described at the beginning of this subsection. As a result, during the secondary streamer phase, the optimal energy transfer efficiency can be obtained if Equation 4.6 is satisfied.
- If a DC bias voltage is used, criterion 4.6 is modified to become:

$$R_r = Z_{out} \cdot \left(1 + \frac{V_{DC}}{V_0} \right) \quad (\text{eq. 4.7})$$

This equation is derived under the assumption that $R_r \cdot C_{DC}$ significantly exceeds the pulse duration. If no DC bias voltage is used, Equation 4.7 reduces to Equation 4.6. For higher DC bias voltages, the resistance R_r has to be increased to obtain optimal matching. The background of this effect is as follows. When matched, the coaxial cable inevitably carries the current I that is determined by its impedance Z_{out} : $I = V_0/Z_{out}$, where V_0 is the pulse voltage on the cable. The ratio of the voltage across the load $V_0 + V_{DC}$ and this current is the impedance of the load when matched, i.e., R_r should be equal to

$(V_0 + V_{DC})/(V_0/Z_{out}) = Z_{out}(1 + V_{DC}/V_0)$. If $R_r \cdot C_{DC}$ is comparable to the pulse duration, the coupling capacitor (partly) discharges during the pulse. As a result, V_{DC} decreases. The required value of R_r now becomes a function of time. Also, the voltage drop across C_{DC} is no longer negligible. V_0 has to be replaced by the actual value (i.e., corrected for the voltage drop across C_{DC}) to obtain the criterion for a well matched R_r .

- As was derived by *Yan(2001)*, the optimal energy transfer efficiency can only be obtained if:

$$C_{DC} \geq \frac{C_h \cdot V_{sg}}{2V_{DC}} \quad (\text{eq. 4.8})^\dagger$$

This criterion describes the relation between the capacitance C_h of the PFL, the capacitance of C_{DC} and the related charging voltages V_{sg} and V_{DC} (see Figure 3.9) on these capacitors, required for optimal energy transfer. Basically, Equation 4.8 relates the amount of charge that both capacitors can deliver into the reactor. The small amount of charge in C_r is neglected. The division by a factor of two is the result of the 2-stage TLT used. From all the charge injected from the PFL into the TLT, only half will transfer into the reactor. The other half reflects back towards the PFL once the pulse is incident on the end of the TLT. *Yan* derived Equation 4.8 based on the following reasoning[‡]: if $V_{DC} \cdot C_{DC} = \frac{1}{2} \cdot C_h \cdot V_{sg}$, i.e., if the equal sign is valid, the voltage difference across C_{DC} after the pulse is zero. All energy stored in C_h and C_{DC} will transfer to the reactor, i.e., optimal matching is obtained. If the inequality is invalid, then after the pulse, C_{DC} becomes negatively charged (as seen from the reactor side). The energy stored in C_{DC} is lost, since for time scales that exceed the pulse duration, the TLT is a short-circuit, i.e., C_{DC} is shorted to ground and the energy in C_{DC} after the pulse is lost. If the inequality in Equation 4.8 is valid, then after the pulse, C_{DC} remains positively charged. The remaining energy in C_{DC} and C_r is available for the next pulse, since at the reactor side, there is no short-circuit path. In practice, this implies that when a DC bias voltage is used and Equation 4.8 is valid, the charging of C_{DC} and C_r starts from an initial voltage level V_∞ . The amount of energy that must be delivered by the DC source is thus less than would have been the case if these capacitors had discharged completely.

When the remaining energy in C_{DC} and C_r is taken into account, less energy has to be supplied by the DC bias source to charge these capacitors to V_{DC} . The “energy usage per pulse” can then be calculated as:

$$\eta_{transfer} = \frac{\int V(t) \cdot I(t) dt}{\frac{1}{2} C_h V_{sg}^2 + \frac{1}{2} (C_{DC} + C_r) \cdot (V_{DC}^2 - V_\infty^2)} \quad (\text{eq. 4.9})$$

[†] This equation is identical to Equation 3.4.

[‡] The equivalent circuit shown in Figure 4.1 cannot be used to prove the validity of Equation 4.8.

where $V(t)$ and $I(t)$ are the measured reactor voltage and current respectively. However, when Equation 4.9 is used it does not become evident how well the source is matched to the reactor. In this thesis the focus is on determining what amount of the energy stored in the modulator for each pulse is used for streamer generation and how this amount can be optimized. To determine the matching, the following equation is therefore used:

$$\eta_{\text{matching}} = \frac{\int V(t) \cdot I(t) dt}{\frac{1}{2} C_h V_{sg}^2 + \frac{1}{2} (C_{DC} + C_r) V_{DC}^2} \quad (\text{eq. 4.10})$$

4.2.3 Combining reactor charging and streamer generation

As can be concluded from Section 4.2.2, in the ideal case, obtaining the maximum energy transfer efficiency only depends on matching R_r to the output impedance of the source, according to Equation 4.7, and obeying Equation 4.8. The situation before streamer generation is more complicated as it shows that, to obtain maximal energy transfer during this stage, the plasma should be ignited at a pre-determined moment (i.e., at a maximum in Figure 4.2a). This criterion seems to impose stringent conditions on the design of the streamer plasma system. However, the efficiency before streamer generation is not of particularly great interest since the purpose of the system is to generate a streamer plasma, not to charge a capacitor. Let us continue the calculations by considering a more realistic situation: first C_r is (partially) charged and at a certain moment $t = \theta$ the streamers are generated. With reference to Figure 4.1: at the moment the pulse reaches the reactor, the switch is open and C_r is charged. At $t = \theta$, the plasma is ignited by closing the switch. For the calculations it has been assumed that the switch closes infinitely fast. Ideally, the parallel combination of C_r and R_r should present an impedance equal to Z_{out} . The required value for R_r was found from simulations. To avoid complications as a result of Equation 4.8, the coupling capacitor has been omitted.

The energy transfer efficiency into the plasma η_{plasma} was determined as the ratio of the energy dissipated in R_r and the energy that would have been dissipated if the switch had been closed from the very start of the pulse. Figure 4.3 shows a typical result ($\lambda_1 = 4$) of the simulations. In the plot, η_{plasma} is plotted as function of the relative time λ_2 . The line indicates the value the efficiency would have if the switch were to close at the corresponding time. The arrow indicates the moment at which the energy transfer efficiency reaches its maximum value when the plasma is not ignited at all (i.e., Figure 4.2). Clearly, as long as the streamer plasma is ignited before the arrow, the energy transfer efficiency to the plasma is at its maximum. The same behavior is seen for every value of λ_1 , i.e., even if this value is smaller than two. In other words, if the plasma ignites quickly, the ratio between τ and $Z_{\text{out}} \cdot C_r$ is not important.

Notice that the maximum efficiency is one hundred percent if the plasma is ignited early enough. This is obviously caused by the criterion selected for the efficiency calculation. In practice, the energy stored in C_r cannot be used completely for plasma generation, since the streamers quench if the voltage drops below a certain value. The remaining energy in C_r will not be dissipated in R_r and consequently, the efficiency drops. Obtaining complete energy transfer is only possible if the amount of energy stored in C_r is negligible compared to the total pulse energy.

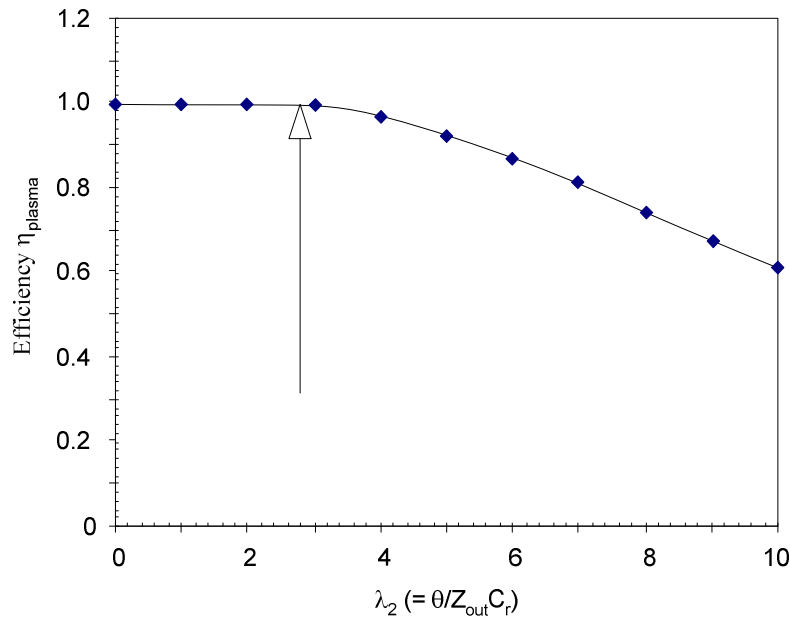


Figure 4.3. Energy transfer efficiency into the streamer plasma as function of the moment the streamers are generated. The example is for $\lambda_1 = 4$. The arrow indicates the moment the energy transfer efficiency to the reactor capacitance reaches its maximum (when no streamers are generated at all).

4.3 Energy transfer efficiency in the experimental situation, comparison with model

4.3.1 Before streamer generation

To determine if the derived model and equations are an accurate description, several experiments were performed. First, the voltage and energy transfer efficiencies before streamer plasma generation, (i.e., the results of Equations 4.3 - 4.5), were compared with experimental results (see Figure 4.4). For this measurement, no coupling capacitor and DC bias voltage were used. Also, the applied voltage was below corona onset, i.e., $\theta \rightarrow \infty$. The agreement is fairly good, in spite of the simplified model used to obtain the equations. For the presented example $\lambda_1 = 1$, i.e., $\lambda_1 < 2$. This implies that the maximum efficiency is not 0.97, but slightly lower (~ 0.90), see Figure 4.2b.

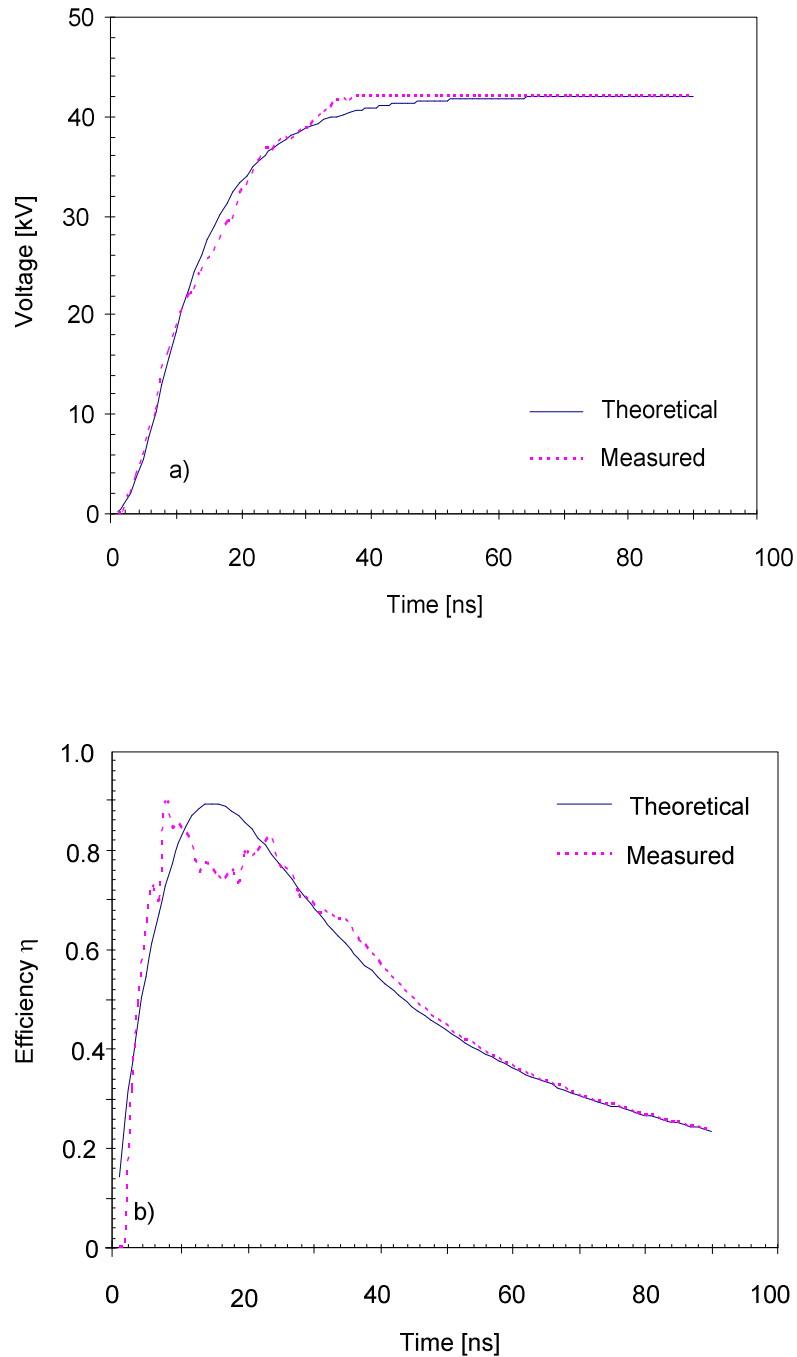


Figure 4.4. a) Calculated voltage waveform compared to measured voltage waveform. b) Energy transfer efficiency as calculated by Equation 4.5. For both plots: $C_T = 80$ pF, $C_{DC} = \infty$, $Z_{out} = 100 \Omega$, $\tau = 8$ ns, $V_0 = 20$ kV (below corona onset).

4.3.2 During streamer generation

4.3.2.1 Plasma impedance

In the model it was assumed that the impedance during plasma generation is purely resistive. The real situation is, however, more complicated. The experimental data on plasma impedance are analyzed in more detail to understand the situation. In Figure 4.5, a collection of data on the ratio of load voltage to current is presented. A typical voltage and current trace is shown in Figure 4.5a. The raw data from the ratio (voltage/current) are plotted in Figure 4.5b. The behavior is as follows: at the start the impedance is high and purely capacitive. As the voltage rises, the impedance drops rapidly. After the plasma ignites, the impedance decreases further to a minimum, with an intermediate rise due to the rising voltage. It reaches a rather constant level during the secondary streamer phase. After the plasma quenches, the impedance once more rises as the reactor becomes a capacitor again. To simplify the interpretation, the contribution of the capacitive reactor current is eliminated from the experimental data. The results in Figure 4.5c clearly reveal a constant impedance phase, a simplification made in the previously described model for the evaluation of the efficiency of plasma energization.

It is interesting to determine what mechanism is responsible for the transition into the constant value platform. By photographing the plasma at the moment the transition occurs, the following important observation was made. This moment always coincides with the moment the primary streamers reach the plate electrode. These moments have been indicated with cross markers in Figure 4.5c. For higher voltages the primary streamer velocity is higher and, as a result, the constant impedance regime is reached sooner. During the primary streamer duration the impedance thus gradually decreases, and the minimal impedance is reached at the end of the primary streamer transit. This automatically implies that if only primary streamers are generated, obtaining well matched systems is not possible. To determine the plasma resistance of the primary streamer, it is not only required to know I_{plasma} but also the voltage drop along the streamers. This voltage drop cannot be measured directly, but instead has to be derived from the length of the streamers and the applied voltage. A commonly used value for the electric field in the streamers, as found in several experimental and theoretical studies, is $5 \text{ kV}\cdot\text{cm}^{-1}$, for air-like mixtures. This so-called stability field E_{st} is the minimal field required for streamer propagation. If, however, the applied electric field is higher than E_{st} , the actual field in the streamer is likely to be higher than E_{st} . Several numerical studies showed that values of $10\text{-}15 \text{ kV}\cdot\text{cm}^{-1}$ are possible [Bab(1997), Pan(2003)]. In the present set-up the average electric field E_{ave} at the moment the primary streamers reach the plate electrode can be determined exactly. At that moment, the voltage across the reactor equals the voltage across the streamer and, since the length of the streamer is known, the average electric field can be calculated. To determine the voltage drop across the streamer at every position of the streamer head, before it reaches the plate electrode, the determined E_{ave} is multiplied by the distance traveled. It is assumed that the value for E_{ave} does not change during primary streamer transit. Values found for E_{ave} are

plotted in Figure 4.6. The average electric field $E_{ave, matched}$ that a matched load would have for the same voltage pulse (for applied V_{sg} , V_{DC} and wire-plate distance) is plotted along the horizontal axis. It can be seen that E_{ave} in the streamer channel does not depend on DC bias voltage and voltage rise rate but rather solely on the applied electric field. The obtained values are larger than the E_{st} values reported in a number of studies but are similar to those obtained in the previously mentioned numerical models.

A typical plasma resistance calculation, with E_{st} and E_{ave} values for this situation, is shown in Figure 4.5d. It can be seen that, when the average electric field E_{ave} shown in Figure 4.6 is used, the plasma resistance is constant throughout the complete voltage pulse. The resistance of primary and secondary streamers is equal. If the value for E_{st} from other studies is used to perform the calculations, the plasma resistance during the primary streamer phase is lower and increases stepwise at the moment the secondary streamer phase starts. Because of this step, it seems logical that this value for the stability field is not a convenient representation for the actual electric field in the streamer channel. However, it is known that at the moment the primary streamer reaches the plate electrode a sudden redistribution of the electric field in the channel can occur. The exact mechanisms for this redistribution are not clear at this moment. Although the exact primary streamer resistance cannot be determined, it can be concluded that it is comparable to the secondary streamer resistance. Nevertheless, even though the resistance of the primary streamers is low, matching can not be optimized during the primary streamer phase. This is caused by the fact that the modulator sees the complete impedance of the load, i.e., the resistance of the streamers plus the capacitance of the gap between the streamer heads and the plate electrode.

The constant resistance of the primary streamers during propagation coincides well with the observations that the ratio of the streamer length over its cross section is constant during propagation. Together with the constant resistance, this would imply that the resistivity of the channel does not change during propagation. For the example shown in Figure 4.5 (using E_{ave} to determine the voltage drop along the streamer) a typical resistivity of $8 \cdot 10^{-3} \Omega \cdot m$ can be calculated. Comparable resistivities were found for other pulse waveforms.

In Figure 4.7 the results of a large collection of impedance measurements is shown. The value of the constant resistance level as function of the applied voltage for various pulse conditions is plotted. As can be seen, independent of pulse width, pulse rise time and DC bias voltage, the plasma resistance tends to become equal to the output impedance of the source, for increasing total reactor voltage. Apparently, the plasma matches automatically to the source if sufficient voltage is applied. The same observation was made by *Yan*. The decreasing plasma resistance for increasing voltages must be caused by changes in plasma generation. A study of the ICCD pictures and the electrical waveforms indicated that for higher voltages the number of streamers increases. As the total plasma resistance is determined by the parallel connection of all the individual streamers, the observed decreasing plasma resistance can be understood. An explanation for why the plasma resistance remains constant once it is equal to the output impedance of the source, even if the voltage is increased further, cannot be provided at the moment.

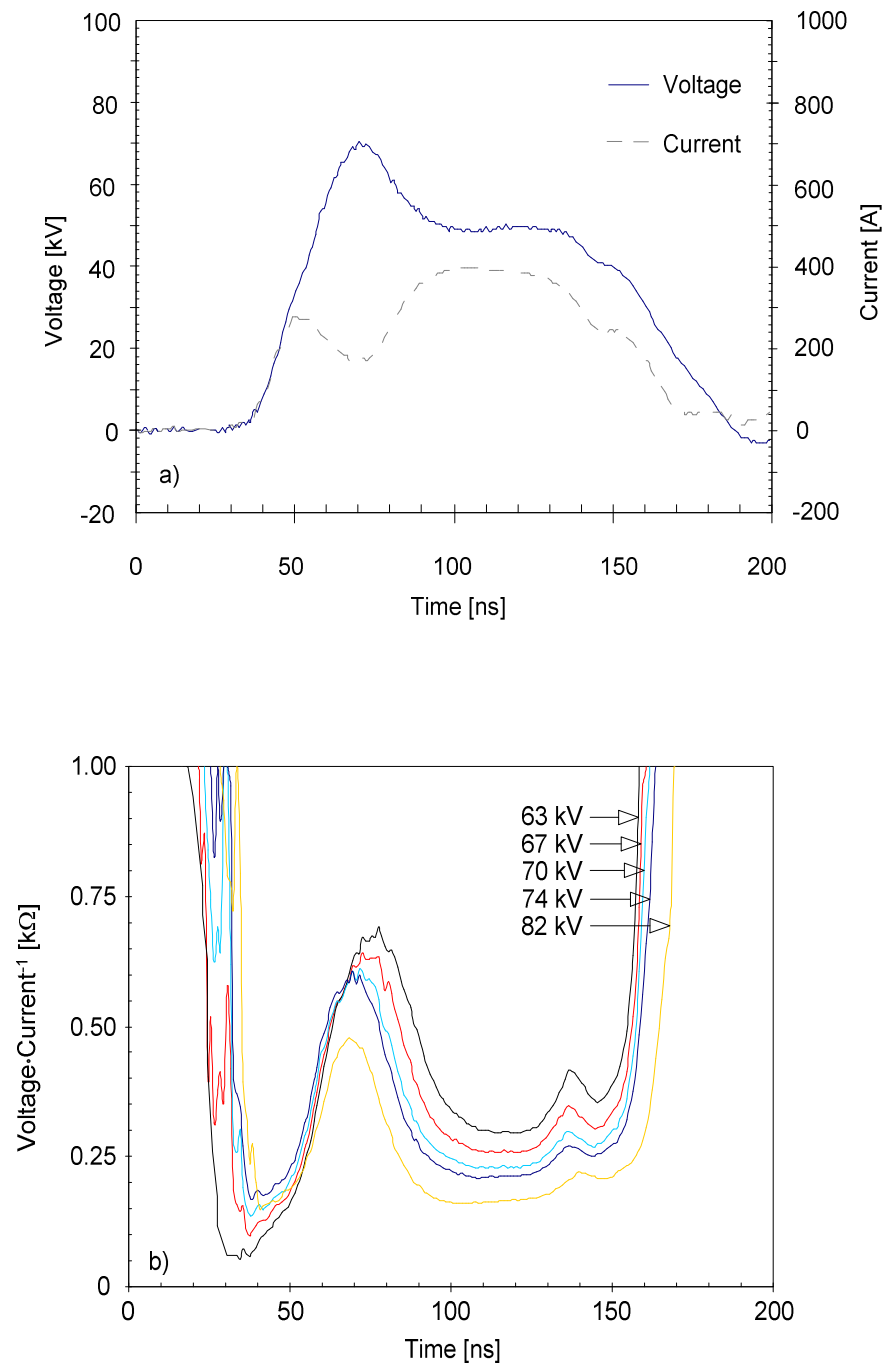


Figure 4.5. Calculations of the load impedance, with peak voltages as indicated. The pulse width was 110 ns for all shown results. a) Typical voltage and current waveform. b) Load impedance as determined by dividing the reactor voltage by the total current.

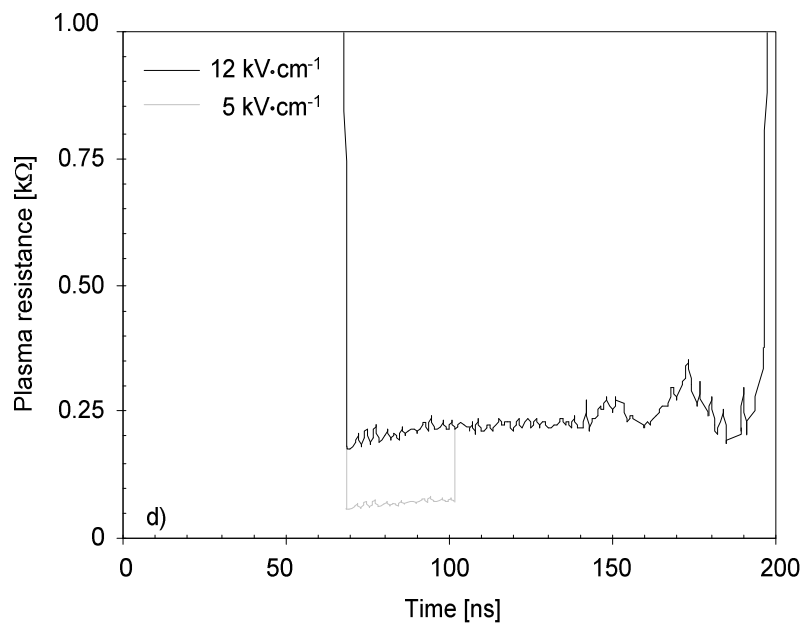
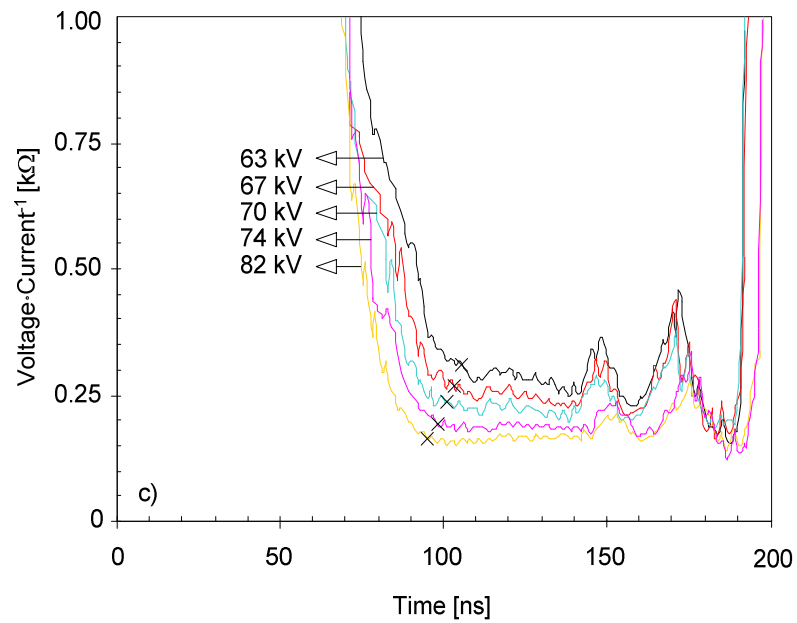


Figure 4.5 Continued. c) Load impedance when using the plasma current only. The crosses indicate the moment the primary streamers have crossed the reactor-gap. d) Plasma resistance calculated by dividing the voltage drop over the streamers by the plasma current. Peak voltage: 82 kV.

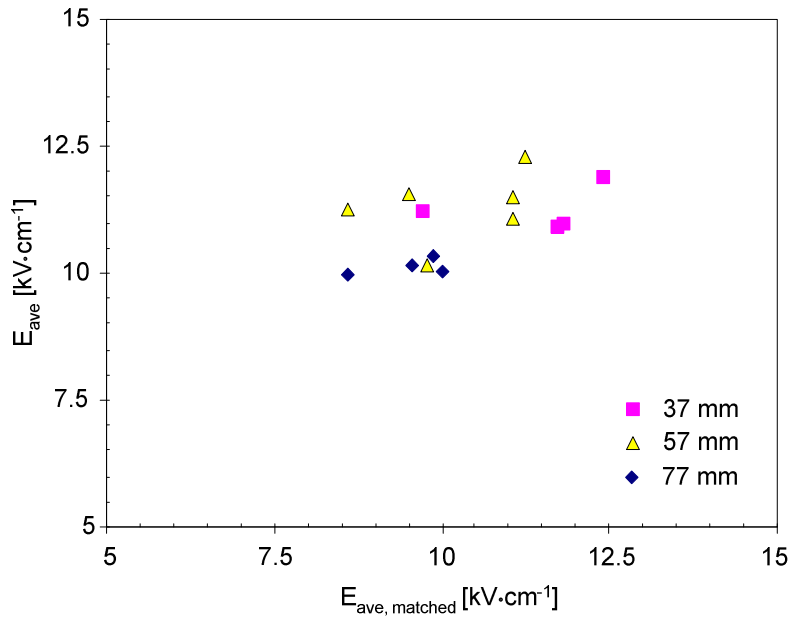


Figure 4.6. Average E-field in primary streamer at the moment it reaches the plate electrode. Markers are for pulse width: 100-200 ns, rise rate: $0.5\text{-}3.0 \text{ kV}\cdot\text{ns}^{-1}$ and DC bias voltage: 0-15 kV. Reactor configuration A, with different wire-plate distance (see legend), was used.

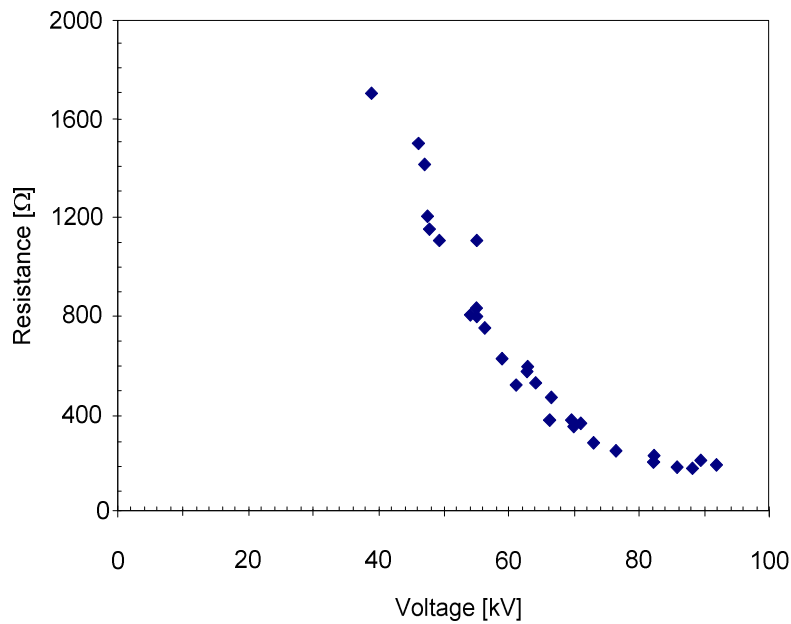


Figure 4.7. Plasma resistance as function of peak voltage. Markers are for pulse width: 100-200 ns, rise rate: $0.5\text{-}3.0 \text{ kV}\cdot\text{ns}^{-1}$ and DC bias voltage: 0-20 kV. Reactor configuration A was used.

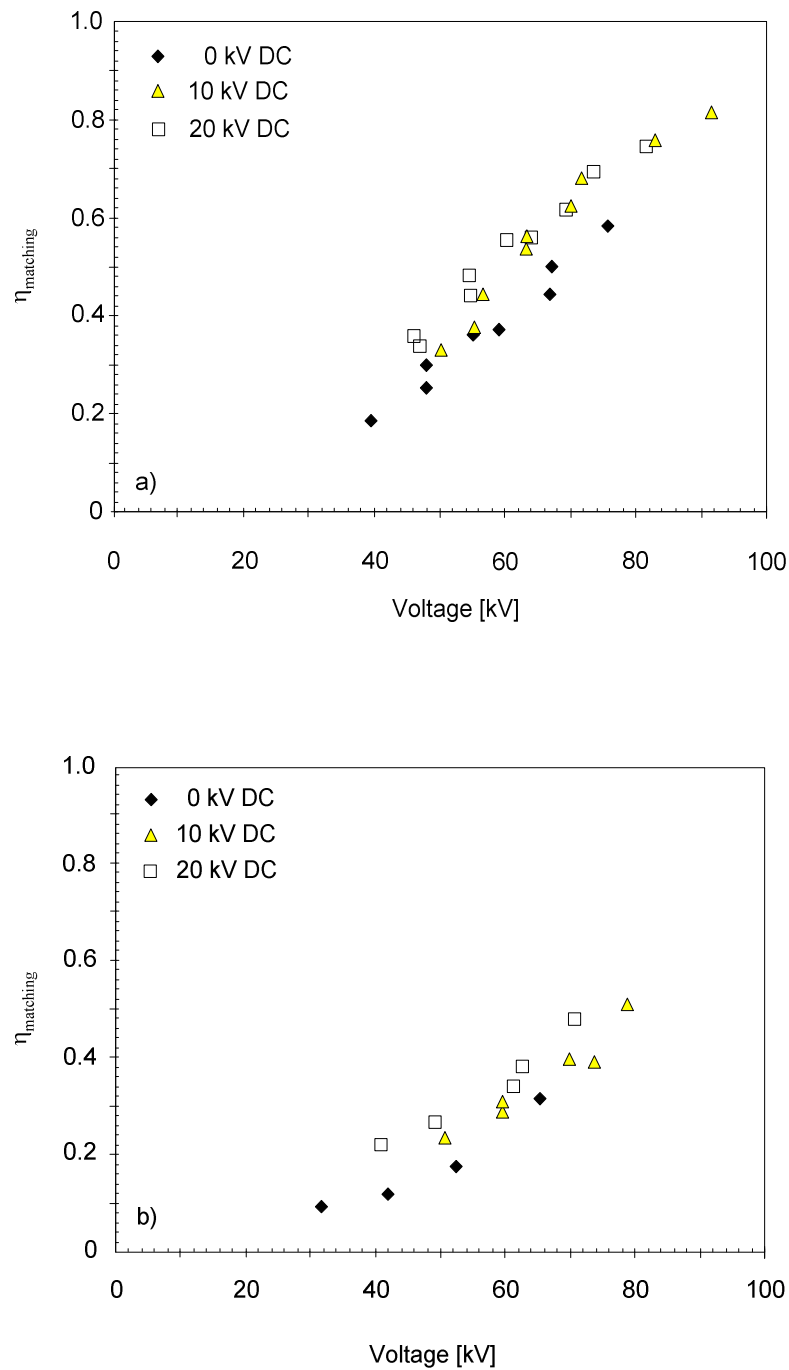


Figure 4.8. Energy transfer efficiency as function of reactor voltage. Measurements are for the exact same conditions as shown in Figure 4.7: rise rate: $0.5\text{-}3.0 \text{ kV}\cdot\text{ns}^{-1}$ and DC bias voltage: $0\text{-}20 \text{ kV}$. a) Pulse widths: $100\text{-}200 \text{ ns}$. b) Pulse widths: $40\text{-}70 \text{ ns}$.

4.3.2.2 Energy transfer efficiency

In the preceding section it was shown that the plasma resistance decreases towards the output impedance of the modulator and that the minimum resistance level is reached sooner if the applied voltage is increased. It seems logical that the energy transfer efficiency between modulator and load can be improved accordingly. This effect is demonstrated in Figure 4.8. The energy transfer efficiency was determined using Equation 4.10. In Figure 4.8a, the energy transfer efficiency as function of reactor voltage for the same data points as presented in Figure 4.7 is shown. The first overall conclusion is that the energy transfer efficiency increases with increasing voltage. It can also be observed that the DC bias has a separate effect, in that higher DC bias voltage values slightly enhance the efficiency. The reason for this increase is the result of the inequality as stated in Equation 4.8, since for increasing DC voltage, the left term of the inequality becomes larger and larger. Less energy is lost for negatively charging C_{DC} and the energy transfer efficiency increases.

Combining the results from the plots in Figure 4.7 and 4.8a, it can be concluded that the highest energy transfer efficiencies are obtained for those situations in which the plasma impedance is closest to the output impedance of the source. By comparing Figures 4.8a and 4.8b it can be seen that the energy transfer efficiency decreases if the pulse duration is reduced. This is caused by the following two effects:

- For short pulses, the time period of constant (minimum) plasma resistance decreases. This implies that the relative time (compared to the total pulse duration) the plasma is well matched to the source is reduced.
- During every pulse, the reactor capacitance C_r (~80 pF) must be charged. When the voltage is 80 kV, this results in 0.26 J. Not all of this energy is used for plasma generation since the streamers are quenched once the voltage is insufficient to maintain the channels. The remaining energy in C_r is then lost. This loss is a considerable portion of the available energy when the pulse width is short.

4.4 Energy transfer efficiency and reactor dimensions

The criteria for well matched systems depend on the reactor dimensions. There are several parameters which affect the matching.

- The applied field strength should be high, as the plasma resistance decreases for higher voltages. This can be accomplished by increasing the pulse voltage, by decreasing the wire-plate distance or by adding a DC bias voltage. The required maximum voltage depends on the reactor configuration.
- By decreasing the wire-plate distance, the energy transfer can be increased considerably, as shown in Figure 4.9. This increase is caused by two effects: firstly the average electric field increases when the wire-plate distance decreases. Higher fields result in decreased plasma resistance and hence improved matching. Secondly, for shorter distances, the primary streamer duration decreases. Therefore, the moment at which the resistance becomes constant is reduced, and the time the load is matched is increased.

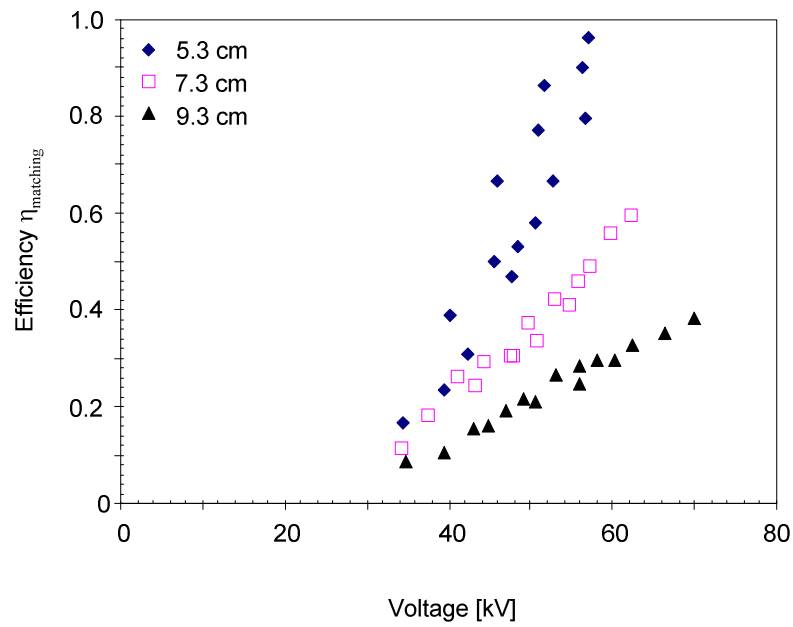


Figure 4.9. Energy transfer efficiency as function of wire-plate distance. Reactor configuration B was used with 7 wires. Pulse width: 100 ns.

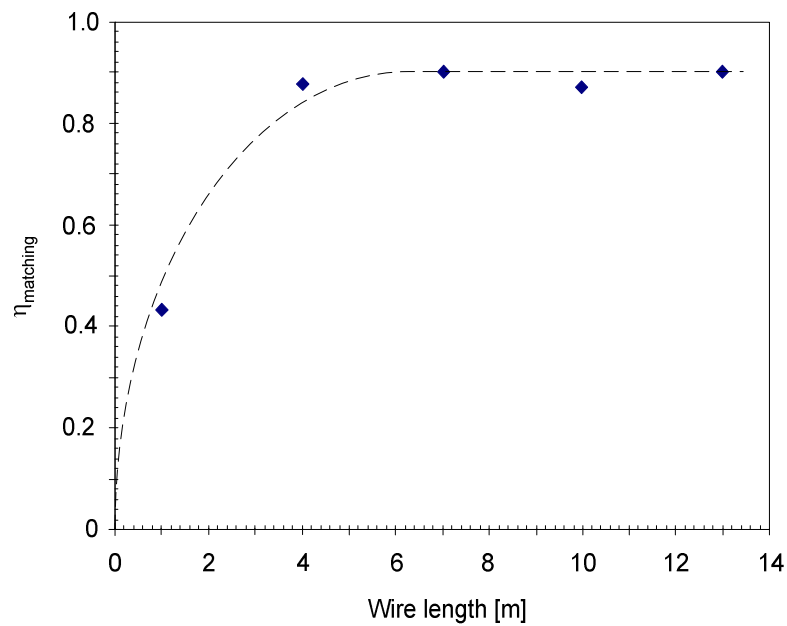


Figure 4.10. Energy transfer efficiency as function of reactor wire length. Reactor voltage was fixed at +61 kV ($V_{DC} = +15$ kV). Pulse widths of 100 ns were used; energy per pulse was 4 J. Wire-plate distance: 5.3 cm.

- The maximum amount of energy a plasma can dissipate per length of reactor wire is limited. In other words, for a specific energy dissipation, a minimum wire length is required. This is demonstrated in Figure 4.10. In reactor configuration B, the number of wires has been increased from 1 to 13. As can be seen, the energy transfer efficiency increases for increasing wire lengths, but stabilizes above a threshold.
- The wire radius (r_{wire}) determines the field (E_{wire}) near this wire, according to Equation 4.11. In this equation, d_{reactor} is the wire-plate distance.

$$E_{\text{wire}} = \frac{V/r_{\text{wire}}}{1 - r_{\text{wire}}/d_{\text{reactor}}} \cdot \frac{1}{\ln(2d_{\text{reactor}}/r_{\text{wire}})} \quad (\text{eq. 4.11})$$

The effect of h on E_{wire} is limited. E_{wire} decreases if the radius is enlarged. This decrease can have two effects. Firstly, the inception probability decreases and thus the streamers are ignited later [Bad(1972), Vel(2003)]. According to Figure 4.3, this can result in decreased energy transfer efficiencies. Secondly, as the inception field decreases, the generated plasma changes since streamer properties like the velocity are determined by the local electric field. As the matching depends on the characteristics of the generated plasma, changes as a result of the altered electric fields can be expected.

In Figure 4.11 it can be seen that for $E_{\text{wire}} < 7 \cdot 10^6 \text{ V}\cdot\text{m}^{-1}$ the energy transfer decreases drastically. This result indicates that the electric field at the wire is too low for efficient streamer generation. For $E_{\text{wire}} > 7 \cdot 10^6 \text{ V}\cdot\text{m}^{-1}$, the energy transfer efficiency only depends on the applied average field and the pulse duration. This finding can be used to determine the maximum wire radius for efficient energy transfer.

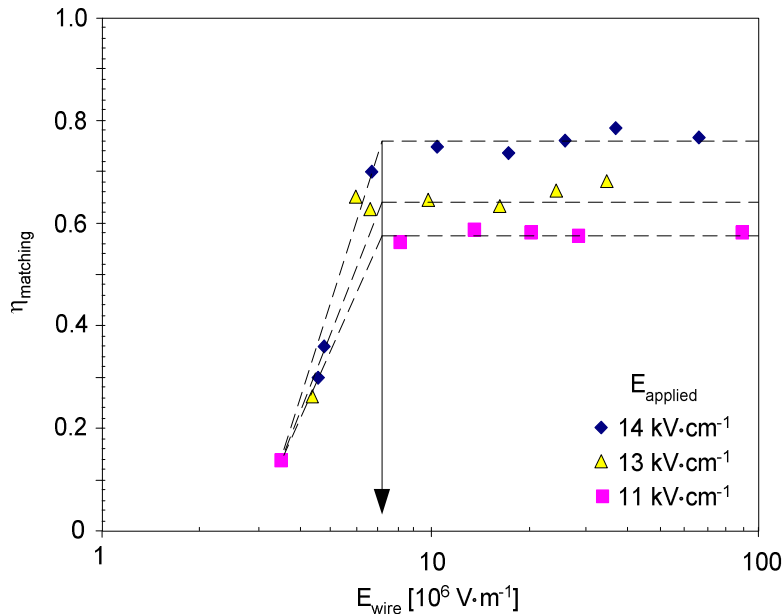


Figure 4.11. Energy transfer efficiency as function of electric field at the wire electrode, for various average electric fields (as a result of the applied voltage). Pulse width: 100 ns; rise rate: $2.8 \text{ kV}\cdot\text{ns}^{-1}$. Wire-plate distance: 5.7 cm.

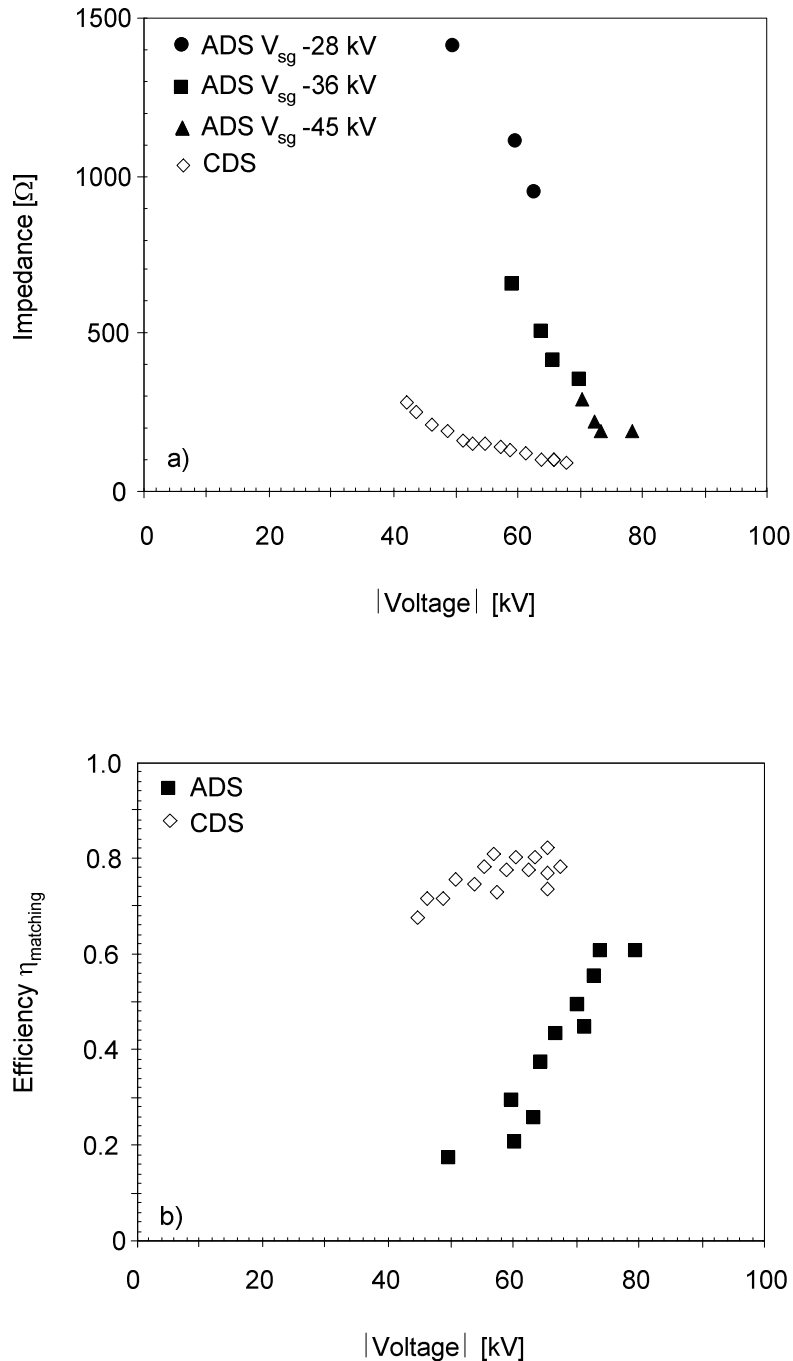


Figure 4.12. Comparison between positive and negative voltage polarity streamers. Reactor configuration A was used. The wire-plate distance was 3.7 cm. Pulse width was fixed at 100 ns. a) Impedance as function of the absolute value of the reactor peak voltage. For the negative polarity the rise-rate was fixed to 1.7-2.0 $\text{kV}\cdot\text{ns}^{-1}$. For the positive polarity rise times of 1.6-3.0 $\text{kV}\cdot\text{ns}^{-1}$ were used. Voltage was varied by varying DC level and charging voltage V_{sg} . b) Energy transfer efficiency for the same markers shown in a).

4.5 Energy transfer efficiency for negative polarity pulses

As is known from the literature, negative polarity streamers (ADS) require a higher electric field to develop than positive polarity streamers (CDS). This behavior is also shown in Figure 4.12a, where the plasma resistance as function of the voltage amplitude is plotted. All measurements were performed on reactor configuration A, with a wire-plate distance of 37 mm. For identical pulses having opposite polarity, the impedance is highest for the ADS. The corresponding energy transfer efficiencies are highest for CDS since for CDS the impedances are closest to the value as described by Equation 4.7. The differences, however, become smaller for higher voltages.

4.6 Conclusions

The modulator-load interaction was analyzed by distinguishing three different regimes: before, during and after streamer generation. From the proposed equivalent circuit, three criteria were derived that are necessary to obtain large energy transfer efficiencies. 1) The plasma should be ignited before the energy transfer to the reactor capacitance reaches its maximum value. 2) The generated plasma should have a resistance according to Equation 4.7. 3) The capacitors C_{DC} and C_h (of the PFL) and their charging voltages V_{DC} and V_{sg} should obey Equation 4.8. It was found that the first two criteria can be fulfilled by applying an electric field $>10\text{-}15\text{ kV}\cdot\text{cm}^{-1}$ for CDS and $>20\text{ kV}\cdot\text{cm}^{-1}$ for ADS. For high electric fields, the inception delay (criterion 1) is low as is the resulting plasma resistance (criterion 2). The minimum load resistance values are obtained during the secondary streamer phase, not during the primary streamer phase. Therefore, it is not possible to match the load to the modulator if only primary streamers are generated (i.e., short pulses and/or long wire-plate distances).

Measurements show that during the secondary streamer phase, the plasma resistance is constant. For increasing voltages, this resistance decreases until it becomes equal to the output impedance of the source. The resistance of the primary streamer was determined by estimating the voltage drop along the streamer, since the resistance value could not be obtained directly from experiments. By combining the results of the electrical measurements and the ICCD pictures, the average electric field of the primary streamer at the moment these streamers connect to the plate electrode was determined. The values obtained only depend on the applied electric field and are, in general, a factor of two larger than the stability field of $5\text{ kV}\cdot\text{cm}^{-1}$, as reported in the literature. To determine the voltage drop across the streamer at every position of the streamer head, the average electric field was multiplied by the distance traveled. By adopting this voltage drop, the plasma resistance could be determined and it was found that the plasma resistances of the primary and secondary streamer phase are equal.

As the plasma resistance is not only determined by the applied voltage but also by other pulse parameters and the reactor configuration, a series of measurements was performed to analyze a complete system. Those parameters that affect the matching for CDS are summarized in Table 4.1. For every parameter, the range in which they were varied during

the experiments is indicated, together with the effect on the matching. For every row in the table, all parameters, except the one mentioned, were kept constant. The reference case was: total applied voltage: 70 kV, pulse width: 100 ns, wire-plate distance: 5.7 cm, wire diameter: 0.4 mm and wire length: 0.9 m.

Table 4.1. Parameters that determine the energy transfer efficiency for CDS

Parameter	Range	To increase matching	Improvement in efficiency [fraction]
Total voltage	63-88 kV (DC 0-15 kV)	Increase	0.59-0.82
Pulse width	40-200 ns	Increase	0.42-0.84
Wire-plate distance [§]	5.3-9.3 cm	Decrease	0.30-0.95
E_{wire}	$> 10^7 \text{ V}\cdot\text{cm}^{-1}$		
Energy per wire length [§]	$< 1\text{-}4 \text{ J}\cdot\text{m}^{-1}$	Decrease	0.43-0.88

Compared to CDS, a well matched ADS system requires pulses with an amplitude that is approximately 50% higher. For the same voltage amplitude, the plasma resistance is higher for the ADS. With increasing voltage amplitude, the difference in matching between the polarities diminishes. Identical to the values shown in Table 4.1, those parameters that affect the matching for the ADS are summarized in Table 4.2. For the ADS, the reference case is: total applied voltage: -70 kV, pulse width: 50 ns, wire-plate distance: 3.7 cm, wire diameter: 0.4 mm and wire length: 0.9 m.

Table 4.2. Parameters that determine the energy transfer efficiency for ADS

Parameter	Range	To increase matching	Improvement in efficiency [fraction]
Total voltage	60-76 kV (DC 0-18 kV)	Increase	0.33-0.60
Pulse-width	50-100 ns	Increase	0.46-0.50
Wire-plate distance	n/a	Decrease	n/a
E_{wire}	n/a	Decrease	n/a
Energy per wire-length	n/a	Increase	n/a

When proper care is taken with regard to system design and the reactor is matched to the power modulator, a large energy transfer efficiency from energy storage capacitor into the plasma can be obtained. A maximum transfer efficiency of 95% has been obtained during the measurements.

[§] This result was obtained using reactor configuration B. Instead of a total voltage of 70 kV, the indicated results are for a total voltage of 60 kV. The other parameters are as for the reference case.

5 Matching the pulsed power system and the radical production process*

In the literature it is often assumed or derived from experimental data that primary streamers are more efficient for radical production than secondary streamers. This assumption is based on the average electron energy in primary streamers being higher due to higher local electric fields. To investigate the validity of this reasoning a series of experiments was performed. It also has to be investigated whether the radical production yield of primary and secondary streamers can be varied. Nair [Nai(2004)] suggested that: “once primary streamer formation is achieved, then further improvement related to energy consumption can only be achieved by controlling radical interactions”. This statement would imply that the radical yield of primary streamers is the same for every arbitrary primary streamer, independent of how they are generated. Here it will be shown that the radical yield of primary streamers is determined by the pulse shape and the reactor configuration. Measurements are presented and discussed that link the pulse parameters and reactor configuration to the O^ radical yield (amount of O^* radicals produced per unit of dissipated energy). ICCD pictures are used to obtain insight into the changes in the generated plasma that are responsible for the observed difference in the yield.*

5.1 Parameters that do not affect the O^* radical yield

Before the results are presented, several parameters, which were varied during the experiments but that did not change the O^* radical yield, are discussed.

- *Pulse repetition rate (prf)*. In Figure 3.14 it was shown that, in the experimental range, the pulse repetition rate does not have an effect on the yield. Measurements performed at different pulse repetition rates can be compared without the need for additional corrections.
- *DC bias voltage*. In Figure 5.1a a typical example of the O^* radical yield as function of the total reactor voltage for various DC voltages is plotted. Clearly, there is no separate effect of the DC bias voltage on the yield. This observation has been made for all measurements. The mechanism responsible for the decrease in yield for increasing total voltage will be discussed in Section 5.2.2.
- *Reactor wire length*. This parameter was varied to study the effect of the energy per pulse per meter on the O^* radical yield. Changes in the yield were not observed, as demonstrated by the example shown in Figure 5.1b.

* Parts of this chapter have already been presented in *Win(2006a, b)*.

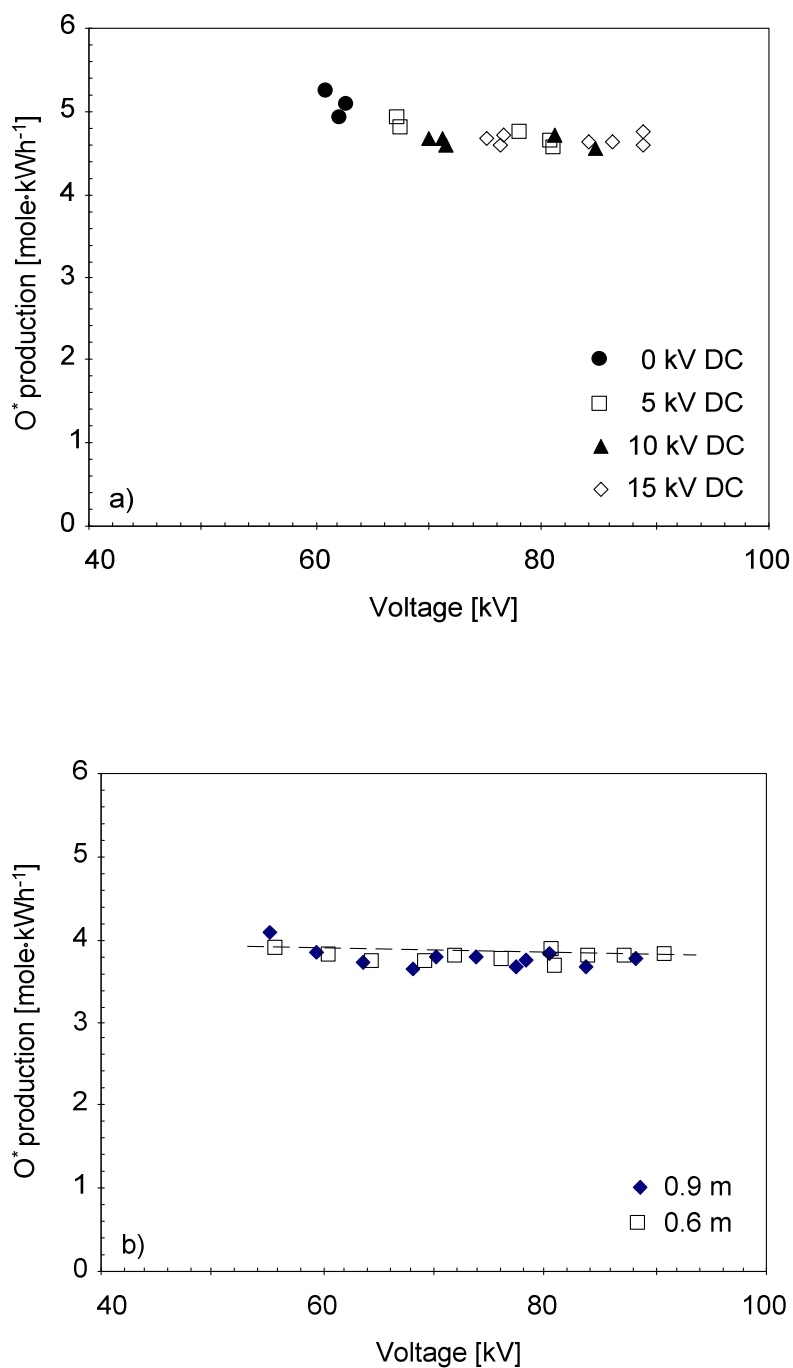


Figure 5.1. a) O^* radical yield as function of reactor voltage. Pulse width: 50 ns, rise rate: 2.3-2.9 kV·ns⁻¹. Energy cost: 7.1-8.2 eV·molecule⁻¹. b) O^* radical yield as function of total voltage and reactor wire length. Pulse width: 100 ns, rise rate 2.3-2.9 kV·ns⁻¹. Energy cost: 9.2-10.7 eV·molecule⁻¹

5.2 Radical yield of cathode directed streamers (CDS)

This section will describe cathode directed streamers only. For all measurements, reactor configuration A was used with the following conditions inside the reactor: airflow: $30 \text{ Nm}^3\cdot\text{h}^{-1}$, RH: 13-18%, temperature: 20-24 °C. Unless stated otherwise, the wire-plate distance, wire length and wire diameter were 57 mm, 0.9 m and 0.4 mm respectively.

First, the effect of the primary streamer duration on the radical production yield is discussed. To facilitate the discussion the following ratio is introduced:

$$R_{\text{primary}} = \frac{T_{\text{primary}}}{T_{\text{pulse}}} \quad (\text{eq. 5.1})$$

where T_{pulse} is the full width at half maximum (FWHM) of the current pulse, corrected for the capacitive current, and T_{primary} is the time the primary streamers need to cross the reactor gap. This latter value can be determined from ICCD pictures. When R_{primary} equals one, the situation arises that the voltage pulse ends at the moment the primary streamers reach the plate electrode. For $R_{\text{primary}} < 1$, part of the pulse energy is dissipated in the secondary streamers. If $R_{\text{primary}} > 1$, the time required for the primary streamers to cross the reactor gap exceeds the pulse duration. In this case the primary streamers stop propagating at a position in between the electrodes because the voltage is zero.

If primary streamers are indeed more efficient for the radical yield, then, in a plot of the yield versus R_{primary} , the maximum should be obtained for $R_{\text{primary}} \geq 1$. There are several mechanisms that can be used to vary R_{primary} :

- T_{pulse} can be varied by changing the length of the PFL.
- T_{primary} can be varied by changing the distance the primary streamer has to travel.
- T_{primary} can be varied by changing the primary streamer velocity.

The first two options can be performed easily by changing modulator and reactor parameters. Controlling the streamer velocity is not straightforward. Below, it will be shown that this can be accomplished by adjusting the pulse rise rate and the amplitude of the applied voltage. In the following two sub-sections, results obtained for the mechanisms described will be presented. The changes in T_{primary} are treated simultaneously. Afterwards, in Section 5.2.3, the results of variations in T_{pulse} and T_{primary} will be combined to obtain O^* radical yield versus R_{primary} plots. Using these plots it will be shown that the O^* radical yield of primary streamers exceeds that of secondary streamers and that the yield of primary streamers is determined by the pulse shape. The conditions required for efficient radical production are then derived.

5.2.1 Effect of T_{pulse} on the O^* radical yield

As it was found that, for the employed wire-plate distances and applied voltages, the transit time of the primary streamers is in the order of several tens of nanoseconds, a pulse width range from 30 to 250 ns was chosen. Shorter pulses were not used since the energy per pulse became too low to be able to perform accurate measurements. Longer pulses were considered unnecessary since the maximum of the yield vs. $R_{primary}$ curve will be near to $R_{primary} = 1$. For long pulses, however, $R_{primary}$ tends to decrease.

Figure 5.2 shows the O^* radical yield as function of the applied voltage for various pulse widths. From these yields, the energy costs to produce an O^* radical can be determined[†]. The lowest yields obtained ($3.0 \text{ mole}\cdot\text{kWh}^{-1}$) are not shown in this figure. Several observations can be made when studying the figure.

Firstly, it can be seen that the chemical efficiency of the plasma can be varied by a factor of ~ 2 by adjusting power modulator settings. An O^* radical yield of $7.0 \text{ mole}\cdot\text{kWh}^{-1}$ could be reached. Even more, the trend of the triangle shaped markers (pulse width 30 ns) does not show any saturation for lower voltages, indicating that higher yields can possibly be obtained. A yield of $7.0 \text{ mole}\cdot\text{kWh}^{-1}$ corresponds to an energy cost of $5.3 \text{ eV}\cdot\text{molecule}^{-1}$. According to literature, the theoretical minimal cost to produce an O^* radical is 3 eV (see Section 2.5.1). The obtained results thus show that more than half of the available energy is used to produce O^* radicals, i.e., the yield of the plasma is excellent. Secondly, the shortest pulses are most efficient for O^* radical production. In Section 5.2.3 it will be shown that this finding can be explained by the reduced radical yield of secondary streamers. Finally, for the short pulses, the yield decreases for increasing voltages. As will be explained in Section 5.2.2, this is caused by the increased primary streamer velocity for higher voltages, i.e., increased contribution from the secondary streamers, which are not as efficient for radical production as primary streamers.

5.2.2 Effect of $T_{primary}$ on O^* radical yield

The two mechanisms for changing $T_{primary}$ (changing primary streamer velocity or changing wire-plate distance) are treated simultaneously since there is a strong correlation between them. From ICCD pictures, the primary streamer velocity can be determined, and as a result $T_{primary}$ can be calculated. The obtained value, however, can only be used as an estimate, since not all primary streamers reach the plate electrode simultaneously (as a result of non-uniform reactor geometry). Figure 5.3 shows the primary streamer velocity as a function of various parameters. It can be seen that the primary streamer velocity increases when: the wire-plate distance is decreased, the applied voltage is increased, or the rise rate is increased.

[†] $X \text{ mole}\cdot\text{kWh}^{-1} = 37.3 / X \text{ eV}\cdot\text{molecule}^{-1}$.

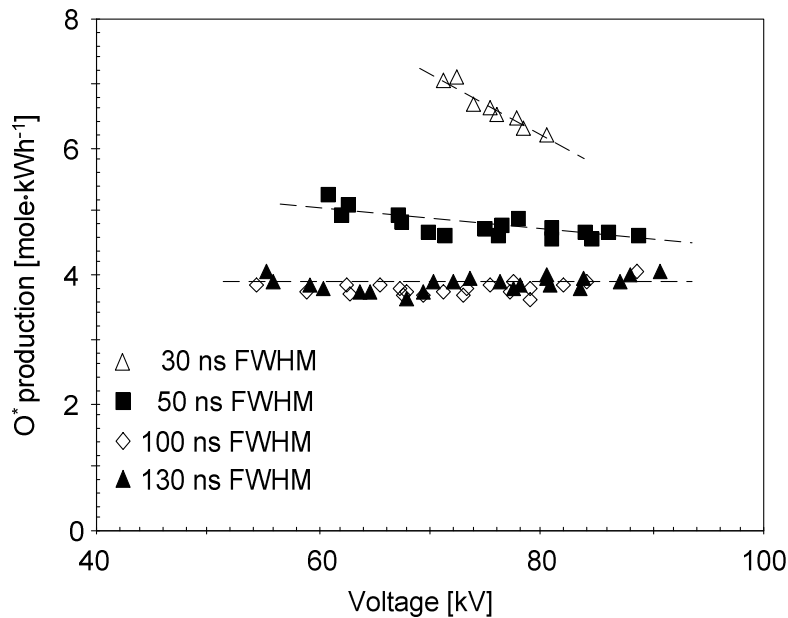


Figure 5.2. O^* radical yield as function of voltage and pulse width. The rise rate of the pulses was fixed $2.2\text{-}2.7\text{ kV}\cdot\text{ns}^{-1}$. DC bias: $0\text{-}20\text{ kV}$. a) Effect of the pulse width. Energy costs ranging from $5.3\text{-}10.5\text{ eV}\cdot\text{molecule}^{-1}$.

The observation that the velocity increases upon increasing the applied voltage or decreasing the wire-plate distance is also reported in the literature [Blo(1997), Cre(1994), Ono(2003a), Tar(2002), Vel(2002), Won(2002)]. The increased velocity indicates that the applied average electric field in the gap is of importance to the streamer propagation velocity. The relation between the electric field and the primary streamer velocity has been discussed in Chapter 2.

An explanation for the increased streamer velocity as function of the voltage rise rate can be provided by considering the moment of plasma ignition. Streamers generated during slow rise rate pulses are created before the maximum voltage is reached, so in fact they are created at lower voltages than indicated in Figure 5.3. The voltage is still increasing towards the maximum during the first stages of streamer propagation. As shown in Figure 5.3b, lower voltages result in lower velocities.

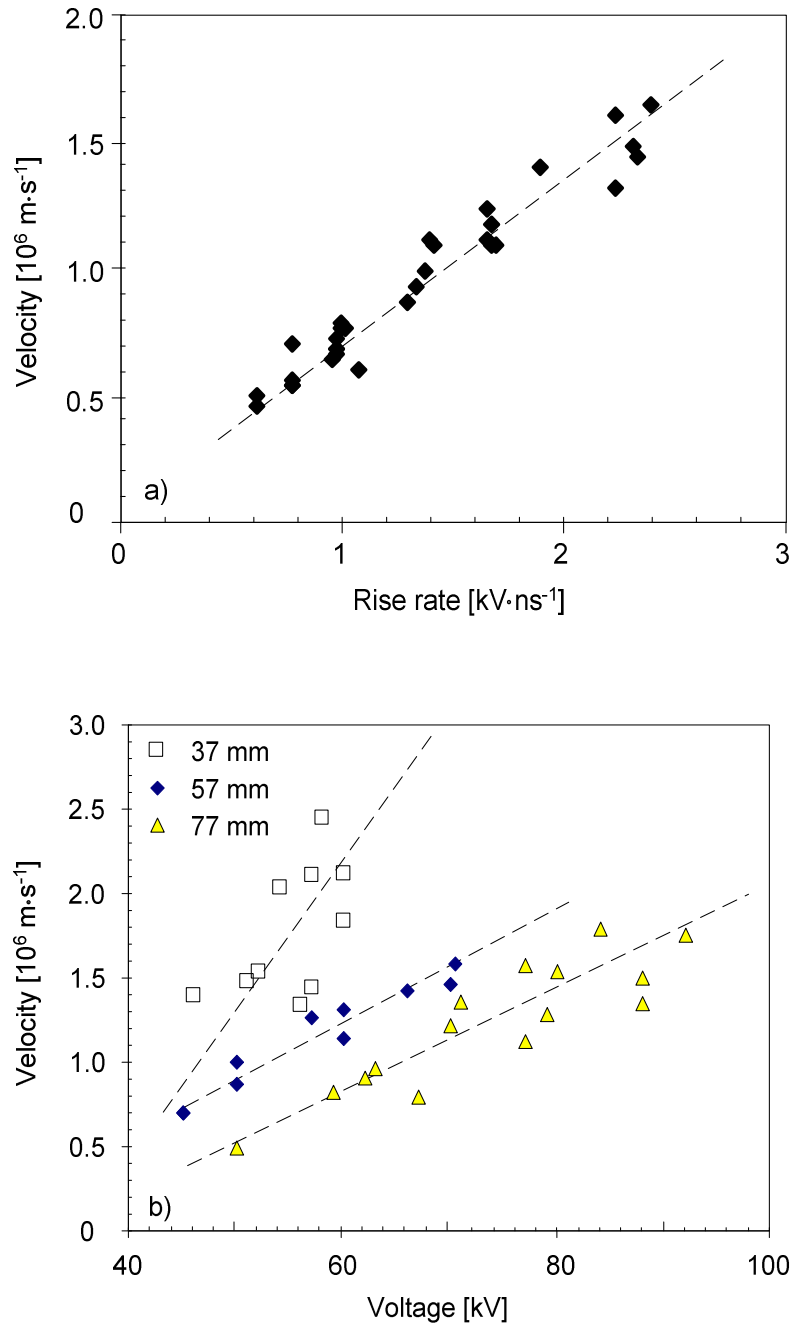


Figure 5.3. Primary streamer velocity in a wire-plate reactor. Results for pulse widths between 30 and 250 ns are shown. a) Wire-plate distance fixed at 57 mm. Peak voltage: 60-70 kV. b) Voltage rise rate fixed at 1.8-2.2 $\text{kV}\cdot\text{ns}^{-1}$.

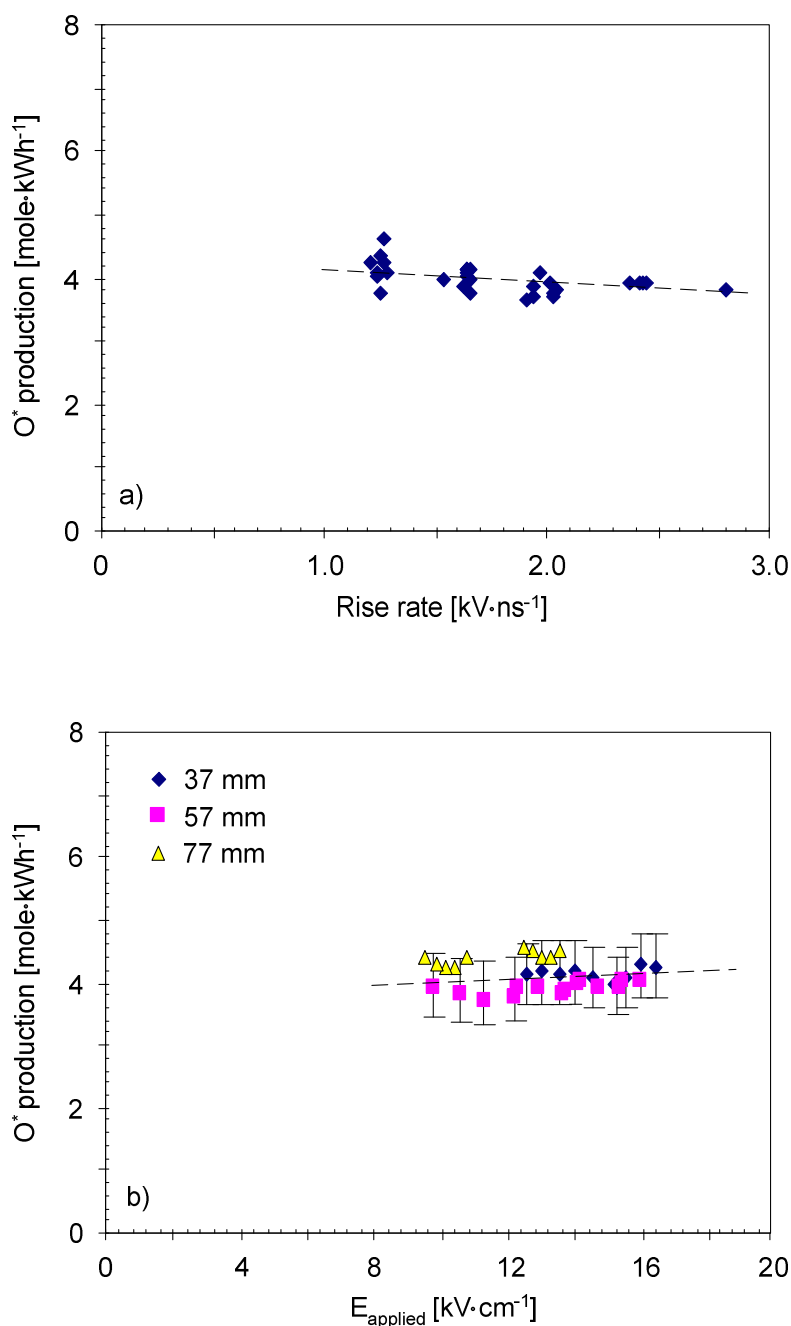


Figure 5.4. a) Effect of the rise rate on the O^* radical yield. The rise rate was varied by changing the reactor voltage and the value of L_{add} . Pulse width: 80 ns, peak voltage: 60-70 kV. Energy costs ranging from 7.9 to 10.1 eV·molecule⁻¹. b) Effect of average electric field on the O^* radical yield. Rise rate: 1.8-2.5 kV·ns⁻¹, pulse width: 100 ns. Energy costs \sim 9.3 eV·molecule⁻¹. The error bars are based upon the calculations discussed in Chapter 2. The different markers correspond to the wire-plate distance.

If the velocity of the primary streamers is increased and the pulse width is fixed, the value of R_{primary} decreases, i.e., an increasing portion of the energy is dissipated by the secondary streamers. Based on the results shown in Figure 5.2 it is therefore expected that the O^* radical yield decreases if the primary streamer velocity is increased. However, the results in Figure 5.4 show that if the rise rate and/or the voltage is increased (i.e., primary streamer velocity is increased), the O^* radical yield does not decrease but remains constant. These results can be explained if the O^* radical yield of the streamers increases when the velocity increases. In Section 5.2.3 it will be shown that this is indeed the case. The increased velocity results in higher O^* radical yields, however, the decreased yield as a result of the decreased value of R_{primary} counterbalances the net production. If short pulses (< 100 ns, $R_{\text{primary}} \rightarrow 1$) are used, the increased yield as a result of increased primary streamer velocities does not completely counterbalance the decreased yield as a result of decreased values of R_{primary} . The net result is that the O^* radical yield decreases if the primary streamer velocity is increased; see, for example, the data for the short pulses in Figure 5.2. For short pulses, the primary streamer duration is the dominant contribution to the complete streamer generation. Changes in R_{primary} then immediately cause variations in the yield, which are not completely counterbalanced by the changes as a result of the velocity.

The obtained results can be compared with values reported in the literature. *Fuj(2006)*, *Nam(2000)* and *Rou(1996)* found the same relation between pulse width and radical yield, although their results are not expressed in terms of R_{primary} and the primary streamer velocity. *Fujiwara* [*Fuj(2006)*] also found that the yield increases if the applied voltage is decreased. The results of the short pulses presented in Figure 5.2 are in agreement with this finding. *Ono* and *Oda* [*Ono(2004)*] used laser induced fluorescence (LIF) to determine the location, in the streamer volume, where ozone is produced. By comparing the results of the LIF measurements with ICCD pictures of the discharges, *Ono* and *Oda* argue that ozone is produced most efficiently in the secondary streamer. In the next section it will be demonstrated that this is definitely not the case. It is believed that the apparent disagreement is the result of the experimental procedure used by *Ono* and *Oda* to determine the yield. They used the ozone concentration directly as basis for the discussion, i.e., the actual O^* radical concentration is not determined. Also, the ratio of the energies dissipated in the primary and secondary streamer is determined indirectly: the amount of light emitted by the discharge was used as a measure for this ratio.

5.2.3 Coherent system of parameters that determine the O^* radical yield for CDS

The results presented in the preceding sections indicate that the radical yield of primary streamers exceeds that of secondary streamers. This observation can be quantified by plotting the radical yield as a function of R_{primary} . In Figure 5.5 the results for primary streamer velocities in the range $1.5\text{-}1.7 \cdot 10^6 \text{ m}\cdot\text{s}^{-1}$ are shown. It can be seen that, for fixed primary streamer velocity, the yield is only determined by R_{primary} . The pulse width and wire-plate distance do not have a separate effect. The highest yields are obtained for values of R_{primary} closest to one. The increase of the yield as a function of R_{primary} is linear.

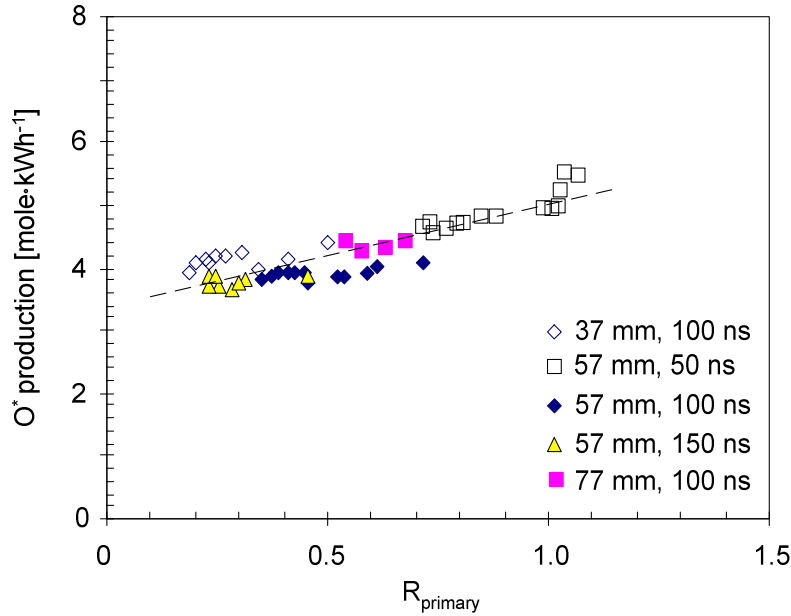


Figure 5.5. O^* radical yield as a function of R_{primary} . The results for different wire-plate distances and pulse widths are shown. Results for primary streamer velocities in the range $1.5\text{-}1.7 \cdot 10^6 \text{ m}\cdot\text{s}^{-1}$.

This result indicates that the radical yield η_{radical} can be modeled as:

$$\eta_{\text{radical}} = R_{\text{primary}} \cdot Y_{\text{primary}} + (1 - R_{\text{primary}}) \cdot Y_{\text{secondary}} \quad (\text{eq. 5.2})$$

where Y_{primary} and $Y_{\text{secondary}}$ are the O^* radical yield of the primary and secondary streamer respectively. In general, these yields will be a function of several plasma parameters.

Figure 5.6a shows that, besides R_{primary} , the primary streamer velocity also has a large effect on the yield. The highest yields are obtained for fast primary streamers. The differences between primary and secondary streamers (i.e., the effect of R_{primary} on the yield) diminish if the velocity decreases.

Figure 5.6b shows the yield as function of the primary streamer velocity. Since it was shown that the value for R_{primary} has a large effect on the yield, a distinction for several regimes of R_{primary} was made. Some clear relations can be found. For a fixed value of R_{primary} , the yield increases linearly with the streamer velocity. Although this velocity can be varied in different ways, the effect on the yield only depends on the streamer velocity. The results show that, to obtain the highest yields, not only should secondary streamers be avoided, but also the velocity of the primary streamers should be as large as possible. If the primary streamer velocity decreases, so does the difference between the primary and secondary streamer radical yield.

To determine the radical yield of primary and secondary streamers separately, the markers as shown in Figure 5.6 must be plotted in a graph of the yield versus R_{primary} for a fixed primary streamer velocity. Then, using Equation 5.2 to fit a straight line through the experimental data, the values for Y_{primary} and $Y_{\text{secondary}}$ can be obtained. Since the measured streamer velocities are continuously distributed (i.e., multiple measurements with exactly the same streamer velocity are rare), the fit had to be made using small velocity intervals. Using a boxcar averaging procedure on basis of the successive intervals, the plot shown in Figure 5.7 can be produced. Only a few error bars (indicating the standard deviation) have been plotted for clarity. This figure shows important findings for the CDS:

- Primary streamers are more efficient for radical production than secondary streamers. The yield of primary streamers is more than twice as large as that of the secondary streamers if the primary streamer velocity is high ($2.0 \cdot 10^6 \text{ m}\cdot\text{s}^{-1}$).
- The radical yield of the primary streamers increases with the primary streamer velocity $v_{s, \text{primary}}$. For velocities above $2.0 \cdot 10^6 \text{ m}\cdot\text{s}^{-1}$, Y_{primary} starts to decrease.
- The yield of the secondary streamers is constant, regardless of the primary streamer velocity (i.e., the applied voltage and rise rate). In Section 5.3.3 it will be shown that the $Y_{\text{secondary}}$ of ADS increases with primary streamer velocity and is significantly higher than the $Y_{\text{secondary}}$ of CDS.

It is not straightforward to explain the relation between Y_{primary} and the primary streamer velocity. As was discussed in Chapter 2, it is assumed that an increased velocity indicates that the local electric field is larger as well. Consequently, the average electron energy is higher. This effect would explain the higher radical yield for increased primary streamer velocities, since the probability that an electron has an energy in excess of the dissociation threshold increases if the average electron energy is increased. If the average electron energy becomes too high, the O^* radical yield starts to decrease again since, according to *Bra(1991)*, the electrons gain so much energy that, instead of dissociating, they prefer to ionize the molecules. This would explain why Y_{primary} decreases for velocities exceeding $2.0 \cdot 10^6 \text{ m}\cdot\text{s}^{-1}$.

Another aspect that must be taken into account in the explanation of the results shown in Figure 5.7 is the following. The radical yield is determined by the product of the number of electrons and the probability that an electron can dissociate a molecule. In other words, the number of free electrons *together* with the electric field distribution must be known to be able to establish a foundation for the observed relation between the streamer velocity and the radical yield. As these data are not available, a well founded explanation for the relation between Y_{primary} and $v_{s, \text{primary}}$ cannot be provided. Nevertheless, according to Figure 5.3, high amplitude, fast-rising pulses should be used to create primary streamers with a high propagation velocity, since these streamers are efficient from a radical production perspective.

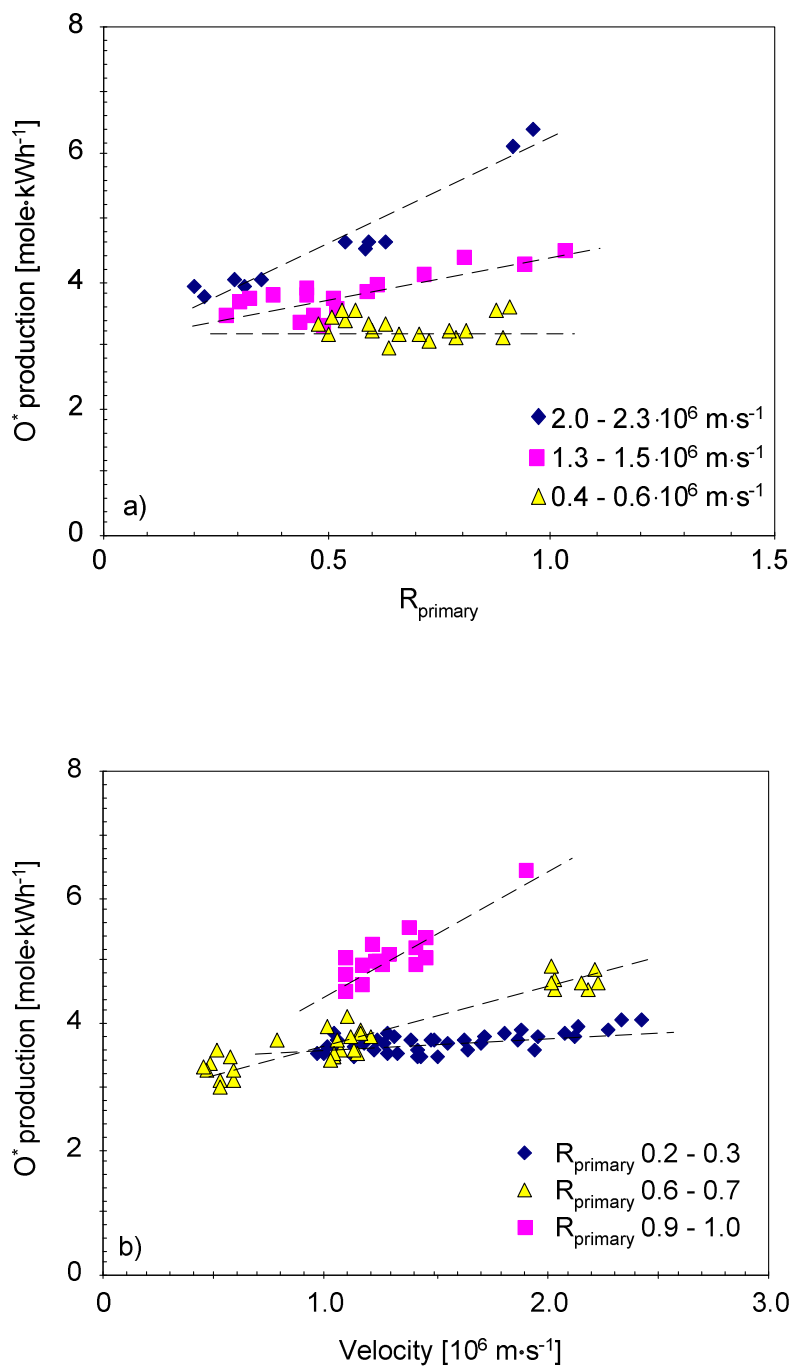


Figure 5.6. O^* radical yield as function of the primary streamer velocity and R_{primary} . Energy costs ranging from 5.7 to 12.4 eV·molecule⁻¹.

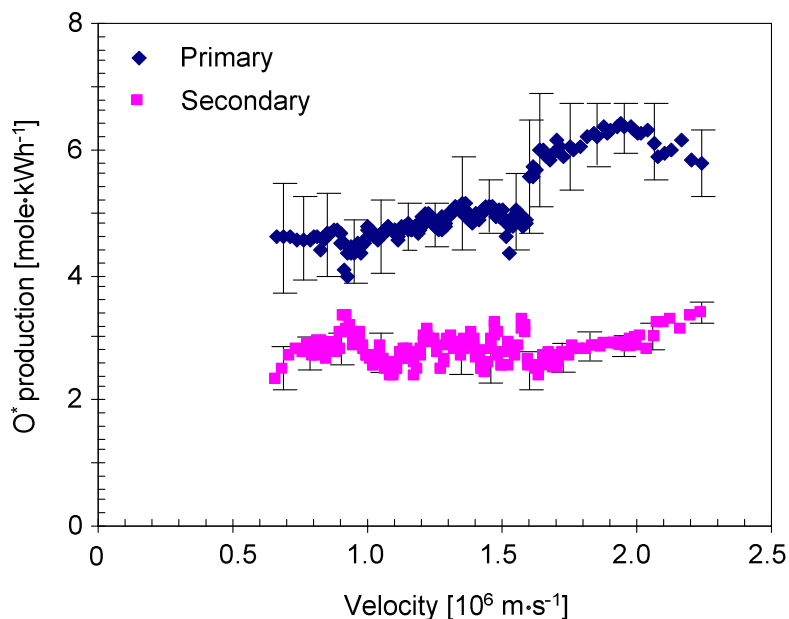


Figure 5.7. O^* radical yield for primary and secondary cathode directed streamers as a function of the primary streamer velocity. The error bars indicate the standard deviation. Results below $0.7 \cdot 10^6 \text{ m}\cdot\text{s}^{-1}$ are not shown, since there was too little measurement data available in this range.

5.3 O^* radical yield of anode directed streamers (ADS) and the comparison to the cathode directed streamers (CDS)

In this section, the O^* radical yield of anode directed streamers will be discussed and compared to that of cathode directed streamers. The presented results (both ADS and CDS) have been obtained on reactor configuration A with a wire-plate distance of 37 mm. During the measurements it was observed that for negative polarity the sensitivity regarding the wire position is high if the applied voltage is low. Misalignment of the wire in the order of a millimeter is enough to result in visual changes to streamer density at opposite sides of the wire. For positive polarity this effect is far less. For the ADS, due to difficulties related to matching (see Figure 4.12) only pulses could be used that resulted in a relatively long secondary streamer phase duration (the low-resistance phase). As a result, R_{primary} values are limited to 0.2-0.5 (see Section 5.3.3).

5.3.1 The effect of T_{pulse} on the O^* radical yield

The value of R_{primary} was varied by changing the pulse width of the applied voltage pulse, i.e., T_{pulse} . Figure 5.8 shows the O^* radical yield as a function of the applied voltage for several pulse widths. The absolute value of the voltage has been plotted, as this simplifies the comparison with the CDS measurements. Since the variation in R_{primary} is limited and the jitter in the measurements is quite large, a separate effect of the pulse width on the radical

yield cannot be observed. However, it will be shown in Section 5.3.3 that the yield increases slightly if the primary streamer phase duration is enlarged relative to the complete discharge duration, i.e., if the pulse width is reduced. Opposite to the situation for CDS, for ADS the O^* radical yield increases for increasing voltages. This observation can be understood when one considers that the duration of the primary streamer phase has an insignificant effect on the production yield. Although the increased streamer velocity does reduce the value of R_{primary} , there is no significant effect on the yield. As will be shown in Section 5.3.2, the primary streamer velocity is enhanced for higher voltages, i.e., identical to the behavior for the CDS. The increase in yield indicates that an increased primary streamer velocity also results in an enhanced yield for the ADS. Another observation is that the yield saturates towards $\sim 8 \text{ mole}\cdot\text{kWh}^{-1}$; this is comparable to the maximum obtained for the CDS.

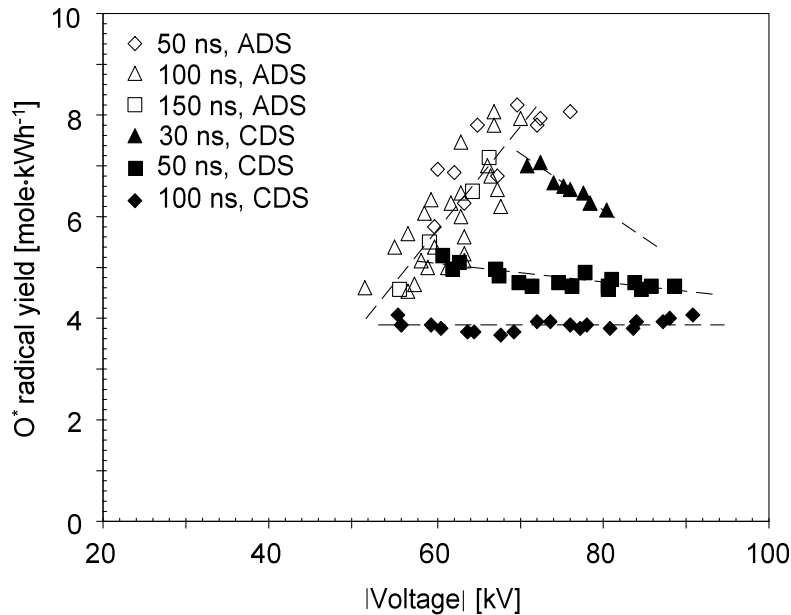


Figure 5.8. O^* radical yield as function of the absolute value of the applied voltage. Rise rates: $2.2\text{-}2.7 \text{ kV}\cdot\text{ns}^{-1}$. The results for CDS are obtained on reactor configuration A with a wire-plate distance of 57 mm.

5.3.2 Effect of T_{primary} on the O^* radical yield

For the ADS, T_{primary} could only be varied by changing the primary streamer velocity. The wire-plate distance could not be enlarged as this resulted in extremely low matching between the modulator and the reactor. Decreasing the wire-plate distance resulted in excessive breakdowns. Figure 5.9 shows the primary streamer velocity as function of the voltage rise rate and the applied voltage. Again, a comparison with the CDS is made. The velocity of positive streamers is slightly larger than that of negative streamers, although the differences are small. Figure 5.10 shows the yield as function of the voltage rise rate and the applied voltage. Here only results for the ADS have been shown. A higher rise rate or applied voltage results in improved yields.

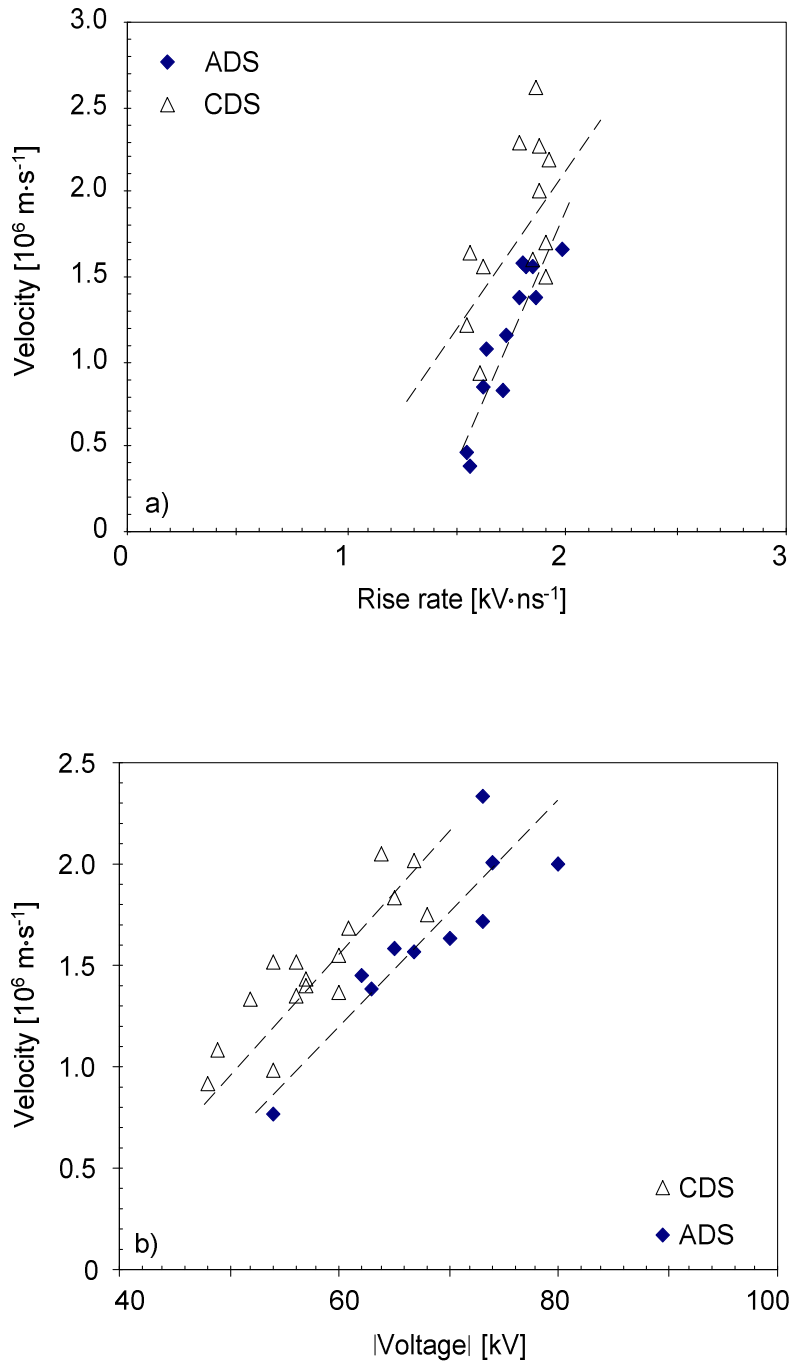


Figure 5.9. Comparison of the primary streamer velocity of the ADS and CDS. a) As function of rise rate. Peak voltages: 55-65 kV. b) As function of applied voltage. Rise rates: 1.6-1.7 $\text{kV}\cdot\text{ns}^{-1}$.

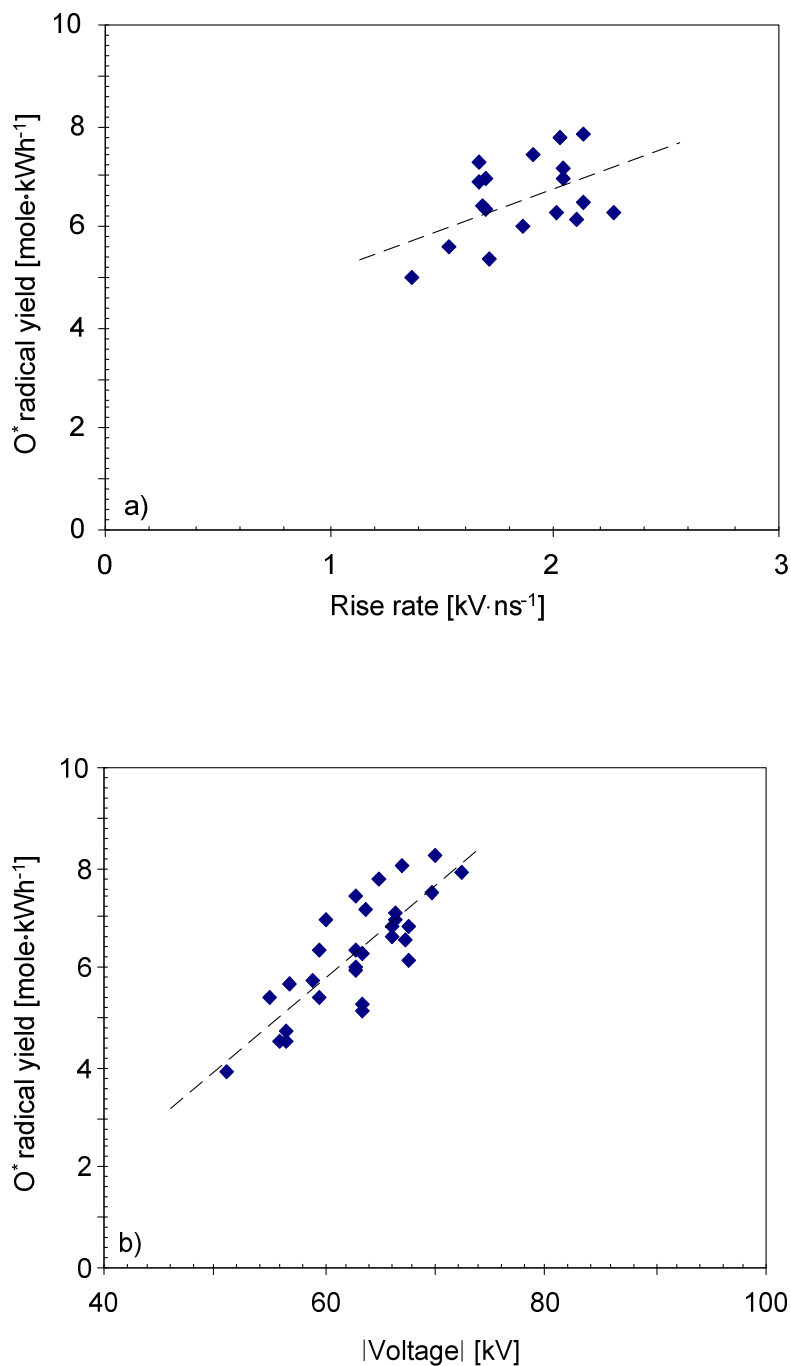


Figure 5.10. a) O* radical yield as function of the voltage rise rate for ADS. The rise rate was varied by changing the reactor voltage and the value of L_{add} . All other parameters were kept constant. Peak voltage: (-)60 – (-)70 kV. b) O* radical yield as function of applied voltage. Rise rate fixed at 1.7-2.0 kV·ns⁻¹.

Combining the results from Figures 5.9 and 5.10 it can be concluded that the O^* radical yield increases if the primary streamer velocity is enlarged. This relation is identical to that made for the CDS.

5.3.3 Coherent system of parameters that determine the O^* radical yield for ADS

For ADS, the same data analysis procedure as used for CDS can be followed to obtain the O^* radical yield of primary and secondary streamers separately, as a function of the primary streamer velocity. First, the O^* radical yield as function of R_{primary} and the primary streamer velocity is determined. Typical results are shown in Figure 5.11. By using Equation 5.2 to obtain a linear fit, Y_{primary} and $Y_{\text{secondary}}$ can be determined. However, from Figure 5.11 it can already be concluded that the inaccuracy of the evaluations is large: 1) The R_{primary} range is limited to 0.2-0.5. When extrapolating the results to $R_{\text{primary}} = 1$ (to determine Y_{primary}) we have to accept a considerable error. 2) The number of data points per velocity interval is limited. 3) The jitter in the measurements is large compared to the results for the CDS.

In Figure 5.12 the results for ADS Y_{primary} and $Y_{\text{secondary}}$ are shown. Only results for primary streamer velocity above $1.2 \cdot 10^6 \text{ m} \cdot \text{s}^{-1}$ are shown, mainly because too little data was available below this velocity. Also the results for the CDS are shown. Some interesting conclusions can be made based upon the results:

- Similar to the Y_{primary} of CDS, the Y_{primary} of ADS is also a function of the primary streamer velocity. In contrast to the $Y_{\text{secondary}}$ of CDS, the $Y_{\text{secondary}}$ of ADS is not constant. Instead, it is a function of the primary streamer velocity.
- For CDS and ADS, Y_{primary} exceeds $Y_{\text{secondary}}$. This difference is assumed to be caused by the large local electric field (and consequently large average electron energy) in the primary streamer-head compared to the field in the secondary streamer channel.
- The ADS Y_{primary} and $Y_{\text{secondary}}$ exceed those of the CDS. A discussion concerning the radical yields of secondary streamers is presented in Section 5.4. An explanation for the different Y_{primary} of CDS and ADS can possibly be found by considering that during the experiments the average applied electric fields for ADS always exceeded those for CDS ($15\text{-}20 \text{ kV} \cdot \text{cm}^{-1}$ vs. $8\text{-}15 \text{ kV} \cdot \text{cm}^{-1}$). However, since both the local electric field and the electron density are unknown, no well founded explanation can be provided.

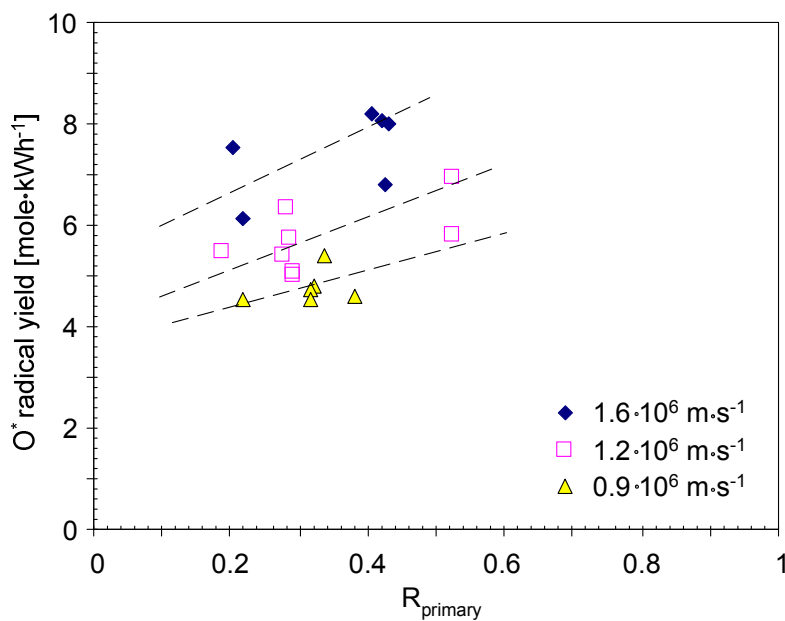


Figure 5.11. Effect of R_{primary} and the primary streamer velocity on the O^* radical yield.

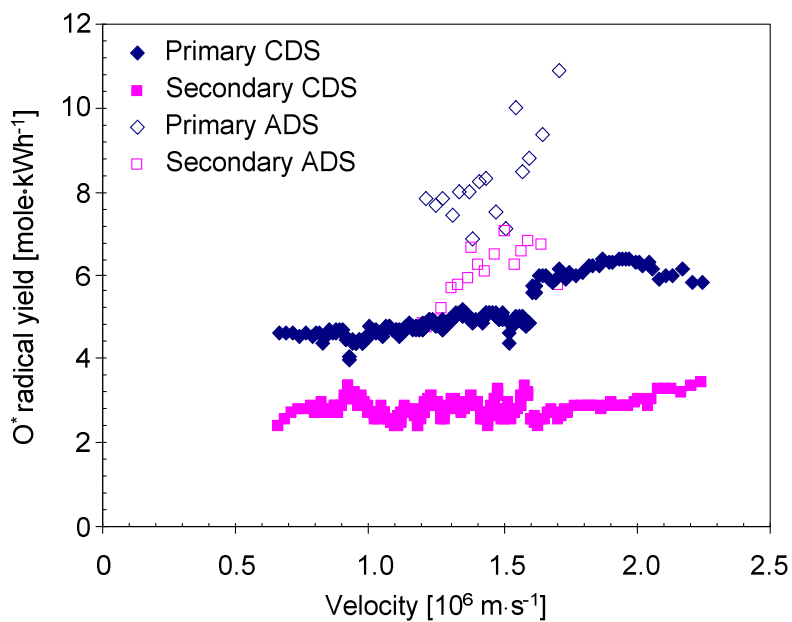


Figure 5.12. O^* radical yield of primary and secondary streamers as function of the primary streamer velocity. Results for ADS and CDS.

5.4 O* radical production by secondary streamers

In the secondary streamer, the electric field is low (see Section 5.4.1) and consequently so is the average electron energy. The probability that an electron becomes sufficiently energetic to dissociate an oxygen molecule is low. Despite the low average electron energy, a considerable amount of O* radicals is produced during the secondary streamer phase (both ADS and CDS). There are two possible explanations for this relatively high yield:

- As already discussed in Section 5.2.3, the radical yield is not only determined by the average electron energy but also by the number of free electrons. If the number of free electrons in secondary streamers is large compared to the number of electrons in the primary streamer head, a considerable amount of radicals can still be produced, despite the relatively low energy of the electrons.
- Secondary streamers are generated in the residue of the primary streamer channel. During the primary streamer transit, metastables are produced. To dissociate metastables, less energy is required (compared to dissociation from the ground-state molecule). In other words, due to the presence of metastables, the average energy required to dissociate molecules decreases.

The high radical yield of secondary ADS compared to the yield of secondary CDS cannot be explained at this moment. The following two remarks can be made however. 1) It seems unlikely that the differences are caused by a higher number of free electrons in ADS since the plasma current of secondary ADS is lower than the plasma current of secondary CDS (see also Figure 4.12) for identical pulses having opposite polarity. A lower plasma current indicates a lower number of free electrons per unit-length of streamer. 2) The differences cannot be explained by considering the electron energy since it will be shown below that the electric field (and hence the average electron energy) in ADS and CDS secondary streamers are comparable.

5.4.1 Electric field in secondary streamers

The statement that the average electric field in the secondary streamer channel is low, can be discussed by using the theory as it was presented in a paper authored by *Sigmond* [Sig(1983)]. The situation for the CDS was discussed; however, here the theory has been tentatively applied to the ADS as well. As was discussed in Chapter 2, according to *Sigmond*, the secondary streamer is a residual plasma channel consisting of two stable parts. Near the wire, a 'high' field region will form with a reduced electric field[‡] of ~ 110 Td, i.e., $27.5 \text{ kV}\cdot\text{cm}^{-1}$. This region will protrude a certain distance k (in cm) into the gap (length d_{reactor} , in cm). In the remainder ($d_{\text{reactor}} - k$) of the gap a 'low' field region will form. The

[‡] The mentioned values are taken from *Sig(1983)* and are based upon available collision data. The values depend on gas composition and in this case only apply to air.

field in this region is in the order of 20 Td, i.e., $5 \text{ kV}\cdot\text{cm}^{-1}$. The length k is determined by the voltage V (in kV) across the gap in such a way that:

$$k \cdot 27.5 + (d_{\text{reactor}} - k) \cdot 6.0 = V \quad (\text{eq. 5.3})$$

Since the values of d_{reactor} and V are known and k can be determined from the ICCD pictures, the validity of this equation can be investigated. As can be seen in Figures 3.16 and 3.17, the secondary streamers are formed almost instantaneously at the moment the primary streamers reach the plate electrode. The length of the secondary streamers varies little with time as long as the applied voltage is constant. For this discussion, the maximum length of the streamers has been used, with the corresponding reactor voltage at that time. Results are shown in Figure 5.13. The length of the secondary streamers has been plotted versus the average applied electric field. The length is expressed as the fraction of the total gap length, i.e., k/d . Several interesting features can be observed when studying this figure. Firstly, the length for ADS is much larger than that for CDS. This is a result of the high voltages required to generate ADS. When the voltage is increased even further, the secondary streamers cross the reactor gap completely. During the measurements this always resulted in complete breakdown. Secondly, the length of the secondary streamer is determined by the average electric field alone. This is as predicted by Equation 5.3.

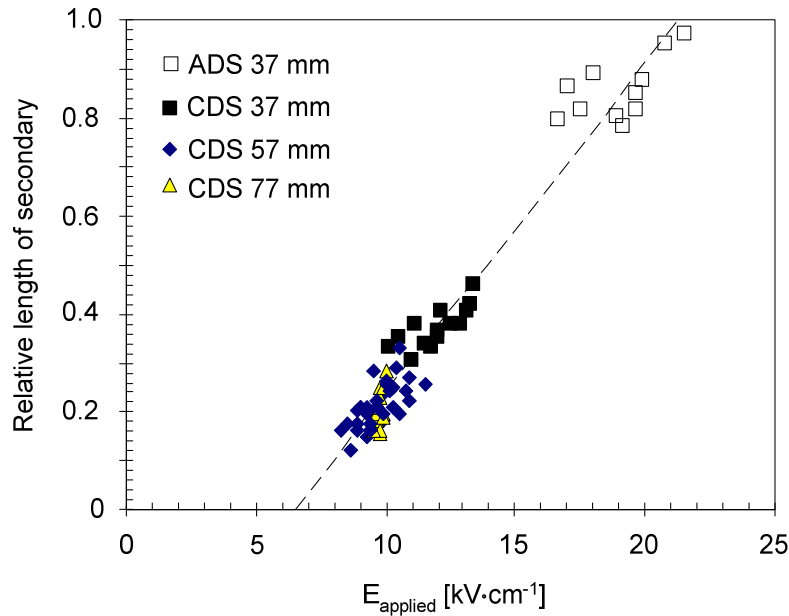


Figure 5.13. Length of the secondary streamer as function of the average applied electric field. For the positive polarity, different wire-plate distances were used (see legend). The line is the theoretical prediction of Equation 5.2. Rise rates: $0.5\text{-}3.0 \text{ kV}\cdot\text{ns}^{-1}$, DC bias: $0\text{-}20 \text{ kV}$.

The line is the result of application of Equation 5.3. The constants that had to be used to obtain a good match between theory and experiment are: $21.5 \text{ kV}\cdot\text{cm}^{-1}$ and $6.5 \text{ kV}\cdot\text{cm}^{-1}$ for the high- and low-field region, respectively (least squares linear fit). It can be seen that the values for the high- and low-field are identical for the CDS and ADS. The obtained values are comparable to those as mentioned by *Sigmond*.

At electric fields of $21.5 \text{ kV}\cdot\text{cm}^{-1}$ the average electron energy is $\sim 2 \text{ eV}$ [Bra(1991)], indicating that electrons with sufficient energy to dissociate an oxygen molecule are a minority (as mentioned in Section 5.4).

5.5 O* radical production versus ozone production

Up until now the discussion has focused on the O* radical yield. It is, however, interesting to look at the ozone yields as well. The general trends as observed for the radical yield also apply to the ozone production. For CDS, the yield of primary streamer outperforms that of the secondary streamer. The yield increases if the primary streamer velocity is increased. For ADS, there is no significant difference between primary and secondary streamer radical yields and, again, the yield increases for increasing primary streamer velocities.

Only a part of the produced O* radicals is used to generate ozone molecules. The main losses are due to the humidity and the high species concentrations in the streamer volume. If dry air is used, considerably higher ozone production yields can be obtained.

Typical ozone yields of $40\text{-}104 \text{ g}\cdot\text{kWh}^{-1}$ and $70\text{-}101 \text{ g}\cdot\text{kWh}^{-1}$ have been obtained for CDS and ADS respectively. These values are high when considering the fact that humid ambient air was used. Similar ozone yields have been obtained in *Bra(1991)*, *Gra(2006)* and *Sam(2000)* for example, although often a small, dry air flow was used. In many other publications [e.g., *Nam(2001)*, *Ono(2004)*, *Šim(2002)*] lower yields have been obtained, comparable to industrial ozonizers: $20\text{-}60 \text{ g}\cdot\text{kWh}^{-1}$. Compared to DBD systems, the pulsed plasma system performs with equal or better efficiency.

5.6 Conclusions

For CDS and ADS, typical O* radical yields were found to be in the range of $3\text{-}8 \text{ mole}\cdot\text{kWh}^{-1}$. The radical yield of primary and secondary streamers, both CDS and ADS, were determined separately.

CDS: primary versus secondary streamer

For CDS, it was found that the O* radical yield of primary streamers exceeds that of secondary streamers (up to a factor of two). The observed differences are contributed to the large electric field in the primary streamer head compared to the field in the secondary streamer. As a result of the high field, the average electron energy will be high as well. The probability that an electron can dissociate a molecule is consequently large.

For primary streamer velocities up to $2.0 \cdot 10^6 \text{ m}\cdot\text{s}^{-1}$ it was observed that the yield of primary streamers is, in principal, a rising function of the velocity. Above $2.0 \cdot 10^6 \text{ m}\cdot\text{s}^{-1}$, the yield starts to decrease again. As was discussed, a well founded explanation for the relation between Y_{primary} and $v_{s, \text{primary}}$ cannot be provided. Both the number of free electrons and the electron energy distribution function have to be known to determine the radical yield. Neither of these parameters were determined during the experiments. The secondary streamer yield was found to be constant.

ADS: primary versus secondary streamer

The observations for the ADS are identical to the ones mentioned above for the CDS: primary streamers outperform secondary streamers and the primary streamer O^* radical yield increases with streamer velocity. In contrast to the situation for CDS, for ADS it was observed that the yield of secondary streamers also increases with the primary streamer velocity. However, as a result of the analytic procedure and the large jitter in the experimental data, the error on these (ADS) results is considerable.

CDS secondary versus ADS secondary streamer

The O^* radical yield of ADS secondary streamers is considerably higher than the yield of the CDS secondary streamers. An explanation could not be provided. However, it was determined that the electric field in the secondary streamers is $22 \text{ kV}\cdot\text{cm}^{-1}$ and does not depend on the voltage polarity. As a result, the differences in yield cannot be explained by differences in the average electron energy. Also, it is unlikely that the number of free electrons in ADS is higher than in CDS, since the plasma current of ADS is lower (for identical pulses having opposite polarity). A lower current indicates a lower number of free electrons per unit-length of streamers.

The yield of ADS secondary streamers was found to be near that of the CDS primary streamers. This finding clearly demonstrates that even though the average electron energy is low, a considerable amount of radicals can still be produced.

CDS primary streamer versus ADS primary streamer

The ADS primary streamer has a significantly higher O^* radical yield than the CDS primary streamer. An explanation for the different Y_{primary} of CDS and ADS can possibly be found when considering that during the experiments the average applied electric fields for ADS always exceeded those for CDS ($15\text{-}20 \text{ kV}\cdot\text{cm}^{-1}$ vs. $8\text{-}15 \text{ kV}\cdot\text{cm}^{-1}$). Other possible explanations include:

- The observed difference is a result of the inaccuracy on the results of the ADS.
- The local electric field in the primary streamer head is highest for the ADS.
- The number of free electrons in the primary streamer head is highest for the ADS.

6 Optimizing the total energy transfer efficiency of the pulsed plasma system

In Chapters 4 and 5 mechanisms were described that can be used to optimize the energy transfer efficiency from the power modulator to plasma generation, and from plasma generation to radical production, separately. The results can be used to determine the total system efficiency. To develop an energy efficient streamer plasma system, not only is it important that the energy dissipated in the plasma is used efficiently for radical production, but also that a maximum amount of the energy the pulse modulator can deliver is used by the plasma. In this chapter the results presented in Chapters 4 and 5 will be combined in order to obtain the total system yield. Design guidelines for systems with high energy conversion efficiency are derived from the presented discussion.

6.1 Combining matching results with radical yield

The total yield η_{system} (amount of O^* radicals produced per unit of energy input from the power grid connection) of the pulsed corona system is determined by the efficiency of the individual steps shown in Figure 1.3. Methods to optimize the second and third step have been presented in Chapters 4 and 5 respectively. The efficiency of the first step was determined in *Yan(2001)* to be approximately 95%. In this thesis the fourth step, improving the chemistry, is not taken into account. The value of η_{system} [$\text{mole}\cdot\text{kWh}^{-1}$] is given by:

$$\eta_{\text{system}} = \eta_{\text{conversion}} \cdot \eta_{\text{matching}} \cdot \eta_{\text{radical}} \quad (\text{eq. 6.1})$$

where $\eta_{\text{conversion}}$ [fraction], η_{matching} [fraction] and η_{radical} [$\text{mole}\cdot\text{kWh}^{-1}$] are the charging efficiency of the PFL (step 1), the matching efficiency (step 2) and the radical yield (step 3) respectively. In this chapter a distinction between CDS and ADS plasmas will be made again.

6.1.1 Cathode directed streamers

When looking at the main conclusions from Chapters 4 and 5, it can be seen that for the CDS optimizing the total yield is not straightforward. For parameters like pulse width and streamer velocity, different settings are required to optimize the different conversion steps. For example, by increasing the pulse width, η_{matching} increases but η_{radical} decreases. Apparently a trade-off must be made.

To facilitate the discussion, Table 6.1 gives an overview of the methods to improve η_{radical} and η_{matching} . From this table it can be concluded that, in particular, the effect of R_{primary} is different for the two conversion steps.

Table 6.1. Methods to improve η_{radical} and η_{matching} for CDS plasmas.

Parameter	η_{matching}	η_{radical}
Rise rate	No effect	Increase
Total voltage	Increase	Increase
DC bias	Increase	No effect
R_{primary}	Decrease	Increase

More insight into the importance of the different mechanisms can be obtained by determining the total system yield using Equation 6.1. As an illustration, Figure 6.1 shows a typical result of the calculations for positive polarity pulses in the case of primary streamer velocities of $1.9 \cdot 10^6 \text{ m}\cdot\text{s}^{-1}$.

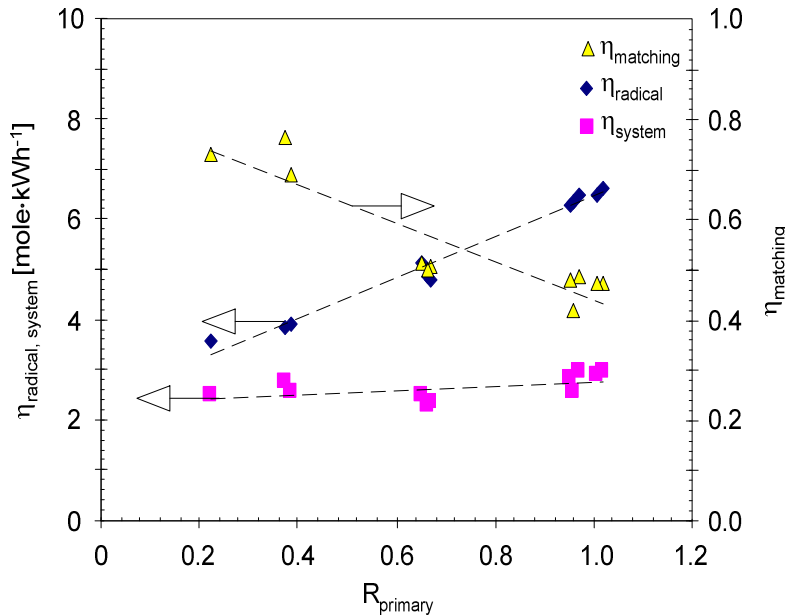


Figure 6.1. Total system yield as function of R_{primary} . The primary streamer velocity was $1.9 \cdot 10^6 \text{ m}\cdot\text{s}^{-1}$.

The net result is that the overall system performance does not depend significantly on R_{primary} . The total system yield is not extremely high: $3.0 \text{ mole}\cdot\text{kWh}^{-1}$. This is caused by the opposite dependencies of η_{radical} and η_{matching} with respect to R_{primary} . With the present system it is not possible to maximize both contributions simultaneously.

Figure 6.2 shows the results for different primary streamer velocities. The figure shows that R_{primary} has no effect on η_{system} if the primary streamer velocity exceeds $2.0 \cdot 10^6 \text{ m}\cdot\text{s}^{-1}$.

For lower velocities, η_{system} increases if R_{primary} is reduced. This result demonstrates that for low primary streamer velocities, if R_{primary} is reduced, the improvement as a result of increased matching outperforms the decrease in O^* radical production.

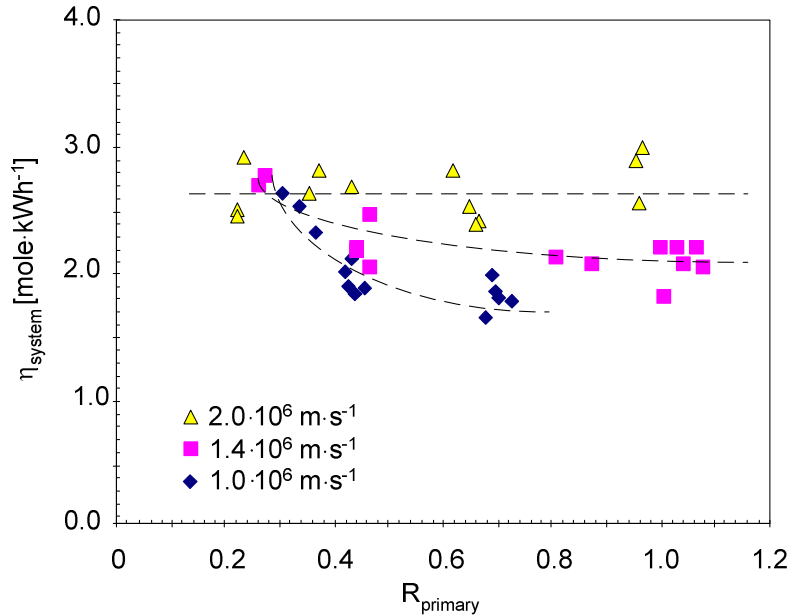


Figure 6.2. Total system yield as function of R_{primary} and the primary streamer velocity. Wire-plate distances between 37 and 77 mm.

total system yield as function of the primary streamer velocity is plotted in Figure 6.3. The jitter in the results is caused by the various values for R_{primary} used to generate the plot. It can be seen that the total system yield increases if the primary streamer velocity is enlarged, although the effect is limited. Nevertheless, it can be concluded that fast rising, high amplitude voltage pulses are required for efficient streamer plasma systems, as these conditions result in the generation of streamers with a high propagation velocity.

A possibility to increase the total system yield is to use a power modulator that reabsorbs the energy not dissipated by the streamers. For such a system, high matching is not necessarily required and a situation with a high radical yield can be chosen, i.e., $R_{\text{primary}} = 1$. In practice, developing such a system is not straightforward. If a load is not well matched, energy has to be re-absorbed on two different time scales. On the short characteristic time scale of the pulse, a non-matched load will result in fast energy reflections. In this case, energy is reflected back from the load. On longer time scales, voltage can remain on the load. In this case, energy remains in the load.

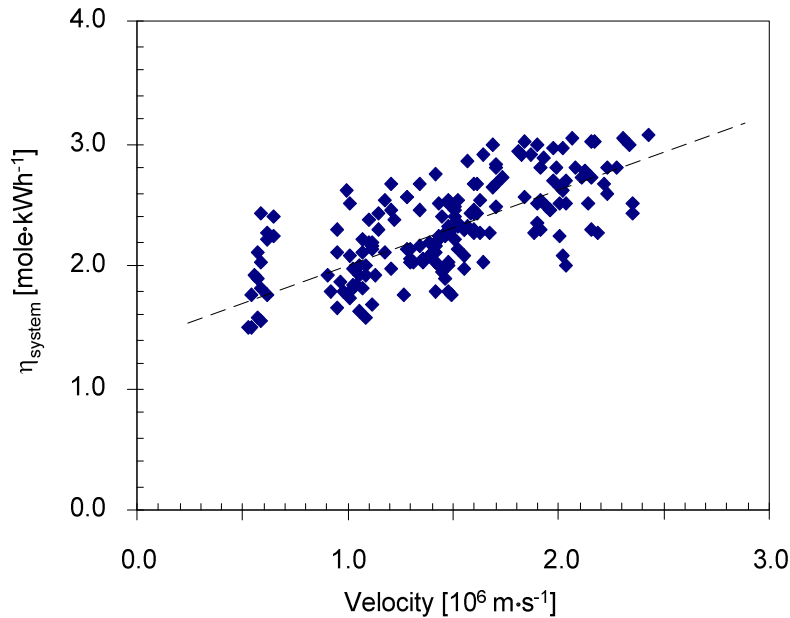


Figure 6.3. Total system yield as function of the primary streamer velocity. The plot shows all the results. The solid line is the least squares linear fit of the data.

To re-absorb the energy remaining in the load after the plasma has quenched, an energy re-absorbing circuit topology as shown in Figure 6.4 can be used. L_{con} is the stray inductance of the reactor connections. In this case, the high-voltage capacitor C_h is discharged into the reactor by a fast uni-directional switch S (for example a thyristor). The energy remaining after the streamers have quenched is resonantly transported back to C_h by the diode D and the inductor L . The value of L can be found by considering that the characteristic timescale of the reactor – $L_{\text{con}} - L - D - C_h$ circuit has to be much longer than that of the $C_h - S - L_{\text{con}} - \text{reactor}$ circuit. This circuit does not re-absorb the fast energy reflections during the pulse. A solution to re-absorb these fast energy reflections cannot be provided at this moment. Additional research is required.

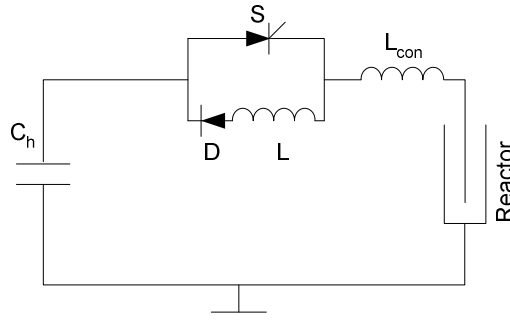


Figure 6.4. Circuit topology for a pulsed power system that reabsorbs the energy reflected after plasma generation. L_{con} is the stray inductance of the reactor connections.

6.1.2 Anode directed streamers

An analysis similar to that made in the discussion above can be made for the results of the negative polarity pulses. The mechanisms to increase η_{matching} and η_{radical} are summarized in Table 6.2. The most important difference compared to the CDS is that R_{primary} has no significant effect¹ on the radical yield for ADS. Therefore the results are now plotted as a function of reactor voltage instead of R_{primary} . Figure 6.5 shows the different contributions to the total system yield. To clearly illustrate the effects, only those data are shown that have a pulse width of 100 ns. In Figure 6.6 all pulse-widths are summarized. The measurements shown are for the complete primary streamer velocity range of $0.8 \cdot 10^6 - 2.0 \cdot 10^6 \text{ m}\cdot\text{s}^{-1}$. In contrast to the situation for the CDS, in this case the contributions of the different conversion steps reinforce each other. If the voltage amplitude is increased, both the matching and the radical yield increase. Logically, the total system yield therefore increases as well.

Table 6.2. Methods to improve η_{radical} and η_{matching} for ADS plasmas.

Parameter	η_{matching}	η_{radical}
Rise rate	No effect	Increase
Total voltage	Increase	Increase
DC bias	Increase	No effect
R_{primary}	Decrease	No effect

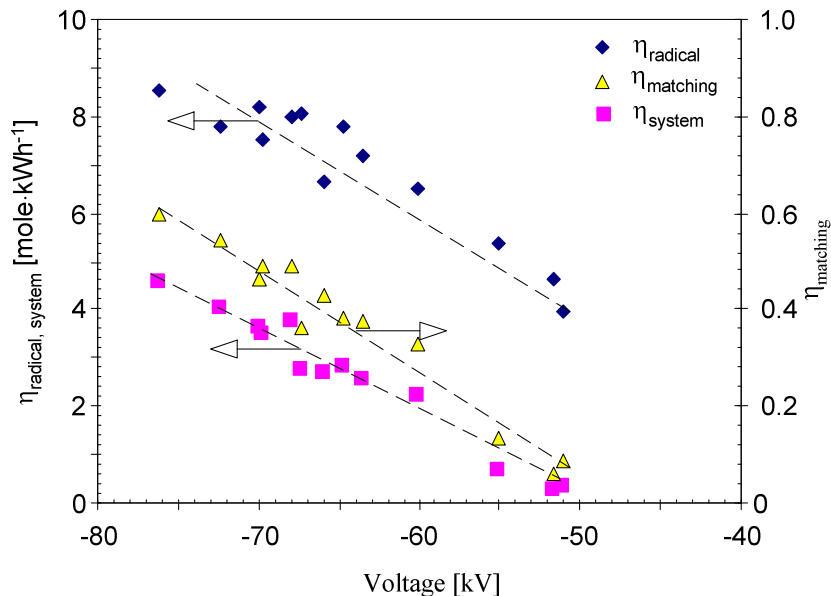


Figure 6.5. Total system yield as function of applied voltage. Primary streamer velocity was $0.8 \cdot 10^6 - 2.0 \cdot 10^6 \text{ m}\cdot\text{s}^{-1}$. Pulse width fixed at 100 ns. The results for measurements with different DC bias voltages are shown.

¹ For the used experimental range, $R_{\text{primary}} = 0.2 - 0.5$.

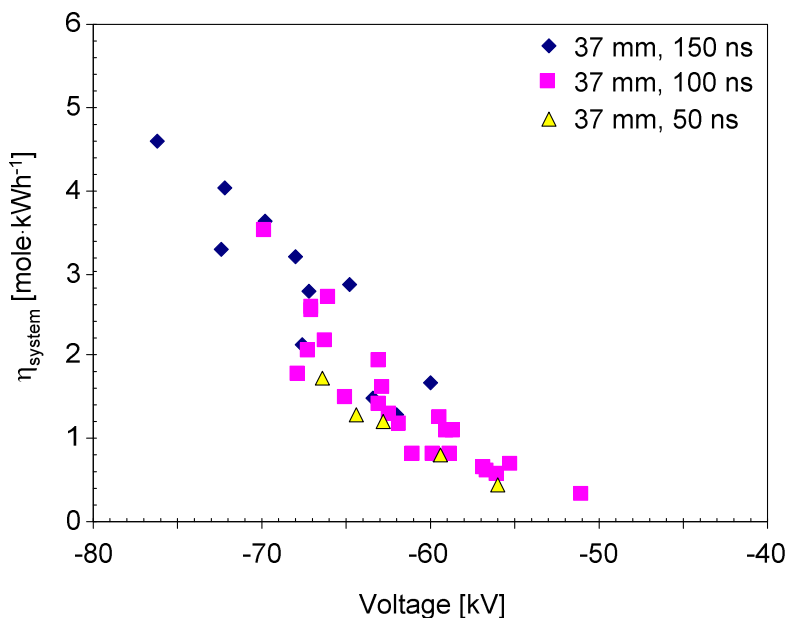


Figure 6.6. Total system yield as function of reactor voltage for ADS. The velocity of the primary streamers varied from $0.8 \cdot 10^6$ - $2.0 \cdot 10^6$ $\text{m} \cdot \text{s}^{-1}$. Wire-plate distance and pulse widths are shown in the legend.

As can be concluded from the presented plots, the total system yield η_{system} increases linearly when the voltage amplitude is increased. The maximum η_{system} obtained is $4.6 \text{ mole} \cdot \text{kWh}^{-1}$, which is considerably more than that of the CDS ($3.0 \text{ mole} \cdot \text{kWh}^{-1}$).

Based upon the findings, it can be stated that for negative-polarity pulses, the pulse width is not particularly important, although a slightly higher η_{system} is obtained for longer pulses. As long as breakdown does not occur, the pulse width can be increased. During measurements it was observed that high-amplitude, 150 ns pulses frequently resulted in breakdown. It is expected that longer pulses cannot be used to generate an efficient streamer plasma. In that case only a reduction of the voltage enables stable operation, but from the presented results it is obvious that this leads to decreased system performance. The applied voltage should be maximized. The rise rate should be maximized as well, since this will result in faster primary streamers, which have a high radical yield.

6.2 Optimizing pulsed power system design: conclusions

High total system yield can be attained when both the matching and the radical yield are optimized. For negative-polarity systems this can be accomplished by increasing the applied voltage. The pulse width is of secondary importance. It is preferable to maximize the rise rate of the voltage pulse, as this results in a higher primary streamer velocity. The total system yield is then increased because of the increased radical yield.

For positive polarities, the situation is more complicated since the criteria to optimize the matching and the radical yield oppose one another. The results show that the effects of the different conversion steps almost cancel. As a result, the value of R_{primary} is not of particular importance to the total system efficiency. The best total yields are obtained when primary streamers with a high propagation velocity are generated. In agreement with the negative polarity case, this can be accomplished when high voltage amplitudes and high pulse rise rates are used. Table 6.3 summarizes the obtained guidelines for the development of efficient streamer plasma systems.

Table 6.3. Guidelines to improve the total system yield.

Parameter	CDS	ADS
Pulse width	No effect	Increase
Rise rate	Increase	Increase
Total voltage	Increase	Increase
DC bias	Increase	Increase
Wire-plate distance	No effect	Decrease

Based upon the finding that the overall system yield for ADS is higher than the yield for CDS (4.6 and 3.0 mole·kWh⁻¹ respectively) it can be concluded that it is preferable to use negative polarity pulses. However, the ADS plasma (compared to the CDS) has the following disadvantages: higher voltages are required, the wire-plate distance is limited, the sensitivity regarding wire misalignment is larger and the working range (maximum voltage, maximum pulse width) is limited as a result of the occurrence of breakdowns. Also, a high system yield is not the only criterion for developing industrial-scale pulsed plasma systems. Designing a system in such a way that a high yield is obtained should not result in an unacceptably low lifetime of the components. In other words, the matching should be high as well. Since positive-polarity systems with excellent matching can be developed, whereas this is not possible for negative-polarity systems, it is not straightforward to discard the former type because of its lower total system yield.

Energy recovery

If an energy recovery system as shown in Figure 6.4 can be developed, the discussion about the total system yield is considerably simplified. Energy is not lost as a result of mismatch, and component wear can be limited. The total system yield is then governed by the radical yield. In this case, positive-polarity systems are preferable. Although the pulse width still has to be limited to ensure that only primary streamers are produced, lower voltages and larger wire-plate distances (compared to negative-polarity systems) can be used. This is preferable from the application perspective.

7 Large scale, energy efficient plasma system*

To illustrate that medium- to large-scale systems, with high energy-transfer efficiency from power grid to plasma generation can be developed, this chapter will describe the hybrid pulsed power system (HPPS), which was designed for an average power up to 30 kW. During this study, the construction of the system was completed and an average power of 17 kW has been realized. The term hybrid was chosen since not only pulses but also a DC bias voltage has been used to energize the reactor. The design parameters of the HPPS system can be found in Table 7.1. After a description of the system (Section 7.1), results will be presented to indicate that good matching can be achieved through careful system design (Section 7.2). At the end of this chapter, the results of an industrial-scale demonstration experiment on odor abatement will be presented (Section 7.3).

Table 7.1. Characteristics of the HPPS corona plasma system: design parameters.

Parameter	Value	Parameter	Value
Average Power	< 30 kW	Rise time (20-80%)	12 ns
Max. pulse voltage	70 kV	Pulse width (FWHM)	50-150 ns
Peak current	3.5 kA	Energy per pulse (EPP)	0 ~ 30 J
Pulse repetition rate	1-1000 pps	Jitter in EPP	1 ~ 2%
DC bias voltage	0-30 kV	Energy transfer efficiency	~90%

7.1 HPPS system

A schematic overview and a photograph of the HPPS system are shown in Figure 7.1. Typical component values are listed in Appendix B.II. Basically, the system is identical to the system described earlier in this thesis (see Chapter 3). The fast pulse-generating circuit was constructed coaxially to reduce stray capacitance and inductance (i.e., enable fast pulse generation). The main differences compared to the system described in Chapter 3 are:

- The high-voltage capacitor C_h is not a pulse-forming line but consists of lumped high-voltage capacitors.
- The 2-stage TLT is constructed from rigid concentric metal tubes instead of coaxial cables. This allows for a free choice of the line impedance Z_0 . As a result, Z_0 values are not limited to those of commonly available coaxial cables. As was shown in Equation 4.4 the rise time of the voltage on a reactor load is inversely proportional to the product of C_r (the reactor capacitance) and Z_{out} (the output impedance of the TLT). For industrial-scale reactors, C_r will be large. If fast rising pulses are required, Z_{out} must be minimized. Also,

* Parts of this chapter have already been published in *Win(2004b,c)*, *Win(2005a)*, *Win(2006d)* and *Yan(2004)*.

the width of the voltage pulses generated by the system is determined by the product $C_h \cdot Z_{in}$, with Z_{in} representing the input impedance of the TLT. For large scale systems, C_h will be large, thus Z_{in} should be minimized if short pulses are required. For the HPPS system, the line impedance was designed to be 10Ω , resulting in a Z_{in} and Z_{out} of 5Ω and 20Ω respectively.

An additional advantage of this low Z_{out} value is that the modulator can deliver a large current at a high voltage. This is especially useful for large volume plasma applications.

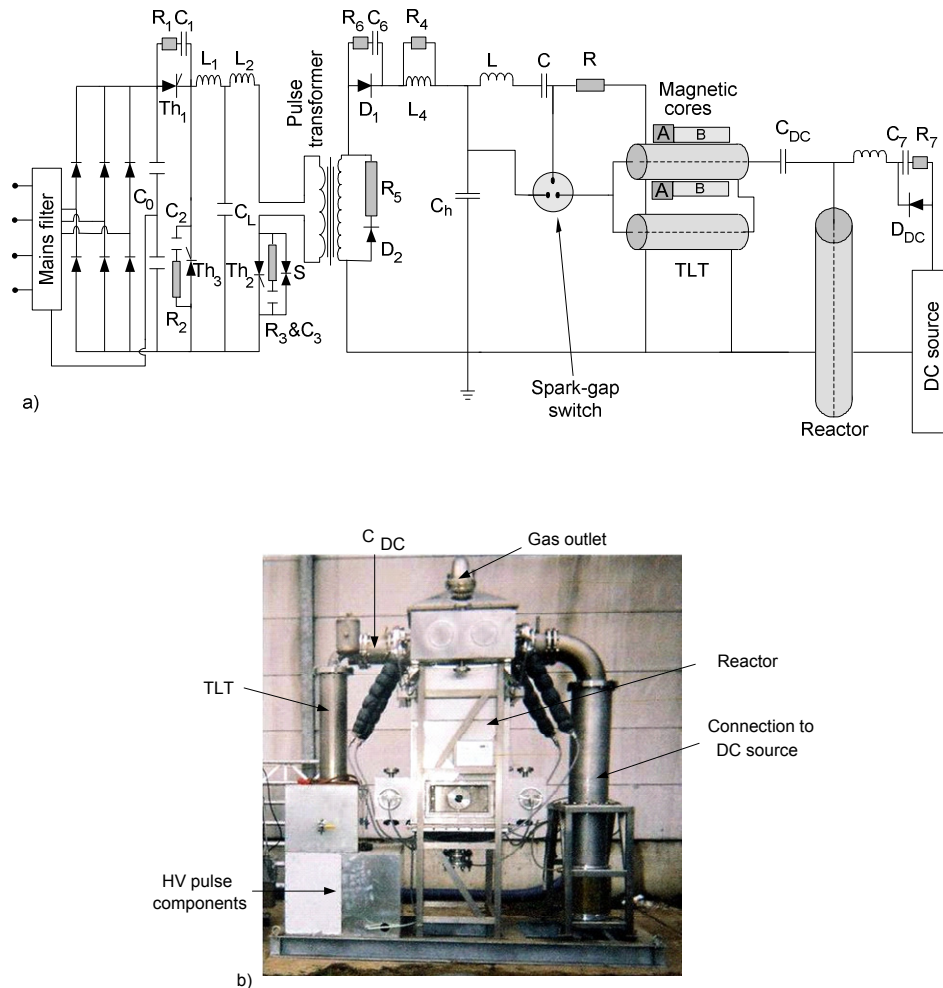


Figure 7.1. a) Schematic overview of the HPPS system. b) Photograph of the system.

- A schematic depiction of the spark-gap switch used in the HPPS is shown in Figure 7.2. The main difference with the coaxial type spark-gap switch described in Section 3.1.4 is the limited lifetime of the copper electrodes (estimated 4 months @ 1000 pps, $10\text{-}20 \text{ J}\cdot\text{pulse}^{-1}$). The lumped high-voltage capacitors are positioned coaxially around the anode to obtain low inductance, i.e., fast switching. The distance between anode and

cathode is 3 mm. The spacing between the anode and the trigger electrode is 0.3 mm. The diameter of the cathode is 40 mm. The switch can be pressurized up to 6 bar and flushed with dry air to obtain stable operation. The flushing air flows through the gap between the anode and the trigger electrode. The air can leave the switch via six exhaust pipes, positioned in a star-shaped configuration.

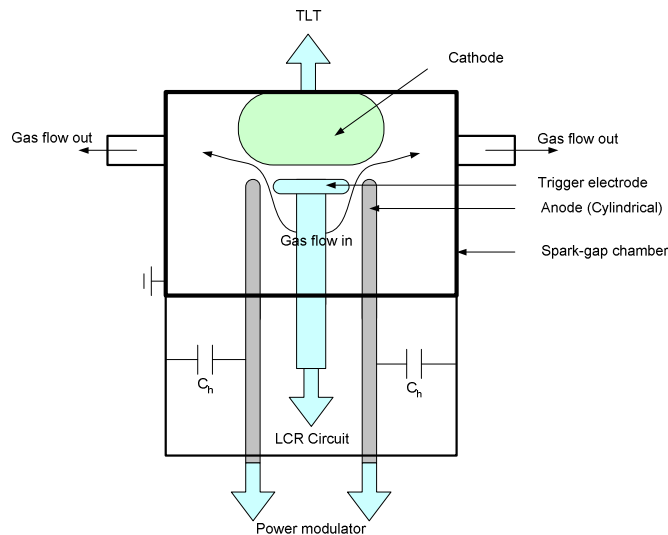


Figure 7.2. Schematic drawing of the spark-gap switch. The high voltage capacitors C_h are positioned coaxially around the anode to reduce the inductance. Suitable high-voltage feed-throughs were constructed at the required positions.

- The developed reactor consists of 16 wire-cylinder reactors in parallel, constructed inside a solid stainless steel cube of $1 \times 1 \times 1 \text{ m}^3$ (see Figure 7.3). The length and diameter of each cylinder are: $1 \times 0.16 \text{ m}$. The selected wire thickness is 3 mm. The reactor has its axis oriented vertically. The connections to the power source are at the top; the gas inlet is at the bottom of the reactor. The cylinder walls can be cooled with water to control the gas temperature. The reactor capacitance C_r was determined to be 320 pF.
- Total system dimensions are: height 4 m, width 2 m, length 4 m, weight 3000 kg. The system can be transported to outdoor locations.

7.2 Electrical characterization

The system is equipped with differentiating sensors: two capacitive sensors, positioned directly before and after the coupling capacitor C_{DC} , to measure the high-voltage pulse waveforms, a capacitive sensor connected to C_h , to determine the capacitor charging voltage V_{sg} , and a one-turn Rogowski coil positioned directly after the TLT to measure the reactor current. A suitable passive integrator was developed for every sensor. The four signals are recorded simultaneously on the oscilloscope. The procedure to determine the actual voltage and current waveforms on the reactor, using the recorded signals, is identical to that described in Section 3.4.1.

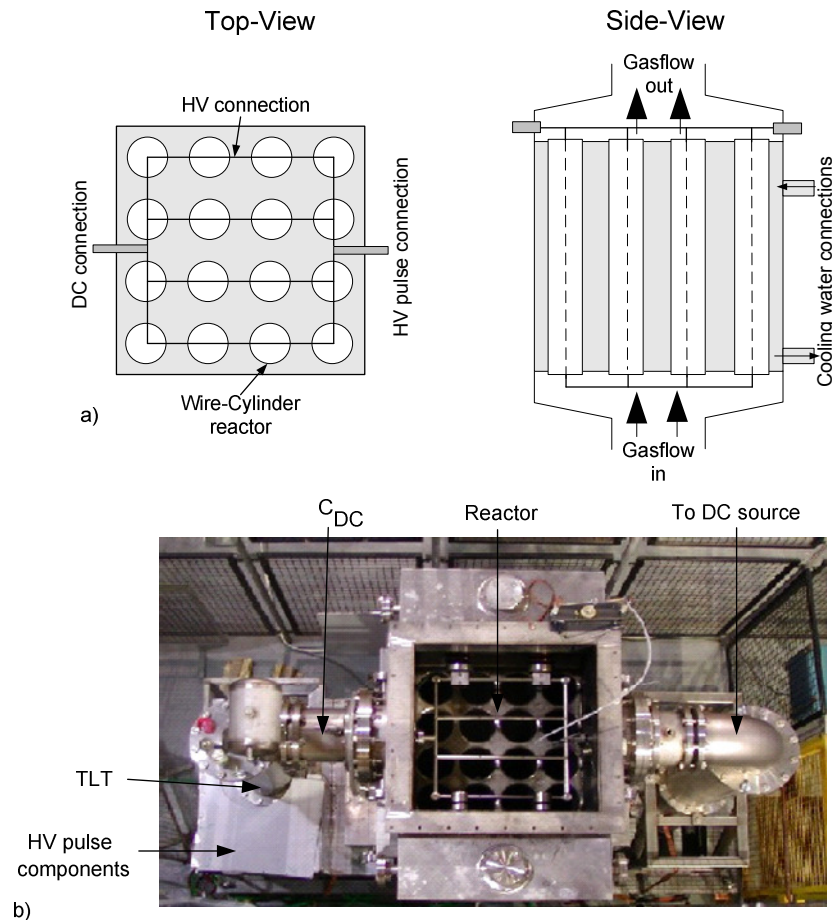


Figure 7.3. a) Top-view and side-view depiction of the reactor. b) Top-view photograph.

Typical voltage, current, power and energy waveforms are shown in Figure 7.4. As can be seen, the voltage rise time (20-80%) is 12 ns. The voltage pulse width (FWHM) is roughly 75 ns. The only pulse parameters that can be varied are: the DC bias voltage V_{DC} (0-30 kV), the energy per pulse (up to 20 J-pulse^{-1} , by increasing C_h and V_{DC}), the pulse width (60-150 ns, by increasing C_h) and the pulse repetition rate (1-1000 pps). The other parameters are fixed.

It was found that the rise time did not depend on the energy per pulse, DC bias voltage and pulse repetition rate. This finding is as expected since the rise time only depends on Z_{out} , C_r (eq. 4.7) and the rise time τ of pulses at the input side of the TLT. This τ is mainly determined by the stray inductance of the spark-gap switch, which is kept as low as possible through proper design of the layout. None of these parameters (Z_{out} , C_r , τ) were changed during the experiments. Consequently, the rise time of the voltage pulse on the reactor should be constant.

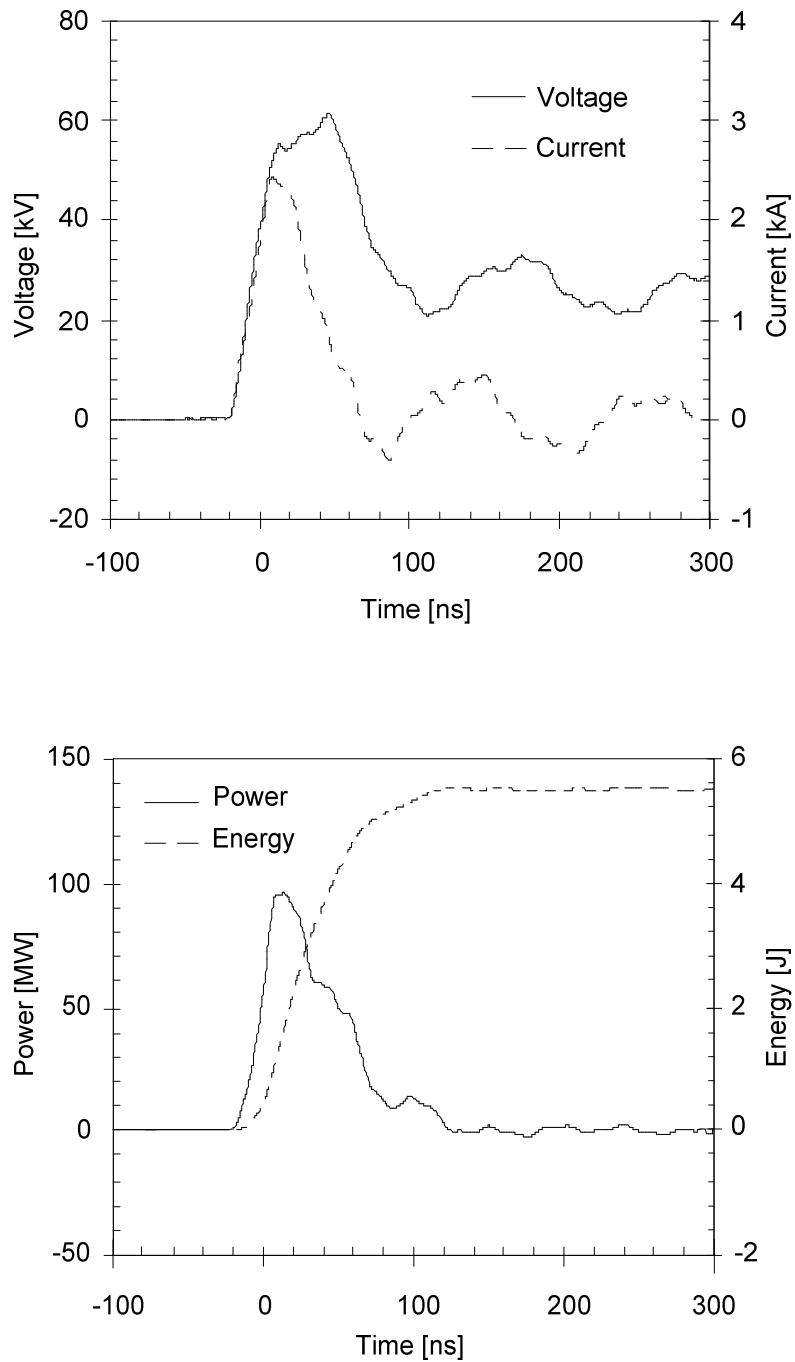


Figure 7.4. Typical electrical waveforms. The pulse to pulse jitter was $< 1\%$. The shown results are the average of 1000 consecutive shots. During the measurements: $C_L \sim 13 \mu\text{F}$ and $C_h \sim 10.6 \text{ nF}$, pulse repetition rate 1000 pps.

At the end of the pulse, the voltage drops below the minimum value required to sustain the plasma. This residual voltage remains on the reactor for some time as a result of the coupling capacitor C_{DC} . Because of the short-circuit path as a result of the TLT, the residual voltage slowly (in comparison to the pulse duration) decreases towards zero. The final voltage it obtains depends on the potential difference across C_{DC} directly after the pulse.

In Figure 7.5a it can be seen that the peak power and the width of the power curve increase for increasing DC voltages. Apparently, since the pulse energy is determined as the integral of the power waveform, the energy per pulse can be increased by increasing the DC bias voltage (see legend). This increase is caused by two mechanisms. Firstly, more energy is available due to the additional energy stored (E_{DC}) by the DC supply in C_{DC} and C_r :

$$E_{DC} = \frac{1}{2}(C_{DC} + C_r) \cdot V_{DC}^2 \quad (\text{eq. 7.1})$$

Secondly, by increasing the DC bias voltage, the total peak voltage on the reactor can be increased. As a result, the matching can be improved (Chapter 4), the matching criterion (Equation 4.8[†]) is better fulfilled, and more of the energy stored in C_h will be transferred to the reactor. This last statement is illustrated by the voltage waveforms on C_h as shown in Figure 7.5b and 7.5c. The capacitor is resonantly charged in about 50 μs to its maximum V_{sg} . The voltage then remains constant until the spark-gap is fired. Some ringing occurs after the switch is closed due to the impedance mismatch between modulator and reactor. Figure 7.5c shows the voltage on C_h on a shorter time scale. It can be seen that the capacitor does not discharge completely but rather to a voltage V_{end} , indicating that not all of the stored energy can be transferred into the reactor. Thus, the energy from C_h used for plasma generation is:

$$E_{C_h} = \frac{1}{2} C_h \cdot (V_{sg}^2 - V_{end}^2) \quad (\text{eq. 7.2})$$

By superimposing a DC bias voltage, both the final voltage V_{end} and the ringing decrease and thus more energy is transferred to the reactor. Obviously, the matching is improved. Besides the economic advantage of having more energy going from C_h into the reactor, there is also the advantage of decreased component stress. Most of the energy that is not used in the reactor is dissipated in the spark-gap switch, the TLT and in the D_2 - R_5 circuit. An example of the energy dissipation in R_5 is shown in Figure 7.5d. At the beginning of the signal a small local increase in dissipated energy can be observed. This is a result of energy dissipated during the charging of C_h . The fast energy rise afterwards occurs after the switch has been fired and is caused by energy reflections from the reactor. Clearly, a higher DC-bias voltage reduces the energy losses significantly.

[†] $C_{DC} \geq \frac{C_h \cdot V_{sg}}{2V_{DC}}$ (eq. 4.8)

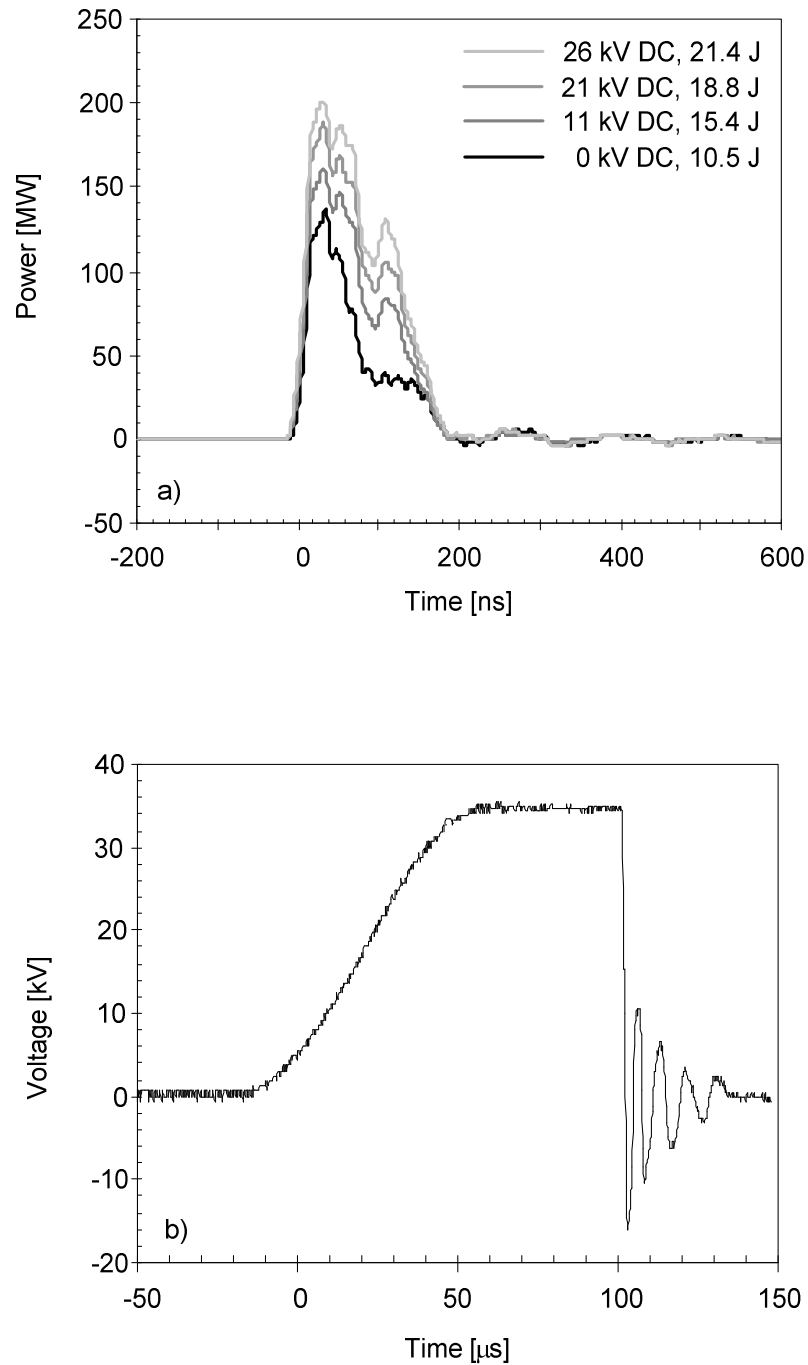


Figure 7.5. a) Power waveforms as function of the DC bias voltage, $C_h=25.8$ nF. The corresponding energy per pulse is indicated in the legend. b) Voltage waveform on C_h ($=25.8$ nF), single shot measurement without DC bias voltage.

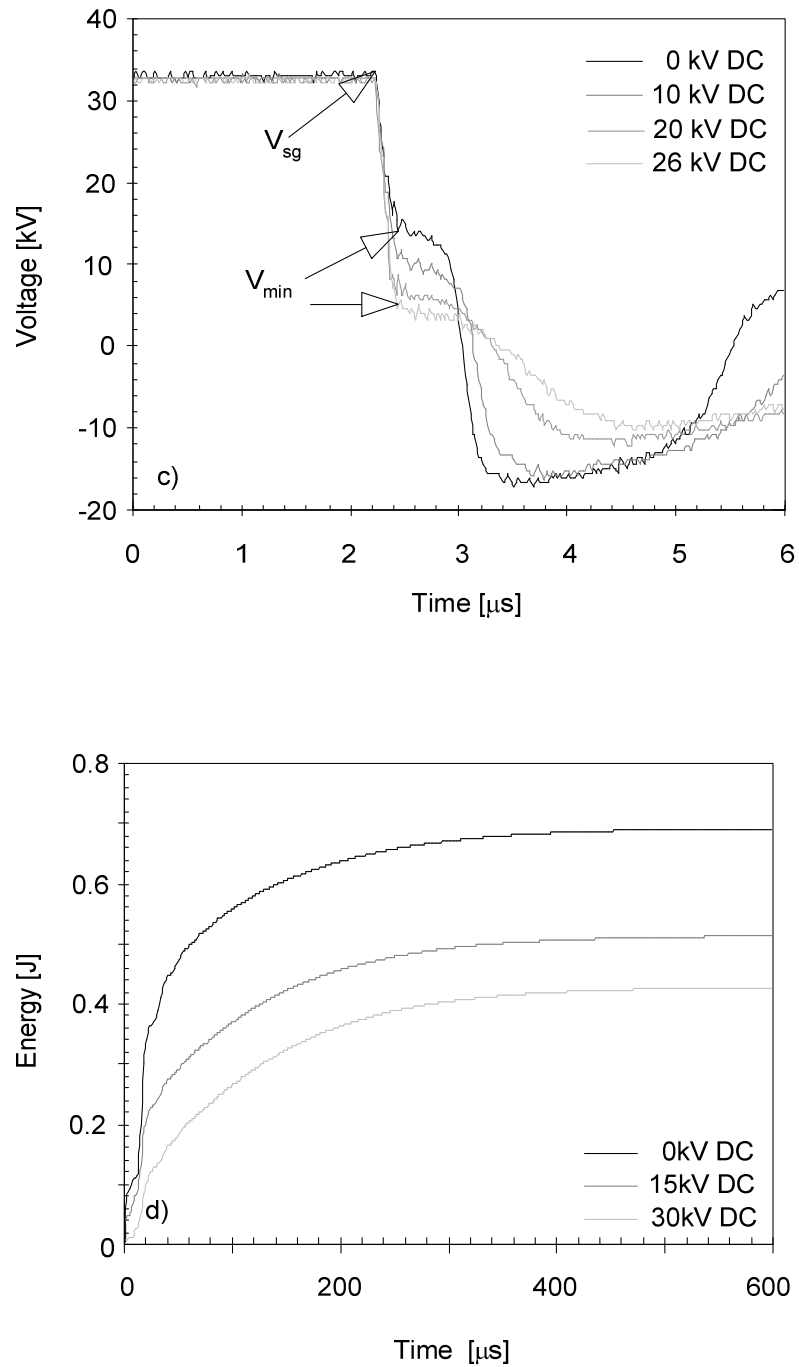


Figure 7.5 (continued). c) Voltage waveforms on C_h after the spark-gap fires as function of DC bias voltage level (single shot measurements). d) Energy dissipation in R_5 resistor as function of the DC bias voltage, $C_h=10.6$ nF.

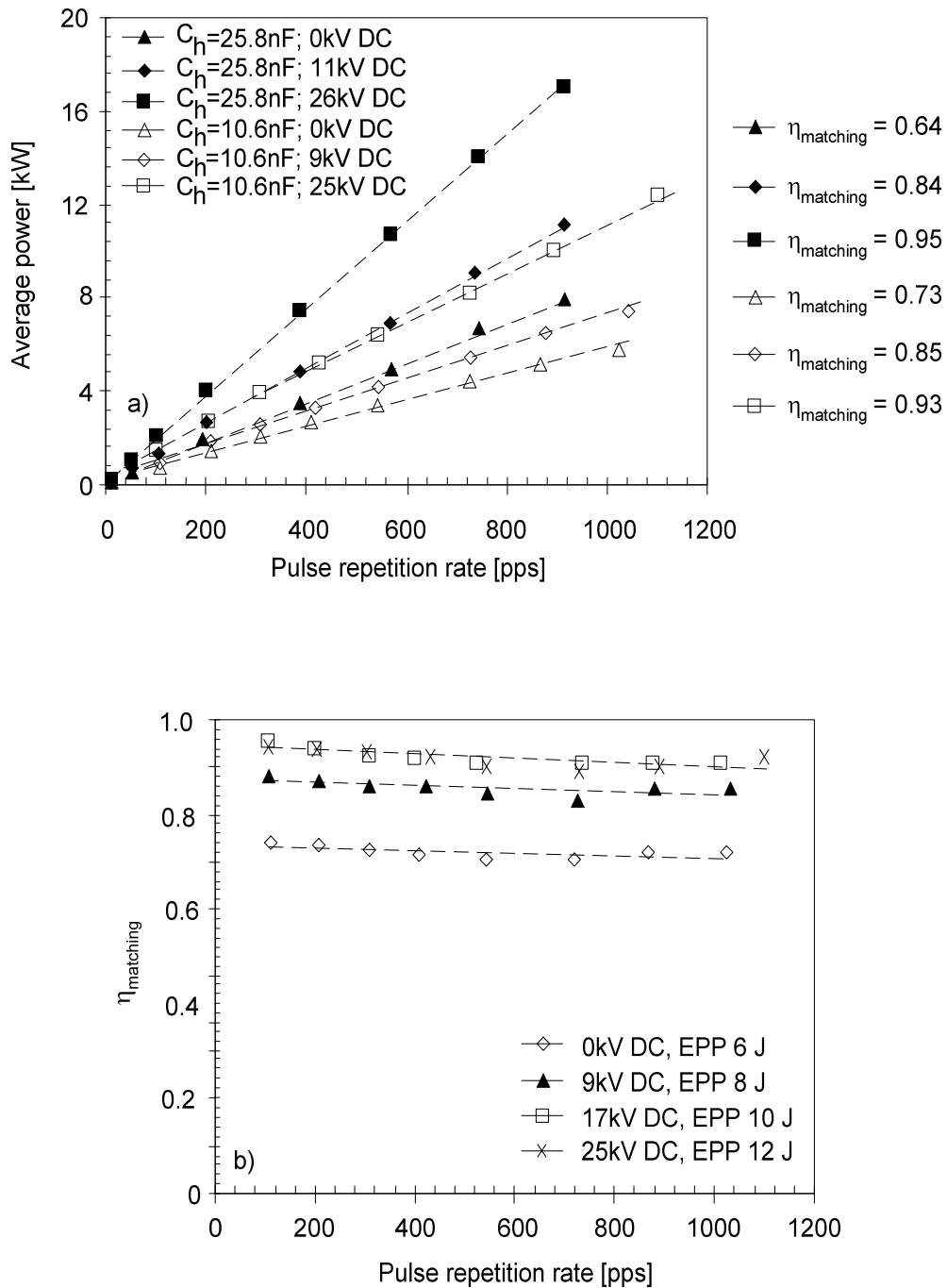


Figure 7.6. Average power (a) and energy conversion efficiency (b) as function of the pulse repetition rate, $C_h=10.6\text{ nF}$. The values listed for η_{matching} and the energy per pulse (EPP) are average values over the complete pulse repetition rate range.

The results shown in Figure 7.6 summarize the experiments performed to optimize the output power and the energy efficiency η_{matching} . The experiments were carried out during test cycles of 5 minutes. Long duration experiments (several hours continuously) were also performed. It was observed that the jitter in average output energy was about 1-2%. No problems occurred during the long duration operation. The output power is changed by varying the pulse repetition rate, the value of C_h and the DC-bias voltage. The results are summarized in Figure 7.6a with a maximum average power of 17 kW. Higher average output powers were not obtained since the maximum airflow in the laboratory facility was insufficient to prevent sparking in the reactor. The energy per pulse decreases slightly as a function of the pulse repetition rate due to the relatively small (6.6 mF) value of the primary energy storage capacitor C_0 . Theoretically, C_0 should be infinitely large to prevent the decrease in energy per pulse completely.

The energy transfer efficiency η_{matching} , calculated from Equation 4.10[‡], is plotted in Figure 7.6b. As shown, the efficiency increases with DC bias voltage due to the improved matching. η_{matching} slightly reduces at higher pulse repetition rates. A maximum energy efficiency of about 95% was obtained. Considering an efficiency from the power grid to the C_h of 95% [Yan(2001)], we can conclude that the total energy conversion efficiency from power grid into plasma generation is about 90%. It is interesting to compare the performance of the HPPS system with other, large scale, pulsed corona systems. For the 120 kW average power modulator described in *Lee(2003)*, the efficiency is about 50%. The 40 kW average power modulator described in *Mok(2001)* has an efficiency of less than 76%. For the system described in *Pok(2004)*, it is less than 50% for 1-2 kW average power. All systems have considerably lower energy transfer efficiency than the presented one. A reason for this is that these systems are based on magnetic pulse compression techniques. Finally, these systems are not capable of dust collection since no DC bias voltage can be applied.

7.3 Industrial demonstration of odor emission abatement using the HPPS

To validate the pollutant removal capabilities of the HPPS system, a feasibility study was performed. Odor removal from air was chosen as the process. The system test was performed at an industrial compost manufacturer, under cold, humid, outdoor conditions. Despite the harsh weather, the system operated without problems.

7.3.1 Process layout

Figure 7.7 shows a diagram of the related production process. Due to the manufacturing process, a large ($250,000 \text{ Nm}^3 \cdot \text{h}^{-1}$) exhaust air flow was produced in the factory. The air contained a large amount of contaminants, often in high concentrations. The contaminants

$$\eta_{\text{matching}}^{\ddagger} = \frac{\int V(t) \cdot I(t) dt}{\frac{1}{2} C_h V_{sg}^2 + \frac{1}{2} (C_{DC} + C_r) V_{DC}^2} \quad (\text{eq. 4.10})$$

mainly consist of VOCs, but H_2S , known for its bad smell, was also present in large concentrations. To meet the legislation requirements, an acid washer and bio-bed filter were already installed, but their performance did not match the emission regulation.

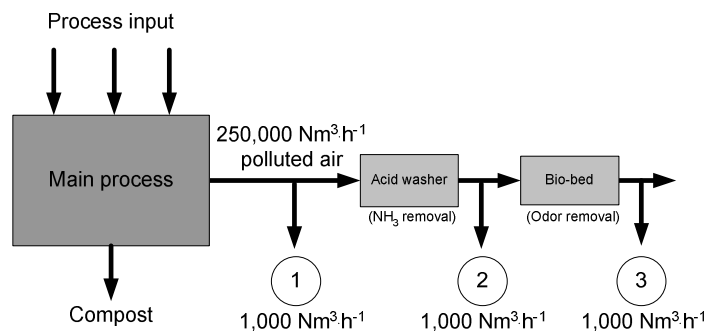


Figure 7.7. Process overview of compost manufacturer.

The HPPS system could be installed at three locations, as indicated in Figure 7.7. The experiments were performed with a sub-stream gas flow of $1,000 \text{ Nm}^3 \cdot \text{h}^{-1}$ (1.2 s residence time in reactor). The air temperature was about 30-40 °C; the relative humidity exceeded 80%. The demonstration involved several hours of continuous operation. Only a few energy densities were used; DC bias voltage was not applied.

7.3.2 Gas analysis

Chemical analyses were performed by a certified lab, PRA OdourNet BV. For the analyses, 40 liters of air from the output of the reactor were sampled in nalophene bags in 30-minute experimental measuring cycles. The bag was placed inside a low pressure container. The air is sampled according to the “lung method” to prevent the odorous gases from coming into direct contact with the pump. To prevent condensation inside the bags and its related absorption, the sampled air was diluted with dry nitrogen. Several techniques were used for gaseous analysis. The Impinger method was used to determine H_2S concentrations. GCMS was used to determine VOC concentrations. The GCMS consists of a Varian 2700 gas chromatograph and a MAT 112S Finnigan mass spectrometer.

The measurements were performed according to Dutch standards [GMT]: Odor concentrations were determined by a panel of 6 people who smelled the air presented to them in different concentrations [Har(1999)]. Starting with an over-diluted sample and progressing steadily to a more pure concentration, the panel had to indicate when the odor could be observed. The corresponding odor concentration then equals $2 \text{ ou}_E \cdot \text{m}^{-3}$ by definition ($\text{ou}_E = \text{odor unit}$). Since the dilution factor is known, the actual odor concentration can be calculated.

Besides odor concentrations, the quality of the odor was also determined by the panel. Quality of the odor is expressed as the “Hedonic” value (H). For different concentrations

(dilution factors), the panel indicated the quality of the air by ranking the air between a Hedonic value of +4 (pleasant odor) and -4 (bad odor). The Hedonic value usually decreases for increasing concentrations. By interpolating the obtained results on a logarithmic scale, the concentration at which a specific Hedonic value is obtained can be determined. According to the Dutch standard [GMT], the measurements must be performed three times to obtain reliable data. During the feasibility study, only single measurements were performed. Consequently, the obtained results can only be used as indication.

7.3.3 Results

Table 7.2. HPPS settings for the various measurements performed

Location	Pulse energy [J]	prf [pps]	Power [kW]	Energy density [J·L ⁻¹]	Measurement name
1	8	250	2.0	7.2	1, High
2	8	100	0.8	2.9	2, Low
2	8	175	1.4	5.0	2, Medium
2	8	250	2.0	7.2	2, High
3	8	100	0.8	2.9	3, Low
3	8	175	1.4	5.0	3, Medium
3	8	250	2.0	7.2	3, High

With reference to Figure 7.7, measurements were performed at the three indicated positions. The energy densities used for the measurements are summarized in Table 7.2. Since the test was only performed to determine feasibility, the number of modulator settings was limited to the ones mentioned in Table 7.2. This implies that the obtained odor removal experiments are not optimized. This was also observed during some of the measurements where an ozone slip in the exhaust of the system was detected. Tables 7.3, 7.4 and 7.5 list the results of the odor concentrations, Hedonic values and VOC measurements respectively. The effects of the acid washer and bio-bed filter have also been added.

Table 7.3. Overview of odor concentration measurements

Measurement name	Input [ou _E ·m ⁻³]	Output [ou _E ·m ⁻³]	Removal efficiency [%]
Acid washer	298,516	147,081	51
Bio-bed	152,430	29,754	80
1, High	270,796	155,707	43
2, Low	320,578	107,409	66
2, Medium	320,578	53,631	83
2, High	320,578	137,040	57
3, Low	29,754	16,646	44
3, Medium	29,754	42,216	-42
3, High	29,754	17,526	41

From Table 7.3 it can be concluded that it is possible to decrease the odor concentrations considerably using the HPPS system, although the bio-bed filter performed satisfactory as well. However, during a separate measurement it was found that the lifetime of the bio-bed filter was limited to two weeks. From this point of view, the HPPS system would be preferable. The measurements performed at position 3 (after the bio-bed filter) show a large variation in removal efficiency. Possibly this variation can be explained by the low input concentrations and the complex chemistry.

Table 7.4. Hedonic measurements

Measurement name	H = -1/2 [ou _E ·m ⁻³]	H = -1 [ou _E ·m ⁻³]	H = -2 [ou _E ·m ⁻³]
Acid washer	1.6	2.3	12.1
Bio-bed	2.3	4.2	14.1
1, High	3.7	10.2	76.6
2, High	13.5	47.3	581.8
3, High	1.2	3.9	39.2

The Hedonic measurements revealed that the quality of the odor improved considerably as a result of the HPPS treatment. Compared to the acid washer and bio-bed filter, the HPPS system performed much better. Again, the measurements at position 3 resulted in the least profitable situation.

Table 7.5. VOC emission abatement

Group	Acid washer		Bio-bed filter		1, High	
	Input [μg·m ⁻³]	Output [μg·m ⁻³]	Input [μg·m ⁻³]	Output [μg·m ⁻³]	Input [μg·m ⁻³]	Output [μg·m ⁻³]
Aromatic CHs	84	96	152	1,208	395	10
Cyclic CHs			0	0	66	0
Aliphatic CHs	74	31	65	413	271	13
Alcohol	2,067	1,943	3,796	184	787	44
Esters	82	231	504	0	0	263
Ketones	3,883	3,658	9,510	1,563	3,881	273
Aldehydes	3,783	1,194	1,305	1,733	946	570
Cl components	0.2	4	443	339	200	0
Organ. sulphur	1,985	1,963	3,348	582	2,363	2
Furans	214	211	219	0	66	10
Organic acid						
Ethers			315	513		
Terpens	16	23	27	57	13	0

Table 7.5 (Continued). VOC emission abatement

Group	2, Medium		2, High		3, High	
	Input [$\mu\text{g}\cdot\text{m}^{-3}$]	Output [$\mu\text{g}\cdot\text{m}^{-3}$]	Input [$\mu\text{g}\cdot\text{m}^{-3}$]	Output [$\mu\text{g}\cdot\text{m}^{-3}$]	Input [$\mu\text{g}\cdot\text{m}^{-3}$]	Output [$\mu\text{g}\cdot\text{m}^{-3}$]
Aromatic CHs	152	101	152	222	1,208	84
Cyclic CHs	0	68	0	42	0	21
Aliphatic CHs	65	430	65	340	413	181
Alcohol	3,796	1,357	3,796	2,384	184	181
Esters	504	35	504	33,458	0	6,415
Ketones	9,510	5,242	9,510	11,859	1,563	4,957
Aldehydes	1,305	35,930	1,305	33,618	1,733	15,544
Cl components	443	135	443	22	339	25
Organ. sulphur	3,348	101	3,348	56	582	209
Furans	219	0	219	0	0	0
Organic acid	0	100	0	0		
Ethers	315	288	315	171	513	109
Terpens	27	0	27	2	57	0

Table 7.5 lists the results of the VOC emission abatement. It can be concluded that the HPPS system is capable of removing many chemical compounds in large quantities. However, some compounds, like esters, ketones and aldehydes, are created in large quantities. The exception is the measurement performed at position 1, immediately at the output of the factory. A total VOC removal efficiency of 85% was obtained at this position.

Esters are organic compounds in which an organic group replaces a hydrogen atom in an oxygen acid. They are created as a result of a condensation reaction between an acid and an alcohol (or phenol). In an aqueous solution, esters can act as a hydrogen-bond acceptor, making them soluble. However, the solubility is not as high as that of its parents: acids and alcohols. In industry, esters are often used for their pleasant smells. Many of the esters can be identified with smells like: apple, cherry, peach, etc. The presence of large quantities of esters in the exhaust gas (2, High) might explain the high Hedonic value found for this measurement. Ketones are chemical compounds in which two carbon atoms are connected to a carbonyl group (-COH). They are produced as a result of oxidation of secondary alcohols. Ketones are polar molecules, making them soluble in water. However, compared to alcohols and acids of the same molecular weight, ketones are more volatile. A well known example of a ketone is acetone, used as a solvent. An aldehyde is an organic compound containing a carbonyl group. They are the results of oxidizing primary alcohols. Upon further oxidation, the aldehydes will be transformed into acids. Aldehydes are polar molecules, making them soluble in water. An example of an aldehyde is formaldehyde, which has a pungent smell. This substance can kill bacteria (disinfectant), but also poses a danger to human health.

The results of the GCMS measurements demonstrate the problems with odor removal at this plant. Due to the large number of chemical compounds present in the exhaust gas, an

extremely complex chemistry is initiated due to the generated plasma. Although no attempt was made in this thesis to describe the chemistry initiated by the HPPS system, it is believed that the VOC abatement efficiency can be increased by:

- Optimizing the modulator settings (pulse-width, amplitude, rise-rate, etc.). Especially the addition of a DC bias voltage might prove useful since particle collection in between the pulses is realized.
- Addition of additives. Spraying water into the reactor, for example, can be beneficial since many of the products leaving the exhaust of the reactor dissolve easily. The possibility of wet chemistry in the reactor is a special benefit of pulsed power systems.

Besides VOCs, H₂S was also present in the exhaust gas. Unfortunately, the detection limit for H₂S was only 0.8 µg·m⁻³. As a result, useful measurements could only be performed for experiments at position 1. At this position, typical input concentrations were 15.3 µg·m⁻³. After plasma treatment, the output concentrations were below the detection limit, so the removal efficiency with the HPPS system exceeded 95%. In comparison with *Wang* [Wan(2001)], (H₂S removal under a gas flow rate of 5.7 m³·min⁻¹, less than 76.0 µg·m⁻³ of H₂S, a discharge power of 1.2 kVA, a removal efficiency of 95%, and a corona energy of 12.6 J·L⁻¹), the present system has the same removal efficiency, but it only consumes 57% as much energy as *Wang's* system.

7.4 Conclusions

It was demonstrated that, with careful system design, a large scale (17 kW average power obtained) and energy efficient (> 90% of power grid energy dissipated by the plasma) system can be constructed.

Fast rising, short pulses can be generated efficiently, despite the large capacitance of the industrial-scale reactor. For the HPPS system, the pulse width is a linear function of the impedance of the TLT. This impedance can be kept low (10 Ω for the HPPS) by constructing the stages of the TLT as concentric metal tubes. This allows the impedance to be chosen freely, and values are not limited to those of commercially available coaxial cables. To obtain short rise times of the pulses, the high voltage pulse generation circuit, starting from C_h, was constructed as a coaxial transmission line. This was done to reduce the effects of stray capacitance and inductance on the switching behavior. By increasing the total applied voltage (in this case by increasing the DC bias voltage), the matching between the modulator and the reactor can be improved.

From the results of the feasibility study, performed at a Dutch compost manufacturer, it can be concluded that the HPPS system is a suitable option for odor abatement. Due to the large and stable average output power and the high energy-conversion efficiency, the system can be used for large-scale industrial applications. However, the process needs to be further optimized to obtain maximum, stable removal efficiencies. Systematic tests with various modulator settings must be performed, and the chemistry has to be studied in detail.

8 Conclusions and recommendations

In this thesis, the interactions between the power modulator, the generated streamer plasma and the resulting chemical processes were studied systematically. The interactions were studied from the energy conversion perspective. Both models and experiments were used to obtain the relevant data. Based upon the obtained results, O radical yields of primary and secondary streamers were quantified in relation to pulse and streamer parameters. Guidelines were derived that can be used to design large-scale, energy-efficient, pulsed plasma systems for pollution emission control. In this chapter, the main conclusions of this thesis are summarized. On the basis of these conclusions some recommendations for future research are addressed.*

8.1 Ozone production as monitor for O* radical yield

To determine the radical yield of the streamer plasma, a key chemical process has been monitored. As many pollutant removal processes are initiated by O* radicals, ozone production from ambient air, which also depends on these O* radicals, was selected as an appropriate process. The chemical model discussed in Chapter 2 is a useful tool to determine the actual O* radical yield by the measurement of the produced ozone, the streamer plasma volume, the relative humidity and the gas temperature. The error in this indirect evaluation of the O* radical yield was determined to be 5-20%, the exact value depending on the input parameters. The largest contribution to this error is the inaccuracy in the determination of the actual streamer volume.

In future experiments it would be desirable to measure the O* radical yield directly and *in situ*, i.e., resolved in time and space in the reactor, during streamer generation in dry air. In this way, the kinetic model can be verified and, if required, adjusted. Also, the streamer regimes where the radicals are produced can then be identified directly. This information could be useful to explain some of the results presented in Chapter 5 of this thesis.

8.2 Optimizing the matching between the pulse modulator and the reactor

To optimize the energy transfer efficiency from the modulator to the reactor, the reactor impedance should be equal to the output impedance of the source. As the reactor impedance varies significantly before, during and after plasma generation, this criterion is not easily fulfilled. An equivalent circuit was used to analyze the reactor impedance as a function of the voltage pulse waveform for these three different stages.

Three criteria were derived that should be obeyed when high energy-transfer efficiencies are desired:

1. The plasma should ignite before the energy transfer to the reactor capacitance reaches its maximum value.
2. The generated plasma should have a resistance equal to the output impedance of the modulator, corrected for the DC bias voltage (Equation 4.7).
3. The charge in the coupling capacitor C_{DC} should be equal to half of the charge in the high-voltage capacitor C_h (compare Equation 4.8).

The matching (i.e., how well the three criteria are fulfilled) depends strongly on the pulse parameters and the reactor configuration. A series of measurements was performed to analyze a complete system. The results can be summarized as:

- Equation 4.8 should be obeyed.
- The applied electric field should be maximized (i.e., maximum voltage and minimum wire-plate distance). The plasma resistance tends to decrease to the output impedance of the source if the electric field is increased (criterion 2). Also, if the applied electric field is large, the inception delay is low (criterion 1). Typical electric fields required to obtain a matched system for CDS: $> 10\text{-}15 \text{ kV}\cdot\text{cm}^{-1}$, for ADS: $> 20 \text{ kV}\cdot\text{cm}^{-1}$.
- The pulse-width should be maximized. The favorable load resistance values are obtained during the secondary streamer phase, not during the primary streamer phase. It is not possible to match the load to the modulator if only primary streamers are generated (i.e., short pulses and/or long wire-plate distances should be avoided).
- For pulse-widths in the range 35-250 ns, the energy dissipation per meter of wire should be limited to values below $1\text{-}4 \text{ J}\cdot\text{m}^{-1}$. In other words, the maximum power density should be limited.
- The electric field on the wire surface should exceed $10^7 \text{ V}\cdot\text{m}^{-1}$, otherwise almost no streamers are generated.

It was also determined that a well matched ADS system requires pulses with an amplitude approximately 50% higher, compared to CDS. For the same voltage amplitude, the plasma resistance is higher for the ADS. For sufficiently high voltages, the difference in matching between the polarities diminishes.

When proper care with regard to system design is taken and the reactor is well matched to the power modulator (at least during the secondary streamer regime), energy transfer efficiencies (from energy storage capacitor into the reactor) of 95% can be attained, as was demonstrated by several experiments.

8.3 Increasing the O^* radical yield of CDS and ADS

For CDS and ADS, typical O^* radical yields were found to be in the range of 3-8 mole $\cdot\text{kWh}^{-1}$. The radical yield (in mole $\cdot\text{kWh}^{-1}$) of primary and secondary streamers, both CDS and ADS, were determined separately. The obtained results are shown in Figure 8.1 and can be summarized as:

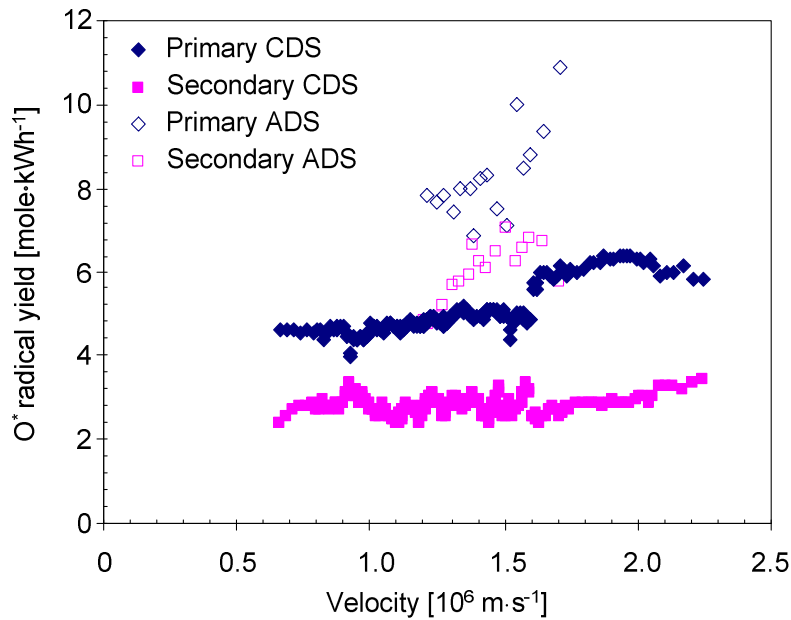


Figure 8.1. O^* radical yield of ADS and CDS primary and secondary streamers as function of the primary streamer velocity. This plot is identical to Figure 5.12.

- For CDS, the O^* radical yield of primary streamers exceeds that of secondary streamers (by up to a factor of two). The observed difference is contributed to the large electric field in the primary streamer head compared to the field in the secondary streamer. For primary streamer velocities up to $2.0 \cdot 10^6 \text{ m} \cdot \text{s}^{-1}$ it was observed that the yield of primary streamers is a rising function of the velocity. Above $2.0 \cdot 10^6 \text{ m} \cdot \text{s}^{-1}$, the yield starts to decrease. The secondary streamer yield was found to be constant. A well founded explanation for the relation between Y_{primary} and $v_{s, \text{primary}}$ could not be provided. Both the number of free electrons and the electron energy distribution function have to be known to analyze the process of the radical yield. Neither of these parameters were determined during the experiments.
- The observations for the ADS are similar to the ones for the CDS: primary streamers outperform (up to a factor of 1.5) the secondary streamers, at least for streamer velocities exceeding $1.2 \cdot 10^6 \text{ m} \cdot \text{s}^{-1}$. Also, the primary streamer O^* radical yield increases for higher streamer velocities. In contrast to the radical yield of CDS secondary streamers, the yield for ADS secondary streamers increases as a function of the primary streamer velocity.
- The O^* radical yield of ADS secondary streamers is considerably higher than the yield of the CDS secondary streamers. An explanation could not be provided. However, it was determined that the electric field in the secondary streamers is $22 \text{ kV} \cdot \text{cm}^{-1}$ and does not depend on the voltage polarity. As a result, the differences in yield cannot be explained by differences in the average electron energy. Also, it is unlikely that the number of free electrons in ADS is higher than in CDS, since the plasma current of ADS is lower (for identical pulses having opposite polarity). A lower current indicates a lower number of free electrons per unit-length of streamers.

- The O^* radical yield of ADS secondary streamers was found to be almost equal to that of the CDS primary streamers. This finding clearly demonstrates that the average electron energy is not the only parameter of interest. A considerable amount of radicals can be produced, even when the average electron energy is low.
- The ADS primary streamer has a significantly higher O^* radical yield than the CDS primary streamer. The different average applied electric fields during ADS and CDS measurements ($15\text{-}20\text{ kV}\cdot\text{cm}^{-1}$ vs. $8\text{-}15\text{ kV}\cdot\text{cm}^{-1}$) was mentioned as a possible explanation for the observed differences. However, since both the local electric field and the free electron density are unknown, no well founded explanation for the difference could be provided.

8.4 The total system efficiency of pulsed power modulators

High total system yield can be obtained when both the matching and the radical yield are optimized. For ADS, both the matching and the radical yield can be enhanced by increasing the applied voltage, see Figure 8.2. The pulse width is of secondary importance. Total system efficiencies of $4.6\text{ mole}\cdot\text{kWh}^{-1}$ have been obtained.

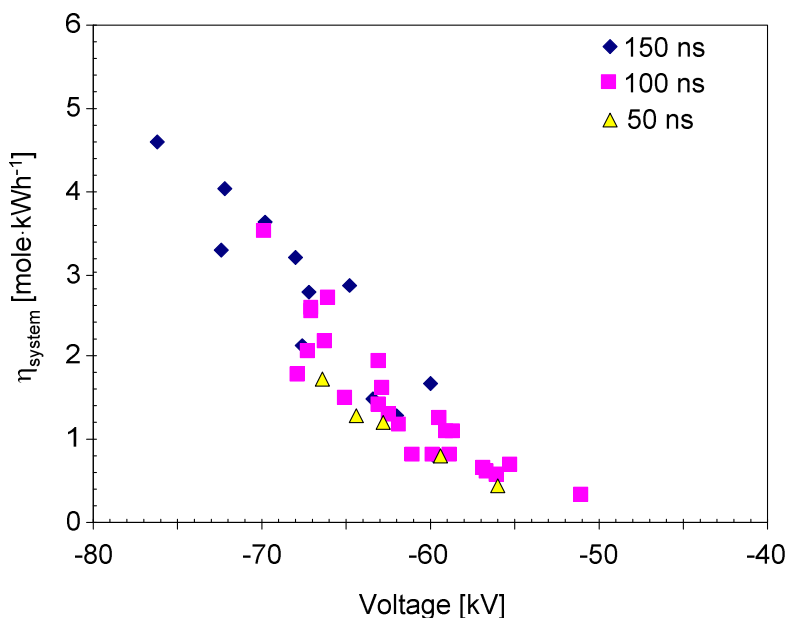


Figure 8.2. Total system yield for ADS as function of applied voltage, for different pulse widths. This plot is identical to Figure 6.6.

For CDS, the situation is more complicated. The matching can be improved by increasing the applied voltage, increasing the pulse width or decreasing the wire-plate distance. All these changes, however, result in decreased radical yields. The changes in matching and in radical yield, as a result of changed system settings, cancel almost completely, resulting in the same total system efficiency η_{system} for almost all combinations

of system settings. A distinction can only be made for low primary streamer velocities (see Figure 8.3). When the velocity is below $2.0 \cdot 10^6 \text{ m}\cdot\text{s}^{-1}$, the highest yields are obtained when R_{primary} (ratio of primary streamer duration to the pulse width) is small. For increasing primary streamer velocities, the effect of R_{primary} on the yield diminishes, eventually disappearing completely when the velocity exceeds $2.0 \cdot 10^6 \text{ m}\cdot\text{s}^{-1}$. The highest efficiencies obtained are $3.0 \text{ mole}\cdot\text{kWh}^{-1}$.

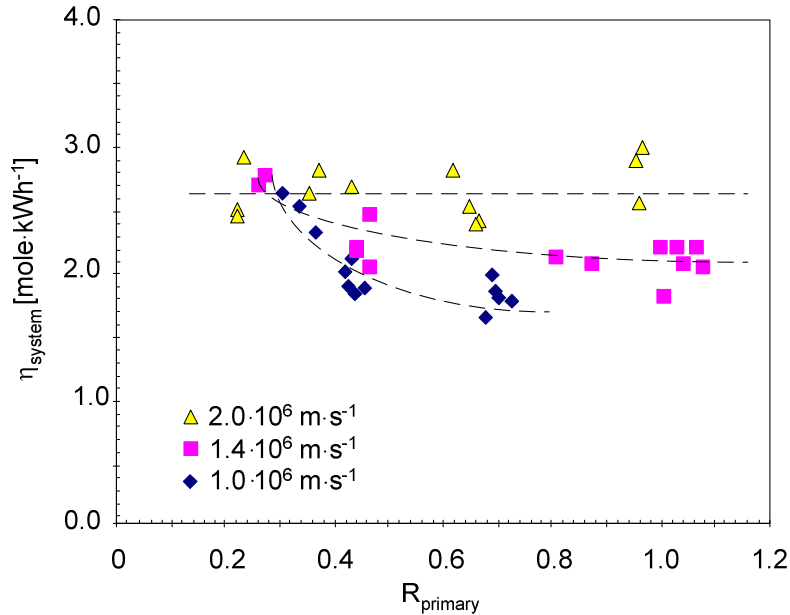


Figure 8.3. Total system yield for CDS as function of R_{primary} and the primary streamer velocity. This plot is identical to Figure 6.2.

A solution for the relatively poor total system efficiency (in comparison to ADS systems) of CDS-based systems can be obtained when a system is designed that recovers the energy not used for plasma generation (reflected energy and leftover capacitive energy of the reactor). The total yield of such a system is then governed by the quality of energy recovery and the radical yield. The system settings can then be chosen in such a way that high radical yields are obtained. It will be a challenge to develop such a system.

8.5 Large-scale streamer plasma generation

It was demonstrated that, with careful system design, a large scale (17 kW average power obtained), and energy efficient system (more than 90% of power grid energy dissipated by the plasma) can be constructed. Measurements clearly demonstrated that, by increasing the total applied voltage, the matching between the modulator and the reactor can be improved.

Fast rising, short pulses can be generated efficiently, despite the large capacitance of the industrial-scale reactor. For the HPPS system, this was accomplished by using a low-

impedance transmission-line transformer and by constructing the high-voltage part of the modulator as a coaxial transmission line. As a result of this latter adjustment, the effects of stray capacitance and inductance on the switching behavior could be reduced.

To validate the pollutant removal capabilities of the HPPS system, a feasibility study was performed. Odor removal from air was chosen as the process. The system test was performed at an industrial plant in which compost is produced. Measurements were performed on a (polluted) gas flow of $1,000 \text{ m}^3 \cdot \text{h}^{-1}$. The best results were obtained with an energy density of $7.2 \text{ J} \cdot \text{L}^{-1}$ (250 pps, $8 \text{ J} \cdot \text{pulse}^{-1}$): the (VOC) pollutant concentration decreased by 87% (from $8.987 \text{ mg} \cdot \text{m}^{-3} \rightarrow 1.185 \text{ mg} \cdot \text{m}^{-3}$). More than 95% of H_2S could be removed simultaneously (from $15.3 \text{ } \mu\text{g} \cdot \text{m}^{-3} \rightarrow < 0.8 \text{ } \mu\text{g} \cdot \text{m}^{-3}$).

The obtained results indicate that the HPPS system is a suitable option for odor abatement. Due to the large, stable average output power and the high energy conversion efficiency, the system can be used for large scale industrial applications. Since the measurements were only performed as a feasibility study, no effort was put into optimizing the pollutant removal efficiency. It is anticipated that the obtained results can be improved if the system is fine-tuned to the pollutant removal process.

8.6 Macroscopic streamer properties

A large amount of valuable data was obtained from time and spatial resolved ICCD photography of the streamer discharges. Streamer generation and propagation as a function of pulse parameters and reactor configuration was studied systematically.

The most interesting observations can be listed as:

- The primary streamer velocity is almost constant during propagation. Typical velocities found are in the order of $10^6 \text{ m} \cdot \text{s}^{-1}$ (CDS and ADS).
- The primary streamer velocity increases linearly with the applied voltage and the pulse rise rate (CDS and ADS).
- The diameter of the streamer increases linearly during transit. Typical diameters found are 0.7-3.0 mm (CDS and ADS).
- The growth of the diameter increases linearly with the applied voltage and the pulse rise rate. Typical velocities found are in the order of $10^5 \text{ m} \cdot \text{s}^{-1}$ (CDS and ADS).
- The number of streamers leaving the corona wire per meter is in the order of 1000-2000 and depends slightly on the rise rate (CDS and ADS).
- The number of streamers arriving at the plate electrode is determined by the average applied electric field. For CDS, below $4\text{-}7 \text{ kV} \cdot \text{cm}^{-1}$, no streamers cross the gap. For higher fields, the numbers of streamers reaching the plate electrode steadily increases to values of several hundreds of streamers per meter of reactor length. The minimum field is $10\text{-}15 \text{ kV} \cdot \text{cm}^{-1}$ for ADS.

- The length of the light-emitting part of the secondary streamer (near the wire, protruding into the gap) is determined by the applied electric field only (CDS and ADS).
- No visual effect of the pulse repetition rate on the streamer generation could be observed for pulse repetition rates up to 400 pulses per second and a gas flow rate of $30 \text{ Nm}^3 \cdot \text{h}^{-1}$.
- If the pulses are superimposed on a DC bias voltage above the corona onset level, the visual streamer appearance changes only slightly, compared to an "only pulse" situation (keeping the total peak voltage the same).
- Streamers (both CDS and ADS) can branch (a single streamer head splitting into two or more individual streamer heads) and interconnect (the merging of two individual streamers to form a single one).

Appendix A.I Ozone

Ozone (O₃) is a tri-atomic molecule consisting of three oxygen atoms. It is created from oxygen molecules (O₂), the much more stable diatomic molecule. Probably the first person to detect and describe ozone was the Dutch chemist Van Marum [Hos(1988)], in 1785. He noticed the characteristic smell of ozone when operating his electrifier. However, he failed to identify the smell as a unique form of oxygen. In 1840, the scientist Schönbein was the first to name the odorous gas ozone. The name ozone is derived from “ozein”, the Greek word for scent. After several studies related to ozone, the first generator was constructed in Germany, by Von Siemens, in the late 1840s. Since then, many ozonizers have been installed in industrial, office, and home applications. Most often ozone generators are constructed as a DBD system. Ozone yields are generally good, and such a system is easy to construct. A possible disadvantage is that the discharge gap is limited to a few millimeters. This results in large, bulky reactors for large gas flows.

At standard temperature and pressure, ozone is in the gas phase. It is a toxic compound, even in low concentrations. Due to health problems related to respiration, MAC values (Maximum Acceptable Concentration) for human exposure to ozone (8 hours per day, 5 days per week) is ~0.06 ppm. Ozone can be recognized by its pale blue color, but more noticeably by its strong smell. Humans are able to detect the presence of ozone at concentrations as low as 0.015 ppmv.

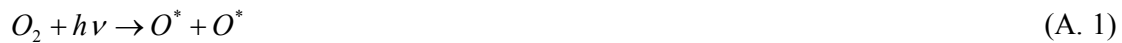
Ozone can be found in natural form in the Earth's atmosphere, in the so-called ozone layer. This layer prevents the sun's harmful UV-B and UV-C radiation from reaching Earth. Due to its strong oxidizing properties, ozone is often used for specific industrial applications. As an oxidizer, only sulfur outperforms ozone. However, like the strong oxidizer chlorine, sulfur is also very toxic. Although ozone is toxic, it does not leave behind harmful compounds after it has reacted with other molecules. This makes it a useful chemical agent for chemical processes such as:

- Chemical applications: disinfection of water, killing bacteria on food-contact surfaces, cleaning and bleaching fabrics, processing of plastics to enable adhesion of inks.
- Consumer applications: sanitation of food, water and household surfaces.
- Pharmaceutical applications: changing the body's antioxidant-pro-oxidant balance, decontamination of operating rooms.
- Etc.

Ozone is an unstable molecule that decays to molecular oxygen with a typical half-life of 10-30 minutes (depending on concentration and temperature). The lifespan of ozone decreases drastically with increasing temperatures. Due to this short lifespan, ozone cannot be produced and transported to the required location, but has to be generated on-site. Ozone can be produced by [Hos(1971)]:

- Electrolysis of sulfuric-acid;
- Photo-chemical treatment of oxygen/air;
- Electrical discharges.

When using the first method, yields of 4-12 g·kWh⁻¹ can be obtained, which is often too little for industrial applications. The continuous requirement for sulfuric-acid is also a disadvantage. Photo-chemical treatment of oxygen/air produces ozone approximately as efficiently as the electrolysis. For this technique, the gas is irradiated with UV light with wavelengths below 300 nm. The photons ($h\nu$) then have sufficient energy to dissociate oxygen molecules. The resulting oxygen radicals subsequently react with O₂ to produce ozone.



where M is a third body particle. In air, M usually is O₂ or N₂.

A problem related to photo-chemical production is that ozone is easily destroyed when irradiating it with UV light. For this technique to become efficient, monochromatic light is thus required with a wavelength optimal for ozone production but with negligible destruction. Wavelengths below 200 nm are usually used. Nevertheless, ozone yields remain relatively low (several g·kWh⁻¹).

The low-yield problem can be overcome using electrical discharges. Yields can be several hundreds of grams per kWh, depending on the gas conditions and energization method. Basically, high energetic electrons are present in electric discharges that can dissociate O₂ molecules and hence initiate ozone production reactions like A. 2.

Appendix A.II Reactions used in kinetic model

Reaction rates are in $\text{cm}^3 \cdot \text{s}^{-1}$ and $\text{cm}^6 \cdot \text{s}^{-1}$ for two and three body collisions respectively. T is the absolute temperature in K. Reactions taken from *Pey(1990)*.

Reaction		Rate-coefficient
$O + O + M \rightarrow O_2 + M$	$M = N_2, O_2$	$\frac{3.8 \cdot 10^{-30}}{T} \cdot \exp[-170/T]$
$O + O_2 + M \rightarrow O_3 + M$	$M = O_2$	$6.9 \cdot 10^{-34} \cdot (300/T)^{1.25}$
$O + O_2 + M \rightarrow O_3 + M$	$M = N_2$	$6.2 \cdot 10^{-34} \cdot (300/T)^2$
$O + O_2 + M \rightarrow O_3 + M$	$M = O_3$	$4.6 \cdot 10^{-35} \cdot \exp[1050/T]$
$O + O_2 + M \rightarrow O_3 + M$	$M = H_2O$	$9.9 \cdot 10^{-34} \cdot \exp[510/T]$
$O + O_3 \rightarrow O_2 + O_2$		$1.8 \cdot 10^{-11} \cdot \exp[-2300/T]$
$O_3 + O_2 \rightarrow O + O_2 + O_2$		$7.3 \cdot 10^{-10} \cdot \exp[-11400/T]$
$O_3 + O_3 \rightarrow O + O_2 + O_3$		$1.65 \cdot 10^{-9} \cdot \exp[-11400/T]$
$N + O + M \rightarrow NO + M$	$M = N_2, O_2$	$1.8 \cdot 10^{-31} \cdot T^{-0.5}$
$N + O_2 \rightarrow NO + O$		$4.4 \cdot 10^{-12} \cdot \exp[-3220/T]$
$N + O_3 \rightarrow NO + O_2$		$2.0 \cdot 10^{-11} \cdot \exp[-1070/T]$
$N + N + M \rightarrow N_2 + M$	$M = N_2, O_2$	$8.3 \cdot 10^{-34} \cdot \exp[500/T]$
$N + NO \rightarrow N_2 + O$		$3.1 \cdot 10^{-11}$
$N + NO_2 \rightarrow N_2O + O$		$2.1 \cdot 10^{-11} \cdot \exp[-800/T]$

Reaction		Rate-coefficient
$NO + O + M \rightarrow NO_2 + M$	$M = N_2$	$1.2 \cdot 10^{-31} \cdot (T/300)^{-1.82}$
$NO + O + M \rightarrow NO_2 + M$	$M = O_2$	$8.6 \cdot 10^{-32} \cdot (T/300)^{-1.82}$
$NO + O + M \rightarrow NO_2 + M$	$M = N_2O$	$1.7 \cdot 10^{-32} \cdot \exp[620/T]$
$NO + O_3 \rightarrow NO_2 + O_2$		$3.6 \cdot 10^{-12} \cdot \exp[-1560/T]$
$NO + NO + O_2 \rightarrow NO_2 + NO_2$		$3.3 \cdot 10^{-39} \cdot \exp[530/T]$
$NO + O_2 \rightarrow NO_2 + O$		$2.8 \cdot 10^{-12} \cdot \exp[-23400/T]$
$NO_2 + O \rightarrow NO + O_2$		$1.7 \cdot 10^{-11} \cdot \exp[-300/T]$
$NO_2 + O + M \rightarrow NO_3 + M$	$M = N_2, O_2$	$9.0 \cdot 10^{-32} \cdot (T/300)^{-2}$
$NO_2 + O_3 \rightarrow NO_3 + O_2$		$1.2 \cdot 10^{-13} \cdot \exp[-2450/T]$
$NO_2 + NO_2 \rightarrow NO + NO + O_2$		$3.3 \cdot 10^{-12} \cdot \exp[-13540/T]$
$NO_2 + NO_3 \rightarrow NO + NO_2 + O_2$		$2.3 \cdot 10^{-13} \cdot \exp[-1000/T]$
$NO_2 + NO_3 + M \rightarrow N_2O_5 + M$	$M = N_2, O_2$	$3.7 \cdot 10^{-30} \cdot (T/300)^{-4.1}$
$NO_3 + O \rightarrow O_2 + NO_2$		$1.0 \cdot 10^{-11}$
$NO_3 + O_2 \rightarrow O_3 + NO_2$		$7.0 \cdot 10^{-34}$
$NO_3 + NO \rightarrow NO_2 + NO_2$		$2.0 \cdot 10^{-11}$
$NO_3 + NO_3 \rightarrow NO_2 + NO_2 + O_2$		$5.0 \cdot 10^{-12} \cdot \exp[-3000/T]$

Reaction	Rate-coefficient
$N_2O + O \rightarrow N_2 + O_2$	$1.7 \cdot 10^{-10} \cdot \exp[-14100/T]$
$N_2 + O_2 \rightarrow N_2O + O$	$1.1 \cdot 10^{-10} \cdot \exp[-55200/T]$
$N_2O + O \rightarrow NO + NO$	$7.2 \cdot 10^{-11}$
$N_2O_5 + O \rightarrow NO_2 + NO_2 + O_2$	$1.0 \cdot 10^{-16}$
$N_2O_5 + M \rightarrow NO_2 + NO_3 + M$	$M = N_2$ $2.2 \cdot 10^{-3} \cdot (T/300)^{-6.1} \cdot \exp[-11080/T]$
$N_2O_5 + M \rightarrow NO_2 + NO_3 + M$	$M = O_2$ $2.0 \cdot 10^{-2} \cdot (T/300)^{-6.1} \cdot \exp[-11080/T]$
$H_2O + O \rightarrow OH + OH$	$1.0 \cdot 10^{-11} \cdot \exp[-550/T]$
$O + OH \rightarrow O_2 + H$	$2.3 \cdot 10^{-11} \cdot \exp[110/T]$
$O_2 + H \rightarrow O + OH$	$3.7 \cdot 10^{-10} \cdot \exp[-8450/T]$
$OH + O_3 \rightarrow HO_2 + O_2$	$1.9 \cdot 10^{-12} \cdot \exp[-1000/T]$
$OH + OH \rightarrow H_2O + O$	$4.5 \cdot 10^{-12} \cdot \exp[-275/T]$
$OH + OH + M \rightarrow H_2O_2 + M$	$M = N_2, O_2$ $6.5 \cdot 10^{-31} \cdot (T/300)^{-0.7}$
$OH + OH \rightarrow HO_2 + H$	$2.0 \cdot 10^{-11} \cdot \exp[-20200/T]$
$OH + HO_2 \rightarrow H_2O + O_2$	$8.3 \cdot 10^{-11} \cdot (T/335)^{0.25}$
$OH + H_2O_2 \rightarrow H_2O + HO_2$	$2.9 \cdot 10^{-12} \cdot \exp[-160/T]$
$HO_2 + O \rightarrow OH + O_2$	$8.0 \cdot 10^{-11} \cdot \exp[-500/T]$

Reaction	Rate-coefficient
$HO_2 + O_3 \rightarrow OH + O_2 + O_2$	$1.4 \cdot 10^{-14} \cdot \exp[-600/T]$
$HO_2 + HO_2 \rightarrow H_2O_2 + O_2$	$4.0 \cdot 10^{-14} \cdot \exp[1200/T]$
$HO_2 + H_2O \rightarrow H_2O_2 + OH$	$4.7 \cdot 10^{-11} \cdot \exp[-16500/T]$
$H_2O_2 + O \rightarrow HO_2 + OH$	$1.0 \cdot 10^{-11} \cdot \exp[-2500/T]$
$H + O_2 + M \rightarrow HO_2 + M$	$M = N_2, O_2$ $5.9 \cdot 10^{-32} \cdot (300/T)$
$H + O_3 \rightarrow OH + O_2$	$1.1 \cdot 10^{-10} \cdot \exp[-480/T]$
$H + O_3 \rightarrow HO_2 + O$	$1.0 \cdot 10^{-11} \cdot \exp[-480/T]$
$H + HO_2 \rightarrow OH + OH$	$4.2 \cdot 10^{-10} \cdot \exp[-950/T]$
$H + HO_2 \rightarrow H_2O + O$	$9.0 \cdot 10^{-13}$
$H + H_2O_2 \rightarrow OH + H_2O$	$5.0 \cdot 10^{-12} \cdot \exp[-1900/T]$
$N_2 + OH \rightarrow N_2O + H$	$5.4 \cdot 10^{-12} \cdot \exp[-40000/T]$
$N + OH \rightarrow NO + H$	$3.8 \cdot 10^{-11} \cdot \exp[85/T]$
$NO + OH \rightarrow NO_2 + H$	$5.2 \cdot 10^{-12} \cdot \exp[-15000/T]$
$NO + OH + M \rightarrow HNO_2 + M$	$M = N_2, O_2$ $6.5 \cdot 10^{-31} \cdot (T/300)^{-2.4}$
$NO + HO_2 \rightarrow NO_2 + OH$	$3.7 \cdot 10^{-12} \cdot \exp[240/T]$
$NO + H_2O_2 \rightarrow HNO_2 + OH$	$1.0 \cdot 10^{-20}$

Reaction	Rate-coefficient
$NO + HO_2 \rightarrow HNO_3^*$	$1.4 \cdot 10^{-13}$
$NO_2 + H \rightarrow NO + OH$	$5.8 \cdot 10^{-10} \cdot \exp[-740/T]$
$NO_2 + OH + M \rightarrow HNO_3 + M^*$ $M = N_2, O_2$	$2.6 \cdot 10^{-30}$
$NO_2 + HO_2 \rightarrow HNO_2 + O_2$	$2.0 \cdot 10^{-14}$
$NO_3 + H_2O \rightarrow HNO_3 + OH$	$5.0 \cdot 10^{-21}$
$N_2O_5 + H_2O \rightarrow HNO_3 + HNO_3$	$5.0 \cdot 10^{-21}$
$HNO_2 + OH \rightarrow NO_2 + H_2O$	$1.3 \cdot 10^{-13}$
$HNO_3 + O \rightarrow NO_3 + OH$	$5.0 \cdot 10^{-15}$
$HNO_3 + OH \rightarrow NO_3 + H_2O$	$1.5 \cdot 10^{-14} \cdot \exp[650/T]$

* Reaction and rate taken from NIST chemical database

Appendix B.I Experimental set-up component values

Table B.I.1. Component values of the power modulator

Component	Value	Remark
L ₁ , L ₂	10-30 μ H	Toroid, air core
L ₄	370 μ H	Solenoid, air core
L	10 μ H	Solenoid, air core
L _{DC}	2 mH	Solenoid, air core
C ₀	3.3 mF	Electrolyte
C _L	2-11 μ F	Polypropylene, matched to C _h , $C_L = n^2 \cdot C_h$
PFL	0.6-3 nF	Coaxial HV cables (100 pF·m ⁻¹)
C _{DC}	1.3-3.9 nF	Ceramic, $C_{DC} \geq V_{sg} \cdot C_h / 2V_{DC}$ (eq. 4.8)
C	30-80 pF	Ceramic, matched to the PFL [Win(2005b), Yan(2001)]
Pulse transformer	1:60 winding ratio	Homemade, oil filled
R	400 k Ω	2W carbon composite
R ₄ , R ₅	10-15 k Ω	Non-inductive, linear disc resistors
D ₁ , D ₂ , D _{DC}	40 kV hold-off, 8 A conducting current	Fast recovery diodes
Magnetic core A	$\mu_r = 245$	Increase sec. mode impedance, Metglas
Magnetic core B	$\mu_r \sim 120$	Absorption of reflected energy, Ferroxcube
Pos. DC supply:	1-30 kV, 15 kW max	
Neg. DC supply:	1-20 kV, 2 kW max	Harmonic oscillator combined with rectifying circuit.

Appendix B.II HPPS component values

Table B.II.1. Component values of the HPPS

Component	Value	Remark
L_1, L_2	10-30 μH	Toroid, air core
L_4	400 μH	Solenoid, air core
L	10 μH	Solenoid, air core
L_{DC}	1.3 mH	Solenoid, air core
C_0	6.6 mF	Electrolyte
C_L	<40 μF	Polypropylene, matched to C_h , $C_L = n^2 \cdot C_h$
C_h	<32 nF	Ceramic
C_{DC}	14 nF	Ceramic, $C_{\text{DC}} \geq V_{\text{sg}} \cdot C_h / 2V_{\text{DC}}$ (eq. 4.8)
C	200 pF	Ceramic, matched to C_h [Win(2005b), Yan(2001)]
Pulse transformer	1:36 winding ratio	NorthStar, oil filled
R	1.1 M Ω	2W carbon composite
R_4, R_5	10-15 k Ω	Non-inductive, linear disc resistors
D_1, D_2, D_{DC}	40 kV hold-off, 8 A conducting current	Fast recovery diodes
Magnetic core A	$\mu_r = 245$	Increase sec. mode impedance, Metglas
Magnetic core B	$\mu_r \sim 540$	Absorption of reflected energy, Ferrite
DC supply	1-30 kV, 15 kW max	

Appendix C.I Details of the coaxial spark-gap switch*

Table C.I.1. Geometric details of the coaxial spark-gap switch

Component	Material	Length [mm]	Diameter [mm]
Anode/Cathode	Brass	114	61
Trigger electrode	Brass	202	65
Ground structure	Stainless steel	252	108

Table C.I.2. Typical characteristics of the coaxial spark-gap switch

Parameter	Value
Max. pressure	7 bars
Max. flow rate	35 Nm ³ ·h ⁻¹
Line impedance	25 Ω
Max. repetition rate	1000 pps
Max. switching voltage	60 kV
Max. average power	10 kW

Appendix C.II Performance validation

This appendix describes the measurements performed to validate the coaxial spark-gap switch performances. The diagnostic tools for the electric measurements are described in Section 3.4.1. For the measurements shown here, the PFL charging voltage (V_{sg}) was fixed at 34 kV (0.75 J·pulse⁻¹). To enable measurements at a high pulse repetition rate, a wire-plate reactor was used as the load, instead of a matched resistive load. In general, due to impedance mismatch between source and reactor, part of the energy reflects back towards the source. This way the recovery time of the switch becomes longer in comparison with a matched resistive load.

Measurements concerning the voltage, pressure, pulse repetition rate, and dry air flow rate are shown in Figures C.II.1 through C.II.4. Each marker in the plots is the result of averaging over 1000 shots. Figure C.II.1 shows the average switching voltage as function of pulse repetition rate. Looking at the line “with gas flow”, a small decrease of the average voltage as function of pulse repetition rate can be seen. This is caused by the decreasing voltage on C_0 for high pulse repetition rates (since $C_0 \neq \infty$). During the measurements this effect was counterbalanced by slightly increasing the input voltage of the source for higher pulse repetition rates.

* Parts of this chapter have already been published in *Win(2005b, c, d)*.

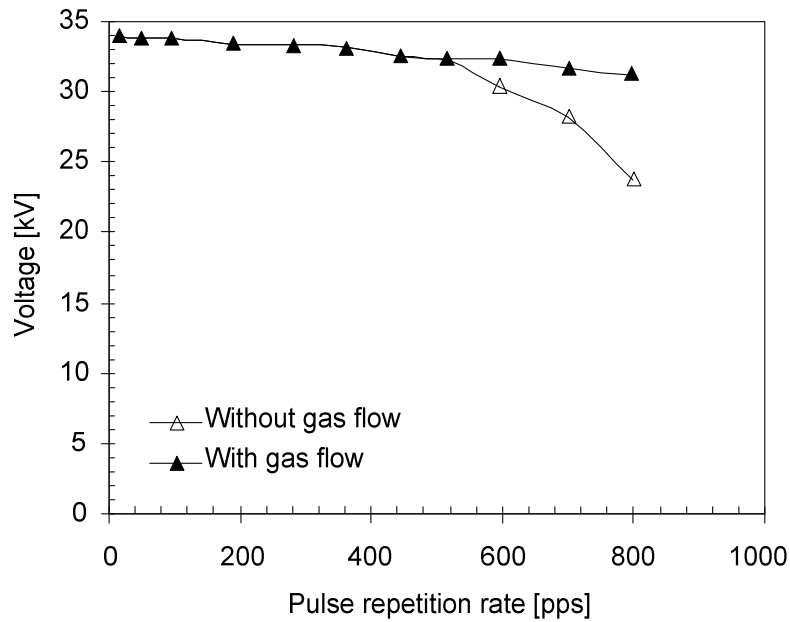


Figure C.II.1. Average switching voltage as function of pulse repetition rate.

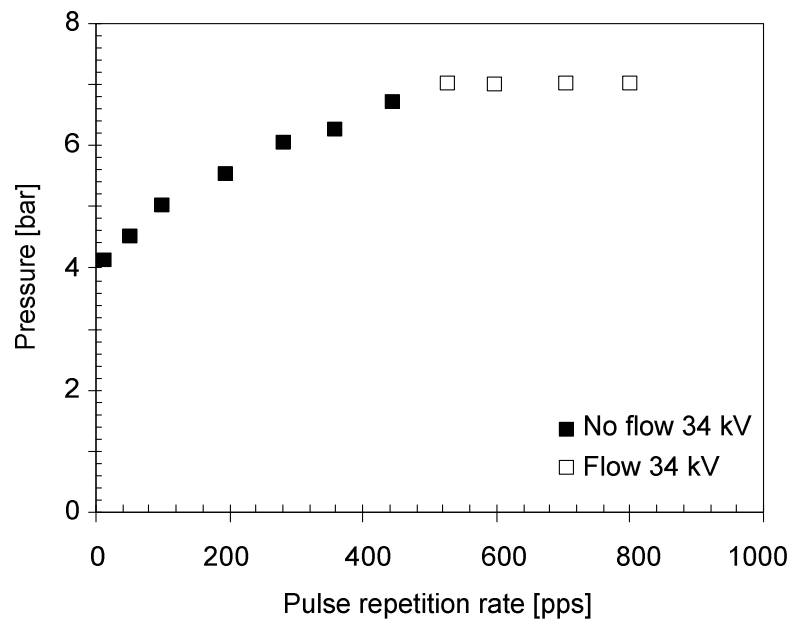


Figure C.II.2. Required spark-gap pressure for stable switching as function of pulse repetition rate. Measurements for 34 kV charging voltage are shown. In the region below the markers the switch will pre-fire. The pressure was determined at the gas inlet of the switch.

At up to ~450 pps no gas flow was needed to prevent pre-firing; it was only necessary to increase the pressure inside the gap (Figure C.II.2, C.II.3). Whether or not the switch was pre-firing was determined by measuring the average switching voltage. For a given pressure and gas flow rate, the measured average switching voltage was compared with the maximum attainable value (optimized pressure and flow rate). A smaller average switching voltage indicates that pre-firing occurs. For higher pressures, the gas in the switch recovers to its original properties more quickly. The typical design of the coaxial spark-gap switch, together with the LCR trigger method, enables operation over a broad pressure range. When switching 34 kV pulses, for example, the pressure can be between 4 and 7 bar.

The obtained recovery time of ~2 ms, for a non-flushed switch, is very short compared to other work [e.g., Bis(1998), Kou(1999), Mac(1997)]. This is probably due to the combination of low energy transfer per pulse, short gap distances and large electrode surfaces. The electrodes act as heat sinks, quickly restoring the gas temperature to the initial temperature. Ions generated during the spark move to the electrodes in less time because of the short distance.

Besides stabilizing the switch by increasing the pressure, the spark-gap switch can also be stabilized by increasing the gas flow rate. For higher gas flows, the spark residue of the preceding sparks is removed from the switch more quickly. This can be seen in Figure C.II.3, where the velocity-pressure as function of pulse repetition rate dependency is shown. The air velocity (in $\text{m}\cdot\text{s}^{-1}$) in the gap was determined as follows:

$$v = \frac{p_2}{p_1} \cdot \frac{F}{A} \quad (\text{eq. C.II.1})$$

in which p_1 is the spark-gap pressure, p_2 (= 1 bar) is the pressure at the exhaust of the switch (where the flow rate measurements were performed), F is the flow rate [$\text{m}^3\cdot\text{s}^{-1}$], determined by measuring the time required to fill a fixed volume to atmospheric pressure with the exhaust gas of the switch, and A (= $3.96\cdot 10^{-4} \text{ m}^2$) is the flow cross section in the gap (between electrodes and trigger).

The markers in Figure C.II.3 indicate the conditions for which the switch fires directly after the charging of the PFL has been completed. For conditions in the region below the markers, the switch might pre-fire. For conditions in the region above the markers, the switch will late-fire. The results clearly demonstrate the beneficial use of both pressure and flow as stabilization method. For most pulse repetition rates, several combinations of pressure and flow rate exist. For continuous operation it is preferred to use a large air flow rate to remove the evaporated electrode material from the gap, preventing its accumulation inside the switch or on the insulators.

To demonstrate the long-term stability of the switch in combination with the resonant charging unit, the system was run continuously for 2.5 hours at 100 pps. An average

measurement of 1000 pulses was performed every minute. The obtained average switching voltage over the complete time period was 34.4 kV, and its standard deviation (expressed as percentage of the average voltage) is 0.7%.

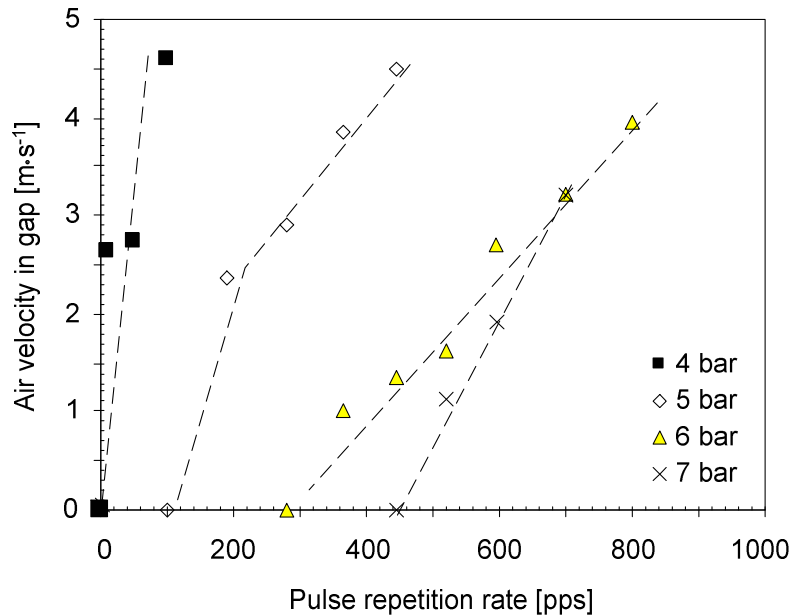


Figure C.II.3. Required air velocity-pressure for stable switching as function of pulse repetition rate. The markers indicate the operating conditions at the limit between pre-firing (below markers) and late-firing (above markers), for a specific pressure.

Another interesting topic for switches is the switching time delay and its jitter. In practice, the switch does not close at the exact same moment the charging has completed. In other words, there is a time delay between complete charging and switch closing, see Figure C.II.4a. This time delay can be determined accurately by using the time derivative of the voltage on the anode (see Figure C.II.4b). Due to the statistical nature of the inception time lag of the discharges, the time delay can vary from one shot to the other. When averaging the time derivative of the voltage on the anode for a large number of shots, a “bell”-shaped distribution as shown in Figure C.II.4c will be observed. The width of this distribution, measured at half the maximum value (FWHM), is used as a measure of the jitter.

Typical results obtained by following this procedure are shown in Figure C.II.5. As can be seen, the maximum pulse repetition rate was limited to 280 pps. Above this frequency the excessive time-jitter prevented accurate measurements. For a fixed pulse repetition rate, the time delay and jitter were varied by changing gas pressure and flow rate. However, only situations without pre-fire were measured (in other words, the jitter is always less than or equal to the time delay). The long time delays are obtained when the pressure is increased.

As a result, the switch closes more difficultly and consequently the jitter increases. For higher repetition rates, the time delay and jitter have similar values. The spark residue from the preceding sparks facilitates switch closing. Late firing cannot be observed anymore, only firing directly or shortly after the charging is completed.

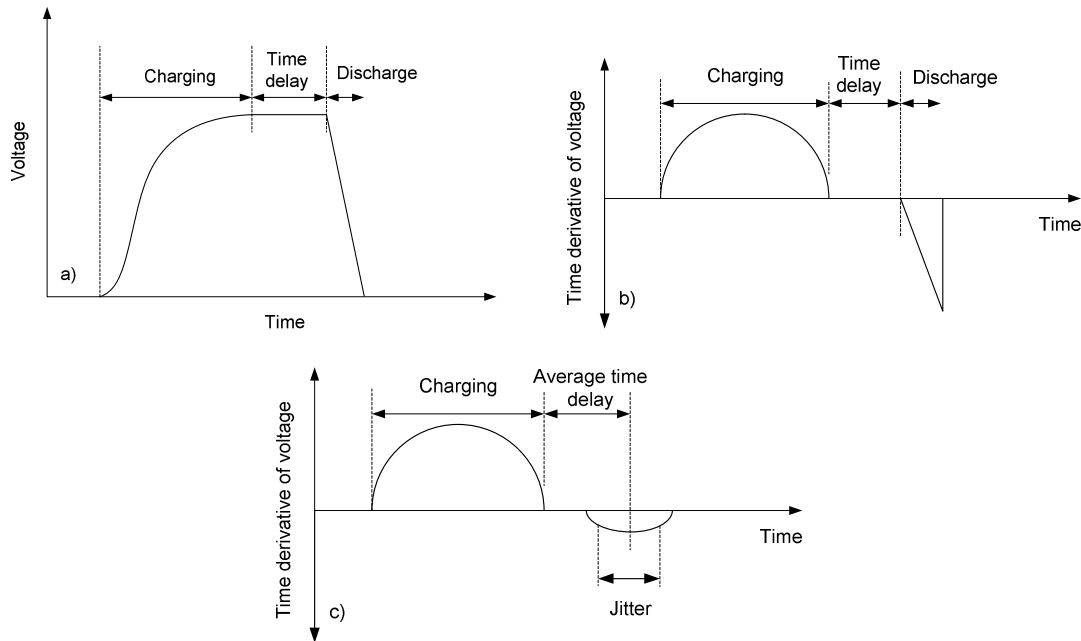


Figure C.II.4. a) Voltage waveform on the anode (PFL side) of the spark-gap switch. For clarity, the discharge time has been greatly enhanced relative to the charging time and the time delay. b) The time derivative of the voltage as shown in a). c) The time derivative of the voltage, averaged over multiple shots.

Measurements regarding the lifetime of the switch have not yet been performed, since this can only be done after a large number of shots (mass or volume difference measurement). However, an estimate of the electrode lifetime of the switch can be made using the following assumptions:

- According to *Kou(1999)*, the erosion rate for brass is $\sim 8 \cdot 10^{-6} \text{ cm}^3 \cdot \text{C}^{-1}$. For 10 J, 60 kV, 100 ns pulses this results in $10^{-9} \text{ cm}^3 \cdot \text{shot}^{-1}$. It is believed that this value is an overestimation of the actual erosion rate. In *Yan(2001)*, the erosion rate was measured to be an order of magnitude less (i.e., $10^{-10} \text{ cm}^3 \cdot \text{shot}^{-1}$) for pulse conditions similar to the ones used in this study.
- The electrode erosion is uniform (see Figure C.II.6).
- The erosion rates for anode, cathode and trigger electrode are equal.
- A layer with a thickness of about 2 mm is allowed to evaporate before the electrodes cannot be used anymore. During the increase of the inter-electrode distance; the pressure has to be decreased to maintain stable switching performance.

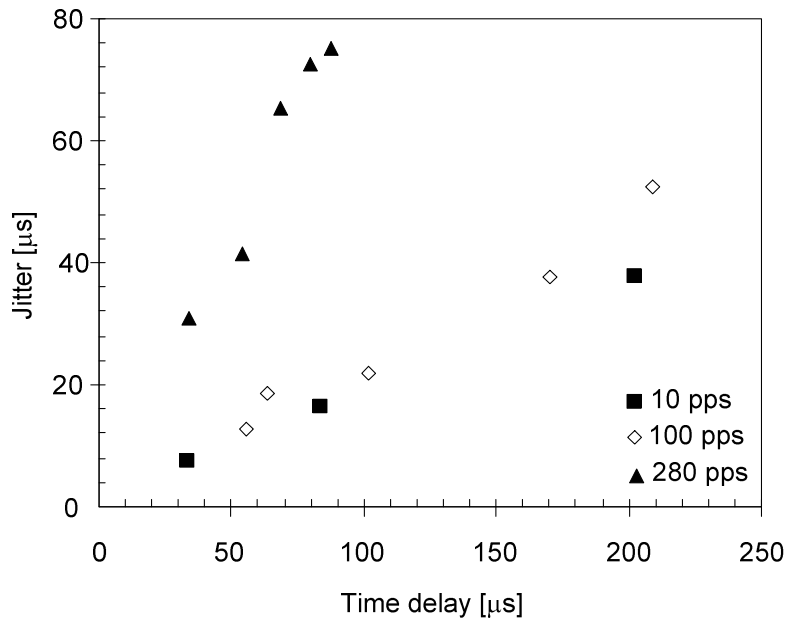


Figure C.II.5. Jitter as function of time-delay and pulse repetition rate.

Using the information presented in Table C.I.1 it can be calculated that about 40 cm^3 of electrode material (for one electrode) is allowed to evaporate. With the erosion rate assumed by *Kou(1999)*, the switch can be used for up to 10^{10} shots, which is equal to a total charge transfer of 10^6 C for the pulse conditions mentioned above. When operated continuously at a repetition rate of 1000 pulses per second, this corresponds to a lifetime of 4 months. This approximation is a lower boundary for the actual lifetime, as it is expected that the erosion rate assumed by *Kou(1999)* is over-estimated (see above).

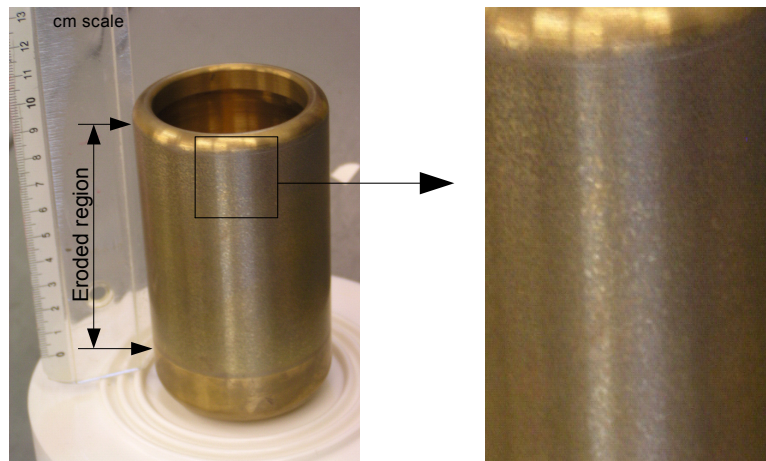


Figure C.II.6. High-voltage electrode and an enlargement of electrode surface. The white disc in the left picture is the high-voltage feed-through.

An observation made when studying the electrode surfaces after the first thousand shots was that the generated arcs do not remain located at the same position. Instead, they move along the surface of the electrodes. Due to the short duration of the arc, the air flow in the gap is of no influence on the arc movement. The movement can be caused by the following effect:

In an electric circuit, if possible[†], the area of the enclosed surface is maximized as a result of the repelling Lorentz forces generated by the current. In other words, the current loop strives to maximize its self-inductance. For the described switch, this can be accomplished by moving the two arcs along the electrode surfaces. Predicting the exact direction of arc movement is difficult, since the current loop is a 3D structure. Nevertheless, as a result of the Lorentz force, the arcs will move along the electrode surfaces.

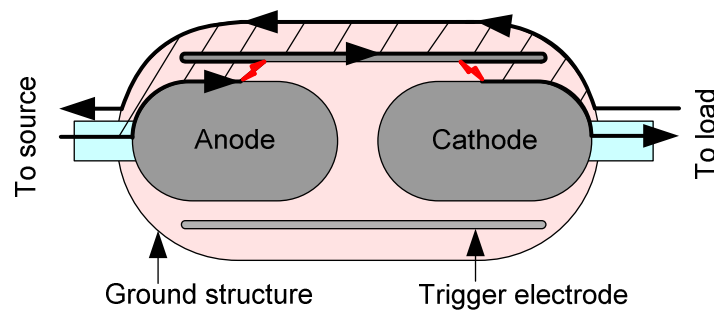


Figure C.II.7. Schematic of the spark-gap switch showing the current path when the switched is completely closed. The enclosed surface area is also indicated. The specific current path on the surface of the trigger electrode is a result of Lenz’s law; the current will distribute in such a manner that varying magnetic flux inside the conductor is minimized.

The effect of the “moving arc” mechanism on the electrode erosion has not yet been taken into account in the foregoing calculation. However, in *Leh(1989)* it was shown that the erosion rate for moving arcs can be a factor of 10 lower than a stationary arc under the same pulse parameters. As a result of the arc movement, the local spot temperature, where the arc connects to the electrode surface, does not increase as much as would be the case for a stationary arc. As the evaporation rate is a positive function of the local temperature [*Leh(1989)*], a moving arc will evaporate less of the electrode material.

Together with the erosion rate as determined in *Yan(2001)*, this implies that the lifetime of the switch as determined using the data provided by *Kou(1999)* might be underestimated by up to 2 orders of magnitude. Based on these arguments it is expected that the actual lifetime of the switch will be several years when operated continuously at 1000 pulsed per second.

[†] Obviously, if the current carrying conductors are rigid, the shape of the enclosed surface cannot be changed.

Appendix D Streamer observations and discussion^{*}

A part of the discussion presented in the preceding chapters was based upon the data obtained from the ICCD pictures. The plasma volume, primary streamer velocity and the length of the secondary streamer could be determined and used for the discussion. However, more data was obtained from the ICCD pictures. Although the obtained results were not required for explaining the efficiency variations of the plasma, they do yield valuable insights that can be used to deepen the understanding of streamer generation and as comparison material for other streamer related studies.

D.1 Side-view photography

In this section, the results obtained from time-resolved and time-integrated side-view photography measurements are discussed.

D.1.1 Effect of pulse repetition rate and of preceding pulses on streamer appearance

During experiments, no differences in plasma generation were observed (see Figure D.1) as function of the pulse repetition rate (ppr, up to 400 pps). All determined parameters (velocity, diameter, etc.) remained unchanged. According to *Pancheshnyi* [Pan(2005)], the plasma appearance should change once the pulse repetition rate is above a few pulses per second. Due to the preceding pulses, altered molecules like meta-stables, ions, attached electrons or excited species might be present. If these species are available in large quantities, the discharge behavior can be changed. Electrons are then more readily produced, and streamers can be formed more easily. The obtained results indicate that this is not the case and, consequently, the claim of *Pancheshnyi* is contradicted. Some care has to be taken with this statement. The resolution of the measurements is limited. Differences might exist that are not distinguishable in the pictures.

During experiments it was also observed that there are no visual differences between the 1st shot of the system and the nth shot ($n \in [10^1, 10^4]$). For the 1st shot, the gas in the reactor is neutral. The only free electrons are created by natural background ionization (like cosmic radiation and radioactivity). For the nth pulse, the situation can be different, as mentioned above. The measurements performed up to a ppr of 400 pps and a gas flow rate of $30 \text{ m}^3 \cdot \text{h}^{-1}$, however, showed no difference between pictures taken during the 1st and the nth shot of the system. A typical example is shown in Figure D.1. This figure shows the distance the streamer head traveled from the wire as a function of time. Other parameters showed similar behavior (not shown in this thesis).

^{*} Parts of this appendix have already been presented in *Win(2006a, b)*.

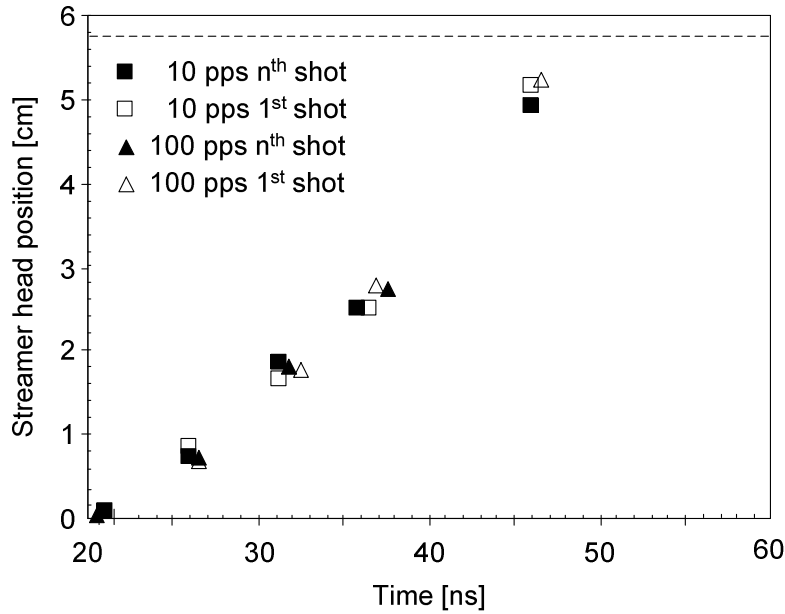


Figure D.1. Effect of pulse repetition rate on streamer head position (from the wire). Also shown is the comparison between the 1st and nth shot of the system. Pulses: 77 kV, 1.6 J·pulse⁻¹, rise rate 2.8 kV·ns⁻¹, pulse width 100 ns.

Since no effects of residual species from preceding pulses can be observed in the visual appearance of the streamers, it has to be concluded that either the concentration of the residue species is too low, or the presence of these species does not alter the streamer mechanism.

D.1.2 Effect of DC bias voltage on streamer appearance

As mentioned in Section 3.1.6, the DC bias voltage has a separate effect on the streamer generation when the DC level exceeds the DC corona onset voltage level. The observed differences are: slightly (10-20%) thinner streamers crossing the gap, more streamers (10-20%) leaving the reactor wire and decreased average light intensity of the ICCD pictures. The streamer velocity was not affected noticeably by the DC level.

Figure D.2 shows a typical example. In this graph, the average light intensity of the ICCD picture (total number of counts divided by the total number of pixels) as a function of the applied voltage is plotted. The results show that the average light intensity increases as the applied voltage is increased. Obviously this is caused by the increased energy dissipation. It can, however, be seen that for a fixed pulse width the curve does not follow a single line. Instead, for those measurements where the applied voltage was above the DC corona onset, a reduced light intensity is measured. When comparing Figure D.2a and D.2b it can be seen that the deviations from the line increase when the pulse width is reduced. This indicates that the differences are mainly to be found in the primary streamer generation.

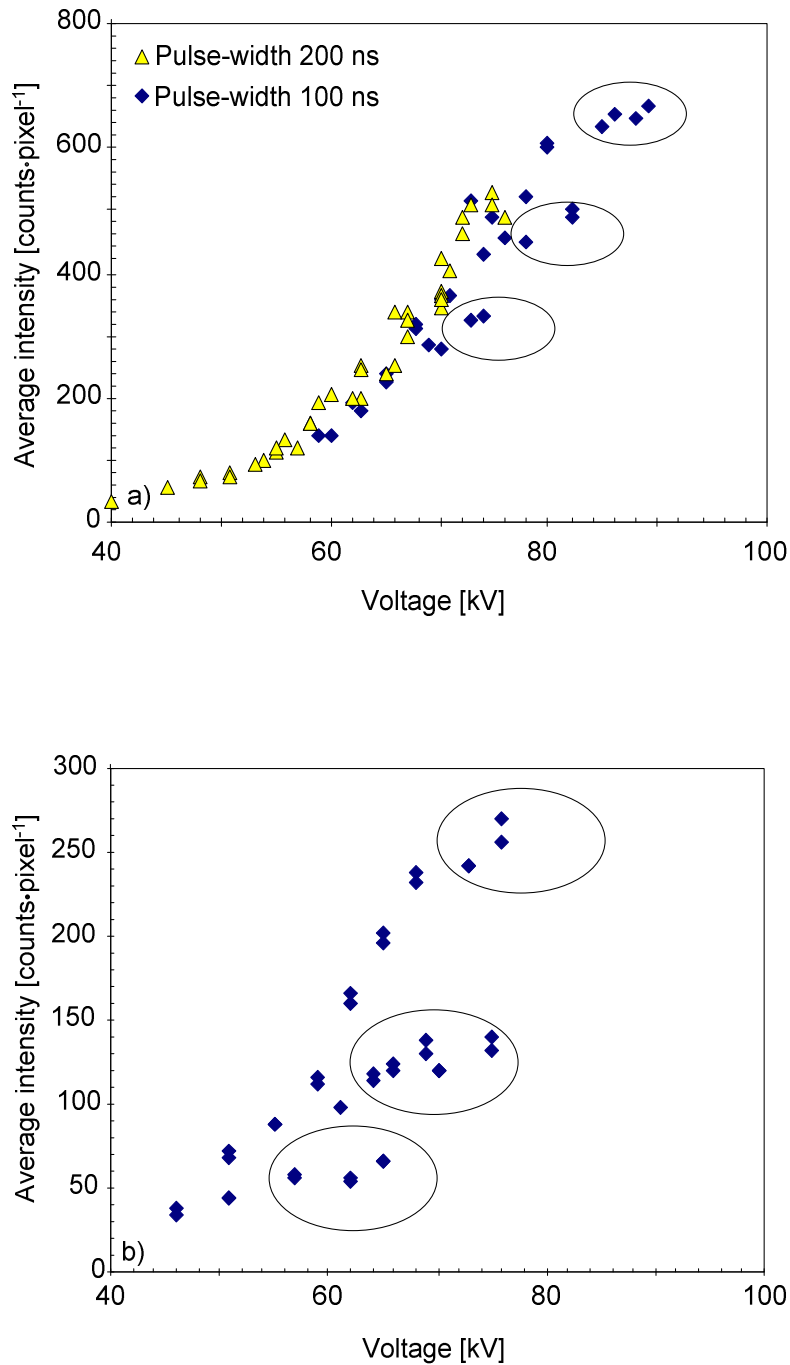


Figure D.2. Average light intensity as function of applied voltage and pulse width. Measurements performed on reactor configuration A with positive polarity pulses. Wire-plate distance fixed to 57 mm. In the circles, except for the 200 ns pulse width results, the measurements with DC voltages above 11 kV are shown. a) Pulse width: 100-200 ns. b) Pulse width: 30 ns.

The DC corona onset voltage was determined in two separate experiments. Firstly, the DC current was measured as function of DC voltage, without the presence of pulses. For this measurement, a shunt resistor was connected in the grounding connection of the reactor, across which the voltage was determined. The result of the measurements can be seen in Figure D.3. Secondly, 400 ns time-integrated, side-view ICCD pictures of the corona wire were taken for various DC bias voltages. Above the DC onset, the plasma appeared as a glow around the corona wire, extending a millimeter into the gap. The average light intensity of the photographs is plotted in Figure D.3. From both measurements it can be concluded that for DC levels above 11 kV, plasma glow is present around the wire. It has to be stressed that the onset voltage is strongly determined by the shape of the active wire. The results shown in Figure D.3 are typical for the employed corona wire with a diameter of 0.4 mm.

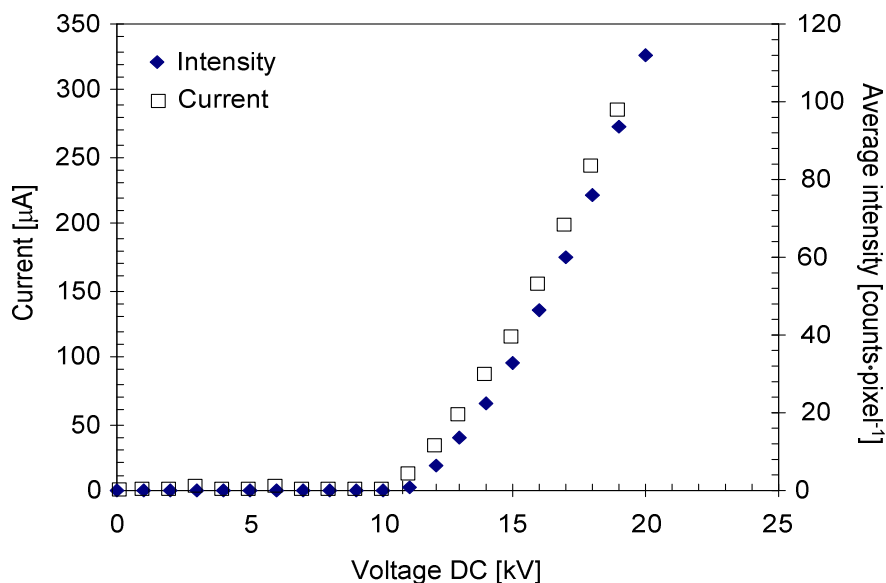


Figure D.3. Determination of DC corona onset level by means of electrical and optical measurements. The shown characteristic is for reactor configuration A, with a wire-plate distance of 57 mm.

Although the energy dissipated in the DC glow is small, and the O^* radical production was determined to be negligible ($< 20 \text{ mmol}\cdot\text{kWh}^{-1}$), this glow has an effect on streamer generation at the moment the pulse is applied to the reactor. As a result of the glow, ionized and excited species are already present in the high electric field. Compared to situations in which no DC corona is present, the streamers can be generated more easily.

D.1.3 Streamer velocity

The primary streamer velocity has already been discussed in Chapters 3, 4 and 5. Therefore only a short summary is presented here. During propagation in the reactor gap, the velocity remains constant. Only near the plate electrode does the streamer accelerate. The

magnitude of this acceleration increases for higher applied voltages. As the local electric field in the streamer head has to increase near the plate due to the proximity effect, this finding supports the idea that the relation between the velocity and the local electric field is a positive one.

The velocity of the streamers increases for increased applied electric fields and for increased voltage rise rates. The streamer velocity for CDS is higher than that for ADS if the same electric field is applied, although the differences are small. Typical values for the velocity are $\sim 10^6$ m·s⁻¹. These values agree well with results in the literature.

D.1.4 Streamer diameter

The streamer diameter (determined as the width at 20% of the maximum value) was determined as function of time for various parameter (pulse and reactor) settings. Near the wire, typical streamer diameters found are in the range of 0.7-1.0 mm. The smallest diameters are found when the applied voltage and/or the rise rate are reduced, i.e., when the applied electric field becomes smaller. During streamer propagation, the diameter increases linearly, up to 2.0-3.0 mm, depending on the applied voltage and rise rate. Only near the plate electrode is an acceleration in the growth observed. This behavior is identical to that of the streamer velocity.

As was mentioned in Chapter 3, these values are almost an order of magnitude larger than those mentioned in the literature. Nevertheless, thicker streamers (up to 1 centimeter diameter) have also been reported [Blo(1997)], usually in situations where large voltages are used.

Figure D.4a shows the diameter growth as function of the voltage rise rate. For this plot, the wire-plate distance was fixed at 57 mm. Only results for positive polarity pulses are presented here. In Figure D.4b the diameter growth as function of applied voltages for different wire-plate distances is shown. For this plot, only the results of pulses with a rise rate of 2.0-2.5 kV·ns⁻¹ have been used. Finally, in Figure D.4c, a comparison between positive and negative voltage polarity is made. In this case, all measurements have been performed on reactor A with a wire-plate distance of 37 mm. The trends are similar to those of the velocity. The diameter growth increases for decreasing wire-plate distance, increasing applied voltages and for increasing rise rate.

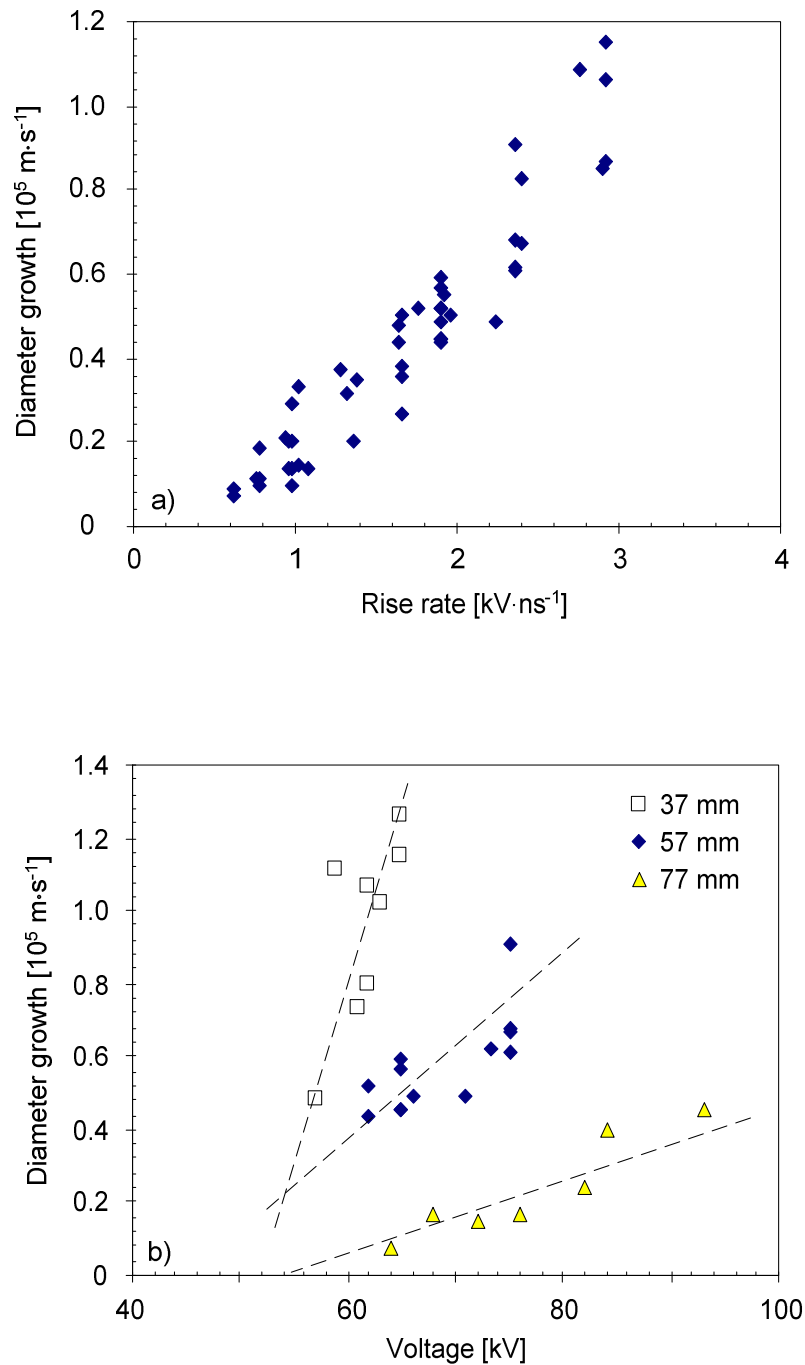


Figure D.4. a) Diameter growth as function of rise rate. Wire-plate distance was 57 mm. Only the results of positive polarity pulses are shown. Applied voltage: 50-85 kV. b) Diameter growth as function of applied (positive) voltage for various wire-plate distances. The rise rate was fixed at 2.0-2.5 kV·ns⁻¹.

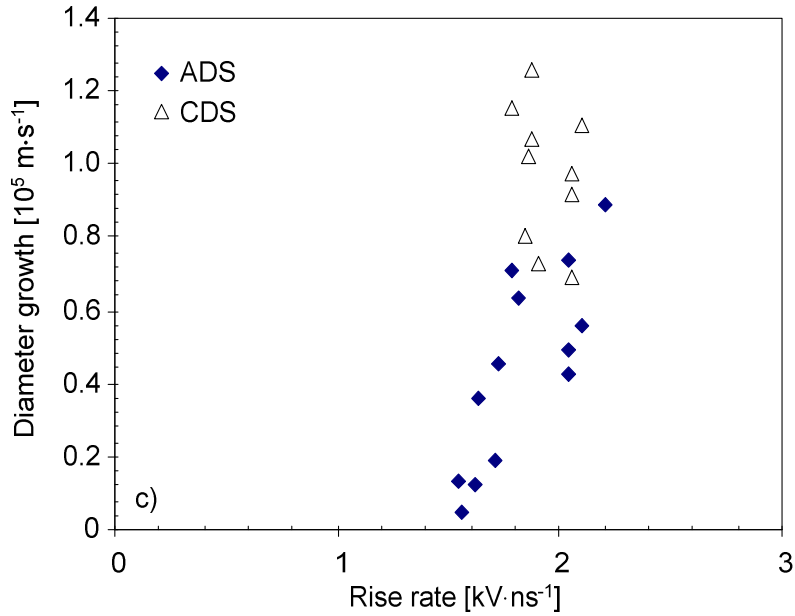


Figure D.4. Continued. c) Comparison between ADS and CDS. The wire-plate distance was fixed at 37 mm. The applied voltage was 60-70 kV.

D.1.5 Streamer density

Figure D.5a shows, for CDS, the number of streamers per meter leaving the wire electrode. The number of streamers increases for increasing voltages. Surprisingly however, more streamers are also generated when the rise rate is decreased. An explanation cannot be provided at this time. It has to be reminded however (see Chapter 3) that the error in the determined number of streamers can be significant (> 20%). In Figure D.5b, the CDS and ADS are compared. The results for both polarities overlap, showing no significant differences between CDS and ADS.

The number of streamers arriving at the plate electrode is not equal to the number of streamers generated at the wire. Many streamers do not cover the complete reactor gap as they extinguish at various intermediate positions. A part of the streamers is quenched as a result of their proximity to other streamers. Another part is lost because not all streamers propagate directly towards the plate electrode (see Section D.2). Figure D.5c shows the number of streamers (per meter of wire) arriving at the plate electrode as function of the applied electric field for CDS. Results for different pulse widths, rise rates and DC bias voltages are shown.

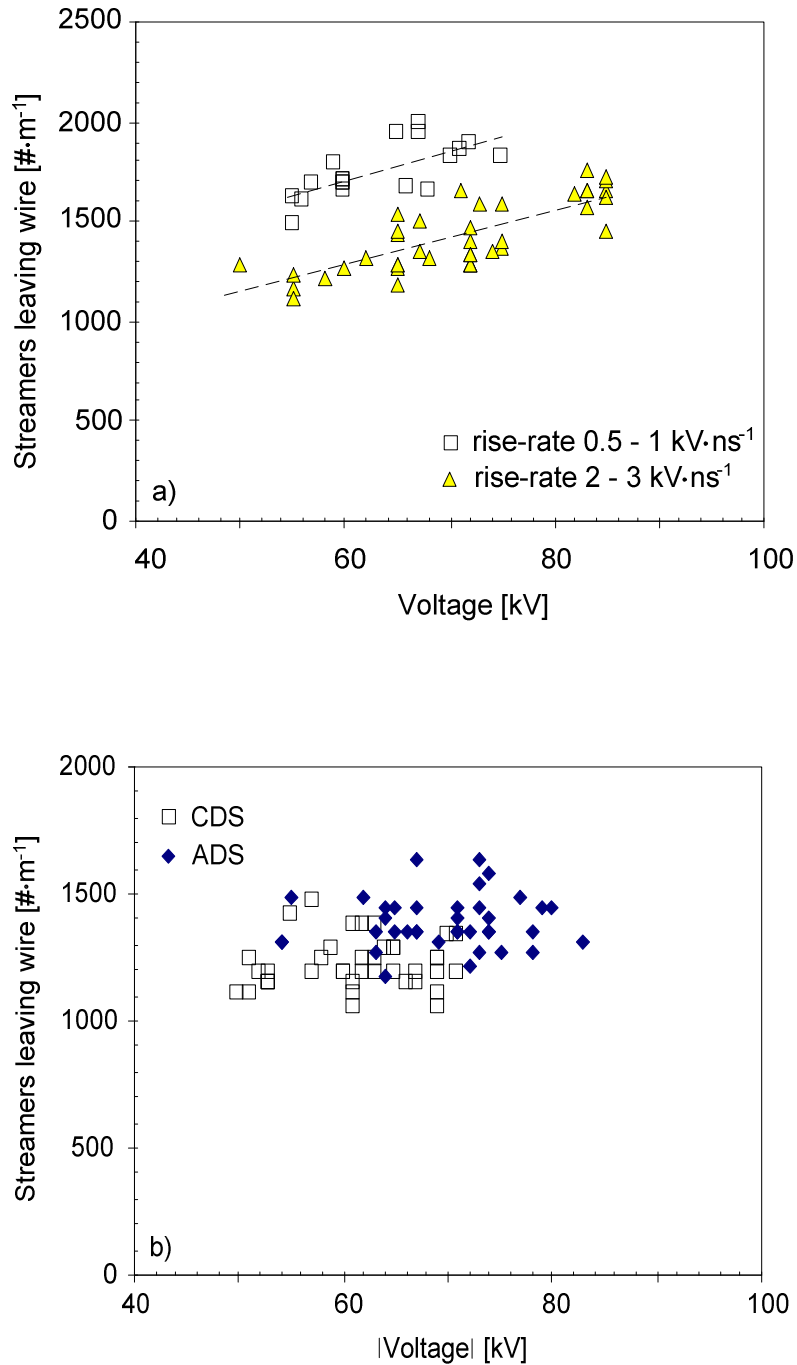


Figure D.5. a) Number of streamers leaving the corona wire as function of applied voltage and rise rate. Results for CDS are shown, wire-plate distance: 57 mm. b) Comparison between CDS and ADS. The wire-plate distance was 37 mm, the rise rate 1.5-2.5 kV·ns⁻¹.

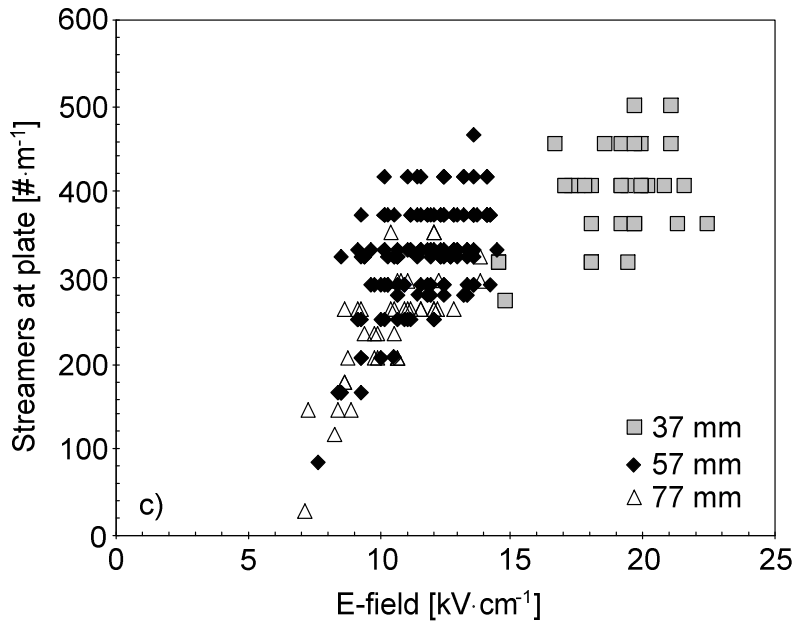


Figure D.5. Continued. c) Number of streamers arriving at plate electrode as function of applied (positive) electric field, for various wire-plate distances. Pulse widths: 100-250 ns, rise rate: 0.5-2.5 kV·ns⁻¹, DC bias: 0-20 kV.

Several interesting observations can be made when studying this figure:

- The significant spread of the data is the result of the error in the interpretation of the ICCD pictures (counting the number of streamers). The spread is not caused by the varied parameters (rise rate, pulse width, DC bias voltage).
- Below 11 kV·cm⁻¹, the number of streamers crossing the complete reactor gap decreases rapidly to zero. Below approximately 4-7 kV·cm⁻¹, no streamers cross the gap anymore. This value is very close to the stability field for the CDS in air, as can be found in the literature: ~5-8.5 kV·cm⁻¹ [Ale(1996), All(1991), Gal(1972), Mor(1997), Rai(1991)].
- At 11 kV·cm⁻¹, an average of 300-350 streamers cross the gap per meter of corona wire. For values above this electric field, the number of streamers increases very gradually.
- For ADS, a similar plot can be generated (not shown in this thesis). The observed behavior is similar to that shown in Figure D.5c, only now the electric fields required to obtain a similar amount of streamers is larger (by a factor of 2).

D.1.6 Secondary streamer length

An extensive discussion about the length of the secondary streamer for CDS and ADS has already been presented in Section 5.4. The secondary streamer is a residual plasma channel consisting of two stable parts. Near the wire, a ‘high’ field region will form, with a reduced electric field of 21.5 kV·cm⁻¹. This region will protrude a certain distance into the

gap. In the remainder of the gap a 'low' field region will form. The field in this region is in the order of $6.5 \text{ kV}\cdot\text{cm}^{-1}$. The length of the high electric field part is determined solely by the amplitude of the applied field. The polarity of the applied voltage does not have a separate effect.

D.2 Top-view photography

Figure D.6 shows a typical example of a top-view ICCD picture. It was found that the specific shape of the streamer paths coincides well with the electric field lines in the gap as a result of the applied voltage. Only near the plate electrode was a discrepancy between the actual streamer paths and the background electric field lines observed. This is probably caused by the fact that the background electric field changes during streamer transit as a result of the presence of the conducting streamer filaments (i.e., the shape of the high potential electrode changes as a result of the conducting streamers).

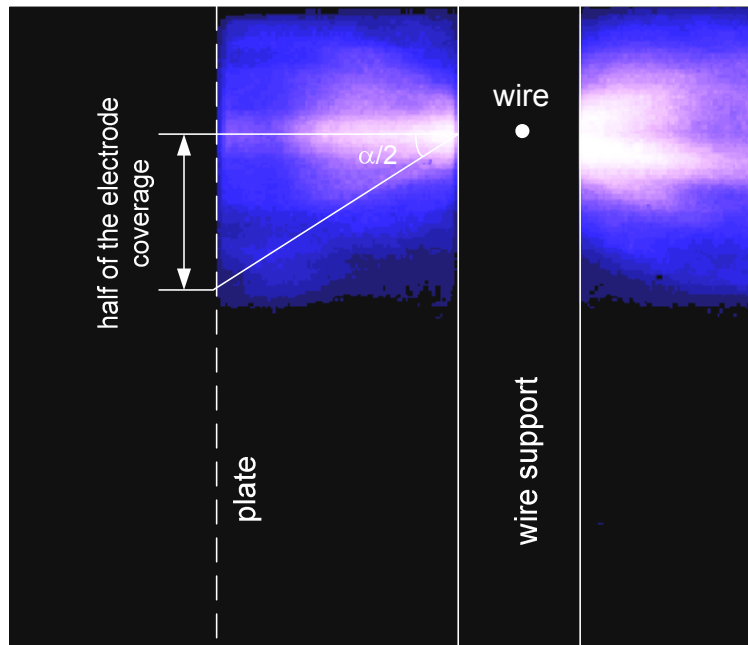


Figure D.6. Top-view picture. Voltage pulse parameter: peak voltage -81 kV , rise rate $2.6 \text{ kV}\cdot\text{ns}^{-1}$, $1.5 \text{ J}\cdot\text{pulse}^{-1}$, pulse width 100 ns , wire-plate distance 37 mm .

Also shown in Figure D.6 is the area of the electrode that is covered with (arriving) streamers. This “electrode coverage” is used in the following as a parameter to characterize the plasma. To obtain a quantitative value for the electrode coverage, the light intensity profile on the plate electrode is plotted as a function of the position. The electrode coverage is then determined as the width of this profile at 20% of the maximum intensity value.

Another parameter used during the following discussion is derived directly from the electrode coverage: the “opening angle” α of the plasma as seen from the wire electrode towards the plate electrode.

D.2.1 Effect of applied voltage, rise time, energy per pulse and pulse width

The measurements presented in this section were all performed on reactor A with a wire-plate distance of 57 mm, a corona wire length of 0.9 m and a diameter of 0.4 mm using positive polarity pulses. Figure D.7 shows a collection of data obtained from the top-view pictures. The average light intensity as function of total reactor voltage is shown in Figure D.7a. The light intensity increases for increasing voltages as can be expected since more energy is dissipated when the voltage is raised. No separate effect of the DC bias voltage can be observed. For shorter pulses, the intensity is lower. This is a direct result of the decreased energy dissipation.

Figure D.7b shows typical examples of the electrode coverage. It can be seen that, as soon as the voltage pulse is sufficiently long and high, the electrode coverage only depends on the total applied voltage. Pulse width, rise time, DC bias voltage, energy per pulse, etc. have no separate effect. This is a strong indication that the opening angle as seen from the wire is only determined by the applied field. For increasing fields, the plate electrode coverage increases. However, this increase saturates once the applied potential reaches 60 kV. Above this value, the plate-electrode coverage has a constant value.

D.2.2 Effect of voltage polarity

The measurements presented in this section were obtained from reactor configuration A with a wire-plate distance of 37 mm. A plot of the average light intensity is not shown here since the observations were similar to the ones shown in Figure D.7a: the average light intensity is proportional to the dissipated energy.

The electrode coverage is shown in Figure D.8. For negative polarity pulses, the coverage is less than that of the positive polarity pulses. This is probably the result of the fact that negative polarity streamers require a larger electric field to propagate.

D.2.3 Effect of reactor configuration

The effect of reactor configuration on the plate-electrode coverage was also examined. Variations as function of the wire length (0.6-0.9 m) were not observed. The wire thickness (0.4-4 mm) also showed no effect on the electrode coverage, indicating that the average applied electric field is the dominant factor, not the field near the wire electrode.

The only reactor parameter that affected the electrode coverage was the wire-plate distance. Results are shown in Figure D.9, in terms of the opening angle. It can be seen that, as a first order approximation, the opening angle is only affected by the average applied electric field.

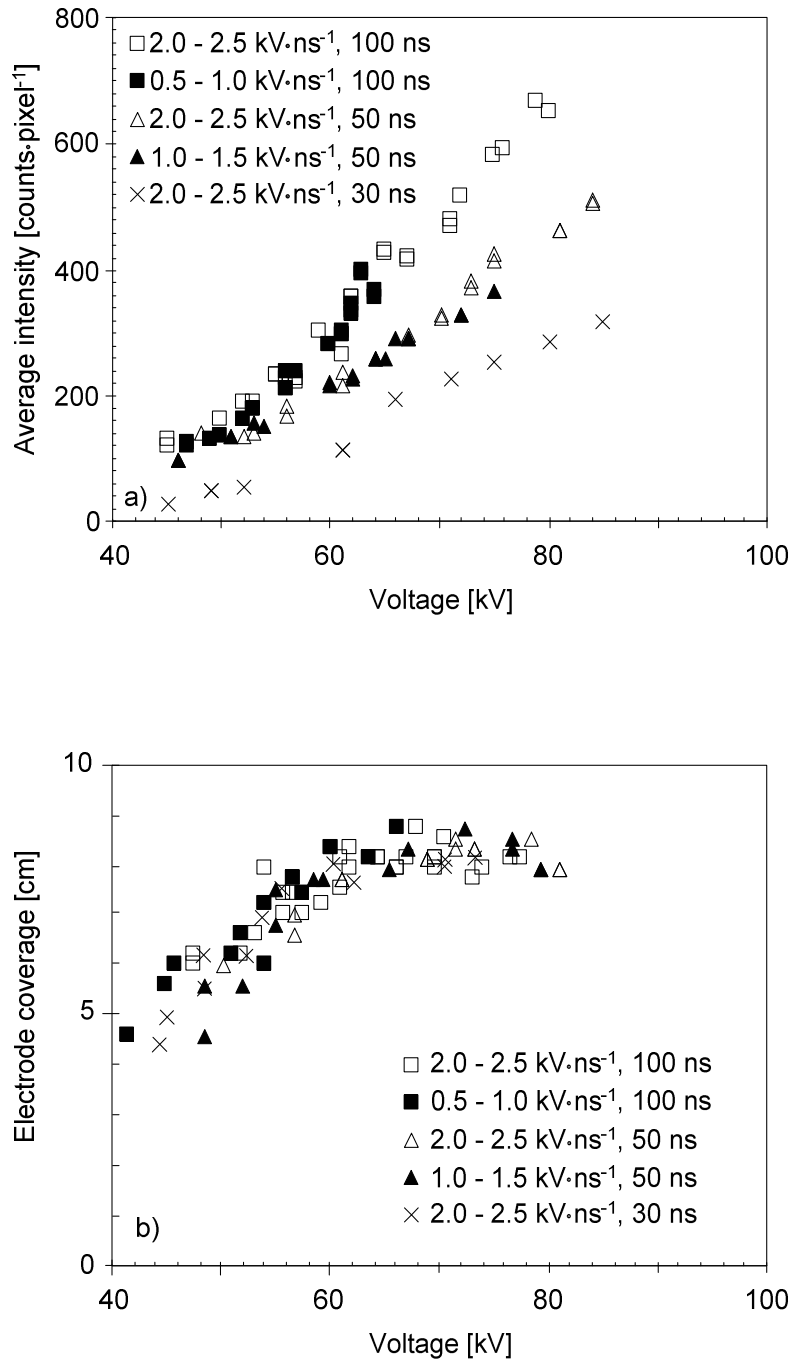


Figure D.7. Overview of results obtained from top-view pictures. Rise rates and pulse widths are specified in the legend. a) Light intensity as function of power modulator settings. b) Electrode coverage as function of power modulator settings.

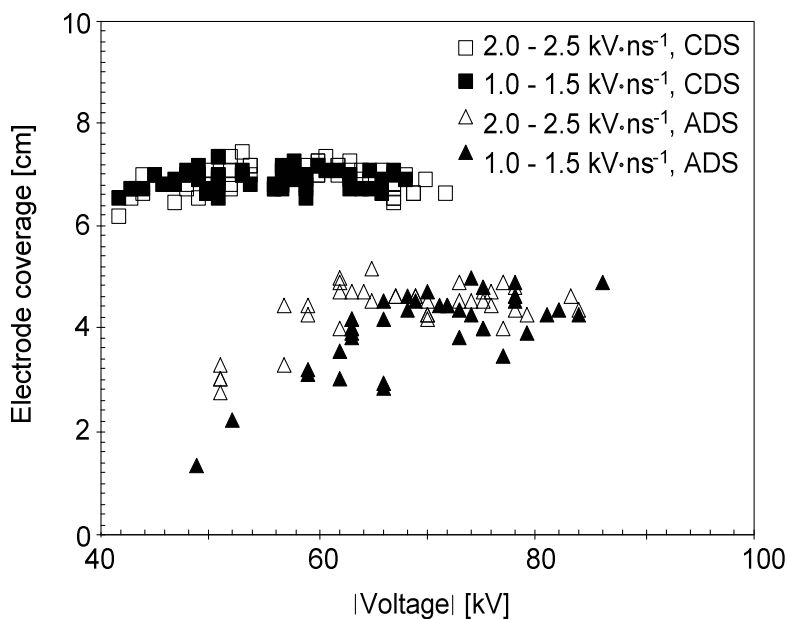


Figure D.8. Plate electrode coverage as function of applied voltage. Reactor configuration A was used with a wire-plate distance of 37 mm. Pulse widths: 70-120 ns.

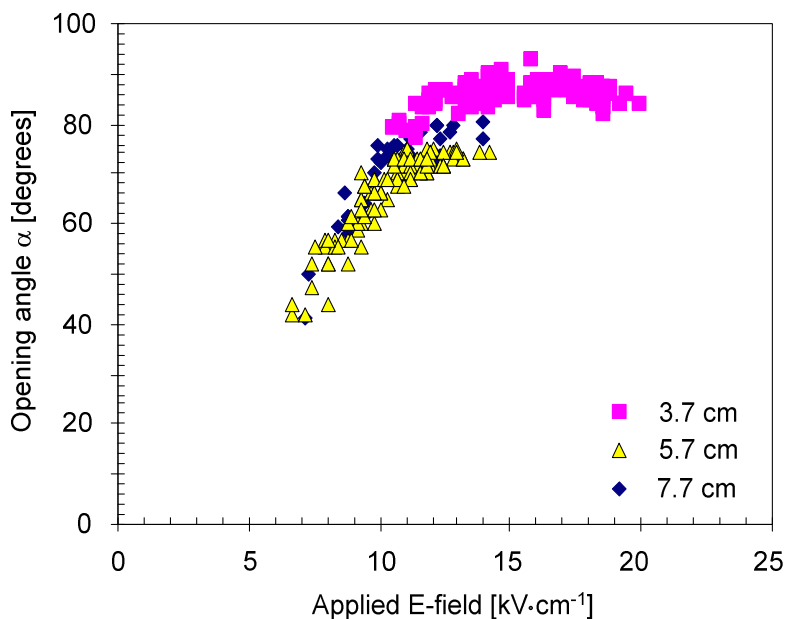


Figure D.9. Opening angle as function of applied electric field. Measurements for different wire-plate distances are shown. Voltage pulse characteristics: positive polarity, rise rate 1.5-2.5 kV·ns⁻¹, pulse width 70-150 ns, DC 0-20 kV.

D.3 Peculiar observations

During the measurements some observations were made that deserve special attention: branching, inter-connecting and re-igniting.

Branching

Branching is the phenomenon that a single streamer head splits into two or more different streamer heads, which continue propagating individually. This effect has been observed by many researchers and can also be seen in nature's lightning flashes. Recently, the occurrence of branching has been modeled by *Mon(2005)* and *Roc(2002)* in negative polarity streamers. It was found that the dimensions of the space-charge layer decrease until the layer becomes infinitesimally thin. Such a boundary exhibits a Laplacian instability, causing the streamer to branch. Provided the electrode gap length is long enough, every streamer was found to branch. During the experiments, branching was mostly observed for low amplitude, positive polarity pulses. It occurs along the complete streamer path; from positions near the wire to positions close to the plate electrode. Multiple branches in a single streamer also occur. An example is shown in Figure D.10a. Negative streamers rarely branch. Only for high voltages was this occasionally observed.

Streamer interconnecting

Streamer interconnecting was seen in many of the time-integrated side-view pictures. An extreme example is shown in Figure D.10b. During interconnection, a streamer traveling towards the plate electrode changes direction rather abruptly towards a neighboring streamer. Upon contact, the deflected streamer merges with the neighboring streamer. This latter one is not disturbed visually. It maintains its original course towards the electrode, with a slightly larger diameter. An explanation for this phenomenon is not available at the moment. Theoretical models are far from predicting such events. A multi-streamer model should become available that takes into account the mutual influence between streamers. Such a model must be 3D in nature. A possible explanation can be found when considering that as a result of the transiting streamers, local space charge effects can become dominant over the background electric field. A streamer that is a little slower, or is not moving completely perpendicular to the plate might sense the space charge field of streamers slightly ahead of its position. If this induced field is strong enough, it is possible that streamers change their direction towards this space-charge. Interconnecting was observed for both positive- and negative-polarity pulses. Almost every picture taken (5 cm of the wire) has at least one interconnecting streamer on it. The number of interconnections increases for decreasing voltages and slower rise times, similar to the occurrence of branching.

Re-ignition

As a result of the voltage reflections, re-ignition of the plasma could sometimes be observed. In those situations where the reflected voltage amplitude was above the streamer inception voltage, new primary streamers were formed. Although these streamers are slower and have a somewhat smaller diameter, they can be classified as primary streamers since they

move throughout the complete reactor gap and disconnect (at least the visible light) from the corona wire. Apparently, the gas in the reactor recovered sufficiently to allow new streamer generation. As stated before, situations in which plasma re-ignition occurred have not been used for the chemical measurements since it is impossible to determine the O^* radical production for all the different streamer phases. In those situations where the voltage reflections were large, the continuous re-ignition of the plasma occasionally led to complete spark breakdown.

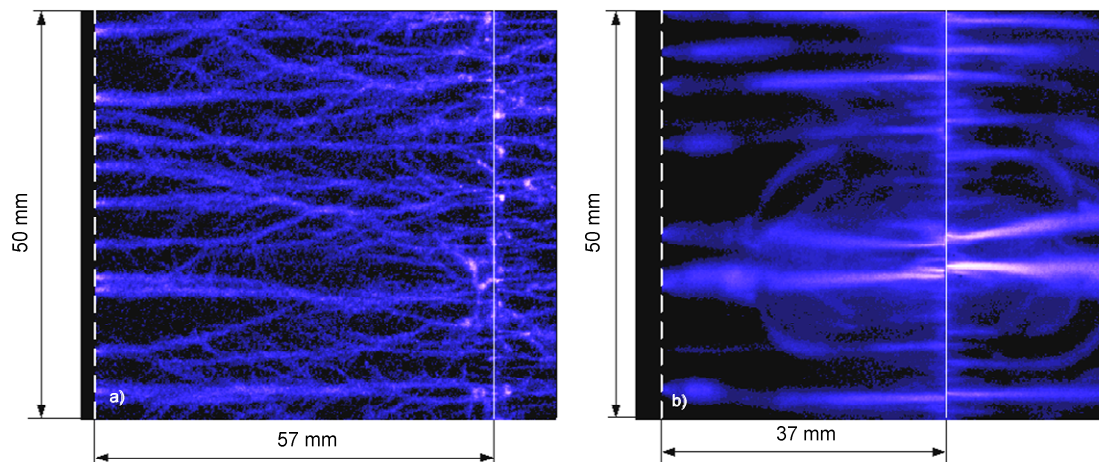


Figure D.10. Example of streamer branching and streamer interconnecting. The solid line indicates the position of the wire. The dashed line is the plate electrode. Time-integrated (400 ns), side-view pictures are shown. a) Pulse width 100 ns, rise rate $1.5 \text{ kV}\cdot\text{ns}^{-1}$, peak voltage +45 kV (no DC bias). b) Pulse width 100 ns, rise time $2.3 \text{ kV}\cdot\text{ns}^{-1}$, peak voltage -79 kV (-15 kV DC).

Bibliography

- Ale(1996) N.L.Aleksandrov and E.M. Bazelyan, “*Simulation of long-streamer propagation in air at atmospheric pressure*”, Journal of Physics D: Applied Physics **29**, pp. 740-752, (1996).
- All(1991) N.L. Allen and M. Boutlendj, “*Study of the electric fields required for streamer propagation in humid air*”, IEE proceedings-A **138**, pp. 37-43, (1991).
- Bab(1997) N. Yu Babaeva and G.V. Naidis, “*Dynamics of Positive and Negative Streamers in Air in Weak Uniform Electric Fields*”, IEEE Transactions on Plasma Science **25**, pp.375-379, (1997).
- Bad(1972) S. Badaloni and I. Gallimberti, “*The inception mechanism of the first corona in non uniform gaps*”, Universita’ Di Padova, Italy, internal report, (1972).
- Bel(2005) Femke van Belzen, Hans G.J.J. Winands, Keping Yan, Zhen Liu, Bert E.J.M. Van Heesch and Guus A.J.M Pemen, “*Optimizing Energy Efficiency Of Pulsed Corona Gas Cleaning Technique: Matching The Reactor To A Pulse Source*”, IEE Pulsed Power Symposium, Basingstoke, United Kingdom, paper number 23, (2005).
- Bis (1998) D. J. Biswas, J. P. Nilaya and U.K. Chatterjee, “*On the recovery of a spark gap in a fast discharge circuit*”, Review of Scientific Instruments **69**, pp. 4242-4244, (1998).
- Blo(1997) P.P.M. Blom, “*High-Power Pulsed Corona*”, Ph. D. Thesis, Eindhoven University of Technology, (1997.)
- Bur(1979) T.R. Burkes, J.P. Craig, M.O. Hagler, M. Kristiansen and W. M. Portnoy, “*A review of High-Power Switch Technology*”, IEEE Transactions on Electron Devices **26**, pp. 1401-1410, (1979).
- Bra(1991) D. Braun, U. Küchler and G. Pietsch, “*Microdischarges in air-fed ozonizers*”, Journal of Physics D: Applied Physics **24**, pp. 564-572, (1991).
- Bri(2005a) T.M.P. Briels, E.M. van Veldhuizen and U. Ebert, “*Experiments on the diameter of positive streamers in air*”, Proceedings of the XXVIIth ICPIG conference, Eindhoven, The Netherlands, no. 04-425, (2005).
- Bri(2005b) T.M.P. Briels, E.M. van Veldhuizen and U. Ebert, “*Branching of Positive Discharge Streamers in Air at Varying Pressures*”, IEEE Transactions on Plasma Science **33**, pp. 264-265, (2005).
- Bri(2006) T.M.P. Briels, J. Kos, E.M. van Veldhuizen and U. Ebert, “*Circuit dependence of the diameter of pulsed positive streamers in air*”, Journal of Physics D: Applied Physics **39**, pp. 5201-5210, (2006).
- Che(2005) J. Chen and P. Wang, “*Effect of Relative Humidity on Electron Distribution and Ozone Production by DC Coronas in Air*”, IEEE Transactions on Plasma Science **33**, pp. 808-812, (2005).
- Cle(1989) J.S. Clements, A. Mizuno, W.C. Finney and R.H. Davis, “*Combined Removal of SO₂, NO_x, and Fly Ash from Simulated Flue Gas Using Pulsed Streamer Corona*”, IEEE Transactions on Industry Applications **25**, pp. 62-69, (1989).
- Cre(1994) Y.L.M. Creyghton, “*Pulsed positive corona discharges, Fundamental study and application to flue gas treatment*”, Ph. D. Thesis, Eindhoven University of Technology, (1994).

- Deu(1993) A.P.J. van Deursen, P.F.M. Gulickx, P.C.T. van der Laan, “*A current and voltage sensor in one unit*”, 8th International Symposium on High Voltage Engineering, Yokohama, Japan, (1993).
- Deu(2006) A.P.J. van Deursen, H.W.M. Smulders, R.A.A. de Graaff, “*Differentiating/Integrating Measurement Setup applied to Railway Environment*”, IEEE Transactions on Instrumentation and Measurement **55**, pp. 316-326, (2006).
- Dha(1987) S.K. Dhali and P.F. Williams, “*Two-dimensional studies of streamers in gasses*”, Journal of Applied Physics **62**, pp. 4696-4707, (1987).
- Din(1990) G. Dinelli, L. Civitano and M. Rea, “*Industrial Experiments on Pulse Corona Simultaneous Removal of NO_x and SO₂ from Flue Gas*”, IEEE Transactions on Industry Applications **26**, pp. 535-541, (1990).
- Ebe(2006) U. Ebert, C. Montijn, T.M.P. Briels, W. Hundsdorfer, B. Meulenbroek, A. Rocco and E.M. van Veldhuizen, “*The multiscale nature of streamers*”, Plasma Sources Science and Technology **15**, pp. S118-S129, (2006).
- Eli(1991) B. Eliasson and U. Kogelschatz, “*Nonequilibrium Volume Plasma Chemical Processing*”, IEEE Transactions on Plasma Science **19**, pp. 1063-1077, (1991).
- Fra(2000) E. Francke, S. Robert and J. Amouroux, “*Hydrodynamic and electrical characterization of a corona discharge plasma reactor*”, High Temp. Material Processes **4**, pp. 139-150, (2000).
- Fuj(2006) M. Fujiwara, “*Short-Pulse Discharge for Simultaneous Pursuit of Energy and Volume-Efficient NO_x Removal*”, Japanese Journal of Applied Physics **45**, pp. 948-950, (2006).
- Gal(1972) I. Gallimberti, “*Mathematical models for the streamer formation in non-uniform gaps*”, Universita' Di Padova, Italy, internal report, (1972).
- Gax(1999) E.H.R. Gaxiola, “*Dielectric breakdown in insulating gases, space charge effects and non-uniform fields*”, Ph. D. Thesis, Eindhoven University of Technology, (1999).
- GMT Document “*Meten en Rekenen Geur*”, publicatiereeks lucht & energie **115**, Ministerie van VROM, 1994 & Nederlandse Emissie Richtlijn Lucht, Lucht **L27**, InfoMil.
- Gor(1994) E.A. Gordeyena and A.A. Matveyev, “*Effect of the waveform of voltage pulses on the efficiency of ozone synthesis in corona discharges*”, Plasma Sources Sci. Technol. **3**, pp. 575-583, (1994).
- Gra(2006) L. R. Grabowski, “*Pulsed Corona in Air for Water Treatment*”, Ph. D. Thesis, Eindhoven University of Technology, (2006).
- Gre(2000) I.V. Grekhov and G.A. Mesyats, “*Physical Basis for High-Power Semiconductor Nanosecond Opening Switches*”, IEEE Transactions on Plasma Science **28**, pp. 1540-1544, (2000).
- Hac(2000) R. Hackam, H. Akiyama, “*Air pollution control by electrical discharge*”, IEEE Transactions on Dielectrics and Electrical Insulation **7**, No. 5, pp. 654-682, (2000).
- Hac(2001) R. Hackham and H. Akiyama, “*Application of Pulsed Power for Removal of Nitrogen Oxides from Polluted Air*”, IEEE Electrical Insulation Magazine **17**, pp. 8-12, (2001).
- Har(1975) G. Hartmann and I. Gallimberti, “*The influence of metastable molecules on the streamer progression*”, Journal of Physics D: Applied Physics **8**, pp.670-680, (1975).

-
- Har(1999) A.P. van Harreveld, P. Heeres and H. Harssema, "A review of 20 Years of Standardization of Odor Concentration Measurement by Dynamic Olfactometry in Europe", *Journal of the Air & Waste Management Association* **49**, pp. 705-715, (1999).
- Hee(1989) E.J.M. van Heesch, A.P.J. van Deursen, M.A. van Houten, G.A.P. Jacobs, W.F.J. Kersten, P.C.T. van der Laan, "Field tests and response of the D/I H.V. measuring system", Sixth International Symposium on High Voltage Engineering, New Orleans, LA, USA, (1989).
- Hos(1971) L.M.L.F. Hosselet, "Ozonbildung mittels elektrischer Entladungen", Ph. D. Thesis, Eindhoven University of Technology, (1971).
- Hos(1988) L.M.L.F. Hosselet, "Martinus van Marum: A Dutch Scientist in a Revolutionary Time", Internal report, Eindhoven University of Technology, (1988).
- Hou(1990) M. A. van Houten, "Electromagnetic Compatibility in High-Voltage Engineering", PhD thesis, Eindhoven University of Technology, (1990).
- Jia(2006) T. Jiang, M.D. Bowden, E. Wagenaars, E. Stoffels and G.M.W. Kroesen, "Diagnostics of electric fields in plasma using Stark spectroscopy of krypton and xenon atoms", *New Journal of Physics* **8**, pp. 1-14, (2006).
- Kel(1964) R. Keller, "Wideband High Voltage Probe", *The review of scientific instruments* **35**, pp. 1057-1059, (1964).
- Ken(1995) J.T. Kennedy, "Study of the avalanche to streamer transition in insulating gases", Ph. D. Thesis, Eindhoven University of Technology, (1995).
- Kim(2004) H-H. Kim, "Nonthermal Plasma Processing for Air-Pollution Control: A Historical Review, Current Issues and Future Prospects", *Plasma Processes and Polymers* **1**, pp. 91-110, (2004).
- Kou(1999) J. M. Koutsoubis, S. J. MacGregor and M. Turnbull, "Triggered Switch Performance in SF₆, Air, and an SF₆/Air mixture", *IEEE Transactions on Plasma Science* **27**, pp. 272-280, (1999).
- Kog(2004) U. Kogelschatz, "Atmospheric-pressure plasma technology", *Plasma Phys. Control. Fusion* **46**, pp. B63-B75, (2004).
- Kul(1997) A.A. Kulikovskiy, "Production of Chemically Active Species in the Air by a Single Positive Streamer in a Nonuniform Field", *IEEE Transactions on Plasma Science* **25**, pp. 439-446, (1997).
- Kul(1998) A.A. Kulikovskiy, "Positive streamer in a weak field in air: A moving avalanche-to-streamer transition", *Physical Review E* **57**, pp. 7066-7074, (1998).
- Kul(2000) A.A. Kulikovskiy, "The role of photoionization in positive streamer dynamics", *Journal of Physics D: Applied Physics* **33**, pp. 1514-1524, (2000).
- Lee(2003) Y. H. Lee, W. S. Jung, Y. R. Choi, J. S. Oh, S. D. Jang, Y. G. Son, M. H. Cho, W. Namkung, D. J. Koh, Y. S. Mok, J. W. Chung, "Application of Pulsed Corona Induced Plasma Chemical Process to an Industrial Incinerator", *Environ. Sci. Technol.* **37**, pp. 2563-2567, (2003).
- Leh(1989) F.M. Lehr and M. Kristiansen, "Electrode Erosion From High Current Moving Arcs", *IEEE Transactions on Plasma Science* **17**, pp. 811-817, (1989).

- Li(2007) C. Li, W.J.M. Brok, U. Ebert and J.J.A.M. van der Mullen, “*Deviations from the local field approximation in negative streamer heads*”, submitted to Journal of Applied Physics.
- Liu(2006a) Z. Liu, K. Yan, G.J.J. Winands, A.J.M. Pemen, E.J.M. van Heesch and D.B. Pawelek, “*Multiple-gap spark gap switch*”, Review of Scientific Instruments **77**, no. 073501, (2006).
- Liu(2006b) N. Liu and V.P. Pasko, “*Effects of photoionization on similarity properties of streamers at various pressures in air*”, Journal of Physics D: Applied Physics **39**, pp. 327-334, (2006).
- Loe(1940a) L.B. Loeb and J.M. Meek, “*The mechanism of spark discharge in air at atmospheric pressure. I.*”, J. Appl. Phys. **11**, pp. 438-447, (1940).
- Loe(1940b) L.B. Loeb and J.M. Meek, “*The mechanism of spark discharge in air at atmospheric pressure. II.*”, J. Appl. Phys. **11**, pp. 459-474, (1940).
- Loe(1965) L.B. Loeb, “*Electrical Coronas, their Basic Physical Mechanisms*”, University of California Press, (1965).
- Low(1992) J.J. Lowke, “*Theory of electrical breakdown in air – the role of metastable oxygen molecules*”, Journal of Physics D: Applied Physics **25**, pp. 202-210, (1992).
- Luq(2007) A. Luque, U. Ebert, C. Montijn and W. Hundsdorfer, “*Photoionization in negative streamers: Fast computations and two propagation modes*”, Applied Physics Letters **90**, number 081501, (2007).
- Mac(1997) S. J. MacGregor, S. M. Turnbull, F. A. Tuema and O. Farish, “*Factors Affecting and Methods of Improving the Pulse Repetition Frequency of Pulse-Charged and DC-Charged High-Pressure Gas Switches*”, IEEE Transactions on Plasma Science **25**, pp. 110-116, (1997).
- Man(2004) G.C.G.M. Manders, “*Conductor to insulator transition and insulator to conductor transition, studied by gas discharges and breakjunctions*”, Ph. D. Thesis, University of Nijmegen, The Netherlands, (2004).
- Mar(1981) E. Marode, “*The glow-to-arc transition in electrical breakdown and discharges in gases*”, Nato ASI Series B: Phys. Vol 89b, ed. E. Kunhardt and L.H. Lueseen, pp. 119-166, (1981).
- Mas(1990) S. Masuda and H. Nakao, “*Control of NO_x by Positive and Negative Pulsed Corona Discharges*”, IEEE Transactions on Industry Applications **26**, pp. 374-382, (1990).
- Mee(194) J.M. Meek, “*A theory of spark discharge*”, Phys. Rev. **57**, pp. 722-728, (1940).
- Mee(1978) J.M. Meek and J.D. Craggs (editors), “*Electrical Breakdown of Gases*”, John Wiley & Sons, ISBN 0-471-99553-3, (1978).
- Mic 8.0 Microcap 8.0.7.0, evaluation version, see webpage: www.spectrum-soft.com
- Miz(1987) A. Mizuno and J. S. Clements, “*Method of Removing SO₂, NO_x and particles from gas mixtures using streamer corona*”, US-patent **4695358**, (1987).
- Mok(2000) Y.S. Mok, “*Efficient Energy Delivery Condition from Pulse Generation Circuit to Corona Discharge Reactor*”, Plasma Chemistry and Plasma Processing **20**, pp. 353-364, (2000).

- Mok(2001) Y. S. Mok, H. W. Lee, Y. J. Hyun, “*Flue gas treatment using pulsed corona discharge generated by magnetic pulse compression modulator*”, Journal of Electrostatics **53**, pp. 195-208, (2001).
- Mon(2005) C. Montijn, “*Evolution of Negative Streamers in Nitrogen: a Numerical Investigation on Adaptive Grids*”, Ph. D. Thesis, Eindhoven University of Technology, (2005).
- Mon(2006a) C. Montijn and U. Ebert, “*Diffusion correction to the Raether-Meek criterion for the avalanche-to-streamer transition*”, Journal of Physics D: Applied Physics **39**, pp. 2979-2992, (2006).
- Mon(2006b) C. Montijn, W. Hundsdorfer and E. Ebert, “*An adaptive grid refinement strategy for the simulation of negative streamers*”, Journal of computational physics **219**, pp. 801-835, (2006).
- Mor(1997) R. Morrow and J.J. Lowke, “*Streamer propagation in air*”, Journal of Physics D: Applied Physics **30**, pp. 614-627, (1997).
- Nai(1996) G.V. Naidis, “*On streamer interaction in a pulsed positive corona discharge*”, Journal of Physics D: Applied Physics **29**, pp. 779-783, (1996).
- Nai(2004) S.A. Nair, “*Corona Plasma for Tar Removal*”, Ph.D. Thesis, Eindhoven University of Technology, (2004).
- Nam(2000) T. Namihira, S. Tsukamoto, D. Wang, S. Katsuki, R. Hackham, H. Akiyama, Y. Uchida and M. Koike, “*Improvement of NO_x Removal Efficiency Using Short-Width Pulsed Power*”, IEEE Transactions on Plasmic Science **28**, pp. 434-442, (2000).
- Nam(2001) T. Namihira, K. Shinozaki, S. Katsuki, R. Hackam, H. Akiyama and T. Sakugawa, “*Characteristics of Ozonizer using Pulsed Power*”, Pulsed Power Plasma Science, Digest of Technical Papers **2**, pp. 1090-1093, (2001).
- Ono(2003a) R. Ono and T. Oda, “*Dynamics of ozone and OH radicals generated by pulsed corona discharge in humid-air flow reactor measured by laser spectroscopy*”, Journal of Applied Physics **93**, pp. 5876-5882, (2003).
- Ono(2003b) R. Ono and T. Oda, “*Formation and structure of primary and secondary streamers in positive pulse corona discharge- effect of oxygen concentration and applied voltage*”, Journal of Physics D: Applied Physics **36**, pp. 1952-1958, (2003).
- Ono(2004) R. Ono and T. Oda, “*Spatial distribution of ozone density in pulsed corona discharges observed by two-dimensional laser absorption method*”, Journal of Physics D: Applied Physics **37**, pp. 730-735, (2004).
- Pan(2001) S.V. Pancheshnyi, S.M. Starikovskaia and A.Yu Starikovskii, “*Role of photoionization processes in propagation of cathode-directed streamer*”, Journal of Physics D: Applied Physics **34**, pp. 105-115, (2001).
- Pan(2003) S.V. Pancheshnyi and A. Yu Starikovskii, “*Two-dimensional numerical modeling of the cathode-directed streamer development in a long gap at high voltage*”, Journal of Physics D: Applied Physics **36**, pp. 2683-2691, (2003).
- Pan(2005) S.V. Pancheshnyi, “*Role of electronegative gas admixtures in streamer start, propagation and branching phenomena*”, Plasma Sources Science and Technology **14**, pp. 645-653, (2005).

- Pas(2002) V.P. Pasko, M.A. Stanley, J.D. Mathew, E.S. Inan and T.G. Wood, “*Electrical discharge from a thundercloud top to the lower ionosphere*”, *Nature* **416**, pp. 152-154, (2002).
- Pem(2003) A.J.M. Pemen, I.V. Grekhov, E.J.M. van Heesch, K. Yan, S. Nair and S.V. Korotkov, “*Pulsed corona generation using a diode-based pulsed power generator*”, *Review of Scientific Instruments* **74**, pp. 4361-4365, (2003).
- Per(1992) P. Persephonis, K. Vlachos, C. Georgiades and J. Parthenios, “*The inductance of the discharge in a spark gap*”, *J. Appl. Phys.* **71**, pp. 4755-4762, (1992).
- Pey(1982) R. Peyrous and R.M. Lapeyre, “*Gaseous products created by electrical discharges in the atmosphere and condensation nuclei resulting from gaseous phase reactions*”, *Atmospheric Environment* **16**, pp. 959-968, (1982).
- Pey(1989) R. Peyrous, P. Pignolet and B. Held, “*Kinetic simulation of gaseous species created by an electrical discharge in dry or humid oxygen*”, *Journal of Physics D: Applied Physics* **22**, pp. 1658-1667, (1989).
- Pey(1990) R. Peyrous, “*The Effect Of Relative Humidity On Ozone Production By Corona Discharge: In Oxygen Or Air – A Numerical Simulation – Part II: Air*”, *Ozone Science & Engineering* **12**, pp. 41-64, (1990).
- Pok(2002) A. Pokryvailo and I. Ziv, “*A hybrid repetitive opening switch for inductive storage systems and protection of DC circuits*”, 25th IEEE Power Modulator Symposium, Hollywood, CA, USA, pp. 612-615, (2002).
- Pok(2004) A. Pokryvailo, Y. Yankelevich, M. Wolf, E. Abramzon, S. Wald, A. Welleman, “*A High-Power Pulsed Corona Source for Pollution Applications*”, *IEEE Transactions on Plasma Science* **32**, No. 5, pp. 2045-2054, (2004).
- Pol 5.1 Polymath 5.1, see webpage www.polymath-software.com
- Puc(1997) V. Puchkarev and M. Gundersen, “*Energy efficient plasma processing of gaseous emission using a short pulse discharge*”, *Appl. Phys. Lett.* **71**, pp.3364-3366, (1997).
- Rae(1939) H. Raether, “*The development of electron avalanches in a spark channel (from observations in a cloud chamber)*”, *Z. Phys* **112**, pp. 464, (1939).
- Rae(1964) H. Raether, “*Electron Avalanches and Breakdown in Gases*”, Butterworths, London, ISBN, (1964).
- Rai(1991) Y.P. Raizer, “*Gas Discharge Physics*”, Springer, ISBN 3-540-19462-2, (1991).
- Rea(1995) M. Rea and K. Yan, “*Evaluation of Pulse Voltage Generators*”, *IEEE transactions on Industry Applications* **31**, pp.507-512, (1995).
- Roc(2002) A. Rocco, U. Ebert and W. Hundsdorfer, “*Branching of negative streamers in free flight*”, *Physical Review E* **66**, no. 035102(R), (2002).
- Rou(1996) R.A. Roush, R.K. Hutcherson, M.W. Ingram and M.G. Grothaus, “*Effects of Pulse Risetime and Pulse Width on the Destruction Of Toluene and NO_x in a Coaxial Pulsed Corona Reactor*”, *Power Modulator Symposium*, Bova Raton, FL, USA, pp. 79-84, (1996).
- Sam(2000) W.J.M. Samaranayake, Y. Miyahara, T. Namihira, S. Katsuki, T. Sakugawa, R. Hackam and H. Akiyama, “*Pulsed Streamer Discharge Characteristics of Ozone Production in Dry Air*”, *IEEE Transactions on Dielectrics and Electrical Insulation* **7**, pp. 254-260, (2000).

- Sei(1986) Seinfeld, J.H. "*Atmospheric chemistry and physics of air pollution*", Wiley, ISBN 0-471-82857-2, (1986).
- Sig(1984) R.S. Sigmond, "*The residual streamer channel: Return strokes and secondary streamers*", *Journal of Applied Physics* **56**, pp. 1355-1370, (1984).
- Šim(2002) M. Šimek and M. Člupek, "*Efficiency of ozone production by pulsed positive corona discharge in synthetic air*", *Journal of Physics D: Applied physics* **35**, pp. 1171-1175, (2002).
- Smi(2002) P.W. Smith, "*Transient Electronics, Pulsed Circuit Technology*", Wiley & Sons, LTD., England, (2002).
- Smu(2001) H.W.M. Smulders, R.A.A. de Graaff, M.F.P. Janssen and G. van Alphen, "*Measurement Systems for AC Traction Power Supply Systems*", International Conference Railway Traction Systems, Capri, Proc. Vol. 2, pp. 139-159, (2001).
- Su(2002) Zhen-Zhou Su, K. Ito, K. Takasima, S. Katsura, K. Onda and A. Mizuno, "*OH radical generation by atmospheric pressure pulsed discharge plasma and its quantitative analysis by monitoring CO oxidation*", *Journal of Physics D: Applied Physics* **35**, pp. 3192-3198, (2002).
- Tar(2002) P. Tardiveau, E. Marode and A. Agneray, "*Tracking an individual streamer branch among others in a pulsed induced discharge*", *Journal of Physics D: Applied Physics* **35**, pp. 2823-2829, (2002).
- Tha(1998) W. J. Thayer, V. C. H. Lo and A.K. Cousins, "*Recovery of a high pulse rate spark gap switch*", 18th IEEE Power Modulator Symposium, pp. 257-264 (1988).
- Tow(1947) J.S.E. Townsend, "*Electrons in Gases*", Hutchinson's Scientific and Technical Publications, London, (1957).
- Vel(1999) E.M. van Veldhuizen (editor), "*Electrical Discharges for Environmental Purposes: Fundamentals and Applications*", New York: Nova Science, ISBN 1-56072-743-8, (1999).
- Vel(2002) E.M. van Veldhuizen and W.R. Rutgers, "*Pulsed positive corona streamer propagation and branching*", *Journal of Physics D: Applied Physics* **35**, pp. 2169-2179, (2002).
- Vel(2003) E.M. van Veldhuizen and W.R. Rutgers, "*Inception behaviour of pulsed positive corona in several gases*", *Journal of Physics D: Applied Physics* **36**, pp. 2692-2696, (2003).
- Vin(1992) A.S. Viner, P.A. Lawless, D.S. Ensor and L.E. Sparks, "*Ozone generation in dc-energized electrostatic precipitators*", *IEEE Transactions on Industry Applications* **28**, pp 504-512, (1992).
- Wag(2006) E. Wagenaars, G.M.W. Kroesen and M.D. Bowden, "*Investigations of Stark effects in xenon Rydberg states by laser-induced fluorescence-dip spectroscopy*", *Physical Review A* **74**, no. 033409, (2006)
- Wan(2001) Y. Wang, "*Odor gas reduction using silent and corona discharge plasma – an experimental study of non-thermal plasma techniques in pollution control*", Ph .D. thesis, University of Minnesota, (2001).

- Win(2004a) G.J.J. Winands, K. Yan, E.J.M. van Heesch, S.A. Nair and A.J.M. Pemen, “*Varying Pulse Parameters To Optimize Pulsed Corona Applications*”, 2nd European Pulsed Power Symposium, Hamburg, Germany, pp. 53-57, (2004)
- Win(2004b) G.J.J. Winands, S.A. Nair, K. Yan, E.J.M. van Heesch and A.J.M. Pemen, “*Generating Pulsed Corona Plasma on an Industrial Scale*”, International Workshop on Cold Atmospheric Pressure Plasmas: Sources and Applications (CAPPSSA), Ghent, Belgium, pp. 108-111, (2004).
- Win(2004c) G.J.J. Winands, S.A. Nair, A.J.M. Pemen, E.J.M. van Heesch and K. Yan, “*A Hybrid-Pulsed Power System for Industrial Applications of Corona Plasma Techniques*”, Hakone IX, Padova, Italy, paper number 8P-01, (2004).
- Win(2005a) G.J.J. Winands, K. Yan, S.A. Nair, A.J.M. Pemen, E.J.M. van Heesch, “*Evaluation of corona plasma techniques for industrial applications: HPPS and DC/AC Systems*”, Plasma Processes and Polymers **2**, Issue 3, pp. 232-237, (2005).
- Win(2005b) G.J.J. Winands, Z. Liu, A.J.M. Pemen, E.J.M. van Heesch, K. Yan, “*Repetitive, triggered, long life-time spark-gap switch for pulsed power applications*”, XXVIIth ICPIG, Eindhoven, The Netherlands, paper number 221, (2005).
- Win(2005c) G.J.J. Winands, Z. Liu, A.J.M. Pemen, E.J.M. van Heesch and K. Yan, “*Long lifetime, triggered, spark-gap switch for repetitive pulsed power applications*”, Review of Scientific Instruments **76**, code 085107, (2005).
- Win(2005d) G.J.J. Winands, Z. Liu, A.J.M. Pemen, E.J.M. van Heesch and K. Yan, “*Novel spark-gap switch design for pulsed power applications*”, IEE Pulsed Power Symposium, Basingstoke, United Kingdom, paper number 27, (2005).
- Win(2005e) G.J.J. Winands, F. van Belzen, K. Yan, Z. Liu, E.J.M. van Heesch and A.J.M. Pemen, “*Optimizing energy efficiency for industrial application of pulsed corona gas cleaning techniques*”, 2nd International Workshop on Cold Atmospheric Plasmas: Sources and Applications (CAPPSSA), Bruges, Belgium, pp. 127-130, (2005).
- Win(2006a) G.J.J. Winands, Z. Liu, A.J.M. Pemen, E.J.M. van Heesch, K. Yan and E.M. van Veldhuizen, “*Temporal development and chemical efficiency of positive streamers in large scale wire-plate reactor as function of voltage waveform parameters*”, Journal of Physics D: Applied Physics **39**, pp. 3010-3017, (2006).
- Win(2006b) G.J.J. Winands, K. Yan, Z. Liu, A.J.M. Pemen, D.B. Pawelek and E.J.M. van Heesch, “*Influence Of Pulse Parameters On Plasma Generation And Chemical Efficiency Of Pulsed Corona Plasma Technique*”, Proceedings of the ISNTPT-5 conference (CD), Oléron Island, France, (2006)
- Win(2006c) G.J.J. Winands, A.J.M. Pemen, E.J.M. Van Heesch, D.B. Pawelek, Z. Liu And K. Yan, “*Increasing The Energy Transfer Efficiency Of Pulsed Corona Systems*”, Euro-Asian Pulsed Power Conference, Chengdu, China, proceedings not yet available, (2006).
- Win(2006d) G.J.J. Winands, K. Yan, A.J.M. Pemen, S.A. Nair, Z. Liu and E.J.M. van Heesch, “*An Industrial Streamer Corona Plasma System for Gas Cleaning*”, IEEE Transactions on Plasma Science **34**, pp. 2426-2433, (2006).

-
- Won(2002) Won J. Yi and P.F. Williams, “*Experimental study of streamers in pure N_2 and N_2/O_2 mixtures and a ≈ 13 cm gap*”, Journal of Physics D: Applied Physics **35**, pp. 205-218, (2002).
- Yam(1998) T. Yamamoto and S. Futamura, “*Nonthermal Plasma Processing for Controlling Volatile Organic Compounds*”, Combust. Sci. and Tech. **133**, pp. 117-133, (1998).
- Yan(1998) K. Yan, H. Hui, M. Cui, J. Miao, X. Wu, C. Boa and R. Li, “*Corona Induced Non-Thermal Plasmas: Fundamental Study and Industrial Applications*”, Journal of Electrostatics **44**, pp. 17-39, (1998).
- Yan(1999) K. Yan, S. Kanazawa, T. Ohkubo and Y. Nomoto, “*Evaluation of NO_x Removal by Corona Induced Non-Thermal Plasmas*”, Trans. IEE of Japan **119-A**, pp.731-737, (1999).
- Yan(2001) K. Yan, “*Corona Plasma Generation*”, Ph.D. thesis, Eindhoven University of Technology, (2001).
- Yan(2004) K. Yan, G.J.J. Winands, S.A. Nair, E.J.M. van Heesch, A.J.M. Pemen, I. de Jong, “*Evaluation of pulsed power sources for plasma generation*”, Journal of Advanced Oxidation Technologies **7**, No. 2, pp. 116-122, (2004).
- Yao(2001) S.L. Yao, E. Suzuki, N. Meng and A. Nakayama, “*Influence of Rise Time of Pulse Voltage on the Pulsed Plasma Conversion of Methane*”, Energy & Fuels **15**, pp. 1300-1303, (2001).
- Yeh(2000) A. Yehia, M. Abdel-Salam and A. Mizuno, “*On assessment of ozone generation in DC coronas*”, Journal of Physics DL Applied Physics **33**, pp. 831-835, (2000).
- Yi(2002) W.J. Yi and P.F. Williams, “*Experimental study of streamers in pure N_2 and N_2/O_2 mixtures and a ~ 13 cm gap*”, Journal of Physics D: Applied Physics **35**, pp.205-218, (2002).

List of Abbreviations

AC	Alternating current
ADS	Anode directed streamer
CDS	Cathode directed streamer
DBD	Dielectric barrier discharge
DC	Direct current
D-I	Differentiating-integrating
EEDF	Electron energy distribution function
EM	Electromagnetic
EMC	Electromagnetic compatibility
EPP	Energy per pulse
ESP	Electrostatic precipitation
FWHM	Full width at half maximum
GCMS	Gas chromatography mass spectroscopy
HPPS	Hybrid pulsed power system
ICCD	Intensified charge-coupled device
IGBT	Insulated gate bipolar transistor
LIF	Laser induced fluorescence
MAC	Maximum acceptable concentration
NTP	Normal temperature and pressure (300 K, 1 bar)
PFL	Pulse forming line
PMT	Photo-multiplier tube
pps	Pulses per second
pr	Pulse repetition rate
PTFE	Poly-tetra-fluoro-ethylene
PVC	Poly-vinyl-chloride
RF	Radio frequency
RH	Relative humidity
TLT	Transmission line transformer
UV	Ultra-violet
VIS	Visual light
VOC	Volatile organic compound

Nomenclature

α	First Townsend ionization coefficient
$\underline{\alpha}$	Net-ionization coefficient ($\alpha - \eta$)
β	Thickness of magnetic core around TLT [m]
γ	Distance between the stages of TLT [m]
δ	Diameter of TLT stage [m]
ΔT	Voltage pulse duration [s]
ΔW	Energy gain/loss during chemical reaction [$\text{eV} \cdot \text{molecule}^{-1}$]
$\varepsilon(\lambda)$	Absorption cross-section [$\text{m}^2 \cdot \text{molecule}^{-1}$]
ε_r	Dielectric constant
η	Attachment coefficient
$\eta(\theta)$	Energy transfer efficiency before plasma generation
$\eta_{\text{conversion}}$	Energy transfer efficiency of the first step (charging of C_L)
η_{matching}	Measured energy transfer efficiency of second step (matching)
η_{plasma}	Theoretical energy transfer efficiency of second step (matching)
η_{radical}	Radical yield [$\text{mole} \cdot \text{kWh}^{-1}$]
η_{system}	Total system efficiency [$\text{mole} \cdot \text{kWh}^{-1}$]
λ_1	System parameter ($= \tau / Z_{\text{out}} \cdot C_r$)
λ_2	Dimensionless time ($= t / Z_{\text{out}} \cdot C_r$)
μ_0	Magnetic permeability in vacuum [$4\pi \cdot 10^{-7} \text{ H} \cdot \text{m}^{-1}$]
μ_r	Relative magnetic permeability
θ	Moment of plasma ignition [s]
τ	Rise-time of voltage pulse at input of TLT [s]
B_{sat}	Saturation field of magnetic core material [T]
c	Speed of light in vacuum [$2.998 \cdot 10^8 \text{ m} \cdot \text{s}^{-1}$]
C^*	Equivalent capacitance of C_{DC} and C_r (in series) [F]
C_{DC}	Coupling capacitor
C_h	High-voltage capacitor, or the capacitance of the PFL [F]
C_L	(Capacitance of) the low-voltage capacitor [F]
c_{O_3}	Ozone concentration [$\text{molecules} \cdot \text{m}^{-3}$]
C_r	Reactor vacuum capacitance [F]
d	Optical path-length for UV absorption [m]
d_{reactor}	Wire-plate distance [cm]
E_{applied}	Applied electric field in reactor [$\text{V} \cdot \text{m}^{-1}$]
E_{ave}	Measured average electric field in primary streamer [$\text{V} \cdot \text{m}^{-1}$]
$E_{\text{ave, matched}}$	E_{ave} in case of matched conditions [$\text{V} \cdot \text{m}^{-1}$]
E_{wire}	Electric field near the wire [$\text{V} \cdot \text{m}^{-1}$]
E_{local}	Local electric field in streamer [$\text{V} \cdot \text{m}^{-1}$]
E_{st}	Stability field in primary streamer channel [$\text{V} \cdot \text{m}^{-1}$]
E/N	Reduced electric field [Td]
f	Pulse repetition rate [pps]; also called prr
F	Gas flow rate in reactor [$\text{m}^3 \cdot \text{s}^{-1}$]
H	Hedonic value

$I_0(\lambda)$	Background intensity spectrum (only air)
$I(\lambda)$	Absorption spectrum (ozone present)
I_{cap}	Capacitive reactor current [A]
I_{HV}	Current as measured using D-I system [A]
I_{plasma}	Plasma current [A]
k	Length of secondary streamer [m]
l	Length of the TLT [m]
L_{add}	Additional inductor in series with spark gap [H]
L_{r}	Inductance of reactor (wiring and plasma) [H]
n	Transformer winding ratio
N	Particle density [m^{-3}]
N_{X}	Number of type-X particles
N_{pulses}	Number of high-voltage pulses
R_{add}	Additional resistor (parallel to reactor, 390 Ω)
r_{begin}	Streamer diameter at corona wire [m]
r_{end}	Streamer diameter near plate electrode [m]
R_{primary}	Primary streamer duration relative to complete pulse
R_{r}	Load resistance [Ω]
r_{wire}	Corona wire radius [m]
S_{arriving}	Total number of streamers arriving at plate electrode
S_{leaving}	Total number of streamers leaving corona wire
T_{primary}	Primary streamer duration [s]
T_{pulse}	Current pulse duration [s]
V_0	Peak voltage at input side of TLT [V]
V_{∞}	Residual voltage on reactor [V]
$v(t)$	Voltage waveform at input side of TLT
V_{applied}	Applied voltage on reactor [V]
V_{DC}	Applied DC bias voltage [V]
V_{end}	Voltage remaining on C_{h} after pulse [V]
V_{HV}	Voltage as measured using D-I system [V]
V_{reactor}	Calculated voltage on reactor [V]
$v_{\text{s,primary}}$	Primary streamer velocity [$\text{m}\cdot\text{s}^{-1}$]
V_{scope}	Voltage on oscilloscope [V]
V_{sg}	Voltage on C_{h} or on the PFL [V]
V_{streamer}	Total streamer volume in reactor [m^3]
W_{pulse}	Pulse energy [J]
Y_{primary}	Primary streamer O^* radical yield [$\text{mole}\cdot\text{kWh}^{-1}$]
$Y_{\text{secondary}}$	Secondary streamer O^* radical yield [$\text{mole}\cdot\text{kWh}^{-1}$]
Z_0	Impedance of coaxial cable [Ω]
Z_{in}	Input impedance of TLT [Ω]
Z_{out}	Output impedance of TLT [Ω]
Z_{s}	Secondary mode impedance [Ω]

Acknowledgement

Wat een heerlijk gevoel om eindelijk aan het dankwoord te kunnen beginnen, want dat kan maar één ding betekenen: het proefschrift is bijna klaar!

Ik wil graag van de gelegenheid gebruik maken om verschillende mensen te bedanken. Om te beginnen mijn 1^e promotor, prof. Jan Blom, voor de mogelijkheid om binnen de vakgroep EPS te kunnen promoveren en voor het creëren van een goede onderzoekssfeer. Dr. Bert van Heesch wil ik bedanken voor het vele werk dat hij verricht heeft met betrekking tot het grondig doornemen van dit proefschrift. Bert, we hebben vele, goede, inhoudelijke discussies gevoerd. Als direct resultaat van deze discussies heb ik zeer veel kunnen leren en is de kwaliteit van dit proefschrift aanzienlijk verbeterd. I would also like to thank prof. Keping Yan who was closely involved during the first three years of the project. Keping, as a result of our numerous discussions I learned a lot, especially with regard to how to be a researcher. A significant part of my current knowledge I obtained by listening to you! Daarnaast wil ik ook de andere leden van de kerncommissie (prof. G.M.W. Kroesen, prof. U. Ebert en prof. C. Leys) bedanken voor de tijd en moeite die zij gestoken hebben in het doorlezen van dit proefschrift en voor het door hen gegeven commentaar. Dr. Guus Pemen wil ik, naast de inhoudelijke discussies, bedanken voor het ‘on-track’ houden van dit project. Afdwalen is altijd eenvoudig, maar dankzij jouw inspanningen is het einddoel altijd goed in focus gebleven.

Ik ben ook veel dank verschuldigd aan verschillende mensen binnen de Technische Universiteit, de faculteit Elektrotechniek en de vakgroep EPS, die elk op hun eigen manier een steentje hebben bijgedragen: Ad van Iersel, Arie van Staalduinen, Cor Martens. Hennie van der Zanden, Huub Bonné, Huub van Leuken, Rene van Hoppe en de mannen van de GTD: bedankt voor jullie bijdrage aan dit project. Mede dankzij jullie is er een prachtige experimentele opstelling gebouwd!

Alle (ex)-medewerkers en (ex)-studenten van de vakgroep EPS wil ik bedanken voor de mooie tijd, de verleende hulp, de leuke gesprekken en de collegialiteit gedurende de afgelopen jaren. Ik zal in de toekomst met plezier terugdenken aan onze samenwerking. Enkele mensen wil ik nog graag in het bijzonder bedanken: Ir. Laurens van Raaij: bedankt voor de gezelligheid en voor het uitvoeren van een groot aantal van de metingen. Je hebt voor een flinke lastenverlichting gezorgd tijdens de afronding van dit project. Dr. Peter Wouters: bedankt voor de nuttige gesprekken, het samen begeleiden van de instructies en de gezellige BBQ's en borrels. Dr. Lex van Deursen: bedankt voor de hulp bij het ontwerp van de D-I sensoren en het verbeteren van de EMC. ‘Mijn’ drie studenten, Rob Smetsers, Femke van Belzen en Leendert Klaasen: bedankt voor het uitvoeren van verschillende experimenten en voor de mogelijkheid om studenten te kunnen begeleiden. Vooral van dit laatste heb ik veel geleerd! I would also like to thank my colleague Ph.D. Liu Zhen. Zhen: thank you for the pleasant conversations and good luck with finishing your own thesis.

Zonder vrienden kom je er natuurlijk ook nooit. Daarom wil ik graag iedereen bedanken die ik (soms jammer genoeg maar af en toe) tegenkom buiten de TU/e werktijden om: Donderdag 's-middag bij de Van-der-Waals borrel, bij een Stiefel-vergadering, of tijdens een avondje stappen. Aan iedereen: bedankt voor jullie vriendschap. Ook iedereen van de vriendengroep in het Zuiden van het land wil ik bedanken. Het is fijn om te weten dat ik bij jullie altijd kan aanschuiven, ook al ben ik vaak hele periodes niet in de buurt geweest. Vooral de gezelligheid rond en tijdens de carnaval zou ik niet graag willen missen.

Als laatste wil ik nog mijn directe familie bedanken voor hun steun door de jaren heen. Mam, pap, Anja, Geert en Veerle, ik ben blij dat jullie mijn naaste familie zijn. Zonder jullie steun was het niet gelukt!

CURRICULUM VITAE

Hans Winands was born in Kerkrade, the Netherlands, on the 27th of March, 1978. He received his secondary education at 'College Sancta Maria', in Kerkrade.

From 1996 until 2002, he studied Applied Physics at the Eindhoven University of Technology. His graduation project in the group Elementary Processes in Gas discharges was carried out at Philips Lighting Eindhoven. His Master's thesis is titled "Helical instabilities in (Na:Ce) Metal Halide Discharge lamps".

This PhD thesis is the result of his research, which he carried out from December 2002 until March 2007 in the group Electrical Power Systems at Eindhoven University of Technology. The subject was the experimental study of (the generation of) streamer discharges for pollutant abatement purposes.

Since January 2007 he works for HMVT Ede, on the development of a streamer plasma based, industrial scale demonstrator for gas-cleaning.